Final Report

Martian Drone

AE3200: Design Synthesis

Group 2

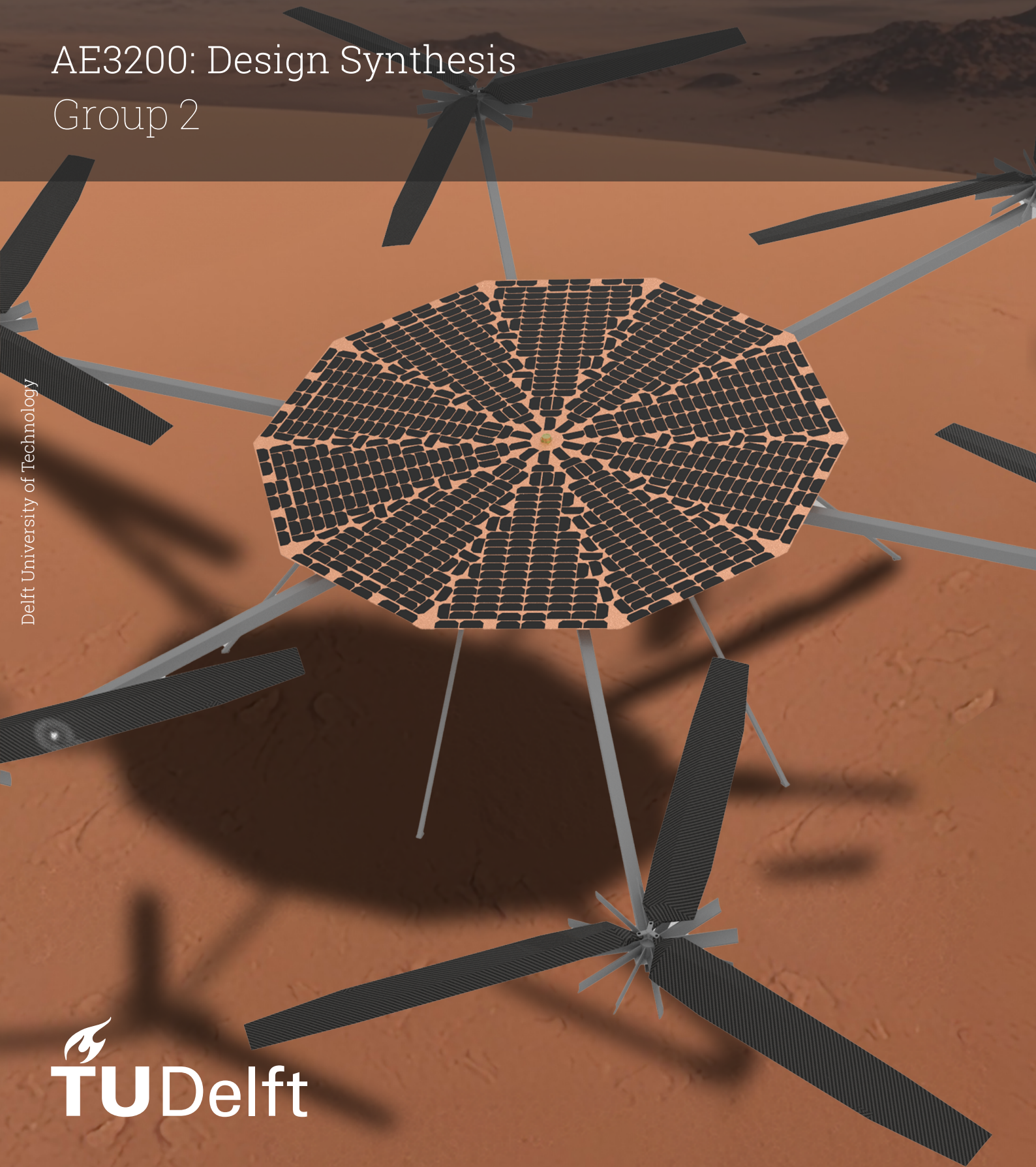

Delft University of Technology

TU Delft

This page is intentionally left blank.

Final Report

Martian Drone

by

Group 2

Student Name	Student Number
Raf Buijsen	5533511
Vini Bull	5326028
Jesse Fleur	5298806
Hanqiu Li Cai	5527708
Florian Mellab	5473349
Dionysios Emmanouil Papaioannou	5468701
Maurits Post	5476798
Salar Ravangouy Mytouei	5533686
Diede van Rheede	5543371
Sebastien Jose Welters	5204968

Version	Date	Authors	Note
1.0	Wednesday 19th June, 2024	All	Draft
2.0	Tuesday 25th June, 2024	All	Final
2.1	Tuesday 26th June, 2024	All	Revised Final

Principal Tutor: A. Sciacchitano
Coaches: P. Gogoi
S. Dewi
Faculty: Faculty of Aerospace Engineering, Delft

TU Delft

Executive Overview

***Authors**: All*

One of the burning questions that has driven Martian exploration in recent years is whether the Red Planet ever hosted alien life. Since the beginning of the space age, humans have tried to solve this question by sending interplanetary vehicles to Mars. This began with orbiters, followed by landers and later on, a more detailed surface exploration began with rovers such as Curiosity and Perseverance. With Ingenuity's inaugural flight on April 19, 2021, the prospect of propelled flight on the Martian atmosphere was proven feasible, facilitating the exploration of much larger and more inaccessible areas. Building upon this breakthrough, the team produced a preliminary design for a Martian aerial drone capable of exploring the surface, identifying rocks with high scientific value, collecting them and transporting them back to a Martian ground station for further analysis and potential sample return to Earth.

This document aims to provide an overview of the design solution and the methodology employed to reach this stage. The design process was driven by the following mission need statement (MNS) and project objective statement (POS):

***MNS**: "Provide a drone capable of continuous flight for 30 minutes on Mars, a flight range of 20 kilometres and identification, collection and transport of three kilograms of Martian rocks."*

***POS**: "Provide a preliminary design for a drone capable of continuous flight for 30 minutes on Mars, a flight range of 20 kilometres and identification, collection and transport of three kilograms of rocks, to be accomplished by 10 students in 10 weeks."*

Scientific Site

Current scientific priorities lie in the characterisation of Martian aqueous basins and the distribution of organic matter [1]. For the Mars Science Environment Laboratory (MSL) and Mars 2020 missions, the scientific community researched over 40 possible locations. These sites were further developed and discussed, resulting in less than ten locations [2, 3]. These two missions were selected as references due to their similar primary scientific objectives to those of the Martian Drone, which shall look for past or present life on Mars. The primary location for the Martian Drone was selected to be the Eberswalde Crater (23.90 °S, 326.74 °E) due to its age, the high probability of river delta remains and presence of clay sediment [1] . One of the reasons why the Eberswalde Crater was not selected for past missions is due to the rocky terrain. For the Martian Drone mission, this is less of a risk, and the Martian drone can fly above the highly rocky terrain. High rock density is also beneficial as it allows for more interesting samples [3]. The exact location is illustrated in Figures 1 and 2.

Using landing simulations, NASA has estimated the success for entry, descent, and landing to be 99.14 % [3]. Location selection impacts the payload instrument selection and atmospheric properties. Thus, the properties of the Eberswalde Crater will be used for future analysis. However, the vehicle is easily adaptable for other locations if a more desirable location is identified.

Market Analysis

In parallel with the design process of the drone, extensive market research was carried out to identify the target segment of the mission. Furthermore, the key stakeholders involved in the mission's scope were determined. These were the project's tutors, who were the main stakeholders of the mission; major space agencies such as NASA and ESA; and finally, the scientific community was interested in the analysis of the Martian environment as a whole. Following the stakeholder analysis, a budget prediction was made for the system based on a statistical analysis of other planetary explorations. From this, a predicted competitive yearly target cost of $30M was derived for the mission. A SWOT analysis of the mission was finally performed on the system by synthesizing the findings of all previous analyses, allowing for the characterisation of the main strengths and weaknesses of the drone from a market perspective. The benefits from this mission not only extend to the scientific community

[1] URL: https://themis.asu.edu/feature/25 [cited on 8 May 2024]

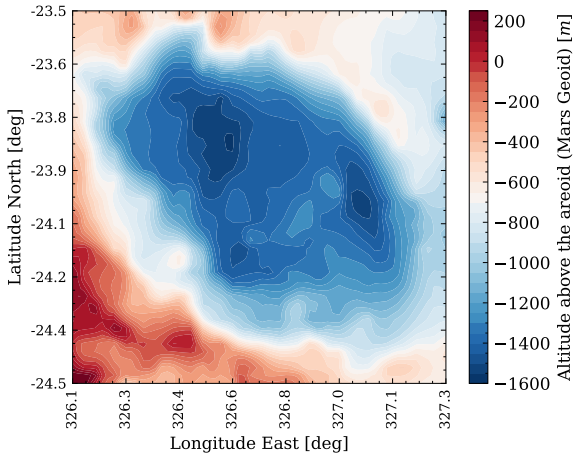

Figure 1: Altitude above areoid of the Eberswalde Crater (24.5° to 23.5°S and 326.1° to 327.3°E) [4]

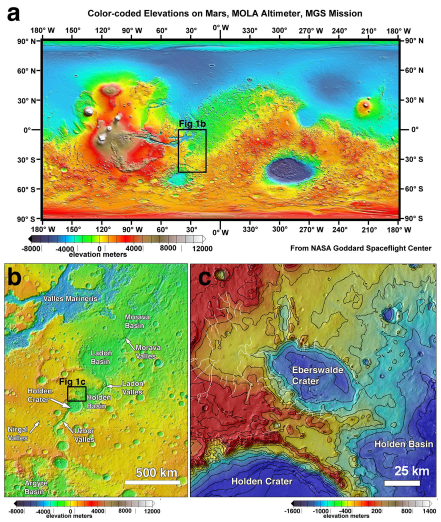

Figure 2: Location of the Eberswalde Crater on Mars [5].

but the benefits to the economy from an investment in this project must not be underestimated. With its target cost of $360M, this project can indirectly support up to 1000 jobs and lead to economic growth in the order of $14bn.

Subsystem Design

The following section will provide the final results of the detailed sizing for each subsystem, along with a summary of the respective methodologies.

Propulsion System

The propulsion system consists of the motors and rotors. Its design began with rotor blade design with the planform design. To minimise the number of input parameters and facilitate blade modelling, the radial dimension from the centre of rotation to the blade tip was normalised, denoted by $\tilde{r}$. Four radial stations were established, from root to tip, including one at each. The root station was not set at the centre of rotation but rather a root cutout, taken to be 8 percent of the rotor radius R. The two intermediate stations were set at 25 % and 75 % of R; the former to allow for a rapid transition from structure-driven airfoils to aerodynamic airfoils, and the latter to ensure the most aerodynamic airfoil is used for the outboard quarter of the blade. The chord and airfoil were inputs at each station, and a quadratic distribution was used to model the blade pitch.

Airfoils with sharp leading edges performed high at low Reynolds numbers and were deemed the most suitable. At the root, a diamond-shaped airfoil was selected, transitioning to a triangular-shaped airfoil and a double-edged plate airfoil along the span of the blade. Using the latter, a 16% to 29% higher lift-to-drag ratio was achieved compared to Ingenuity's CLF5605 airfoil [6].

After the main design tool was finished, an optimisation tool was developed to optimise the geometry of the rotor blades so that the required power per rotor was minimised. Inputs to the algorithm were the rotor radius, number of blades, and the total mass of the drone. Outputs included the optimised blade geometry, the blade's chord and pitch distribution, and the minimised power per rotor. Constraints were also defined, with the primary one being a thrust-to-weight ratio of 1.3, allowing one rotor inoperative flight and maximising controllability. The final results of the rotor and the blades followed from this algorithm and iterations with other subsystems.

Table 1: Rotor results

Optimised blade parameters

Station	Chord	Pitch	Airfoil
8 %R	19.2 cm	15.55°	*Diamond*
25 %R	27.8 cm	14.00°	*Triangular*
75 %R	19.6 cm	10.84°	*Double-edged plate*
100 %R	17.4 cm	10.05°	*Double-edged plate*

Key rotor characteristics

Parameter	Value	Unit
Number of blades	3	–
Rotor radius	1.20	m
Rotor solidity	0.163	–
Max. rotor power	1108	W

The rotor outputs correspond to each of the six rotors in hover, the limiting condition [7]. From here, using the peak power and rotor radius, a customised version of Plettenberg's NOVA 1 rotor is selected off the shelf to provide the required torque and RPM for each rotor [2] .

Electrical Power System

The electrical power system (EPS) plays a key role for the functioning of the Martian drone, responsible for providing a reliable power supply to all onboard systems. The design process to arrive at this architecture was based on a bottom-up approach, building up to a solar array architecture from a power usage profile encompassing all the drone's subsystems, then to a battery architecture and finally to the power distribution architecture. Solar PV panels of 3 m^2 area will fulfil power generation functions, featuring state-of-the-art Quadruple Junction solar cells. A 2375 W h Li-ion battery will provide the drone with power storage functions. At the core of the drone's power management and distribution architecture, a power conditioning and distribution unit will control the operation of the solar arrays, charging/discharging of the battery, control of the power delivery to the propulsion system's six motors and voltage conversion for the drone's low voltage systems. A summary of the EPS architecture is provided in Table 2.

A final EPS design performance analysis was carried out to determine the expected charge time. From this analysis, the drone can perform flights according to the required flight profile throughout the year, although the charge time fluctuates greatly between winter and summer. At its end-of-life, users can expect the drone to replenish its batteries within one sol for 54% of the year and within two sols for 83% of the year.

The team decided to design the drone's propulsion system for a thrust-to-weight ratio of 1.3 to provide a robust and controllable design. A key risk was identified regarding the peak power delivery to the propulsion system during the landing sequence that must be addressed in the detailed design phase of this mission.

Table 2: EPS architecture summary

EPS architecture parameters	Values	Units
Solar array area	3.02	m^2
Solar array configuration	*20S45P*	-
Solar cell type	*Azur Space QJ Solar Cell 4G32C - Advanced* [3]	-
Solar array mass	6.04	kg
Battery capacity	2375	W h
Battery cell type	*LG's Lithium-ion INR 21700 M50LT* [4]	
Battery configuration	*17S9P*	-
Battery mass	10.25	kg
Wire type for propulsion	*Triple AWG12 aluminium wires*	-
Harness and PCDU mass	3.82	kg
EPS total mass	20.11	kg
EPS total cost (Flight Model)	687	k€, FY2024

Thermal Control System

The thermal control system (TCS) is crucial for sustained operations. It provides and maintains all systems within their survival or operational temperatures. It was found that the motor and battery systems are critical components, and a TCS is to be designed for these systems. The same method can be used to develop the TCS for other systems, which is left for future phases.

From the analysis, cooling fins were developed for the motor, ensuring the excess heat generated by the motors is radiated away. These cooling fins are coated with white paint to increase the emissivity coefficient and reduce the absorptivity coefficient. For the battery, a heater and insulator were designed to ensure that the battery was kept in its temperature range. Additionally, it is coated with electroplated gold to ensure a low emissivity coefficient. The resulting design parameters for the systems are illustrated in Tables 3 and 4. The motor

Following the mission profile and propulsion power, and taking into account solar radiation, albedo, planetary thermal radiation, convection, conduction, internal heating and radiation outwards, Figures 3 and 4 are generated for the extreme cases of the motor and battery temperature. As can be seen, neither the battery nor the motor exceeded their limit temperatures, which was the primary goal of the TCS.

[2]URL: https://plettenbergmotors.com/product/nova-1-en/ [cited on 18 June 2024]

[3]URL: https://satsearch.co/products/azur-space-qj-solar-cell-4g32c-advanced [cited on 19 June 2024]

[4]URL: https://f.hubspotusercontent10.net/hubfs/6584819/Cell%20Spec%20Sheets/LG/Lithium%20Ion%20LG%20INR%2021700%20M50LT%202021-LSD-MBD-b00002_21700_M50LT_PS_Promotion_V1.pdf [cited on 19 June 2024]

Table 3: Motor fin parameters

Parameter	Dimension	Unit
L_{fin}	6.28	cm
H_{fin}	15	cm
t_{fin}	2.2	mm
θ	35.7	deg
m_{fin}	0.671	kg
N_{fin}	12	-
ϵ	0.92	-
α	0.2	-

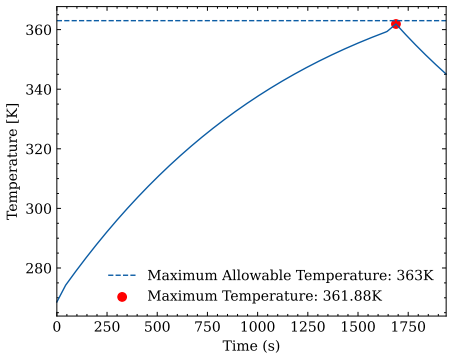

Figure 3: Motor temperature during flight with heater fins on the hottest sol (Areocentric longitude at 255°)

Table 4: Battery heater and insulation parameters

Parameter	Dimension	Unit
t_{ins}	1	cm
k_{ins}	0.035	$W\,m^{-1}\,K^{-1}$
t_{air}	1.5	cm
k_{air}	0.0209	$W\,m^{-1}\,K^{-1}$
$m_{insulator}$	297	g
ϵ	0.03	-
α	0.23	-
P_{heater}	10 to 25	W

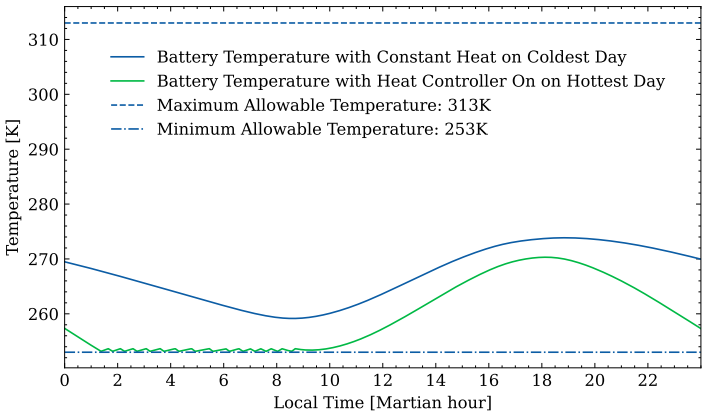

Figure 4: Temperature of the battery with insulator and heater during the hottest sol (Areocentric longitude at 255°) and coldest day (Areocentric longitude at 101°)

Guidance, Navigation and Control

The Martian drone's guidance, navigation and control system will use a state-of-the-art Lidar-Visual-Inertial odometry algorithm called LVI-SAM [8]. This algorithm relies on tightly coupling the incoming data from the camera, the lidar and the IMU (Inertial Measurement Unit) in order to accurately determine the states and position of the vehicle in the environment while performing SLAM (Simultaneous Localization And Mapping). This subsystem will rely on the following odometry sensors and algorithms, which will allow for the determination of the full vehicle state with high accuracy.

Table 5: Component list for the GNC subsystem

Sensor Type	Model	Mass [kg]	Power [W]	Data Rate [Mbit s^{-1}]	Note	Dimensions [m]	Cost [€]
Sun Sensor	Aquila Sun Sensor	0.037	0.15	0.0008	-	0.034 × 0.040 × 0.020	11 215
IMU	InvenSense IIM-46230	0.016	0.144	0.0144	Two are included for redundancy	0.023 × 0.023 × 0.0085	790
Inclinometer	Murata SCA100T	0.0012	0.02	0.0002	-	0.016 × 0.011 × 0.005	166
OBC	Nvidia Jetson AGX Xavier 64GB	0.28	15	1092000	Data rate is data handling rate Two are included for redundancy	0.1 × 0.087 × 0.005	3100
Lidar	Velodyne Puck	0.49	12	57.6	Dimensions are diameter x length	0.103 x 0.073	3700
Laser rangefinder	Lightware LW20-C IP67	0.02	0.715	0.01552	-	0.0195 x 0.0302 x 0.035	350
Fisheye camera	Intel RealSense T265	0.06	1.5	162.8	Data rate assumed streaming Two are included for redundancy	0.108 × 0.0245 × 0.0125	880
Storage device	Exascend PR4 NVMe 15.36TB	0.01	7.5	28000	Data rate is data upload rate	0.1 × 0.07 × 0.007	5000

Furthermore, a preliminary flight computer and controller was developed for the drone in order to prove the controllability of the system. A highly detailed nonlinear dynamic model was implemented, taking into account numerous factors such as motor lag, atmospheric disturbances and other uncertainties. A cascaded PID-like controller was implemented, illustrated in Figure 5, with different control loops active at different stages of flight.

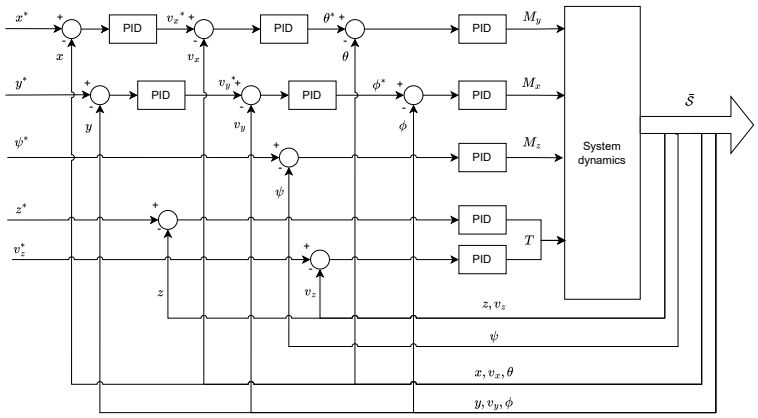

Figure 5: Cascaded PID architecture

Payload Instrumentation

In order to allow for the identification of scientifically significant rock samples, the drone has a need for scanning equipment that is capable of rock identification. To this it was decided that a RGB camera[5] [6] and multispectral camera[7] [8] would be used. A multispectral camera is sensitive to a selection of specific wavelengths of light, for the drone the choice was made for the four wavelengths, based on minerals present in the selected crater[9]: 1.0 µm, 1.4 µm, 1.9 µm and 2.0 µm. These two cameras will work together to generate a 3D mapping of the selected area, first from a high altitude, from which a smaller area is selected using a geology identification algorithm (like what has been developed for Perserverance[9]). Then a smaller area is selected that is deemed the most interesting, which is scanned from a lower altitude from which a rock sample is selected, using rock identification algorithm[10][11], to be collected. An overview of how the algorithm fits within the sample identification can be seen in Figure 6. Once the drone has landed over the sample, and it has been collected, the

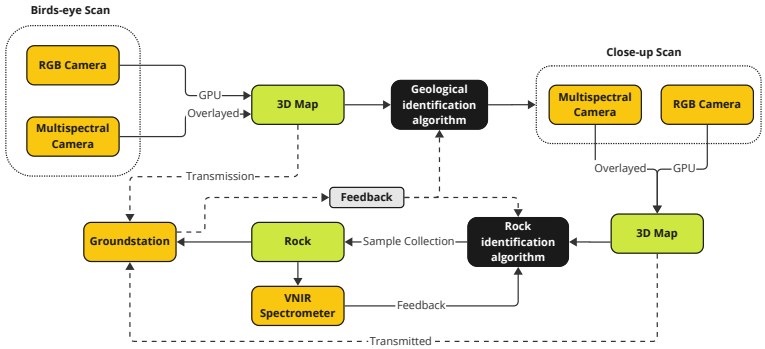

Figure 6: Flow diagram showing the general flow of the role of the rock detection algorithms within the mission profile.

sample will scanned again, to gather initial data and confirm that it indeed should be collected. For this a Visual and Near-InfraRed (VNIR) spectrometer has been selected[12], that can scan the sample in wavelengths from 0.5 µm to 3.65 µm. Since the sample will likely be in the shade of the drone, a tungsten-halogen lamp has been selected to illuminate the sample[10] , and a UV light is selected for even more data gathering[11] . The mass and power of the selected instruments are shown in Table 6.

To analyze the performance of the scanning equipment, it was analyzed in the different scanning configurations. The result of the scanning analysis can be seen in Table 7, where the birds-eye is the higher altitude scan, and

[5]URL: https://www.edmundoptics.eu/p/bfs-u3-50s4c-c-usb-31-blackflyr-s-color-camera/49878/ [cited on 17 June 2024]
[6]URL: https://www.edmundoptics.eu/f/c-series-fixed-focal-length-lenses/13679/ [cited on 17 June 2024]
[7]URL: https://spectraldevices.com/products/custom-camera [cited on 17 June 2024]
[8]URL: https://www.edmundoptics.eu/p/8mm-focal-length-lens-1quot-sensor-format/17859/ [cited on 17 June 2024]
[9]URL: https://www.zooniverse.org/projects/hiro-ono/ai4mars/about/results [cited on 17 June 2024]
[10]URL: https://www.thorlabs.com/thorproduct.cfm?partnumber=SLS201L/M [cited on 14 June 2024]
[11]URL: https://www.bol.com/nl/nl/p/draagbare-blacklight-draagbare-blacklight-uv-lamp-met-led-zaklamp-vals-geld-detector-geocaching/9200000036383815/?referrer=socialshare_pdp_www [cited on 19 June 2024]

Table 6: Scanning instrumentation results

Instrument	Mass	Power
RGB camera	0.14 kg	3 W
Multispectral camera	0.26 kg	4 W
VNIR spectrometer	1.8 kg	5 W
Tungsten-Halogen lamp	1 kg	9 W
UV light	0.1 kg	4 W

Table 7: Performance RGB and Multispectral camera

	Birds-eye		Close-up	
	RGB	*Multispectral*	*RGB*	*Multispectral*
GSD	45.7 mm	188 mm	6.09 mm	25.0 mm
Motion blur	0.38 mm	0.84 mm	0.025 mm	0.055 mm
Scanning time	289 s	421 s	36.0 s	48.0 s

the close-up scan is the lower altitude and, therefore, higher resolution scan.

Communication System

The Martian Drone is capable of autonomous operations, still the drone needs to be able to communicate with Earth to monitor the drone and send mission briefings to the drone. This led to the requirement STK-USER-07: "The Martian Drone shall be capable of real-time communication with a Mars ground station." The drone was, therefore, sized for communication with the ground station. Later in the design process, it was found that on Mars, due to the thin atmosphere, communication for the chosen frequency range from 906 MHz to 924 MHz is limited to a distance of 4.4 km from the ground station[13]. This also means that the aforementioned stakeholder requirement could not be met. Since the communication range was now shortened significantly and the fact that the attenuation on Mars is very low, the required power was found to be 0.29 W, which was found from Figure 7.

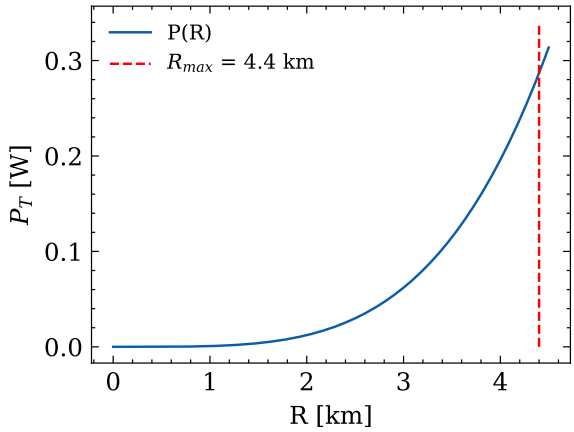

Figure 7: Required transmission power [W] as a function of range [km], showing the maximum communication range of 4.4 km

Given the low power requirement, a simple monopole antenna was selected for the drone communication system. The drone has two monopole antennas (for redundancy), each of which has a length of 15 cm and a mass of 210 g.

Structures and Materials

The drone's structure has three main components: the bus, rotor arms, and landing struts. A sizing method has been established for each component, and a load analysis has been performed. Utilizing in-house developed design tools, the cross-sections of the rotor arms and landing struts have been selected and optimized. A material selection was performed based on Ashby's method in parallel with the sizing. The final structural designs have been validated using FEM analysis and are summarized in Table 8.

Table 8: Overview of Structure Results

Rotor arm structure results

Parameter	Value	Unit
Material	*Beryllium*	-
Cross-section type	*Hollow Rectangular*	-
Outer height	60	mm
Inner height	58	mm
Outer width	40	mm
Inner width	38	mm
Mass	0.638	kg
Max. stress	35	MPa
Max. deflection	4	mm
Max. angular deflection	0.076	deg
Natural frequency	16.38	Hz
Material cost	2185.8	€

Landing struts structure results

Parameter	Value	Unit
Material	*Beryllium*	-
Cross-section type	*Hollow Rectangular*	-
Outer height	15	mm
Inner height	13	mm
Outer width	15	mm
Inner width	13	mm
Length	0.7564	m
Mass	0.078 363	kg
Max. stress	250	MPa
Max. deflection	20.2	mm
Material cost	268.5	€

Bus structure results

Param	Value	Unit
Material	*Cyanate Ester/CF*	-
Shape	*Hexagonal*	-
Radius	0.7	m
Plate height	20	cm
Plate length	80.8	cm
Plate thickness	1	mm
Total mass	3.64	kg
Material cost	797.16	€

Rotor blade structure results

Param	Value	Unit
Material	*Cyanate Ester/HM CF*	-
Cross-section type	*Variable*	-
Length	1.2	m
Thickness	0.1	mm
Pin diameter	10	mm
Lug width	26.8	mm
Mass	76	g
Max. stress	59.49	MPa
Max. lug stress	38.7	MPa
Natural frequency	19.2	Hz
Material cost	299.6	€

Rock Collection System

For the rock collection system, the team designed a robotic arm capable of picking up rocks up to 3 kg in mass and 10 cm^2 in size. The primary motivation for choosing a robotic arm over other systems, such as a linear motion rail system, is its superior range of motion and storage efficiency. The robotic arm mimics the structure of a human arm, comprising a claw (hand), a forearm, and an upper arm, with each section optimised for weight and motor performance. The claw is designed as a peel-clamshell hybrid, using four fingers, ensuring the claw can pick up the rock, store it securely and have digging capabilities.

For the design critical loading cases were analysed to ensure the claw and arm could handle the stresses involved in the rock collection process. The critical loading case for the claw was found to be when the rock was resting entirely on one finger. Furthermore, the arm's critical loading case was found to be in a completely horizontal position, meaning all weights acted perpendicular to the length of the arm.

At each joint in the robotic arm, motors were selected to allow for efficient movement of the entire arm. Specifically, one motor is used to control the claw, two motors are present in the wrist for rotation in two degrees and one motor is in the elbow. Finally, two motors are placed in the drone bus, to control the motion of the shoulder. All motors were selected based on the required torque at each location and were off-the-shelf products from Maxon group [12] A summary of the selected motor-gear combination at each location is provided in Table 9

The final design iteration optimized material, motors, and geometric parameters, ensuring the robotic arm met all functional requirements. In the end, the claw is made from BMI/HS carbon fibre with a quasi-isotropic layup, while the arms use Cyanate ester/HM carbon fibre with a quasi-isotropic. Both materials provide the necessary strength and minimise deflection while optimising the weight of the entire structure. A summary of the final design parameters and structural performance of the arm and claw is provided in Table 10

[12]URL: https://www.maxongroup.nl/maxon/view/catalog/ [cited on 19 June 2024]

Table 9: Motors and gears selected for each motor location in the robotic arm and their performance. Please note all motors are brushless and contain Hall sensors

Motor Location	Motor	Gear	Available Torque [N m]	Required Torque [N m]
Claw	ECX SPEED 16 M Ø16 mm	GPX 19 HP Ø19 mm	2.0	1.25
Wrist	EC-max 22 Ø22 mm	GP 22 HP Ø22 mm	3.4	2.66
Forearm	EC-max 30 Ø30 mm	GP 32 HP Ø32 mm	8.0	7.86
Upper arm	EC 45 flat Ø42.9 mm	GP 42 C Ø42 mm	15.0	14.95

Table 10: Design parameters for final claw and arm design of the rock collection system and the stresses experienced by the structures

Claw design parameters and performance values

Parameter	Value	Unit
Claw Length	0.15	m
Finger Width	0.084	m
Finger Depth	0.038	m
Flange Thickness	0.001	m
Web Thickness	0.001	m
Total Claw Mass	0.228	kg
Maximum Shear Stress	0.138	MPa
Maximum Bending Stress	7.07	MPa
Maximum Bending Deflection	0.029	mm

Arm design parameters and performance values

Parameter	Forearm	Upper Arm	Unit
Length	0.25	0.30	m
Outer Diameter	0.035	0.035	m
Inner Diameter	0.034	0.034	m
Mass	0.045	0.054	kg
Maximum Shear Stress	0.387	0.439	MPa
Maximum Bending Stress	24.44	49.80	MPa
Maximum Bending Deflection	0.365	1.137	mm
Maximum Torsional Stress	3.689	8.680	MPa
Maximum Angular Deflection	0.089	0.252	°

Final Design Overview

Combining the results from each subsystem as presented in the previous section, the final design of the hexacopter was synthesized. The final mass and power budgets of the drone are given by Table 11:

Table 11: MEALS final budget breakdown

Mass budget

	Mass	Unit
Payload	8.85	kg
Scanning	3.30	kg
Collection	2.55	kg
Rock	3.00	kg
Avionics	1.55	kg
GNC	1.30	kg
Comms	0.25	kg
Propulsion	4.50	kg
Motors	2.50	kg
Rotors	2.00	kg
Power	20.18	kg
Array	6.04	kg
Battery	10.25	kg
Other	3.89	kg
Thermals	5.65	kg
Fins	5.35	kg
Heating	0.30	kg
Structures	7.95	kg
Bus	3.65	kg
Arms	3.83	kg
Struts	0.47	kg
Subtotal	48.68	kg
Contingency	2.44	kg
Total	51.12	kg

Power budget

	Power	Unit
Payload	45	W
Scanning	10	W
Collection	35	W
Rock	-	W
Avionics	55	W
GNC	54	W
Comms	1	W
Propulsion	7387	W
Motors	7387	W
Rotors	-	W
Power	-	W
Array	-	W
Battery	-	W
Other	-	W
Thermals	25	W
Fins	-	W
Heating	25	W
Structures	-	W
Bus	-	W
Arms	-	W
Struts	-	W
Subtotal	7512	W
Contingency	376	W
Total	7888	W

Furthermore, the final design was modelled in CATIA to detail the layout of the components in the drone assembly:

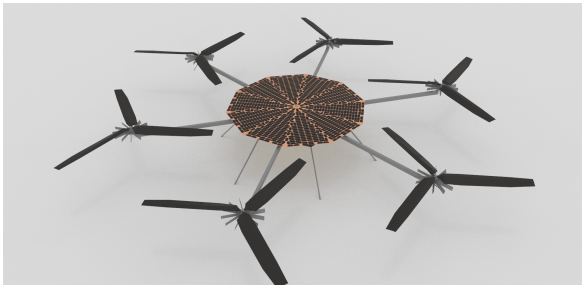

Figure 8: Isometric view of the preliminary drone assembly

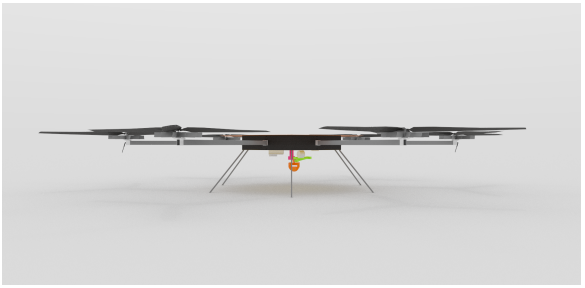

Figure 9: Side view of the preliminary drone assembly

User Requirement Compliance

The following table shows the compliance of the final design with respect to the stakeholder requirements. The asterisk indicates that the requirement is complied with following the currenty analysis, but requires further testing to fully verify.

Table 12: User requirement compliance matrix

Req. ID	Requirement	Complied?	Reason for non-compliance
STK-USER-01	The Martian Drone shall be capable of continuous flight for 30 minutes on Mars.	Yes*	
STK-USER-02	The Martian Drone shall be capable of a total flight range of 20 km.	Yes*	
STK-USER-03	The Martian Drone shall be able to transport a mass of 3 kg of rock samples.	Yes*	
STK-USER-04	The Martian Drone shall be able to store a volume of rock samples of 10 cm x 10 cm x 10 cm.	Yes*	
STK-USER-05	The Martian Drone shall be capable of operation in the Martian atmosphere.	Yes*	
STK-USER-06	The Martian Drone shall be capable of take-off and landing on Martian soil.	Yes*	
STK-USER-07	The Martian Drone shall be capable of real-time communication with a Mars ground station.	No	Infeasible in the Martian environment
STK-USER-08	The Martian Drone shall make use of renewable energy sources for the propulsion system.	Yes	
STK-USER-09	The Martian Drone shall make use of renewable energy sources for the power system.	Yes	
STK-USER-10	The Martian Drone shall be capable of autonomous operation.	Yes*	
STK-USER-11	The Martian Drone shall be capable of object identification to detect rock types.	Yes*	
STK-USER-12	The Martian Drone shall be capable of picking up rock samples.	Yes*	
STK-USER-13-I	The Martian Drone costs for design, building, testing, and getting the drone to Mars shall be within 300M€	Yes	
STK-USER-14-I	The Martian Drone shall help answer the question: "Did life ever exist on Mars?"	No	Can only be verified after mission completion
STK-USER-15-I	The Martian Drone shall be faster than the current fastest land rover, faster than 0.152 $\mathrm{km\,h^{-1}}$	Yes	
STK-USER-16	The Martian Drone shall be capable of transporting rock samples.	Yes*	

Contents

Nomenclature **xiii**

1 Introduction **1**

2 Concept Overview **2**
- 2.1 Scientific Mission . . . 2
  - 2.1.1 Mission Site Selection . . . 2
- 2.2 Concept Trade-off . . . 2
  - 2.2.1 Proposed Concepts . . . 2
  - 2.2.2 Trade-off Criteria . . . 3
  - 2.2.3 Trade-off Results . . . 4

3 Technical, Cost and Schedule Risks **5**
- 3.1 Risk Registries . . . 5
- 3.2 Risk Maps . . . 13

4 Requirements **15**
- 4.1 Stakeholder Requirements . . . 15
- 4.2 Constraints . . . 15
- 4.3 Mission Requirements . . . 17
- 4.4 System Requirements . . . 17
- 4.5 Killer, Key and Driving Requirements . 20

5 Economic Feasibility **21**
- 5.1 Market Analysis . . . 21
  - 5.1.1 Stakeholder Map . . . 21
  - 5.1.2 Similar Missions . . . 22
  - 5.1.3 Target Cost . . . 23
  - 5.1.4 New Markets . . . 23
- 5.2 SWOT Analysis . . . 23
- 5.3 Return on Investment . . . 24

6 Sustainable Development Strategy **25**
- 6.1 End-Of-Life Considerations . . . 25
- 6.2 Environmental Sustainability . . . 25
  - 6.2.1 Sustainable Production . . . 26
  - 6.2.2 Product's Contribution . . . 26
- 6.3 Social and Economic Sustainability . . . 26

7 Operations and Logistics **27**
- 7.1 Concept of Operations . . . 27
- 7.2 Martian Ground Station . . . 27
- 7.3 Flight Profile . . . 29

8 Propulsion **30**
- 8.1 Requirements . . . 30
- 8.2 Rotor Blade Design . . . 31
  - 8.2.1 Radial Stations . . . 31
  - 8.2.2 Airfoil Selection . . . 31
  - 8.2.3 Blade Model . . . 33
- 8.3 Rotor Blade Optimisation . . . 37
- 8.4 Results . . . 38
- 8.5 Motor Selection . . . 39
- 8.6 Verification and Validation . . . 40

9 Electrical Power System **41**
- 9.1 Requirements . . . 41
- 9.2 Environmental Challenges . . . 42
- 9.3 Methodology . . . 44
- 9.4 Verification and Validation . . . 51
- 9.5 Results . . . 51

10 Thermal Control System **53**
- 10.1 Requirements . . . 53
- 10.2 Methodology . . . 54
  - 10.2.1 Thermal Balance . . . 54
  - 10.2.2 Time Dependant Analysis Method 55
  - 10.2.3 Motor Thermal Design Methodology . . . 56
  - 10.2.4 Battery Thermal Design Methodology . . . 57
- 10.3 Verification and Validation . . . 57
- 10.4 Results . . . 57
  - 10.4.1 Motor TCS Results . . . 58
  - 10.4.2 Battery TCS Results . . . 59
  - 10.4.3 Total TCS Results . . . 60

11 Guidance, Navigation and Control **61**
- 11.1 Requirements . . . 61
- 11.2 Methodology . . . 62
  - 11.2.1 Guidance and Navigation . . . 62
  - 11.2.2 Control . . . 64
- 11.3 Verification and Validation . . . 68
- 11.4 Results . . . 68
  - 11.4.1 Sensor Selection . . . 68
  - 11.4.2 Control . . . 69

12 Payload Instrumentation **71**
- 12.1 Requirements . . . 71
- 12.2 Methodology . . . 71
  - 12.2.1 Spectrometer Selection . . . 71
  - 12.2.2 Camera Selection . . . 72
  - 12.2.3 Rock Detection Algorithm . . . 72
  - 12.2.4 Scanning Performance . . . 73
- 12.3 Results . . . 74
- 12.4 Verification and Validation . . . 74

13 Communications **75**
- 13.1 Requirements . . . 75
- 13.2 Methodology . . . 75
  - 13.2.1 Data Budget . . . 75
  - 13.2.2 Link Budget . . . 76
- 13.3 Results . . . 76
- 13.4 Verification and Validation . . . 77

14 Structures and Materials **78**
- 14.1 Requirements . . . 78
- 14.2 Methodology . . . 78
  - 14.2.1 Drone Structure Layout . . . 78
  - 14.2.2 Sizing . . . 79
  - 14.2.3 Loading . . . 81

14.2.4 Safety Factors 83
14.2.5 Pin Connections 83
14.2.6 Vibrations 83
14.2.7 Design Tools 84
14.2.8 Material Selection 86
14.3 Results 87
14.3.1 Rotor Arms 87
14.3.2 Landing Struts 88
14.3.3 Bus 88
14.3.4 Rotor Blade 89
14.4 Verification and Validation 90
14.4.1 Verification 91
14.4.2 Validation 91
15 Rock Collection System **94**
15.1 Requirements 94
15.2 Design Introduction 94
15.3 Methodology 95
15.3.1 Structural Breakdown 95
15.3.2 Loading 95
15.3.3 Design Tools 98
15.3.4 Material Selection 100
15.3.5 Motor Selection 101
15.4 Verification and Validation 101
15.4.1 Verification 101
15.4.2 Validation 102
15.5 Results 102
16 Final Design **104**
16.1 System Iteration 104
16.2 Budgets 105
16.3 Electrical Block Diagram 106
16.4 Hardware Diagram 106
16.5 Software, Data Handling and Communication Diagram 107
16.6 System Layout 108
16.7 Functional Flow and Breakdown Structure 109
17 Design Feasibility Analysis **112**
17.1 Performance Analysis 112
17.1.1 Rotor Wake 112
17.1.2 Forward Flight 113
17.1.3 Flight Performance 114
17.2 Sensitivity Analysis 116
17.3 Compliance Matrix 117
17.4 Verification and Validation Procedures . 119
17.5 RAMS Analysis 120
18 Future Development **122**
18.1 Manufacturing, Assembly and Integration Plan 122
18.2 Project Design and Development Logic 123
18.3 Cost Breakdown Structure 127
19 Conclusion **129**
References **131**

Nomenclature

Acronyms

A Analysis

AF Active area Factor

AR Aspect Ratio

AWG American Wire Gauge

BEMT Blade Element and Momentum Theory

BET Blade Element Theory

BMI Bismaleimide

BOL Beginning Of Life

CAD Computer-Aided Design

CF Capacity Factor

CF Carbon Fibre

CF Compression Factor

CNC Computer Numerical Control

CNSA China National Space Administration

COM Communication System

CR Cost Risk

CRS Cruise

CS Control System

CST Constraints

CT Cost

D Demonstration

DC Direct Current

DE Differential Evolution

DEP Double-Edged Plate

DOD Depth Of Discharge

DOF Degree Of Freedom

DOT Design Options Tree

DPL Deployment

DR Data Rate

DSE Design Synthesis Exercise

DSN Deep Space Network

EDL Entry, Descent and Landing

EM Engineering Model

EMC Electromagnetic Compatibility

ENV Environmental

EOL End Of Life

EPCU Ensemble de Préparation des Charges Utiles

EPS Electrical Power System

FBD Free Body Diagram

FBS Functional Breakdown Structure

FEM Finite Element Method

FFD Functional Flow Diagram

FL Focal Length

FM Figure of Merit

FM Flight Model

FRR Flight Readiness Review

GaAS Gallium Arsenide

GaN Gallium Nitride

GE General

GLARE Glass Reinforced Aluminium

GNC Guidance, Navigation and Control

GND Ground Station

GNSS Global Navigation Satellite System

GOV Government

GPS Global Positioning System

GSD Ground Sampling Distance

HM High-Modulus

HS High-Strength

I Inspection

ID Identifier

IMU Inertial Measurement Unit

IPT Interplanetary Travel

IR Infrared

JAXA Japan Aerospace Exploration Agency

LAU Launch

LEG Legal

LEO Low Earth Orbit

Li-ion Lithium-ion

Li-poly Lithium-polymer

LIO Lidar-Inertial Odometry

LIS Lidar-Inertial System

LMSE Landed Martian Surface Exploration

LND Landing

LV Launch Vehicle

LVI-SAM Lidar-Visual-Inertial odometry via Smoothing And Mapping

LVP Launch Vehicle Provider

MCD Mars Climate Database

MD Martian Drone

MEALS Martian Explorer for Astrobiological and Lithological Studies

MNS Mission Need Statement

MPPT Maximum Power Point Tracker

MRN Mars Relay Network

MSH Mars Science Helicopter

MSL Mars Science Laboratory

MSN Mission

MT Momentum Theory

OBC On-Board Computer

OPS Operations

PCDU Power Conditioning and Distribution Unit

PCM Phase-Change Material

PF Packing Factor

PID Positional, Integral, Derivative controller

PLD Scientific Payload and Instrumentation

POS Project Objective Statement

PRD Production

PRO Propulsion System

PV Photovoltaic

QI Quasi-Isotropic

QM Qualification Model

R Resource

R Review

RCS Rock Collection System

RE Re-Entry

RF Radio Frequency

RGB Red, Green, Blue

RPM Revolutions per Minute

RTG Radioisotope Thermoelectric Generator

rx Resolution

SA Solar Array

SAF Safety

SER Sustainability and Environmental Risk

SF Safety Factor

SIL Software-In-the-Loop

SLAM Simultaneous Localization and Mapping

SOC State Of Charge

SPF Single Point of Failure

SPI Serial Peripheral Interface

SR Schedule Risk

SSD Single Shot Detection

STK Stakeholders

STR Structures

SWOT Strengths, Weaknesses, Opportunities, and Threats

SYS System

T Test

T Time

TCS Thermal Control System

TM Team

TR Technical Risk

TRL Technology Readiness Level

TST Testing

TV Thermal Vacuum

U Unit

UART Universal Asynchronous Receiver and Transmitter

UD Unidirectional

UHF Ultra-High Frequency
UN United Nations
USB Universal Serial Bus
UV Ultra-Violet
V&V Verification and Validation
VIO Visual-Inertial Odometry
VIS Visual-Inertial System
VNIR Visual and Near-InfraRed
VSA Vibrations, Shock and Acoustic

Greek Symbols

α	Absorbtivity	-
α	Thermal diffusivity	$m^2\,s^{-1}$
δ	Degradation rate	
δ	Displacement	m
ϵ	Emissivity	-
η	Efficiency	-
γ	Ratio of specific heats	-
λ	Inflow ratio	-
λ	Wavelength	nm
λ_h	Turbulence height factor	-
μ	Advance ratio	-
μ	Dynamic viscosity	$N\,s\,m^{-2}$
μ_s	Static Friction Coefficient	-
ν	Kinematic viscosity	$m^2\,s^{-1}$
ν	Poisson's Ratio	-
Ω	Rotational speed	$rad\,s^{-1}$
ω_n	Natural frequency	Hz
Φ	Torsional displacement	rad
ϕ	Roll angle	rad
ψ	Heading	rad
ρ	Density	$kg\,m^{-3}$
ρ	Resistivity	Ω
ρ	Specific density	$kg\,m^{-2}$
σ	Bending stress	MPa
σ	Normal stress	MPa
σ	Solidity	-
τ	Shear stress	MPa
θ	Incidence angle	rad
θ	Pitch angle	rad
θ	Slope angle	rad
ξ_t	Turbulence process	-
ζ	Damping ratio	-

Roman Symbols

$\bar{\mathcal{F}}$	Input force and moments vector	-
$\dot{Q}$	Heat Rate	W
$\mathcal{K}$	Turbulence process factor	-
Nu	Nusselt number	-
Pr	Prandtl number	-
Re	Reynolds number	-
A	Area	m^2
B	Gebhart factor	-
B	Tip Loss Factor	-
b	Albedo factor	-
b	Number of Bits	bit
b	Width	m
b_{px}	Bits per pixel	$bit\,px^{-1}$
C	Capacity	
C	Received power	W
C	Specific cost	$€\,kg^{-1}$
c	Chord	m
C/N_0	Received power-to-noise ratio	-
c_d	Section drag coefficient	-
c_i	Turbulence factor along axis i	-
c_l	Section lift coefficient	-
C_P	Power coefficient	-
C_P	Specific heat capacity	$J\,kg^{-1}\,K^{-1}$
C_T	Thrust coefficient	-
D	Distance	m
D	Drag	N
d	Distance	m
E	Energy	J
E	Young's Modulus	MPa
E_b	Bit Energy	
F	Force	N
F	View factor	-
f	Drag area	m^2
f	Frequency	Hz
G	Gain	-
g	Gravitational acceleration	$m\,s^{-2}$
H	Height	m
h	Altitude	m
h	Heat transfer coefficient	$W\,m^{-2}\,K^{-1}$
h	Height	m
I	Area moment of inertia	
I	Current	A
i	Incidence angle	rad
I_s	Solar Irradiance	$W\,m^{-2}$
J	Mass moment of inertia	$kg\,m^2$
J	Polar moment of inertia	
K	Stress concentration factor	-
k	Thermal conductivity	$W\,m^{-1}\,K^{-1}$
L	Length	m
L	Loss	-
l	Length	m
l	Rotor arm length	m
L_{FG}	Propagation loss	-
M	Bending Moment	N m
M	Mach number	-
m	Mass	kg
N	Normal Force	N
N_0	Noise power	W
P	Load	N
P	Power	W
p	Perimeter	m
R	Radius	m
R	Reference Frame	-
R	Resistance	Ω
R	Rotor radius	m
r	Radial distance	m
r_f	Landing distance from target	m
R_{sp}	Specific gas constant	$J\,kg^{-1}\,K^{-1}$
S	Solar flux	$W\,m^{-2}$
T	Temperature	K
T	Thrust	N
T	Torque	N m
t	Thickness	mm
t	Time	s
T_s	System noise temperature	K
V	Shear Force	N
V	Velocity	$m\,s^{-1}$
V	Voltage	V
v	Downwash velocity	$m\,s^{-1}$
v	Velocity	$m\,s^{-1}$
W	Weight	N
w	Distributed Weight	N
w	Width	m
w_i	Least squares weight set i	-
W_t	Wiener process	

Superscripts

$*$ Setpoint
$\tilde{}$ Non-dimensionalised

Subscripts

B Body
d Dynamic
h Hover
I Inertial
i Induced
o Profile
p Parasite
$pics$ Pictures
$pxls$ Pixels
T Turbulence
t Tip

1 Introduction

***Author**: Salar*

Humanity continues to push the boundaries of planetary science, with the exploration of Mars being a key frontier. The quest to find life on the red planet is a primary interest of the scientific community, with NASA's Ingenuity helicopter being the latest proof-of-concept for an unmanned aerial vehicle on Mars. This report details the design of the Martian Explorer for Astrobiological and Lithological Studies (MEALS), a hexacopter to identify and collect rock samples on Mars for analysis. The first of its kind, MEALS will result in scientific breakthroughs thanks to its ability to access rough terrain inaccessible to existing rovers such as Perseverance.

This report provides an overview of all MEALS subsystems and how they work together to help the drone achieve its function and meet its requirements. Every subsystem was developed using design tools that allowed for the optimised design of its components and system-wide iteration.

The structure of the report is as follows: Chapter 2 reviews the work done before the subsystem design phase, including the trade-off of concepts for the drone. Chapter 4 lists all stakeholder, mission and system requirements which are to be met by the drone. Following this, Chapter 3 presents development risks in the form of registries and maps. The existing market analysis and sustainability strategy are updated and presented in Chapter 5 and Chapter 6 respectively. In order to set up the subsystem design, Chapter 7 provides an overview of operational and logistical matters, as well as a flight profile.

The subsystem design begins with propulsion (PRO) in Chapter 8, where a detailed rotor design is carried out alongside motor selection. Chapter 9 presents the electrical power subsystem (EPS) development, including the battery, solar array and power distribution. Next, the thermal control (TCS) subsystem design is described in Chapter 10, particularly motor cooling fins and battery insulation. Chapter 11 consists of the guidance, navigation and control (GNC) subsystem, selecting navigation sensors and ensuring the controllability of the drone. Chapter 12 provides an overview of the scientific payload and instrumentation (PLD) subsystem design, where scanners and cameras for rock identification are selected. Subsequently, the communications (COM) subsystem is developed in Chapter 13, arriving at link and data budgets. Chapter 14 (STR) provides a full structural design of the drone, determining masses and selecting materials. Lastly, the rock collection mechanism's robotic arm (RCS) is designed in Chapter 15.

Once all subsystem design tools are developed, a system-wide iteration is carried out in Chapter 16, until the drone mass converges. Simultaneously, this results in mass and power budgets, for which breakdowns are provided in the same chapter. This chapter also includes diagrams explaining the flow of system components, mission functions and the development process. Chapter 17 analyses the feasibility of the system through two approaches; first, a performance analysis is carried out, primarily making use of the design tool from the propulsion subsystem; then, a sensitivity analysis containing additional system-wide iterations verifies the robustness of the final design concerning user requirements. Compliance of subsystems with their corresponding requirements is checked, and the system verification and validation (V&V) procedure is outlined. Finally, Chapter 18 contains a production plan, cost breakdown structure and development plan of future design phases.

2 Concept Overview

Author: Li

In this chapter, a summary of the main design steps taken for the Martian Drone up until the concept selection is presented to the reader. First, in Section 2.1, the primary Science Environment goals of the mission are described, from which the landing site selection is followed. Furthermore, the environmental properties of the selected site are also detailed and divulged in the section. Subsequently, the proposed configurations considered for the design concept trade-off are presented in Section 2.2, along with the definition of the trade criteria and weights. The chapter will finally conclude with the selected concept after performing the numerical trade-off. This final concept is further explored in detail during the current design stage.

2.1. Scientific Mission

In the attempt to find alien life on the Red Planet, the geological history and composition analysis has become of fundamental importance to the scientific community. In line with the research efforts, interplanetary vehicles such as landers and rovers have been sent to Martian soil. The slow speed of such vehicles limited the area they could cover, significantly limiting the scientific returns they provided. With the inaugural flight of Ingenuity, the aerial flight was proven possible in the Martian atmosphere. Building upon this, the team will develop an aerial drone capable of identifying and sampling rocks and performing similar scientific missions.

2.1.1. Mission Site Selection

Current scientific priorities lie in the characterisation of Martian aqueous basins and the distribution of organic matter [1]. For the Mars Science Environment Laboratory (MSL) and Mars 2020 missions, the scientific community researched over 40 possible locations. These sites were further developed and discussed, resulting in less than ten locations [2, 3]. These two missions were selected as references due to their similar primary scientific objectives to those of the Martian Drone, which shall look for past or present life on Mars. The primary location for the Martian Drone was selected to be the Eberswalde Crater (23.90 °S, 326.74 °E) due to its age, the high probability of river delta remains and presence of clay sediment [1] . One of the reasons why the Eberswalde Crater was not selected for past missions is due to the rocky terrain. For the Martian Drone mission, this is less of a risk, and the Martian drone can fly above the highly rocky terrain. High rock density is also beneficial as it allows for more interesting samples [3]. The exact location is illustrated in Figures 2.1 and 2.2. Using landing simulations, NASA has estimated the success for entry, descent, and landing to be 99.14 % [3]. Location selection impacts the payload instrument selection and atmospheric properties. Thus, the properties of the Eberswalde Crater will be used for future analysis. However, the vehicle is easily adaptable for other locations if a more desirable location is identified.

2.2. Concept Trade-off

Due to the mission's broad constraints, various design possibilities must be considered when developing the drone. To ensure the optimal configuration was selected, the team first brainstormed all the possible concepts and configurations that a Martian aerial drone could take. These ranged from fixed-wing concepts to balloons and pseudo-helicopters. Then, they were compiled into a Design Options Tree (DOT), from which the infeasible ones were eliminated. The remaining ones were subsequently sized and compared in a systematic manner.

2.2.1. Proposed Concepts

Following the DOT, four main concepts were considered feasible and explored in greater detail during the preliminary design phase. These are namely:

- **Multicopter**: characterised by multiple rotors arranged symmetrically around the aircraft.
- **Tiltwing**: Characterized by a fully moving wing, which transitions from vertical during takeoff to

[1] URL: https://themis.asu.edu/feature/25 [cited on 8 May 2024]

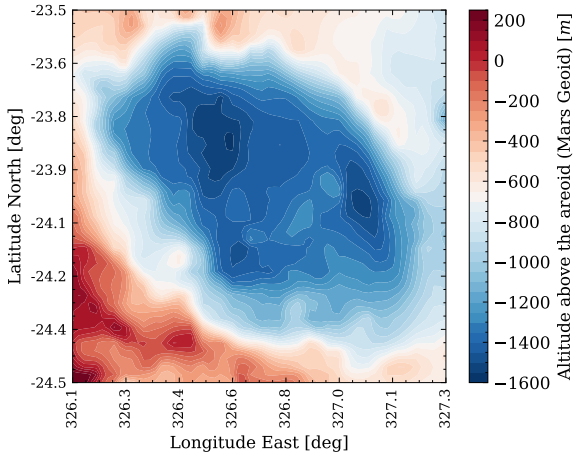

Figure 2.1: Altitude above areoid of the Eberswalde Crater (24.5° to 23.5°S and 326.1° to 327.3°E) [4]

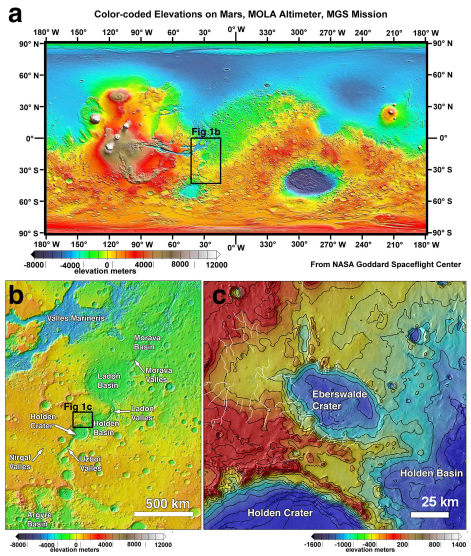

Figure 2.2: Location of the Eberswalde Crater on Mars [5].

horizontal during cruise.

- **Tiltrotor**: Similar to the tiltwing concept, except the wing is fixed; the rotors are the only moving parts.
- **Airship**: Generates lift due to a density difference between the ambient air and the lifting gas inside the vehicle.

These configurations were then sized, leading to a set of initial mass and power budgets, which will be used to perform the numerical trade-off. Note that for the multicopter configuration, a total of 6 rotors is deemed optimal at this stage, whereas for the tiltwing and tiltrotor configurations, it is 2.

2.2.2. Trade-off Criteria

The previously defined configurations will be compared following the following criteria and weights.

- **Propulsive energy required**: To account for both the take-off and cruise power, a mission profile was chosen to calculate the required energy for all design options. This mission consisted of taking off and flying at maximum endurance power for 20 min. A high criterion weight was assigned due to the close link between total propulsive energy and the total system performance in mass and versatility/availability to perform multiple mission cycles. Thus, for the trade-off, it was assigned a criterion weight of **35%**.
- **Controllability**: A high level of controllability over the drone is required to retrieve rocks accurately. This characteristic of the system is fundamental to the mission's success for both retrieval and mapping purposes. Thus, it was assigned a comparatively high weight of **25%**
- **Design complexity**: The complexity of the design was an important aspect to consider for the trade-off analysis since it could be used as a proxy for the risk associated with each design concept. To quantify the design complexity, defining and counting the number of complex systems per concept was decided. A complex system was defined as "Critical moving parts in the system" whose failure would have catastrophic impacts on the mission. Complex systems are significantly more difficult to design and lower the system's reliability. Nonetheless, due to the early stages of the design, the numbers of identified complex systems were highly inaccurate, although they still provided an idea for each configuration. Due to this reason, this criterion was assigned a weight of **15%**.
- **Total system mass**: According to historical trends, the system's mass is directly linked to cost. This can be explained due to lower manufacturing and launch costs. All subsystems scale up with system mass, including the lift that must be generated in flight. A moderate criterion weight was assigned to the total system mass, as the initial estimations were purely based on preliminary analyses of the configurations. However, it was still considered a relevant metric due to its relation to the final system cost, leading to a criterion weight of **15%**.
- **Velocity for maximum range**: The velocity for maximum range indicates the time to complete one mission and the area that can be covered in one flight. As the velocity for maximum range does not theoretically

impact, on a fundamental level, the system's capabilities to carry out the scientific mission, it was assigned a relatively lower weight of **10%**. Nonetheless, it influences the system's versatility and improves the operational range, justifying its inclusion in the trade criteria.

The possible scores and their respective ranges are summarized in Table 2.1:

Table 2.1: Criteria summary

Criterion	Deficient (Score: 1)	Correctable (Score: 2)	Good (Score: 3)	Excellent (Score: 4)
Propulsive Energy	>2625 W h	(2200, 2625] W h	[1300, 2200] W h	<1300 W h
Controllability	No horizontal control or constant altitude control	Horizontal control and maintain altitude	Altitude, horizontal and lateral control	Good + extra DOF
Mass	>123 kg	(90, 123] kg	[74, 90] kg	<74 kg
Design Complexity	>9 complex systems	[7, 9] complex systems	[5, 6] complex systems	<5 complex systems
Velocity at Max Range	<5 m s^{-1}	[5, 10] m s^{-1}	(10, 15] m s^{-1}	>15 m s^{-1}

2.2.3. Trade-off Results

A numerical trade-off was performed using the previously defined criteria and weights, leading to the results presented in Table 2.2.

Table 2.2: Trade-off summary, where the total score is the sum of the scores multiplied by the weight of each criterion, normalized to 100.

Criterion (Weight) / Configuration	Energy (35)	Controllability (25)	Mass (15)	Design Complexity (15)	Velocity at Max Range (10)	Total Score
Tiltwing	1676 W h **(3)**	**(3)**	70 kg **(4)**	7 cmplx sys. **(2)**	87 m s^{-1} **(4)**	**77.5**
Tiltrotor	2789 W h **(1)**	**(3)**	81 kg **(3)**	6 cmplx sys. **(3)**	94 m s^{-1} **(4)**	**60**
Blimp	74 W h **(4)**	**(2)**	77 kg **(3)**	4 cmplx sys. **(4)**	10 m s^{-1} **(3)**	**81.25**
Hexacopter	1929 W h **(3)**	**(4)**	49 kg **(4)**	9 cmplx sys. **(2)**	35 m s^{-1} **(4)**	**83.75**

From Table 2.2, it can be seen that the best-performing configuration will be the hexacopter, followed closely by the airship concept. To ensure the validity of these results, a Monte Carlo sensitivity analysis was carried out, varying the criteria weights randomly 10 000 times. The sensitivity analysis results remained positive for the hexacopter configuration, which will be the concept to be fully designed during the project's current stage. The results of the initial sizing can be seen in Figures 2.4 and 2.5.

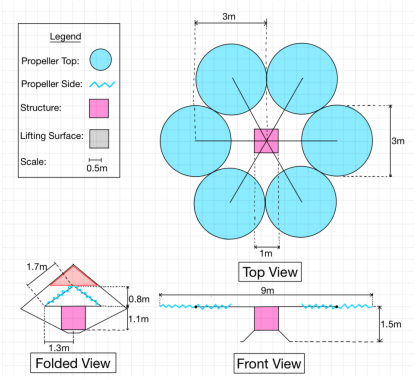

Figure 2.3: Technical sketch of the hexacopter concept

Figure 2.4: Sizing results from initial sizing

Output	Value	Unit
m	46.48	kg
$m_{battery}$	10.25	kg
m_{motor}	3.32	kg
m_{rotors}	7.35	kg
$m_{structure}$	6.73	kg

Figure 2.5: Performance results from initial sizing

Output	Value	Unit
P_{hover}	7686	W
P_{cruise}	5765	W
$E_{mission}$	1929	W h
$E_{battery}$	2411	W h
V_{cruise}	34.9	m s^{-1}

3 Technical, Cost and Schedule Risks

***Authors**: Sebastien*

The risks for the development of the Martian Drone were defined in previous phases and have been updated and presented in this chapter. Each risk is assigned a unique identifier, including a description and rating for probability and impact. Additionally, one or more mitigation strategies are formulated for risk with an elevated rating, resulting in a mitigated likelihood and impact. If the mitigated probability and impact are still considerable, a contingency strategy is also planned, providing a line of action for the case where the risk is realised.

The impact criteria are defined on a scale comprising five qualitative levels, ranging from negligible (score 1) to severe (score 5):

- **Negligible**: Barely noticeable effect on the mission performance; failure to meet the requirement would not affect mission success.
- **Minor**: Some inconvenience or small disruption of the mission performance could affect the secondary mission if the requirement is unmet.
- **Moderate**: Noticeable consequences on the mission performance and degradation of the secondary mission if not addressed appropriately.
- **Major**: Significant disruption of the mission performance, mission success is questionable if requirement is not met.
- **Severe**: Catastrophic consequences on the mission performance, failure to meet the requirement would result in mission failure.

Similarly, the probability criteria range from very unlikely (score 1) to very likely (score 5):

- **Very Unlikely**: The event is highly improbable, with a chance of occurrence only under exceptional conditions.
- **Unlikely**: The event is not anticipated under normal circumstances but may occur occasionally.
- **Possible**: The event could reasonably be expected to occur under normal circumstances.
- **Probable**: The event will likely occur several times during the mission.
- **Very Likely**: The event is certain to occur multiple times throughout the mission.

Each risk's expected impact and probability combination result in a pre-mitigation risk map. After mitigation procedures are identified, a post-mitigation risk map can also be constructed, allowing an overview of the influence of the mitigation strategies. The responsible technical department for each risk is also provided.

First, the risks for all design concepts, impact, and probability of occurrence are presented in risk registries in Section 3.1. Then, the risks for all design concepts are presented in risk maps to illustrate the effect of the mitigation strategies in Section 3.2. This section also formulates requirements to reflect the mitigation strategies.

3.1. Risk Registries

***Authors**: Sebastien* The following risk registries present all identified risks for the Martian Drone. The risks identified include the schedule risks, as presented in Table 3.1, the cost risks, as presented in Table 3.2, the sustainability and environmental risks, presented in Section 3.1, and lastly, the operational and subsystem specific risks, respectively in Tables 3.4 and 3.5. The identifier, risk description, probability, impact, mitigation strategies and contingency strategies are noted for each risk in these registries,

Table 3.1: Schedule risk registry

Risk-ID	Risk	Probability	Impact	Mitigation Strategies	Mitigated Probability	Mitigated Impact	Contingency Strategy	Responsible
SR-PRD-01	Manufacturing of a part fails, and it has to be remade.	Possible	Minor	Audit manufacturers on their past build quality, reducing the probability of part failure.	Unlikely	Minor		Manufacturing Lead
SR-PRD-02	Workers go on strike.	Unlikely	Major	Provide a healthy, transparent working environment, reducing chances of major strikes.	Very Unlikely	Major	Sit down with people on strike to devise a plan for a better workspace and pay.	Team Leader
SR-PRD-03	Parts manufacturers have a backlog in their production.	Possible	Moderate	Set clear deadlines and develop margins for backlog, reducing probability.	Unlikely	Moderate	Sign a production contract with an alternative manufacturer.	Manufacturing Lead
SR-PRD-04	Testing facilities are not available due to unforseen circumstances.	Unlikely	Moderate	Book testing facilities far in advance, with back-up dates as well	Very Unlikely	Moderate	Identify alternative testing facilities, prioritise testing activities	Testing Lead
SR-PRD-05	Delays occur in delivery of (a) part(s) that is made by an external party	Probable	Moderate	Maintain regular communications with external parties to oversee their progress and identify potential future delays	Possible	Moderate	Determine the larger impact on the production timeline and decide whether to make the part with another manufacturer	Business Lead
SR-PRD-07	Parts do not pass the quality control	Probable	Moderate	Audit manufacturers on their past build quality, choose the appropriate production processes	Possible	Moderate	Implement additional quality control measures	Systems Engineer
SR-PRD-08	Integration issues with the launch vehicle occur	Possible	Major	Maintain transparency in communication, conduct integration testing well in advance	Unlikely	Major	Have backup launch vehicles identified, implement a buffer in the project schedule	Project Manager
SR-LAU-01	Launch is postponed due to bad weather	Probable	Moderate	Monitor weather patterns closely and identify multiple launch windows	Probable	Minor	Delay the launch to the next available launch window	Project Manager
SR-LAU-04	The conditions on Mars do not allow for timely entry	Probable	Moderate	Select landing sites with favourable weather conditions	Possible	Moderate	Have alternative entry trajectories, determine backup landing sites	Project Manager
SR-LAU-05	Delays in the Drone's deployment sequence	Possible	Minor	Reduce number of critical components	Unlikely	Minor		Project Manager
SR-OPS-01	Drone cannot fly due to unfavourable weather conditions on Mars	Probable	Major	Continuous monitoring of weather conditions, select take-off window and destinations with favourable conditions	Possible	Major		Project Manager
SR-OPS-02	Unexpected software glitches that need to be solved cause extra delays in the operation of the Drone	Probable	Major	Implement thorough software testing and verification and validation procedures.	Unlikely	Major	Implement redundant and backup software modules	AVN Lead
SR-OPS-03	The drone cannot fly due to insufficient power provided by the power subsystem	Possible	Major	Implement energy-efficient systems, integrate larger energy storage systems	Unlikely	Major	Have backup power supplies available, develop emergency power conservation protocols	EPS Lead

Table 3.2: Cost risks

Risk-ID	Risk	Probability	Impact	Mitigation Strategies	Mitigated Probability	Mitigated Impact	Contingency Strategy	Responsible
CR-PRD-01	Labor costs are increased more than expected	Probable	Moderate	Apply financial margins accounting for the labour cost trends	Probable	Minor	Make use of cost budget margins to account for additional costs	Business Manager
CR-PRD-02	Inflation causes a universal increase in the initially estimated costs more than expected	Possible	Moderate	Apply financial margins corresponding to the trend of the inflation rate	Possible	Minor	Make use of cost budget margins to account additional costs	Business Manager
CR-PRD-03	Transport costs for transportation of vehicle from and to the test site, launch, and storage more than expected	Possible	Moderate	Plan sustainable transportation on Earth	Probable	Minor	Make use of cost budget margins to account for additional costs	Business Manager
CR-PRD-07	Further testing required on expensive testing facilities	Possible	Major	Reserve more time and budget for highly specialized testing campaigns	Possible	Minor		Systems Engineer
CR-PRD-10	Unforeseen technical challenges occur during development	Possible	Major	Keep track of high-risk technical parts and prioritize production and test	Possible	Minor		Systems Engineer
CR-PRD-13	Supply chain disruptions cause an increase in costs	Possible	Moderate	Maintain backlog and relations with alternative suppliers. Have fixed price contracts with partners	Possible	Minor		Business Manager
CR-LEG-01	Unforeseen costs related to regulatory approvals of the mission	Possible	Moderate	Monitor regulatory changes before they are established and plan accordingly; Use contingency margins for quantifiable regulations	Unlikely	Minor		Systems Engineer
CR-LEG-02	Intellectual property disputes leading to additional costs	Unlikely	Minor		Very Unlikely	Minor		Project Manager
CR-OPS-01	Mission is extended beyond the original timeline, increasing operational costs beyond initial estimation	Unlikely	Major	Reserve budget portion for the possibility of extended operations. Develop plan to request for more budget.	Unlikely	Minor		Systems Engineer
CR-SAF-01	Accidents occur that result in legal action	Very Unlikely	Moderate		Very Unlikely	Moderate		Project Manager
CR-LAU-01	Launch delays due to external factors lead to an increased facility, storage, personnel or equipment costs	Possible	Major	Minimize needs for expensive storage and equipment	Possible	Minor		Business Manager
CR-LAU-02	Launch vehicle cost increases	Possible	Major	Reserve spot on launcher early on at fixed contract cost	Unlikely	Major	Communicate frequently with the launch provider to know if any costs change early on	Business Manager

Table 3.3: Sustainability & environmental risks

Risk-ID	Risk	Probability	Impact	Mitigation Strategies	Mitigated Probability	Mitigated Impact	Contingency Strategy	Responsible
SER-01	Introduction of microorganisms from Earth, contaminating the Martian environment and affecting future scientific studies aimed at detecting life forms on Mars	Unlikely	Severe	Usage of cleanrooms during the development process to control the level of biological contamination	Very Unlikely	Severe		Project Manager
SER-02	Contamination of martian environment due to chemical leakage of the drone or small debris (e.g. lubricants)	Unlikely	Moderate	Moderate the usage of chemicals during the design and development of the drone, as well as ensuring high reliability, such that leakages are less probable.	Very Unlikely	Moderate		Project Manager
SER-03	Introduction of orbital debris around Earth	Probable	Major	Use reusable launchers if possible, plan EOL operations accordingly to minimise the creation of orbital debris. (e.g., single-stage insertion, minimising separable parts, etc.)	Unlikely	Moderate		Project Manager
SER-04	Introduction of orbital debris around Mars	Probable	Moderate	Design orbital insertion such that minimal debris is created and plan EOL operations accordingly to minimise the creation of orbital debris (e.g., single-stage insertion, minimising separable parts, etc.)	Unlikely	Moderate		Project Manager
SER-05	Contamination of the Martian environment due to degradation after EOL	Possible	Moderate	Develop a detailed plan for EOL operations and reduce estimated degradation contamination	Unlikely	Minor		Project Manager

Table 3.4: Global & operational technical risks

Risk-ID	Risk	Probability	Impact	Mitigation Strategies	Mitigated Probability	Mitigated Impact	Contingency Strategy	Responsible
TR-PRD-03	Imperfections in manufactured parts	Probable	Moderate	Design parts with margins in mind	Probable	Minor	Implement more thorough quality control measures	Systems Engineer
TR-PRD-05	Drone fails during total system testing	Possible	Major	Do tests on parts before integration	Possible	Moderate	Identify root cause and implement relevant design modifications	Systems Engineer
TR-PRD-06	Drone is damaged during transportation	Possible	Major	Ensure the drone is handled carefully and account for all transportation loads. Add protection devices for transportation	Unlikely	Minor		Systems Engineer
TR-LAU-01	The launch vehicle fails	Unlikely	Severe	Choose a reliable and flight-proven launch vehicle	Very Unlikely	Severe		Systems Engineer
TR-LAU-02	Communication with the launch vehicle is lost causing temporary communication blackout	Possible	Major	Ensure no critical systems need to be in communication during lift-off	Possible	Minor		Systems Engineer
TR-LAU-03	Drone is damaged during launch	Possible	Severe	Perform stress tests to verify if the drone is capable of withstanding the launch loads	Very Unlikely	Major	Check which systems have failed and determine whether the mission can still be partially completed	Systems Engineer
TR-CRS-01	Transit orbit insertion burn is partially successful	Possible	Severe	Have secondary opportunities for and implement correction burns	Unlikely	Moderate		Systems Engineer

Continued on next page

Table 3.4: Global & operational technical risks (Continued)

TR-CRS-02	Landing orbit insertion burn fails	Possible	Major	Conduct thorough pre-flight test, implement backup systems	Unlikely	Moderate	Use backup system, else the mission is not salvageable	Systems Engineer
TR-LND-01	Drone is damaged during atmospheric entry	Very Unlikely	Severe	No mitigation possible	Very Unlikely	Severe	Check which systems have failed and determine whether the mission can still be partially completed	Systems Engineer
TR-LND-02	Drone crashes on Martian surface	Very Unlikely	Severe	No mitigation possible	Very Unlikely	Severe	Check which systems have failed and determine whether the mission can still be partially completed	Systems Engineer
TR-COM-01	Communication of system with ground station cannot be established on startup	Unlikely	Major	Ensure the drone is equipped with an autonomous system to perform corrections for the COM system and software	Very Unlikely	Moderate		COM Lead
TR-GND-02	Communication between ground station and Earth is not established	Unlikely	Major	Have autonomous system equipped with measures to reestablish communication links if not reestablished after a determined amount of time.	Very Unlikely	Moderate		COM Lead
TR-OPS-03	System does not pass pre-flight checks	Possible	Moderate	Establish redundant procedures to overcome failed checks during testing.	Possible	Minor	Attempt manual override of checks	OEC Lead
TR-OPS-15	Space weather events cause damage on system	Possible	Major	Shield components susceptible to dust damage; Develop operations that can help remove dust	Possible	Minor	Perform dust removal operations	OEC Lead
TR-OPS-DEP-01	Landing struts fail to deploy	Possible	Major	Utilise simple mechanisms and test them rigorously.	Unlikely	Major	Try to shake it out in flight. If that fails, perform reconnaissance missions only.	Structures lead
TR-OPS-DEP-02	Solar array fails to deploy fully	Possible	Moderate	Utilise simple mechanisms and test them rigorously. Design power system with safety factor.	Unlikely	Minor	Try to deploy the solar array again. If it partially fails, switch to reduced power mode.	Structures lead
TR-OPS-DEP-03	One or more rotor blades fail to unfold	Possible	Severe	Utilise simple mechanisms and test them rigorously. Design for single rotor failure.	Unlikely	Moderate	Try to unfold the rotor blades again.	Structures lead
TR-OPS-DEP-04	Antenna fails to deploy	Unlikely	Severe	Utilise simple mechanisms and test them rigorously. Add a backup antenna.	Very Unlikely	Minor	Try to deploy the main antenna again. If that fails, use a backup system.	Structures lead
TR-OPS-DEP-05	One or more propeller arms fail to deploy	Possible	Severe	Utilise simple mechanisms and test them rigorously. Design for single propeller failure.	Unlikely	Moderate	Try to deploy the propeller arm(s) again.	Structures lead
TR-OPS-EOL-01	EOL operations are initiated before transmitting final data	Possible	Major	Regularly backup onboard data to the ground station and Earth. Ensure all data has been backed up before performing EOL ops	Possible	Negligible	Attempt data recovery	OEC Lead
TR-OPS-EOL-02	EOL strategy conflict with the interests of other present or future missions on Mars	Possible	Moderate	Investigate impact of EOL strategy from an external perspective before applying it	Unlikely	Moderate	Adjust EOL strategy if possible	OEC Lead

Table 3.5: Subsystem technical risks

Risk-ID	Risk	Probabilit	Impact	Mitigation Strategies	Mitigated Probability	Mitigated Impact	Contingency Strategy	Responsible
TR-PRO-01	Dust accumulation in the motors	Very Likely	Major	Shield motors from the environment. Choose motors with a closed design.	Unlikely	Major	Perform dust removal operations. Monitor the performance and thermals of the affected motor.	PRO Lead
TR-PRO-02	Motor failure on the ground	Unlikely	Severe	Monitor motor health status on-ground. Develop a reliable motor by extensive testing.	Very Unlikely	Severe	Reduce mission frequency and/or motor utilisation if rapid degradation is detected or performance is severely affected. Try to turn the motor on and off.	PRO Lead
TR-PRO-03	Motor failure in-flight	Unlikely	Severe	Have redundancy in the control in case of single motor failure. Monitor vibrations of motors in flight. Perform extensive tests on motors.	Very Unlikely	Severe	Perform emergency landing if performance is severely affected. Try to turn the motor on and off.	PRO Lead
TR-PRO-04	Damaged rotor blade in-flight	Unlikely	Major	Have redundancy in control. Monitor vibrations of blades in-flight. Select strong and tough materials.	Very Unlikely	Major	No future use of the propeller arm if performance is severely affected. Perform emergency landing.	PRO Lead
TR-PRO-05	Damaged rotor blade on descent near a sloped surface	Unlikely	Major	Have sufficient ground clearance.	Very Unlikely	Major	Cut-off power supply to the rotor if performance is severely affected	PRO Lead
TR-EPS-01	Solar array degrades faster than expected	Unlikely	Moderate	Consider EOL performance, including dust abrasion and radiation damage to solar cells	Unlikely	Minor	Switch to reduced power mode.	EPS Lead
TR-EPS-02-I	Solar array is damaged due to exposure to Martian dust	Unlikely	Major	Design with a safety margin and protective layer. Place solar arrays in a location less exposed to dust and small rocks. Analyse the risks posed by dust clouds during takeoff and landing.	Very Unlikely	Moderate	Switch to reduced power mode.	EPS Lead
TR-EPS-03	Battery degrades faster than expected	Unlikely	Major	Consider end-of-life performance in the design. Keep the depth of discharge within manufacturer recommendations.	Unlikely	Minor	Reduce depth of discharge and/or reduce flight frequency if degradation rate is faster than expected.	EPS Lead
TR-EPS-04-I	Battery suffers permanent damage due to exposure to extreme cold temperatures	Possible	Severe	Shield battery from environmental factors. Closely manage battery temperature. Design a reliable battery heating system.	Very Unlikely	Severe	-	EPS Lead
TR-EPS-05	Wired connection is severed	Unlikely	Severe	Design protective structure around wires. Remove any single points of failure.	Very Unlikely	Moderate	Divert power to a secondary system.	EPS Lead
TR-EPS-07	Solar arrays power generation decreases due to dust accumulation	Very Likely	Moderate	Design solar arrays with a margin for dust coverage. Develop dust removal operation with the rotors	Possible	Minor	Perform dust removal operations in flight	EPS Lead
TR-EPS-08	The battery is overloaded, meaning the required power cannot be delivered to the motors	Possible	Severe	Take design margins into account on peak discharge rate capabilities when selecting battery cells. Look into the possibility of using capacitors to provide peak power bursts.	Unlikely	Severe		EPS Lead

Continued on next page

Table 3.5: Subsystem technical risks (Continued)

TR-STR-01	The landing struts deform plastically during hard descent	Unlikely	Moderate	Design with a safety margin.	Very Unlikely	Moderate	Account for uneven take-off and landing.	STR Lead
TR-STR-02	The fingers of the rock collection mechanism deform plastically	Unlikely	Major	Design with a safety margin.	Very Unlikely	Major	Update rock collection mechanism software to function with deformed fingers	STR Lead
TR-STR-03	Plastic deformation of arms of the rock collection mechanism	Unlikely	Major	Design with a safety margin.	Very Unlikely	Major	Update rock collection mechanism software to function with deformed arms	STR Lead
TR-STR-04	Plastic deformation of propeller arms resulting in a higher probability of blade interactions	Unlikely	Major	Design with a safety margin.	Very Unlikely	Major	Account for different thrust vectors.	STR Lead
TR-STR-05	Rotor arm folding mechanism fails after deployment	Possible	Severe	Safety mechanism that locks arm in deployed position	Unlikely	Severe	Attempt to lock the arm by applying reverse thrust to the rotor	STR Lead
TR-STR-06	Rough landing causes damage to vital hardware	Possible	Severe	Implement shock absorption in landing gear	Unlikely	Severe	Attempt to lock the arm by applying reverse thrust to the rotor	STR Lead
TR-STR-08	Drone tips over on a slope	Possible	Major	Account for tipping in the structural design	Very Unlikely	Major	Perform reverse thrust manoeuvre to untip the drone	STR Lead
TR-COM-01	During transmission communication link is lost	Possible	Moderate	Make communication system redundant	Possible	Minor	Back-up communicated data, and try to re-establish the link later.	COM Lead
TR-GNC-01	Navigation sensor malfunctions in flight	Possible	Severe	Have redundant sensors	Possible	Minor	Try to switch navigation sensors off and on, or use a payload camera for navigation.	AVN Lead
TR-GNC-02	Navigation sensor malfunctions on the ground	Possible	Moderate	Have redundant sensors	Possible	Negligible	Try to switch navigation sensors off and on or use payload camera as navigation.	AVN Lead
TR-GNC-03	State determination software fails on the ground	Possible	Minor	Extensive testing of software before implementation.	Unlikely	Minor	Patch software.	AVN Lead
TR-GNC-04	State determination software fails in flight	Possible	Severe	Extensive software testing before implementation.	Unlikely	Severe	Land using payload camera and patch software.	AVN Lead
TR-GNC-05	Sensors do not accurately determine the drone's state	Unlikely	Major	Test the sensors rigorously. Keep a margin into account for the control system. Have secondary sensors ready.	Unlikely	Minor	Use other systems for state determination	AVN Lead
TR-PLD-01	Scanning sensors fail	Possible	Severe	Add shock absorbers for payload instruments, monitor temperatures closely. Design a navigation camera to allow basic rock identification.	Unlikely	Major	Try to switch payload sensors on and off. If that fails, use a navigation camera for basic rock identification.	PLD Lead
TR-PLD-02	Payload software fails	Possible	Severe	Extensive testing of the software before implementation. Design a navigation camera to allow basic rock identification.	Unlikely	Major	Patch error. If that fails, use a navigation camera for basic rock identification.	PLD Lead
TR-PLD-03	Motors in rock collection mechanism fail	Possible	Severe	Extensive testing of the motor in mechanism	Unlikely	Severe	Try to turn off and on.	PLD Lead

Continued on next page

Table 3.5: Subsystem technical risks (Continued)

TR-PLD-04	Rock collection mechanism is obstructed during unfolding	Possible	Minor	Extensive testing of mechanism movement capabilities	Unlikely	Minor	Abort picking up a chosen rock, move to another interesting rock.	PLD Lead
TR-PLD-05	Rock collection mechanism is obstructed during folding	Possible	Major	Extensive testing of mechanism movement capabilities	Unlikely	Major	Attempt to lock mechanism in most efficient position.	PLD Lead
TR-PLD-06	Rock collection mechanism cannot pickup rock as it's submerged in dust	Unlikely	Minor	Design rock collection mechanism have digging capabilities	Very Unlikely	Minor	Abort picking up a chosen rock, move to another interesting rock.	PLD Lead
TR-PLD-07	Rock collection mechanism cannot pickup rock due to weight and size restrictions	Possible	Major	Accurate analysis of rock size and weight, and system to ensure the mechanism does not break itself trying to pick it up	Unlikely	Moderate	Abort picking up a chosen rock, move to another interesting rock.	PLD Lead
TR-TCS-01	Heating Fin gets damaged resulting in a less efficient heat rejection system for the propulsion motor	Unlikely	Minor	No mitigation necessary as a single blade damage results in 1 % difference in efficiency	Unlikely	Minor		TCS Lead
TR-TCS-02	Failure of thermocouples for all systems	Possible	Minor	Use reliable sensors. Stress test the thermal control system. Add redundant sensors.	Unlikely	Minor		TCS Lead
TR-TCS-03	Failure of thermal control software resulting in extreme temperatures for the battery and electronics	Possible	Moderate	Use software with very high reliability. Stress test the thermal control system.	Unlikely	Moderate		TCS Lead

3.2. Risk Maps

***Authors**: Sebastien*

This section presents risk maps and vital tools for risk analysis. They provide a visual representation of potential major risks and the effects of the corresponding mitigation strategies. The non-mitigated and mitigated risk map for the schedule, cost, and environmental and sustainability risks are illustrated in Tables 3.6 and 3.7 respectively. Similarly, the technical risk maps are illustrated in Tables 3.8 and 3.9.

Table 3.6: Risk map before mitigation for the schedule, cost and environmental risks

Probability \ Impact	Very Unlikely	Unlikely	Possible	Probable	Very Likely
Severe		SER-01			
Major		SR-PRD-02 SR-OPS-02 CR-OPS-01	SR-PRD-08 CR-PRD-07 CR-PRD-10 CR-LAU-01 CR-LAU-02	SER-03	
Moderate	CR-SAF-01	SR-PRD-04 SR-OPS-01 CR-PRD-08 SER-02	SR-PRD-03 SR-PRD-07 SR-LAU-04 CR-PRD-02 CR-PRD-03 CR-PRD-13 CR-LEG-01 SER-05	SR-PRD-05 CR-PRD-01 SER-04	
Minor		CR-LEG-02	SR-PRD-01 SR-LAU-05 SR-OPS-03	SR-LAU-01	
Negligible					

Table 3.7: Mitigated risk map for the schedule, cost and environmental risks

Probability \ Impact	Very Unlikely	Unlikely	Possible	Probable	Very Likely
Severe	SER-01				
Major		SR-PRD-08 CR-LAU-02			
Moderate	SR-PRD-02 SR-PRD-04 SR-LAU-04 SR-OPS-02 CR-SAF-01 CR-PRD-08 SER-02	SR-PRD-03 SR-PRD-05 SR-PRD-07 SER-03 SER-04			
Minor	SR-OPS-01 CR-LEG-02	SR-PRD-01 SR-LAU-05 SR-OPS-03 CR-LEG-01 CR-OPS-01 SER-05	CR-PRD-02 CR-PRD-07 CR-PRD-10 CR-PRD-13 CR-LAU-01	SR-LAU-01 CR-PRD-01 CR-PRD-03	CR-PRD-01 CR-PRD-03
Negligible					

Table 3.8: Risk map before mitigation for the technical risks

Probability \ Impact	Very Unlikely	Unlikely	Possible	Probable	Very Likely
Severe	TR-LND-01 TR-LND-02	TR-LAU-01 TR-OPS-DEP-04 TR-PRO-02 TR-PRO-03 TR-EPS-05	TR-LAU-03 TR-CRS-01 TR-OPS-DEP-03 TR-OPS-DEP-05 TR-EPS-04-I TR-EPS-08 TR-STR-05 TR-STR-06 TR-GNC-01 TR-GNC-04 TR-PLD-01 TR-PLD-02 TR-PLD-03		
Major		TR-PRD-04 TR-COM-01 TR-GND-02 TR-PRO-04 TR-PRO-05 TR-EPS-02-I TR-EPS-03 TR-STR-02 TR-STR-03 TR-STR-04 TR-GNC-05	TR-PRD-05 TR-PRD-06 TR-LAU-02 TR-CRS-02 TR-OPS-15 TR-OPS-DEP-01 TR-OPS-EOL-01 TR-STR-08 TR-PLD-05 TR-PLD-07		TR-PRO-01
Moderate		TR-EPS-01 TR-STR-01	TR-OPS-03 TR-OPS-DEP-02 TR-OPS-EOL-02 TR-COM-01 TR-GNC-02 TR-TCS-03	TR-PRD-03	TR-EPS-07
Minor		TR-PLD-06TR-TCS-01	TR-GNC-03 TR-PLD-04 TR-TCS-02		
Negligible					

Table 3.9: Mitigated risk map for the technical risks

Probability \ Impact	Very Unlikely	Unlikely	Possible	Probable	Very Likely
Severe	TR-LAU-01 TR-LND-01 TR-LND-02 TR-PRO-02 TR-PRO-03 TR-EPS-04-I	TR-EPS-08 TR-STR-05 TR-STR-06 TR-GNC-04 TR-PLD-03			
Major	TR-PRD-04 TR-LAU-03 TR-PRO-04 TR-PRO-05 TR-STR-02 TR-STR-03 TR-STR-04 TR-STR-08	TR-OPS-15 TR-OPS-DEP-01 TR-PRO-01 TR-PLD-01 TR-PLD-02 TR-PLD-05			
Moderate	TR-COM-01 TR-GND-02 TR-EPS-02-I TR-EPS-05 TR-STR-01	TR-CRS-01 TR-CRS-02 TR-OPS-DEP-03 TR-OPS-DEP-05 TR-OPS-EOL-02 TR-PLD-07 TR-TCS-03	TR-PRD-05		
Minor	TR-OPS-DEP-04 TR-PLD-06	TR-PRD-06 TR-OPS-DEP-02 TR-EPS-01 TR-EPS-03 TR-GNC-03 TR-GNC-05 TR-PLD-04 TR-TCS-01 TR-TCS-02	TR-LAU-02 TR-OPS-03 TR-EPS-07 TR-COM-01 TR-GNC-01	TR-PRD-03	
Negligible			TR-OPS-EOL-01 TR-GNC-02		

4 Requirements

***Authors**: Sebastien, Jesse*

This chapter focuses on the identification of the requirements of the mission. The requirement analysis provides a basis for the design process, ensuring a streamlined and structured understanding of the mission's objectives. Design concepts can then be evaluated to comply with the specified mission and system requirements. To achieve this, a distinction is made between stakeholder, mission and system requirements. Stakeholder requirements are top-level requirements that include the customer's desires and the constraints imposed by the stakeholder. Stakeholder requirements also include the team's personal goals. On the other hand, mission requirements represent the functionalities the product must attain to comply with the stakeholders' needs. Lastly, system requirements are related to the mission's different interfaces. These requirements outline the capabilities and performance standards the system needs to achieve.

Section 4.1 introduces the stakeholder requirements of different parties. Different types of constraints can be identified from these stakeholder requirements, as discussed in Section 4.2. Sections 4.3 and 4.4 list the mission and system requirements, respectively. Killer, key and driving requirements can be identified from these requirements, as discussed in Section 4.5.

4.1. Stakeholder Requirements

The stakeholders for this project include the user of the final product (ID: STK-MD), relevant government bodies (ID: STK-GOV), the design team (ID: STK-TM) and the launch vehicle provider (ID: STK-LVP). In this project, the relevant government bodies are NASA, ESA, and the local governments during the production and testing of the system. Each stakeholder has a set of stakeholder requirements that must be satisfied. The stakeholder requirements are specified in Table 4.1.

4.2. Constraints

In this section, the constraints are listed in Table 4.2. Constraints impact requirements and limit the development of the system. Constraints (CST) are divided into legal constraints (LEG), time constraints (T), cost constraints (CT), resource constraints (R), operational constraints (OPS), environmental constraints (ENV), launch vehicle constraints (LV), safety constraints (SAF), and landing constraints (LND). These result from stakeholder requirements and different phases in the mission.

Table 4.1: Stakeholder requirements

ID	Requirement
Launch Vehicle Provider	
STK-LVP-01	The Martian Drone shall fit inside the launch vehicle.
STK-LVP-02	The Martian Drone shall comply with the maximum payload mass for the launch vehicle.
STK-LVP-03	The Martian Drone shall withstand the loads of the launch vehicle during flight.
STK-LVP-04	The Martian Drone shall withstand the vibrational loads of the launch vehicle during flight.
STK-LVP-05	The Martian Drone shall withstand the acoustic loads of the launch vehicle during flight.
STK-LVP-06	The Martian Drone shall not interfere with the EM of the launch vehicle.
STK-LVP-07	The Martian Drone shall withstand the shock loads of the launch vehicle during flight.
STK-LVP-08	The Martian Drone shall withstand the temperature conditions during flight and pre-flight conditions specified by the launch provider.
STK-LVP-09	The Martian Drone shall withstand the transport loads to the launch vehicle.
STK-LVP-10	The Martian Drone shall comply with the cleanliness regulations of the launch vehicle provider.
STK-LVP-11	The Martian Drone and the team shall comply with the safety regulations of the launch provider.
STK-LVP-12	The Martian Drone shall be launched from the launch sites of the launch provider.
User	

Continued on next page

Table 4.1: Stakeholder requirements (Continued)

STK-USER-01	The Martian Drone shall be capable of continuous flight on Mars for 30 min.
STK-USER-02	The Martian Drone shall be capable of a total flight range of 20 km.
STK-USER-03	The Martian Drone shall be able to transport a mass of 3 kg of rock samples.
STK-USER-04	The Martian Drone shall be able to store a volume of rock samples of 10 cm × 10 cm × 10 cm.
STK-USER-05	The Martian Drone shall be capable of operation in the Martian atmosphere.
STK-USER-06	The Martian Drone shall be capable of take-off and landing on Martian soil.
STK-USER-07	The Martian Drone shall be capable of real-time communication with a Mars ground station.
STK-USER-08	The Martian Drone shall use renewable energy sources for the propulsion system.
STK-USER-09	The Martian Drone shall use renewable energy sources for the power system.
STK-USER-10	The Martian Drone shall be capable of autonomous operation.
STK-USER-11	The Martian Drone shall be capable of object identification to detect rock types.
STK-USER-12	The Martian Drone shall be capable of picking up rock samples.
STK-USER-13-I	The Martian Drone costs for design, building, testing and getting the drone to Mars shall be within 300 M€.
STK-USER-14	The Martian Drone shall help answer the question: "Did life ever exist on Mars?"
STK-USER-15-I	The Martian Drone shall be faster than the current fastest land rover, faster than $0.152\,\mathrm{km\,h^{-1}}$
STK-USER-16	The Martian Drone shall be capable of transporting rock samples.
Governmental Entities and Space Agencies	
STK-GOV-01	The Martian Drone and the operations shall comply with the regulations of the country's space agency.
STK-GOV-02	The Martian Drone and pre-launch operations shall comply with local government regulations.
STK-GOV-03	The Martian Drone and operations shall comply with the Outer Space Treaty, formally the Treaty on Principles Governing the Activities of States in the Exploration and Use of Outer Space, including the Moon and Other Celestial Bodies.
Team	
STK-TM-01	The preliminary design phase shall be completed with 10 full-time team members.

Table 4.2: Constraints

ID	**Requirement**
Legal	
CST-LEG-02	The Martian drone and its operations shall comply with the Outer Space Treaty of the United Nations [5] .
CST-LEG-02-01	The Martian drone shall avoid contamination of space and Mars.
CST-LEG-02-02	The Martian drone shall avoid harming space and Mars.
CST-LEG-02-03	The Martian drone shall "be used exclusively for peaceful purposes."
CST-LEG-02-04	The Martian drone mission shall be carried out for the benefit and in the interests of all countries and shall be the province of all mankind".
CST-LEG-03	The Martian drone, its operations and the team shall comply with the regulations of the launch site.
CST-LEG-04	The Martian drone, its operations and the team shall comply with the regulations of the space agency.
CST-LEG-05	The Martian drone, its operations and the team shall comply with the regulations of the country's governments.
Time	
CST-T-01	The team shall complete a preliminary system design within 50 working days.
CST-T-02	The project shall mitigate delays due to unforeseen circumstances (e.g. pandemic, geopolitical situation).
CST-T-03	The Martian Drone shall be launched by the year 2035.
Cost	
CST-CT-01	The cost for design, building, testing and getting the drone to Mars shall not exceed FY24€ 100M (NOTE: changed to FY24€ 300M).
CST-CT-01-01	The production budget shall not exceed FY24€ 118M.
CST-CT-01-02	The testing budget shall not exceed FY24€ 32M manufacturing and assembly budget.
CST-CT-01-03	The launch budget shall not exceed FY24€ 123M.
CST-CT-01-04	The operations and EOL budget shall not exceed FY24€ 27M.
Resources	
CST-R-01	The preliminary design of the Mars Drone shall be completed by 10 full-time team members.
Operation	
CST-OPS-01	The Martian Drone shall operate using renewable energy sources.
CST-OPS-01-01	The electrical power system shall operate using renewable energy sources.

Continued on next page

Table 4.2: Constraints (Continued)

CST-OPS-01-02	The propulsion system shall operate using renewable energy sources.
CST-OPS-02	The Martian Drone shall have a source of power.
CST-OPS-03	The Martian Drone shall not undergo a rapid unscheduled disassembly event.
Environmental	
CST-ENV-01	The Martian Drone shall operate in the Martian environment.
CST-ENV-01-01	The Martian Drone shall operate in a low-density environment.
CST-ENV-01-02	The Martian Drone shall operate in a low-temperature environment.
CST-ENV-01-03	The Martian Drone shall operate in a high radiation environment.
CST-ENV-01-04	The Martian Drone shall operate in a dusty environment.
CST-ENV-01-05	The Martian Drone shall operate in an environment with high wind speeds.
CST-ENV-01-06	The Martian Drone shall operate in an environment with magnetic fluctuations.
CST-ENV-02	The Martian Drone shall survive interplanetary travel to Mars.
CST-ENV-02-01	The Martian Drone shall survive in a near vacuum.
CST-ENV-02-02	The Martian Drone shall survive in an extreme temperature environment.
CST-ENV-02-03	The Martian Drone shall survive in an extreme radiation environment.
CST-ENV-03	The Martian Drone shall survive entry to the Martian atmosphere.
Launch Vehicle	
CST-LV-01	The Martian Drone shall fit inside the launch vehicle.
CST-LV-02	The Martian Drone shall comply to the maximum payload mass for the launch vehicle.
CST-LV-03	The Martian Drone shall be undamaged during the launch.
CST-LV-04	The Martian Drone shall be transported to the launch site.
Safety	
CST-SAF-01	The Martian Drone shall be safe to handle during production.
CST-SAF-01-01	The Martian Drone shall be safe to handle during manufacturing.
CST-SAF-01-02	The Martian Drone shall be safe to handle during assembly.
CST-SAF-02	The Martian Drone shall be safe to handle during testing.
CST-SAF-03	The Martian Drone shall be safe to transport.
Landing	
CST-LND-01	The Martian Drone shall have a separate landing system.
CST-LND-02	The Martian Drone shall have the landing system integrated into the same launch.

4.3. Mission Requirements

In this section, the mission requirements (MSN) are provided, as listed in Table 4.3. The mission requirements define the goals for the entire development and operations of the mission and flow from the project's primary user and stakeholder requirements.

Table 4.3: Mission requirements

ID	Requirement
MSN-01	The Martian Drone shall communicate with a Mars ground station in real-time.
MSN-02	The Martian Drone shall operate in the Martian atmosphere.
MSN-03	The Martian Drone shall be capable of continuous flight for 30 minutes on Mars.
MSN-04	The Martian Drone shall be capable of a total flight range of 20 km.
MSN-05	The Martian Drone shall be able to identify Martian rocks.
MSN-06	The system shall be able to collect rocks.
MSN-07	The system shall be able to transport rocks.
MSN-08	The Martian Drone shall be able to take off and land on the Martian surface.
MSN-09	The Martian Drone shall operate autonomously.
MSN-10	The Martian Drone shall help answer the question: "Did life ever exist on Mars?" by analysing aqueous deposits.

4.4. System Requirements

This section provides the system requirements (SYS); see Table 4.4. The system requirements flow from the mission, constraints, and stakeholder requirements. Each requirement is thus also traced, and traceability is provided

to ensure the primary requirements are completed. The requirements are divided into multiple parts. Initially, all requirements regarding the pre-Mars mission operations are listed, namely launch vehicle requirements (LV), interplanetary travel/cruise requirements (IPT), re-entry requirements (RE), deployment requirements (DPL), production requirements (PRD), and testing requirements (TST) in. Additionally, requirements regarding Mars operations are provided, including general requirements (GE).

Lastly, the system requirements shall be verified to ensure they are met. The verification method is noted as a single letter, requiring a key for interpretation. Each method of requirement verification is detailed below.

- **Analysis (A)**: requires theoretical and empirical methods in agreement with the Stakeholders
- **Demonstration (D)**: requires the operation or relevant function to be performed during the mission or of a test article.
- **Inspection (I)**: requires visual determination of physical characteristics
- **Review (R)**: requires the use of approved documentation that shows beyond doubt that the requirement is met
- **Test (T)**: requires functions and performance to be measured of a part of the system under representative simulated environments

Some requirement values may be uncertain at this development phase and are denoted with (TBC), "to be confirmed". Subsystem requirements are discussed in their respective chapters.

Table 4.4: System requirements

ID	Requirement	Traceability	Verification Method
	Launch vehicle requirements		
LV-SYS-01-I	The system shall be safely transported to Guiana Space Centre's launch site.	CST-LV-04, CST-SAF-03	D
LV-SYS-02	The system shall be integrated with the Ariane 64 rocket.	CST-T-03	D
LV-SYS-02-01	The system payload attachment system shall comply with that of the launch vehicle.		I, D
LV-SYS-02-02	The system shall comply with the allowable COG height of the launch vehicle (see [14, p. 4-2]).		A
LV-SYS-02-03	The system shall be integrated following the integration procedures of the launch vehicle provider.		R
LV-SYS-03	The system in launch configuration shall fit within the constraints of the launch vehicle.	CST-LV-01; CST-T-03	D
LV-SYS-03-01-I	The system volume in launch configuration shall not exceed the launch vehicle's maximum payload dimensions.		I
LV-SYS-03-01-01	The system length in launch configuration shall not exceed 4.6 m [14, p. 5-5].		I
LV-SYS-03-01-02	The system width in launch configuration shall not exceed 4.6 m [14, p. 5-5].		I
LV-SYS-03-01-03	The system height in launch configuration shall not exceed 18 m [14, p. 5-6].		I
LV-SYS-03-02	The system launch mass shall not exceed 6900 kg, the launch vehicle maximum payload mass [14, p. 2-11].		I
LV-SYS-03-03	The system shall not interfere with the launch vehicle's RF system (see [14, fig. 4.2.3.8.a]).		D
LV-SYS-03-05	The system shall comply with the cleanliness regulations of the launch vehicle.		R
LV-SYS-04	The system shall withstand the launch environment.	CST-LV-03	D
LV-SYS-04-01	The system shall withstand -6 g to 2.5 g of longitudinal launch loads [14, tab. 3.2.1.a].		T
LV-SYS-04-02	The system shall withstand ± 1.8 g of lateral launch loads [14, tab. 3.2.1.a].		T
LV-SYS-04-06	The system shall withstand the launcher acoustic pressure environment (see [14, fig. 3.2.6.2.b]).		T
LV-SYS-04-07	The system shall withstand the launcher shock loads during the stage separations of the launcher (see [14, fig. 3.2.7.a]).		T
LV-SYS-04-08	The system shall withstand a temperature environment during the vehicle's launch.		T
LV-SYS-04-09	The system's fundamental primary lateral frequency shall be larger than 6 Hz [14, p. 4-4].		T

Continued on next page

Table 4.4: System requirements (Continued)

LV-SYS-04-10	The system's fundamental primary longitudinal frequency shall be larger than 20 Hz [14, p. 4-4].		T
Interplanetary Travel/Cruise Requirements			
IPT-SYS-01	The system shall withstand the in-space environment during cruise.	CST-ENV-02	D
IPT-SYS-02	The system shall be capable of cruising to Mars.	MSN-02	D
IPT-SYS-03	The cruise phase of the system shall take no longer than 7.0 ± 0.5 months.		D
Re-entry Requirements			
RE-SYS-01	The system shall withstand the re-entry environment into the Martian atmosphere	CST-ENV-03	D
RE-SYS-01-01	The system shall withstand 12.9 g (TBC) of reentry loads [15, tab. 8].		A
RE-SYS-01-07	The system shall withstand a maximum heat flux of 2.12×10^6 W m^{-2} during Martian entry [15, tab. 8].		A
RE-SYS-01-08	The system shall withstand a total heat load of 5.769×10^7 J m^{-2} during Martian entry [15, tab. 8].		A
RE-SYS-03-I	The system entry mass shall be (89 ± 5) % of the launch mass [18] .	CST-LND-01; CST-LND-02	
RE-SYS-04	The Martian Drone shall withstand the landing environment	CST-ENV-03	D
RE-SYS-05	The Martian Drone and ground system mass shall be (23 ± 5) % of the launch mass [19] .	CST-LND-01; CST-LND-02	
Deployment Requirements			
DPL-SYS-01-I	The system shall be capable of deploying into operation configuration.	CST-LV-01	D
DPL-SYS-01-02	The system shall take 3.0 ± 0.5 months for initial checkout, including deployment and testing[20] .		A, D
DPL-SYS-02-I	The system shall be capable of activating into mission-ready configuration.	GE-SYS-06	D
DPL-SYS-02-01	The system shall be able to activate autonomously.		T,D
DPL-SYS-02-02	The system shall be able to be activated remotely.		T, D
Production Requirements			
PRD-SYS-01	The system shall be manufacturable.	TR-PRD-01	D
PRD-SYS-01-01	The system shall be safe to manufacture.	CST-SAF-01-01	D
PRD-SYS-01-02	The system shall be sustainably manufacturable.		A, D
PRD-SYS-01-03	The system shall be manufacturable within 16 ± 1 months.	CST-T-03	D
PRD-SYS-02-I	The system shall be integratable into the EDL configuration (including the skycrane and ground station).	CST-LND-01	D
PRD-SYS-03	The system shall be assemblable.	TR-PRD-04	D
PRD-SYS-03-01	The system shall be safe to handle during assembly.	CST-SAF-01-02	D
PRD-SYS-03-02	The system shall be sustainably assemblable.		D
PRD-SYS-03-03	The system shall be assemblable within 20 ± 1 months.	CST-T-03	D
Testing Requirements			
TST-SYS-01	The system shall be tested within 36 ± 2 months.	CST-T-03	D
TST-SYS-02	The system shall be safe to test.	CST-SAF-02	A, D
General System Requirements			
GE-SYS-01	The system shall follow the safety factors set by NASA in NASA-STD-5001B.	CST-LEG-04	I
GE-SYS-02	The Martian Drone shall not pollute Mars.	CST-LEG-01-01	D
GE-SYS-03	The system shall be stable.	MSN-09	A, D
GE-SYS-04	The system shall be controllable.	MSN-09	A, D
GE-SYS-05	The Martian Drone shall remain within operating temperature.	MSN-02	A, D
GE-SYS-06	The Martian Drone shall be autonomous.	MSN-09	D
GE-SYS-07	The Martian Drone shall be faster than 0.152 km h^{-1}.	STK-MD-15	A

4.5. Killer, Key and Driving Requirements

The requirements introduced in the previous sections can be subdivided into three main types: key, driving, or killer. Identifying these requirements is key to guiding the team through the design process. Determining killer requirements is especially important, as these drive the design to an unacceptable extent. Improper identification can lead to severe unforeseen design implications later in the project. The killer requirements shall be discussed and changed with the stakeholders to make the mission possible. All key, driving and killer requirements are listed in Section 4.5. After a discussion with the primary stakeholders, more budget was allocated to the development of the Martian Drone; thus, CST-T-01 was changed to FY24€ 300M, and it is no longer a killer requirement.

- **Killer**: "A killer requirement drives the design to an unacceptable extent [16]."
- **Key**: "Key requirements are of primary importance to the sure, a driving requirement, a potential killer requirement or a requirement that is known to have an elevated risk [16]."
- **Driving**: "A driving requirement is a requirement that drives the design more that average [16]."

Table 4.5: Killer, key and driving of requirements

ID	Requirement/Constraint
	Killer
CST-T-01	The cost for design, building, testing and getting the drone to Mars shall not exceed FY24€ 100M
	Key
MSN-02	The Martian Drone shall operate in the Martian atmosphere
MSN-03	The Martian Drone shall be capable of continuous flight for 30 minutes on Mars.
MSN-04	The Martian Drone shall be capable of a total flight range of 20 km.
MSN-07	The system shall be able to transport rocks
	Driving
MSN-05	The Martian Drone shall be able to identify Martian rocks
MSN-06	The system shall be able to collect rocks
LV-SYS-04	The system shall withstand the launch environment
RE-SYS-01	The system shall withstand the re-entry environment into the Martian atmosphere

5 Economic Feasibility

***Authors**: Vini, Florian* This chapter considers the economic feasibility of the project. This starts with a market analysis in Section 5.1. A SWOT analysis, which considers the strengths, weaknesses, opportunities, threat of the product, is then discussed in Section 5.2. Finally, a discussion regarding the return on investment is provided in Section 5.3.

5.1. Market Analysis

***Authors**: Vini*

In this section, a market analysis is performed. This analysis results in a stakeholder map for the Martian Drone mission in Section 5.1.1. Then, in Section 5.1.2, comparable missions are identified. Section 5.1.3 provides the approach used to establish the initial cost target for the project. In Section 5.1.4, new markets for the product are investigated.

5.1.1. Stakeholder Map

The first step in conducting a market analysis is determining and mapping all potential stakeholders. These include parties interested in the program, those influenced by it, and those influencing it, such as regulatory parties. Figure 5.1 displays a map where stakeholders are assessed based on their influence and interest in the project.

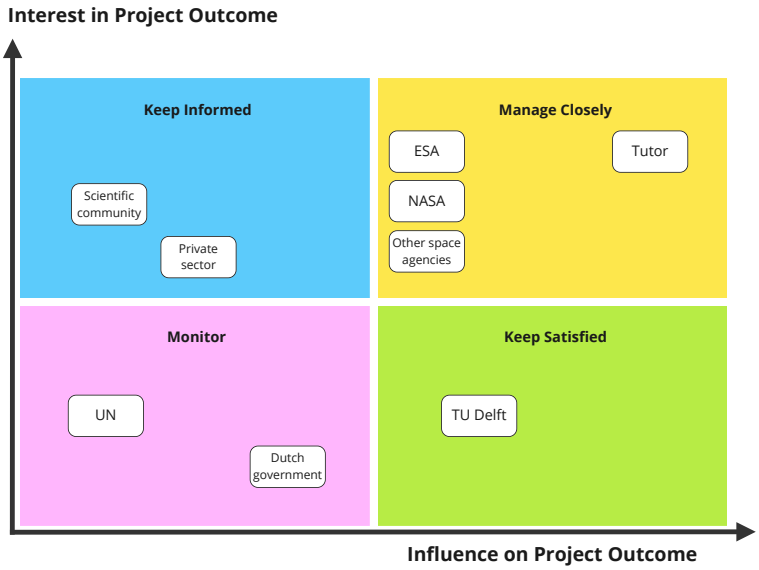

Figure 5.1: Stakeholder map for the Martian Drone mission.

All space agencies are considered to have an equivalent, significant influence on the project outcome. Besides the project tutor, they are the only (potential) client, as it is assumed they have the required financial means. NASA and ESA are ranked higher in interest than other space agencies because of their larger budgets and collaboration on the NASA-ESA Mars Sample Return mission. Private sector companies such as SpaceX may be interested in the outcome of the drone, but as they are more profit-driven, it is unlikely they will be interested in acquiring the project. Regulatory agencies include the United Nations (UN) and the Dutch government, specifically due to the UN's Outer Space Treaty and the Dutch National Space Law. The drone is designed in TU Delft's facilities, and as a result, it significantly influences the project. Lastly, the scientific community may be interested in the technologies used in drones and the scientific discoveries they have made. Lastly, any potential life on Mars may be affected by the project.

5.1.2. Similar Missions

The second step in conducting a market analysis is exploring the current market landscape for the designed mission. For this, the mission type must be defined. The Martian Drone's primary function is to perform geological surveys and collect samples for analysis. This categorizes it as a landed Martian surface exploration (LMSE henceforth) mission. Though it will be a drone, its function of collecting samples separates it from purely remote sensing missions in Mars orbit. NASA's yearly spending on this category of missions is summarized in Figure 5.2.

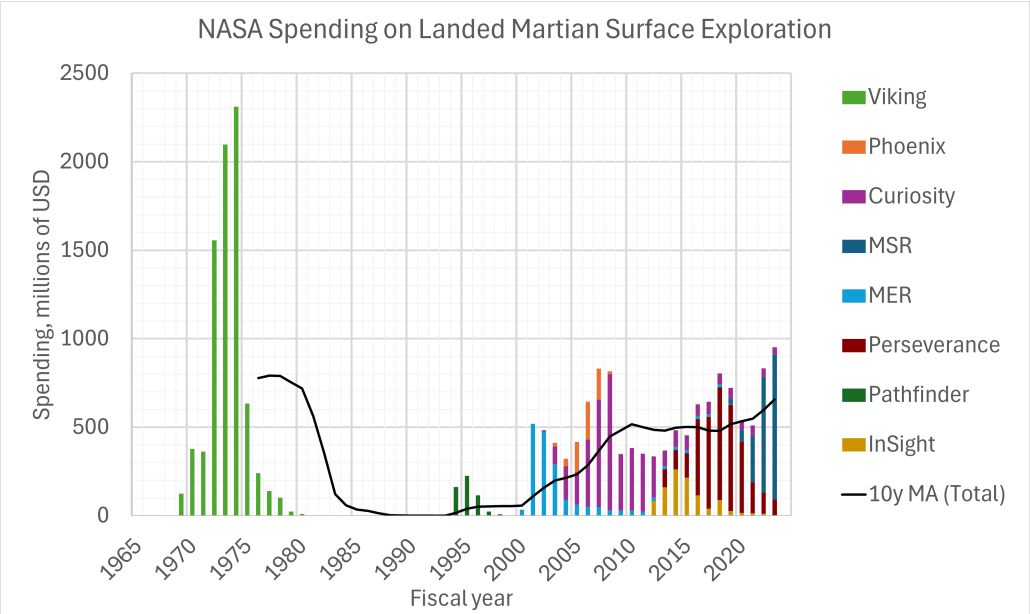

Figure 5.2: NASA historical LMSE spending by mission.[1]

Figure 5.2 provides an insight into NASA's demand for Martian surface exploration, particularly via landed missions which, by including the 10-year moving average, provides more precise and direct scientific value.

Other space agencies like ESA, JAXA, CNSA, and Roscosmos have also expressed interest over the last few decades. To estimate their potential budgets, it has been assumed that all space agencies would spend the same percentage of their total budget on such missions. Based on the data gathered in Figure 5.2, NASA spends approximately 2.5% of their total budget, approximately $600M in 2022. Data from the year 2022 is used since it is the most recent year with available values for the total budgets of each space agency. The total budgets of the interested parties and their potential budgets in the LMSE market are summarized in Table 5.1.

Table 5.1: Total and estimated potential LMSE budgets for various space agencies in 2022.

Agency	Total Budget [bn$]	Potential LMSE Budget [M$]
NASA	24.0[2]	600
ESA	7.5[3]	188
JAXA	1.7[4]	42
CNSA	11.9[5]	299
Roscomos	2.9[6]	73

From Table 5.1, the yearly LMSE market volume can be estimated as the sum of the yearly budgets of the five primary space agencies involved. This comes out to a total of approximately $1.2bn.

[1] URL: https://www.planetary.org/space-policy/planetary-exploration-budget-dataset [cited 1 May 2024]
[2] URL: https://www.planetary.org/space-policy/nasas-fy-2022-budget [cited 30 April 2024]
[3] URL: https://www.esa.int/ESA_Multimedia/Images/2022/01/ESA_budget_2022 [cited 30 April 2024]
[4] URL: https://www.jaxa.jp/about/transition/ [cited 30 April 2024]
[5] URL: https://www.euroconsult-ec.com/press-release/new-historic-high-for-government-space-spending-mostly-driven-by-defense-expenditures/ [cited 30 April 2024]
[6] URL: https://arstechnica.com/science/2021/10/putin-slashes-russias-space-budget-and-says-he-expects-better-results/ [cited 30 April 2024]

To maximise potential market share, a target cost must be set, which can be accessed by all major parties in the market. Given the estimated yearly budgets in Table 5.1, the smallest budget allocation will likely come from JAXA, Japan's national space agency. JAXA is predicted to allocate approximately $40M per fiscal year to an LMSE project. Applying a margin of 25% since the entire budget cannot be assumed to be allocated to a single mission, a target yearly cost cap of $30M is set on the Martian Drone mission. This is valuable for establishing a cost target for developing the drone.

5.1.3. Target Cost

The main purpose of this market analysis is to develop an initial cost target for the project so that a competitive budget can be determined. This projection can be made using the yearly cost cap as a reference.

Costs in this section include design formulation, implementation, operations, and the journey to Mars. It is useful to start from the cost profile of a similar mission over time, such as Perseverance and Ingenuity. Perseverance developed between 2013 and 2021 for nine years and will be taken as an estimate for the required development time. Ingenuity performed its mission over three years, and this will be used as an estimate for the operational time. With a total mission length of 12 years and a yearly budget of $30M, a target cost of $360M can be assumed.

It is crucial to assess this target cost concerning possible competition. The project must not be too expensive and attractive to potential clients, above other alternatives. Whilst there is no existing competition with the same function, NASA and ESA, alongside AeroVironment, have proposed a Mars Sample Recovery Helicopter as part of the NASA-ESA Mars Sample Return program. This helicopter will be designed based on Ingenuity. Currently, AeroVironment has received a $10M [7] contract from NASA for a preliminary design of the drone. Considering that $80M was spent on developing Ingenuity, it is reasonable to expect that the full development of such a helicopter will require far more than $90M to build and send to Mars. As a result, a target development cost of $360M requires a higher budget than the competition, However, the added value of this new technology, regarding the ability to search a large and less accessible area, could make the project more appealing to larger stakeholders such as NASA, ESA, and CNSA. The mission cost budget will be estimated in Section 18.3 to determine whether this target is achievable.

Whereas NASA is likely to continue working with AeroVironment, ESA is incentivised to acquire the project as it is European-based. Assuming other space agencies will allocate the majority of their budgets to in-house development, the Martian Drone's market share can be estimated by assuming ESA allocates the necessary $30M per year maximum. This evaluates to a 2.5% share in the market of all landed Martian surface exploration missions.

5.1.4. New Markets

There is a potential for expansion into new markets in the future. For instance, the drone could be repurposed as a navigation aid for a rover on Mars, similar to Ingenuity. Additionally, the vehicle can be adapted to transport goods over rugged terrain to support human presence on Mars. Furthermore, new technologies used in drones have potential in other applications. If, for example, a rotorcraft design is developed, advanced airfoil design for low Reynolds numbers can be used in any laminar flow projects requiring high performance. Tools employed in the scientific payload are likely to have utility in various sample identification or collection contexts. The results from the drone's flight performance will also play a vital role in verifying future rotorcraft missions.

5.2. SWOT Analysis

***Authors**: Vini*

Figure 5.3 illustrated the SWOT (strengths, weaknesses, opportunities, threats) analysis of the Martian Drone mission from the market analysis.

This SWOT analysis condenses insights from the market analysis. Potential partnerships with space agencies offer valuable opportunities for future projects. The drone's strengths lie in its cost-efficiency and high performance, enabling a first-mover advantage. However, limitations include a small, less-experienced development team, and threats such as regulatory hurdles due to new technologies should be addressed to facilitate market entry.

[7] URL: https://www.avinc.com/resources/press-releases/view/aerovironment-awarded-10-million-contract-by-nasa-jpl-to-co-design-and-develop-two-helicopters-for-mars-sample-return-mission [cited on 1 May 2024]

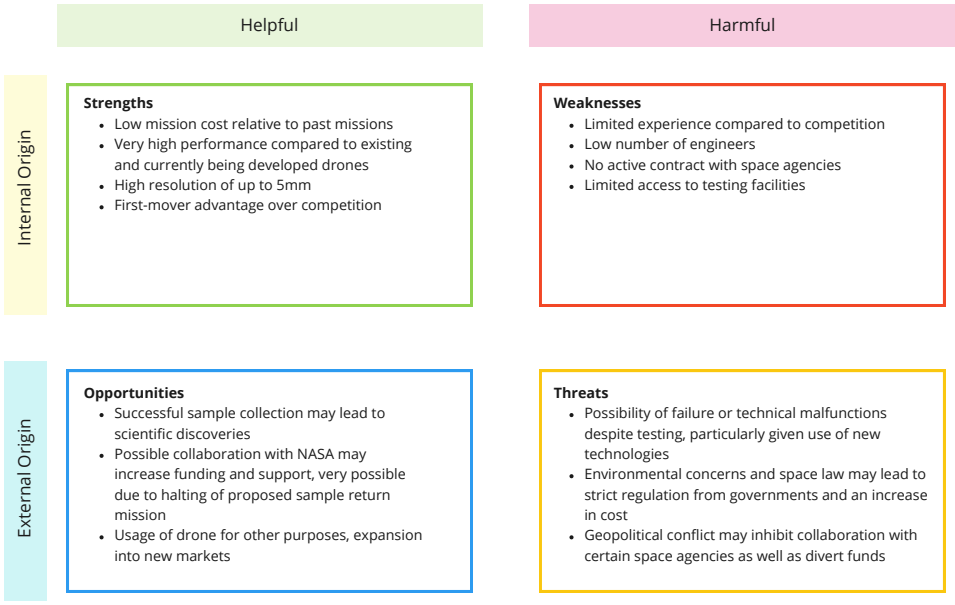

Figure 5.3: SWOT analysis of the Martian Drone.

5.3. Return on Investment

***Authors**: Florian*

The objective of the Martian drone mission is scientific, namely, to contribute to humankind's quest to determine if life ever existed on Mars. A project of this nature is not expected to return a profit to its investors directly. However, as the development of this project will likely rely on public funds, it is important to consider its economic viability in a broader context critically.

Firstly, this mission will contribute to the international scientific community by providing much more data than what current Mars exploration missions are capable of. This data will help us understand if life ever existed on Mars and hopefully contribute to answering humanity's most fundamental questions on the origins of life, inspiring generations to come. On top of this primary goal, the drone will also map the Eberswalde crater in high resolution over its lifetime, potentially contributing to identifying a suitable location for human settlement on Mars.

The development of this mission will rely on international cooperation, regardless of which space agency decides to adopt this project. Indeed, major space exploration missions often involve close collaboration between international partners, including space agencies, private companies and the scientific community. Strengthening existing partnerships and fostering new ones will accelerate the sharing of research and expertise globally and contribute to improving diplomatic relations.

Additionally, the mission's development will necessitate a diverse range of skilled professionals, including engineers and scientists. This will lead to the creation of high-value jobs, driving growth in the technology and aerospace sectors. For example, NASA estimates that the $2.5bn curiosity mission indirectly supported up to 7000 jobs. Combining all aspects of this mission, from the development of the drone itself to the launch vehicle to all the necessary components, the Martian drone mission with its target cost of $360M could support 500 to 1000 jobs across the industry.

Although quantitatively analysing the return on investment of this mission is difficult, when considering all the impacts on society of this mission, the benefits are expected to outweigh the cost of development greatly. According to the National Space Society, NASA's major space exploration missions generate an economic growth between 7 and 40 times the value of their initial investment when considering the value of spinoff technologies [8] . In this sense, the economic benefit of this project could reach $14000M from an investment of $360M.

[8]URL: https://nss.org/settlement/nasa/spaceresvol4/newspace3.html [cited on 14 June 2024]

6 Sustainable Development Strategy

***Authors**: Maurits*

This chapter addresses the sustainable development strategy for the Martian Drone project and highlights the product's contributions to the sustainability initiative. The strategy has been split into multiple factors contributing to sustainability.

The end-of-life considerations for the Martian Drone are discussed in Section 6.1. Furthermore, environmental sustainability contributions are explored in Section 6.2, and social and economic sustainability contributions are discussed in Section 6.3. Lastly, to ensure the strategy is complete, the 17 sustainable development goals set out by the United Nations [17] are used as a basis.

6.1. End-Of-Life Considerations

One of the most important considerations in the life cycle assessment is the operations at the system's end-of-life conditions. Multiple scenarios have to be analysed to set up end-of-life operations accurately. These scenarios range from the best-case scenario of a fully functional drone to the worst-case scenario of a crash landing.

In the best-case scenario, the drone is still fully operational after completing the mission. This entails that after the two years scheduled to perform the mission, the drone is still fully capable of autonomous flight, identifying and collecting rocks, and navigating the Martian environment. Furthermore, all communications systems are fully intact, and data can still be sent to and from Mars and the drone.

In other scenarios, it depends heavily on which subsystems have deteriorated to an unacceptable level or are completely inoperative. The failure of the power, propulsion and thermal systems results in a complete system breakdown, as the drone can no longer fly. In this scenario, the drone will make the last observations, communicate its location to the ground station, and switch it off. The drone's position may be used during any recycling plans, which is explored later in this section.

The failure of other systems will only affect the mission performance and not result in an inoperative drone. In these cases, the drone will continue to make observations, gathering more scientific data to communicate to the ground station. The drone is intended to stay close to the ground station so that its location is known in case of complete system failure, and it can communicate with it.

In the worst-case scenario, the drone crash lands and becomes fully inoperative. In this condition, the drone will likely be completely lost. The drone would have communicated its location before crashing. This information might be valuable for future recovery or exploration missions to the Eberswalde crater.

Since the investment cost for retrieval missions outweighs the potential gains from recycling, it is difficult to set up an elaborate recycling plan. However, if the landing or crash location is known, future missions could use this information to retrieve or re-use parts of the Martian Drone. Depending on the mission's requirements, this may include structural elements or entire systems. With the manned Martian mission idea gaining traction, the possibility of human retrieval becomes increasingly more likely while still improbable.

6.2. Environmental Sustainability

To help facilitate the setting up of strategies for minimizing the project's environmental impact, the United Nations' sustainable development goals were analyzed. It was determined that the project could contribute positively to achieving two of these goals, which are [17]:

- **Goal 9**: "*Build resilient infrastructure, promote inclusive and sustainable industrialization and foster innovation.*"
- **Goal 12**: "*Ensure sustainable consumption and production patterns.*"

A handful of possible strategies for the Martian Drone and its development to contribute positively to achieving these goals is described in this section. First, Section 6.2.1 explores the strategies related to sustainable production. Afterwards, Section 6.2.2 details the product's contribution to environmental sustainability.

6.2.1. Sustainable Production

Using sustainably sourced materials and sustainable manufacturing processes is important in limiting the Martian drone's environmental impact. The embodied energy of the system, the amount of energy necessary to go from the raw material to a material suitable for part manufacturing, is an excellent measurement for this. It is, therefore, vital to understand the environmental impact of aerospace materials.

The mining and refining of metals require large quantities of water and energy. The exact embodied energy of the entire process is affected by various factors such as the ore grades, grind size, mine depth and mining technique [18]. Some materials may require additional purification processes that add additional emissions and energy usage. Lastly, the transportation of the metals throughout the process should also be considered.

Composite materials such as carbon fibre composites or GLARE (GLAss REinforced aluminium) have varying embodied energies. Some fibres can, however, be recycled, lowering their embodied energy [19]. The other component of composite materials, the matrix, also significantly affects the choice of material due to the recyclability, the required raw materials and the production process.

Embodied energy is often measured in joules per kilogram. It is, therefore, dependent on the system's weight. Consequently, other material properties, such as Young's modulus, yield strength and density, and cross-sectional parameters, should be taken into account.

6.2.2. Product's Contribution

Apart from the development and production process, the product itself can also contribute to achieving the sustainability goals presented above. As per requirements STK-USER-08 and STK-USER-09, the Martian Drone shall use sustainable energy sources during its mission. The combination of these strict requirements and the extreme environment found on Mars will drive innovation during the drone's development.

Solar array technology and power storage systems will undergo a significant innovative phase during the development of the Martian Drone. This may result in substantial progress in power generation and storage technologies, increasing the amount of Green Energy and reducing dependency on fossil fuels.

Lastly, due to the development of the Martian drone, further technological advancements concerning lightweight and durable materials are expected. This may also improve the quality of other vehicles, leading to less maintenance, lower material usage, and more optimised manufacturing techniques.

Aside from technological advancements, keeping the Martian environment undisturbed during the mission is also integral for environmental sustainability since the drone will disturb the environment while collecting rocks. The drone is designed to collect solely interesting rocks, keeping the rest of the environment undisturbed. This is done through up-close scanning of the rocks to confirm they are of interest to the mission.

6.3. Social and Economic Sustainability

Similar to environmental sustainability, the team revisited the United Nations' sustainable development goals for social and economic sustainability to determine the strategies fit for the Martian Drone project. It was determined that two goals were specifically fitting for this DSE, namely [17]:

- **Goal 8**: "*Promote sustained, inclusive and sustainable economic growth, productive employment and decent work.*"
- **Goal 17**: "*Strengthen means of implementation and revitalize the Global Partnership for Sustainable Development.*"

The development of the Martian Drone would lead to job creation in the space exploration and technology industry. This will provide productive employment in a variety of fields. In addition, it is also important to remember the operations of the Martian Drone on Earth. Despite the minimal operations required for an autonomous nature, commanding and monitoring the drone is still occasionally necessary. A regularly rotating schedule to avoid long hours is needed to ensure a sustainable work environment.

Lastly, the drone's ability to collect and analyze Martian rocks could have economic implications, such as identifying valuable minerals for future exploitation or boosting the goal of colonizing Mars. The project can also reduce inequality by establishing international collaboration and knowledge sharing. Collaboration can be sought with scientists, engineers, and researchers from different countries to leverage diverse expertise and resources. Moreover, by openly sharing the research findings, methodologies, and technologies, the project can contribute to revitalising the global partnership.

7 Operations and Logistics

***Authors**: Florian, Diede*

In this chapter, the operations and logistics of the mission are discussed. First, the general concept of operations is presented in Section 7.1, covering all aspects of the mission timeline from launch operations to entry, descent and landing (EDL) and surface operations on Mars. The operations related specifically to the Martian ground station, a key element in the concept of operations, are discussed in Section 7.2, focusing on the functions that this system must perform within the scope of this mission. Finally, the flight profile for a mission is provided in Section 7.3.

7.1. Concept of Operations

Phase I - Launch and Cruise Operations: The mission operations begin with the launch from Earth, aimed for May 2035. The drone and the ground station will be integrated into a cruise vehicle and launched together. The Ariane 6 launcher will provide the Earth's escape velocity, placing the cruise vehicle on a Hohmann transfer orbit to Mars. The cruise vehicle will also perform mid-cruise trajectory corrections in preparation for arrival at Mars. After a seven-month transfer, the cruise vehicle will increment velocity to decelerate and manoeuvre into a Martian orbit.

Phase II - Entry, Descent and Landing (EDL): Once established in orbit around Mars, the entry vehicle will separate from the cruise vehicle and begin atmospheric entry. The entry vehicle holding the ground station and the drone will re-utilise the aeroshell technology developed for NASA's Mars 2020 mission [20]. A side view and top view of the aeroshell, with the drone inside, are illustrated in Figure 7.3 and Figure 7.4, respectively. The entry vehicle will pass through maximum dynamic pressure and deploy a parachute. In anticipation of landing, the ground station and the drone will separate from the entry vehicle, and a powered descent mechanism will softly bring the vehicles down to the surface. The Mars 2020 aeroshell had a maximum radius of 4.5 m and a height of 2.8 m [20]. A sketch of the folded view of the drone in the aeroshell is presented in Section 7.2.

Phase III - Surface Operation on Mars: Shortly after touchdown on Martian soil, the drone will begin the initial deployment phase. This includes the extension of the arms, unfolding the rotor blades, and deploying solar arrays. The drone and ground station will perform system checks, and a communication link between the two will be established. After the system checks are passed, the core scientific mission can begin. The operational concept for performing the core mission includes receiving a mission briefing from the ground station, autonomously flying to the designated area, performing reconnaissance and sample collection, and returning to the ground station where the ground station will analyse the sample. The ground station will transmit the scientific data back to Earth using either the Mars Relay Network[1] or the mission's cruise vehicle. The operational concept for the communication link is depicted in Figure 7.1. The scientific mission will be repeated for at least two years before the end-of-life operations, further expanded in Chapter 6, are performed.

An overview of the operations concept for the mission broken down into these three phases is presented as a block diagram in Figure 7.2.

7.2. Martian Ground Station

Since a drone design is limited by mass, a ground station must be on Mars to support the drone operations. To reduce costs, the ground station will be launched with the drone to fit in the aeroshell, serving as the drone's landing capsule. It will encase the drone, provide structural support, and connect it with the aeroshell and retro-boosters.

For the ground operations of the drone, the ground station needs to be able to perform the following functions:

- Provide communication link to Earth through the Mars Relay Network (MRN)
- Retrieve samples from drone

[1] URL: https://eyes.nasa.gov/apps/mrn/index.html#/mars [cited on 17 May 2024]

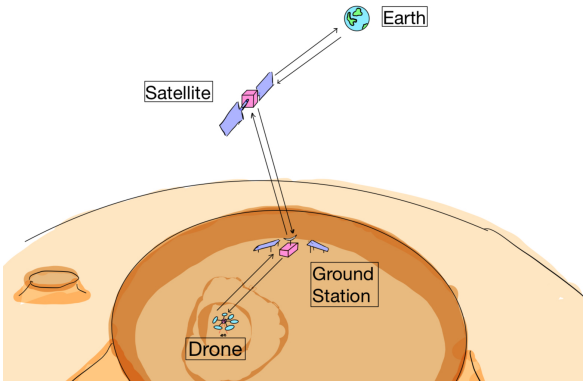

Figure 7.1: Sketch of the communication link concept including the drone, a Martian ground station, a relay satellite in Mars orbit and a ground station on Earth.

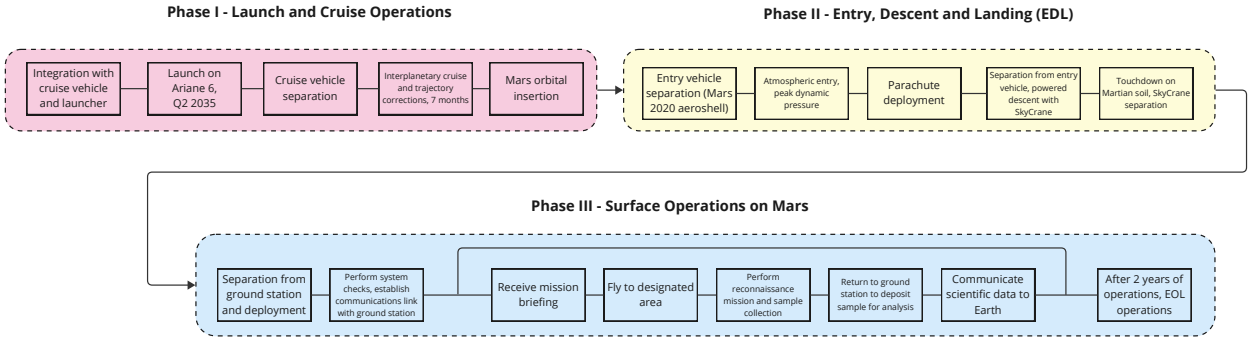

Figure 7.2: Concept of operations diagram.

- Perform additional analysis
- Prepare samples for future sample return mission

The ground station requires several key components to perform its functions. First, a power generation and storage system is essential, as all operations depend on a reliable power source. This system will consist of solar arrays mounted on the sides of the ground station. Additionally, the station will need batteries to ensure continuous operation. These batteries must be maintained at optimal temperatures with a thermal management system.

To communicate with the drone and Earth, it will need transmitting and receiving antennas suitable for both the drone and orbiting satellites. Lastly, the ground station needs to be able to do additional research on the

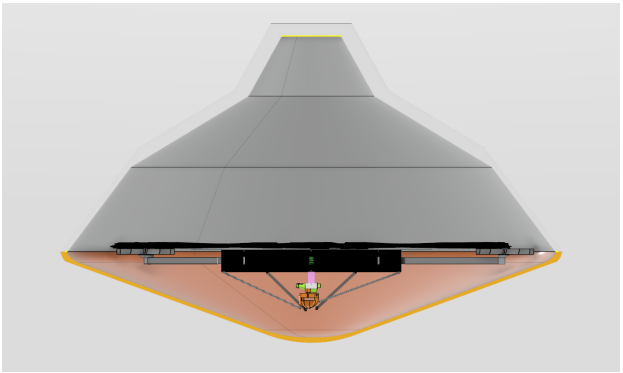

Figure 7.3: Side view of the aeroshell with the drone inside.

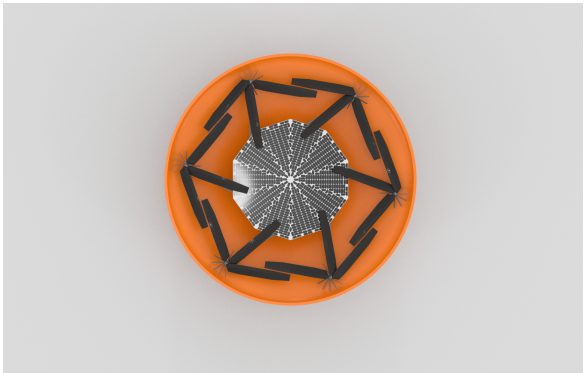

Figure 7.4: Top view of the aeroshell with the drone inside.

samples. A grabbing arm will be needed to retrieve the samples from the drone, which might also contain a drill bit to gather core samples from the collected rock sample. More sophisticated spectrometers can also be added to the ground station since mass is not a constraint for the ground station. This could include a VNIR

(visual-near infrared) and/or an X-ray spectrometer. The latter has a higher priority since the drone will already perform a VNIR spectrometer, see Chapter 12. Lastly, a storage system for the collected samples needs to be on board, which will be similar to the one on Perseverance [2] . Since we expect to gather a lot of samples, it might not be possible to store all of them for return. Consequently, a good selection needs to be made, and since it will be possible to return to sites, it is wise to be conservative with storing samples for sample return. It is deemed that all of this should be feasible within the currently designed mission. However, this must be confirmed later when the ground station is sized.

7.3. Flight Profile

The operations for the scientific mission are based on a two-day mission concept. On the first day, the drone flies to a designated area, performs scanning operations, and collects samples. On the second day, the drone flies back to the ground station to deposit the sample for further analysis. This profile can be broken down into phases illustrated in Table 7.1. In Figure 7.5, the flight profile for a scanning mission consisting of these flight phases is provided.

Table 7.1: Flight phases and their respective duration for a typical scanning flight.

Flight phase	**Time**
Takeoff and climb to 100 m	45 s
Cruise	1000 s
Descend to 75 m	15 s
Birds-eye scan	420 s
Descend to 10 m	20 s
Close up scan	30 s
Descend and land	30 s
Total flight time	1560 s

After this flight, if a sample of interest has been identified, the drone will acquire the sample with its rock collection mechanism. The drone will recharge once its battery is sufficiently charged and return to the ground station. The return flight requires the same cruise time, but the scanning operations are omitted.

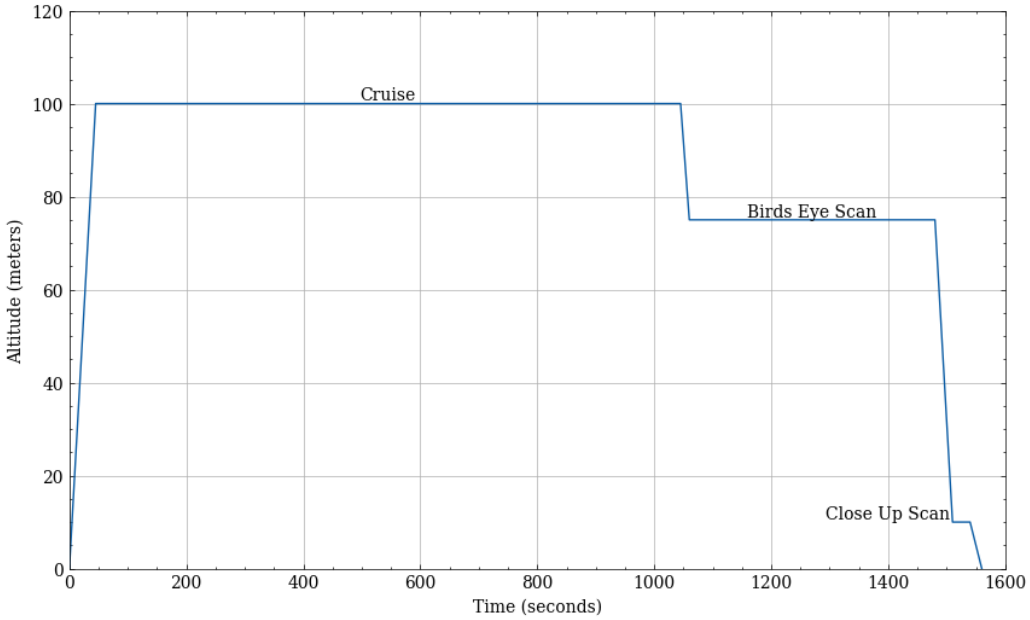

Figure 7.5: Flight profile for a scanning mission.

[2]URL: https://science.nasa.gov/mission/mars-2020-perseverance/rover-components [cited on 17 June 2024]

8 Propulsion

***Authors**: Salar, Jesse*

The thin atmosphere on Mars creates significant aerodynamic challenges for a controlled and sustained flight of autonomous drones. Traditional helicopters designed for Earth's dense atmosphere cannot simply be adapted for Martian conditions without substantial modifications. On Earth, rotors can rely on relatively low rotational speeds to generate sufficient thrust. However, the Martian atmosphere requires rotors to spin at much higher speeds and have larger surface areas to achieve the same effect. For instance, at 2800rpm, Ingenuity's 1.2 m long rotors spin ten times faster than helicopters on Earth[1] . Additionally, the motors must be lightweight and capable of delivering sufficient torque at the high rotational speeds. This requires extensive research in propulsion design, including optimising blade pitch, length, and shape to maximise the rotors' aerodynamic efficiency and minimise their power consumption.

This chapter is divided into five main sections. Section 8.1 lists the requirements the propulsion system has to fulfil, both qualitatively and quantitatively. Then, in Section 8.2, a methodology is presented to design the drone's rotors and blades. This procedure consists of parametrising the planform of the blades, selecting suitable airfoils and discussing the underlying theory of the blade model. Section 8.3 describes the optimisation tool developed to find the ideal rotor and rotor blade geometry to achieve the desired drone performance and meet its requirements. Section 8.4 presents the optimisation procedure results and lists the final subsystem design's most important output values. Section 8.5 describes the reasoning behind selecting a suitable motor for the propulsion system. Lastly, Section 8.6 provides the verification and validation procedures of the developed design tool.

8.1. Requirements

Below, in Table 8.1, the requirements used to design the propulsion system are presented. Each requirement is presented with an ID to ensure they're easily distinguishable and a verification method.

Table 8.1: Requirements for the propulsion system design

ID	Requirement	Verification Method
PRO-SYS-01	The propulsion system shall have a mass of at most 15.7 kg	Inspection
PRO-SYS-02	The propulsion system shall use no more than 18750 W of power	Demonstration
PRO-SYS-03	The propulsion system shall provide the required forces for operation	Demonstration
PRO-SYS-04	The propulsion system shall have a total power efficiency of at least 70%	Test
PRO-SYS-05	The propulsion system shall utilise only renewable sources of propulsion	Inspection
PRO-SYS-06	The propulsion system shall be able to perform dust removal operations	Demonstration
PRO-SYS-03-10	The propulsion system shall produce enough thrust with two rotors inoperative	Demonstration
PRO-SYS-03-01-I	The propulsion system shall provide the required thrust in hover	Demonstration
PRO-SYS-03-02-I	The propulsion system shall provide the required thrust in cruise	Demonstration
PRO-SYS-03-03-I	The propulsion system shall provide the required thrust in takeoff and climb	Demonstration
PRO-SYS-03-04-I	The propulsion system shall provide the required thrust in descent and landing	Demonstration
PRO-SYS-02-01	The propulsion system shall use at most 16000 W of power in hover	Demonstration
PRO-SYS-02-02	The propulsion system shall use at most 12000 W of power in cruise	Demonstration
PRO-SYS-02-03	The propulsion system shall use at most 18750 W of power in takeoff and climb	Demonstration
PRO-SYS-02-04	The propulsion system shall use at most 18750 W of power in descent and landing	Demonstration
PRO-SYS-07	The propulsion system shall be capable of operating at a maximum motor temperature of at least 350 K	Demonstration

[1]URL: https://science.nasa.gov/solar-system/planets/mars/10-things-mars-helicopter/ [cited on 13 June 2024]

8.2. Rotor Blade Design

The design of the rotors began with the rotor blade. For this, a combination of blade element theory and momentum theory was used. The rotor blade was designed for hover, which is the limiting condition in terms of power consumption.

8.2.1. Radial Stations

For the blade design, the radial position from its centre of rotation through to its tip was nondimensionalised with respect to the rotor radius, reducing its range of values between 0 and 1. This is denoted by $\tilde{r} = r/R$. This allowed for isolation of R, the rotor radius, as a design variable. To set up a basis for the input parameters that define the blade, the planform was divided into four radial stations over $\tilde{r}$: The value of $\tilde{r}_3$ was required to be

Table 8.2: Non-dimensionalised radial stations.

i	0	1	2	3
$\tilde{r}_i$	0.08	0.25	0.75	1.00

1.00 to avoid the need for extrapolation to the tip. For this same reason, $\tilde{r}_0$ is located at the root. However, the root does not start at the center of rotation $\tilde{r} = 0$. This is due to two factors: the geometry would be limited at the root, and there needs to be room between the shaft and the blade for the rotor hub and bearing. Additionally, aerodynamic influence of the inflow near the root would be minimal [7]. The root is thus placed at $\tilde{r}_0 = 0.08$, using a slightly more conservative value than NASA's $\tilde{r}_0 = 0.07$ [21]. The first intermediate value $\tilde{r}_1 = 0.25$ was kept near the root, since the Reynolds number over the blade increases rapidly at low radial positions [7]. The station of $\tilde{r}_2 = 0.75$ is added near the tip at for geometrical reasons; the chord at the tip is often lower than for the rest of the blade, so a station near the tip prevents the tip chord from affecting the chord around the middle of the blade; it also allows for a more aerodynamic airfoil at the tip (where the blade experiences the most airflow), explained in the subsequent section.

8.2.2. Airfoil Selection

Selecting suitable airfoils is a crucial aspect of the design process to achieve the desired performance of the drone. Especially in the context of the demanding Martian atmosphere, leading to low Reynolds numbers across the blades and strong viscous effects.

Around and below a Reynolds number of 50 000, conventional airfoils perform poorly due to laminar separation without reattachment, leading to high pressure drag and reduced lift. Additionally, airfoil performance in this range is highly dependent on flow and airfoil conditions [22]. Due to the thick boundary layer at low Reynolds numbers, the effective camber of the airfoil reduces, having a negative effect on the generation of lift. The strong viscous effects also lead to higher resultant losses in the turbulent boundary layer and higher friction drag compared to a laminar boundary layer [21].

In this context, flat and cambered plates with sharp leading edges present a viable alternative since they can outperform smooth airfoils with rounded leading edges and due to their relatively constant performance. Sharp leading edges create a high adverse pressure gradient, causing flow separation and vortex shedding at the leading edge. These vortices can prevent total flow separation and promote turbulent reattachment of the boundary layer. Other sharp leading-edge geometries, like triangular and polygonal airfoils, have also been investigated, performing similarly to the flat and cambered plates at low Reynolds numbers [22]. Because of the aforementioned reasons, a choice was made only to select airfoils with sharp leading edges for the rotor blades. A similar approach to Johnson et al. [21] was taken, where each station is assigned a different airfoil, which provides a solid baseline to the preliminary design of the blades. Moreover, only optimised airfoil profiles were investigated to push the boundaries of blade design and maximise the blades' potential. These airfoils have rather unconventional shapes, and are specifically designed for low Reynolds number operations.

Since each blade is divided into four stations, different airfoils could be selected. Due to the lack of data available for such low Reynolds number airfoils, and XFOIL's, or similarly XFLR5's, inaccuracy in predicting the aerodynamic performance for Re < 20 000 [24], estimates of the aerodynamic data were limited. Additionally, plotting the airfoils for Re > 20 000 in XFOIL was not feasible, due to unknown geometries of certain airfoils and XFOIL's inability to analyse sharp edges. Therefore, existing low Reynold number airfoil concepts for Mars were researched, and slight inaccuracies are present in the model, as the available data is not tailored to the drone's

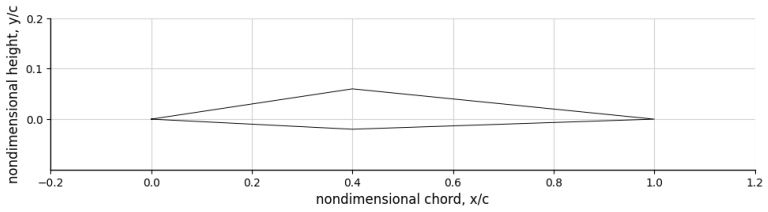

(a) Diamond-shaped airfoil for station 0 [21].

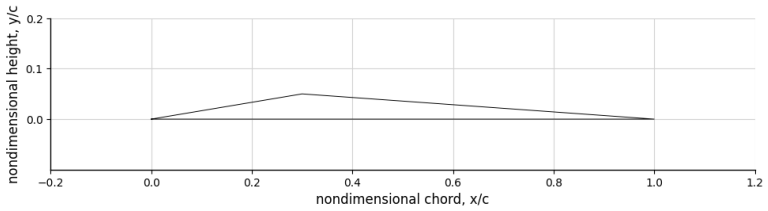

(b) Triangular-shaped airfoil for station 1 [23].

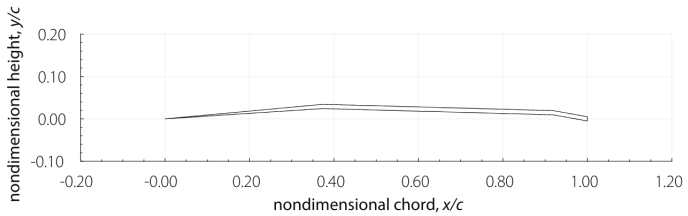

(c) Double-edged plate for station 2 and station 3 [6].

Figure 8.1: Chosen airfoils for the four radial stations, non-dimensionalised.

specific design conditions. After thorough research, three different airfoils were deemed the most suitable, presented in Figure 8.1.

For the airfoil at the root, an airfoil with a relatively high thickness was considered to ensure structural integrity during flight. For this, an optimised diamond-shaped airfoil with a maximum thickness of 8 % at 40 % of the chord was chosen, as reproduced from Johnson et al.[21]. Using an optimisation algorithm, Johnson et al. were able to optimise a parameterised airfoil geometry, using a small set of variables. Aerodynamic data was derived from [25], consisting of lift coefficient and drag coefficient at different angles of attack for Re = 15 000. The reproduced profile is illustrated in Figure 8.1a.

Station 1 allows for a thinner airfoil. Bruni [26] analysed five blade profiles and concluded that a triangular airfoil exhibits superior performance at low Reynolds numbers compared to the nominal profiles. Similar to Munday's findings [23], Bruni observed a significant increase in the lift curve's slope for the triangular airfoil at an angle of attack around 9 degrees. CFD analysis confirmed that this increase is due to a reattached separation bubble forming between either the leading or trailing edge, and the point of maximum thickness. Alternatively, Yang [27], noted that the presence of detached bubbles above the airfoil's upper surface, combined with the almost unchanged pressure under its lower surface, lead to a considerable amount of thrust. A major drawback of this phenomenon is observed when the Reynolds number decreases to 800, which is well-below the design Reynolds number of station 1. As such, a triangular-shaped airfoil was used for this station, with a maximum thickness of 5 % located at 30 % of the chord, as reconstructed in Figure 8.1b. From Munday et al. [23], relevant data was only available at Re = 3000 and Re = 10 000. To stay in range with the previous station, data recorded at Re = 10 000 was selected.

For both station 2 and station 3, a double-edged plate (DEP) airfoil from Koning et al. [22] was chosen, illustrated in Figure 8.1c. Koning et al. optimised airfoils for Martian rotor applications, leading to a 16 % to 29 % higher lift-to-drag ratio compared to Ingenuity's CLF5605 airfoil. At high Mach numbers, both the cambered plate and the double-edged plate airfoils were significantly better, with DEP airfoils excelling at M = 0.90. The high performance of the DEP airfoil can be explained by a 'critical angle of attack', where separation shifts from the upper surface crest to the leading edge, causing a nonlinear lift curve. Compressibility at high Mach numbers increases this angle, explaining the strong performance of the DEP airfoil [6]. Data recorded [22] at Re = 10 117, for M = 0.50 and M = 0.70, was used for station 2 and station 3 respectively. Data for M = 0.90 at Re = 30 351 was also available, but since it was decided to limit the tip Mach number to 0.70, this data was omitted.

Figure 8.2a and Figure 8.2b display the lift and drag curves, respectively, for the selected airfoil at each station. The difference between stations 2 and 3 is caused by an increased Mach number at the latter. A decrease in drag can also be observed for station 3's DEP airfoil beyond an angle of attack of 8°. It is uncertain whether this phenomenon reflects reality. Consequently, any subsequent results, that require the third station to exceed an 8° angle of attack, should be treated cautiously and require additional verification.

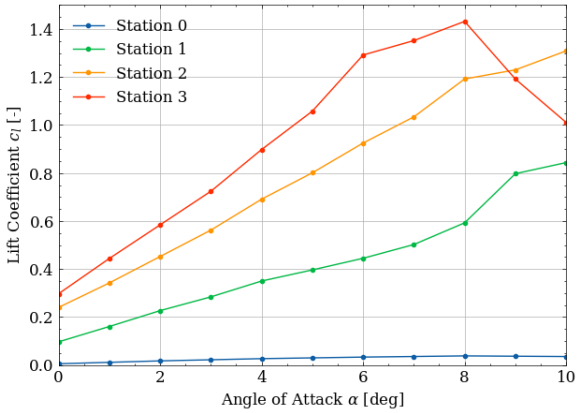

(a) Lift curves for airfoils at each radial station

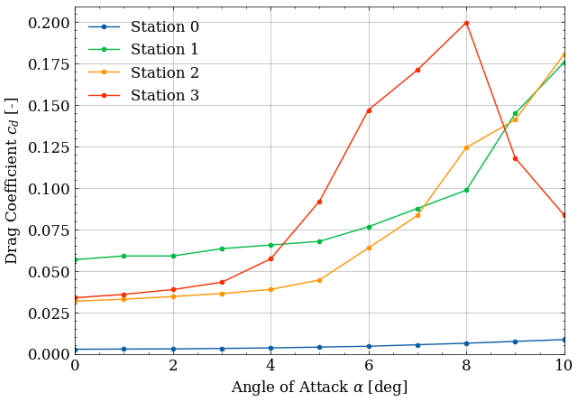

(b) Drag curves for airfoils at each radial station

Figure 8.2: Airfoil aerodynamic coefficient plots

8.2.3. Blade Model

The blade model begins by defining the design parameters, as follows:

- Number of blades N
- Rotor radius R
- Airfoil at radial stations Airfoil($\tilde{r}_i$)
- Nondimensionalised chord at radial stations $\tilde{c}(\tilde{r}_i)$
- Pitch distribution parameters $\theta(\tilde{r}_0)$, $\theta(\tilde{r}_3)$, $\frac{\mathrm{d}\theta}{\mathrm{d}\tilde{r}}(\tilde{r}_0)$

Alongside these, a set of environmental and airflow properties are considered:

- Ratio of specific heats γ
- Specific gas constant R_{sp}
- Ambient temperature T_a
- Air density ρ
- Air viscosity μ
- Maximum tip Mach number in hover M_t

The hover tip Mach number was used to calculate the hover thrust and power, directly leading to sizing. A value of 0.7 was selected, consistent with existing literature on Mars [21]. For the remaining parameters, the location of the scientific mission is known from Chapter 2. Values for this location at the time of day and solar longitude with the lowest air density were taken. This is because the minimum air density corresponds to the most power required to counteract the rotorcraft weight. The Mars Climate Database was used to obtain these values [4].

Preprocessing

The model defines the blade geometry and functions by interpolating input parameters over the radial stations. In this section, N_{blades} and R are assumed to be given for an iteration. The former must be an integer. The latter does not affect the radial geometry, rather just scales the blade; the minimum value where the thrust requirement is met is always desirable due to the dimensional limitations and structural integrity of the blade. Thus both are manually optimisable. Airfoils at the radial stations have already been selected Section 8.2.2.

Figure 8.3 displays the flow of this process. The nondimensionalised chord $\tilde{c} = c/R$ is interpolated linearly between each radial station. For a given rotor radius, this gives the chord distribution. Using the quarter chord

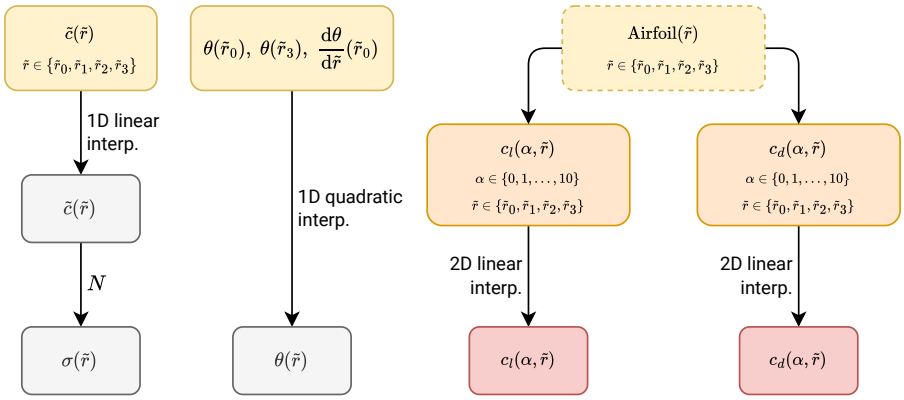

Figure 8.3: Blade input processing

as the reference line gives equations for the leading and trailing edges, defining the planform geometry:

$$x_{\text{LE}}(\tilde{r}) = \frac{1}{4}R\tilde{c}(\tilde{r}) \qquad x_{\text{TE}}(\tilde{r}) = -\frac{3}{4}R\tilde{c}(\tilde{r}) \tag{8.1}$$

In Equation 8.1, $x = 0$ at the quarter chord line for a given blade. The solidity over the blade, used to calculate thrust and power coefficients, is computed directly from the nondimensionalised chord:

$$\sigma(\tilde{r}) = \frac{\mathrm{N}}{\pi}\tilde{c}(\tilde{r}) \tag{8.2}$$

The pitch parameters are used to define the pitch as a function over the blade. A quadratic function was decided as it would be able to resemble most nonlinear curves whilst still requiring just 3 parameters to iterate over. The parameters are the pitch at the root $\theta_0 = \theta(\tilde{r}_0)$, the pitch at the tip $\theta_3 = \theta(\tilde{r}_3)$, and the spanwise rate of change of the pitch at the root $\theta_0' = \frac{d\theta}{d\tilde{r}}(\tilde{r}_0)$. This defines a unique quadratic function $\theta(\tilde{r})$ presented in Equation 8.3, and is preferable to defining the pitch at each station which would require cubic interpolation and may result in various extrema (changes in the sign of the pitch slope), undesirable for manufacturing and structural loads.

$$\theta(\tilde{r}) = \theta_0 + \theta_0'(\tilde{r} - \tilde{r}_0) + \frac{\theta_3 - \theta_0 - \theta_0'(1 - \tilde{r}_0)}{(1 - \tilde{r}_0)^2}(\tilde{r} - \tilde{r}_0)^2 \tag{8.3}$$

Lastly, airfoil data is given as the section lift and drag coefficients over integer angles of attack α from 0 to 10. These are interpolated linearly over both the α and $\tilde{r}$ dimensions, providing a continuous lift curve $c_l(\alpha)$ and drag curve $c_d(\alpha)$ distribution over continuous spanwise blade sections.

Spanwise Distributions

Blade element theory (BET) and momentum theory (MT) can be used in conjunction (BEMT) to determine the angle of attack, lift coefficient and inflow distributions over the blade. Figure 8.4 illustrated the flow of this process.

Equation 8.4 presents the differential thrust coefficient as calculated from BET and MT, respectively [7].

$$\mathrm{d}C_T = \frac{1}{2}\sigma c_l \tilde{r}^2 \mathrm{d}\tilde{r} \qquad \mathrm{d}C_T = 4\lambda^2 \tilde{r}\mathrm{d}\tilde{r} \tag{8.4}$$

In Equation 8.4, λ is the inflow, which is the ratio of air inflow velocity to the horizontal fluid velocity of the blade. In this case, rather than assuming it is constant over the disk, it is considered as a distribution over the blade, similar to the remaining variables in the equation. Combining the equations in Equation 8.4 gives:

$$c_l = \frac{8}{\sigma\tilde{r}}\lambda^2 \tag{8.5}$$

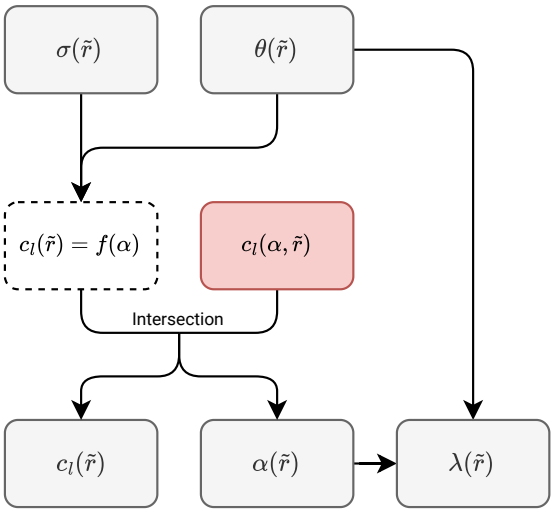

Figure 8.4: Lift coefficient, angle of attack and inflow computation.

The inflow angle at a blade section is given by [7]:

$$\phi = \tan^{-1} \lambda = \theta - \alpha \tag{8.6}$$

Equation 8.6 describes that the inflow angle is also the difference between the angle of attack and the pitch angle. Given that the pitch and solidity distributions are known, this provides a constraint between the section lift coefficient c_l and the angle of attack α for a given blade section at a radial position $\tilde{r}$:

$$c_l(\tilde{r}) = \frac{8}{\sigma\tilde{r}} \tan^2 (\theta(\tilde{r}) - \alpha(\tilde{r})) \qquad \{\alpha \leq \theta\} \tag{8.7}$$

Combining this with the airfoil $c_l(\alpha)$ curve and finding the intersection provides c_l and α at a given blade section $\tilde{r}$, as σ and θ are known from $\tilde{r}$. An example is illustrated in Figure 8.5. Since inflow cannot be negative, the pitch defines the upper bound of the angle of attack, leading to a unique solution.

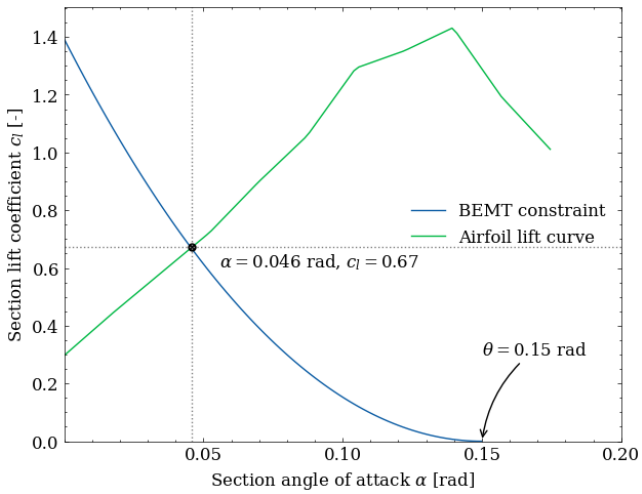

Figure 8.5: Example calculation of section angle of attack and lift coefficient at a given radial position.

This elegant approach leads to the section lift coefficient c_l and angle of attack α both as a function of $\tilde{r}$. This angle of attack can be subtracted from the pitch to get the inflow angle ϕ, and using Equation 8.6, the inflow λ can also be calculated for each blade element, making it a function of $\tilde{r}$.

It is useful to keep in mind that this constraint exists due to the pitch and chord being *model* inputs, allowing for this approach; this does not mean they are *design* inputs, since an optimisation algorithm iterates over different combinations of model inputs to find the ideal values to meet the design requirements.

Thrust and Power Coefficients

Having calculated all spanwise variables, the thrust and power coefficients of the rotor in hover can be calculated. Throughout this section Figure 8.6 can be used as a reference for the context of the performed calculations.

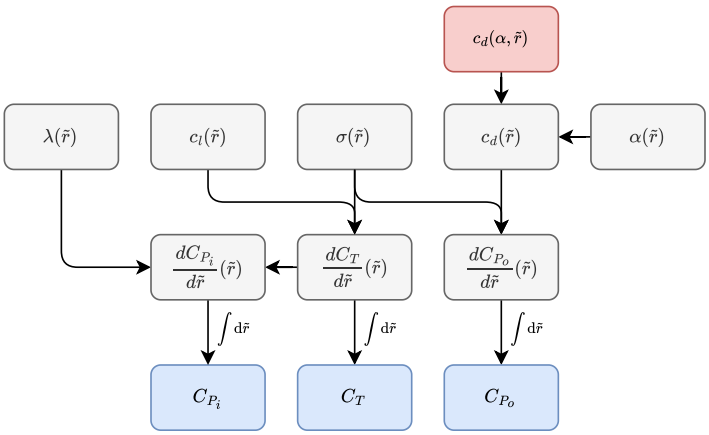

Figure 8.6: Thrust and power coefficient computation.

Using (either side of) Equation 8.4, the differential thrust coefficient of each blade element can be calculated. Prior to integrating, tip loss must be taken into account. The thrust prediced by BET is nonzero up until the tip, but in reality it drops off to zero for a finite blade. The approach suggested by Johnson is to assume that beyond the $\tilde{r} = 0.97$ point (the "tip loss factor" B), the blade produces no lift (but still experiences profile drag); this is generally consistent with experimental data [7].

Integrating the differential thrust until the tip loss factor of $B = 0.97$ calculates the thrust coefficient of the full rotor disk:

$$C_T = \int \mathrm{d}C_T = \int_{\tilde{r}_0}^{B} \frac{1}{2}\sigma(\tilde{r}) \cdot c_l(\tilde{r}) \cdot \tilde{r}^2 \mathrm{d}\tilde{r} \tag{8.8}$$

The differential induced power coefficient of a blade section is given by [7]:

$$\mathrm{d}C_{P_i} = \lambda \mathrm{d}C_T = \lambda \frac{1}{2}\sigma c_l \tilde{r}^2 \mathrm{d}\tilde{r} \tag{8.9}$$

Losses due to nonuniform inflow are already accounted for by the BEMT constraint in Section 8.2.3 and the tip loss factor in integration. Proceeding similarly as before to calculate the induced power coefficient of the rotor:

$$C_{P_i} = \int \mathrm{d}C_{P_i} = \int_{\tilde{r}_0}^{B} \lambda(\tilde{r}) \cdot \frac{1}{2}\sigma(\tilde{r}) \cdot c_l(\tilde{r}) \cdot \tilde{r}^2 \mathrm{d}\tilde{r} \tag{8.10}$$

Knowing the angle of attack distribution $\alpha(\tilde{r})$ allows for the calculation of the section drag coefficient over the blade. From here, blade element theory is applied to calculate the differential profile power coefficient, due to the drag experienced by the rotor blades [7]:

$$\mathrm{d}C_{P_o} = \frac{1}{2}\sigma c_d \tilde{r}^3 \mathrm{d}\tilde{r} \tag{8.11}$$

Integrating (tip loss does not apply here) provides the profile power coefficient of the rotor:

$$C_{P_o} = \int \mathrm{d}C_{P_o} = \int_{\tilde{r}_0}^{1} \frac{1}{2}\sigma(\tilde{r}) \cdot c_d(\tilde{r}) \cdot \tilde{r}^3 \mathrm{d}\tilde{r} \tag{8.12}$$

Thrust and Power

The calculated thrust and power coefficients can be dimensionalised by the tip speed calculated from constants:

$$a = \sqrt{\gamma R_{sp} T_a} \qquad V_t = M_t a \tag{8.13}$$

The disk area is also used, given by $A = \pi R^2$ for a given rotor radius R.

For thrust, the dimension is proportional to density, disk area and the square of the tip speed [7]:

$$T = C_T \rho A V_t^2 \tag{8.14}$$

Equation 8.14 calculates the thrust produced by one rotor disk; given that the design is a hexacopter, the full rotor thrust is six times this value.

For power, the tip speed dimension is cubed instead [7]:

$$P_i = C_{P_i} \rho A V_t^3 \qquad P_o = C_{P_o} \rho A V_t^3 \tag{8.15}$$

Summing gives the total power required:

$$P = P_i + P_o \tag{8.16}$$

These values are used to design the optimal rotor for a given thrust requirement, as power is the limiting factor for battery and thermal system sizing.

8.3. Rotor Blade Optimisation

After the rotor design tool was constructed, an optimization tool was implemented into the model. This tool was used to determine the optimal blade geometry, minimising the required rotor power.

A schematic overview of the optimisation process is provided in Figure 8.7. Relevant constraints are first discussed. Then, the objective and optimisation inputs, as well as the chosen algorithm, are presented.

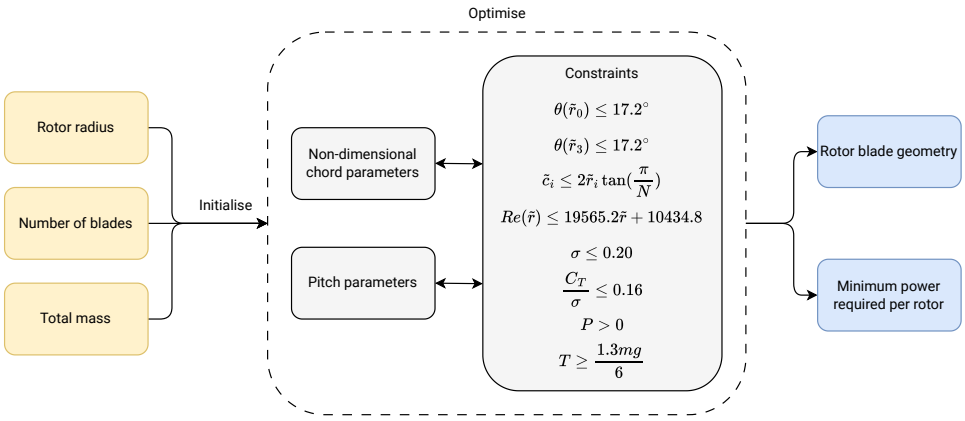

Figure 8.7: Rotor blade optimisation process for minimum rotor power.

Constraints

To obtain consistent and practical results, and achieve maximum efficiency from the optimiser, constraints were first defined. These constraints were extrapolated from literature and geometrical considerations. The former applied to performance metrics of the rotor, while the latter concerned defining bounds for the pitch and chord parameters.

First, the pitch angles at the root and tip chords were limited to 17.2°. This was done to avoid excessive angles of attack, as stall was reached at angles of 10° for most airfoils. Next, the maximum non-dimensional chord parameters were established using the number of blades and the radial positions of the chords, as defined by Equation 8.17:

$$\tilde{c}_i \leq 2\tilde{r}_i \tan\left(\frac{\pi}{\mathrm{N}}\right) \tag{8.17}$$

where N is the number of blades per rotor. Equation 8.17 was derived using geometry, where the sides of a polygon represented the maximum chord at an arbitrary station.

The performance constraints included bounds on the Reynolds number, thrust and solidity. For the Reynolds number, it was decided that the Reynolds number at root and the tip should never exceed 12 000 and 30 000, respectively. Between these two points, linear interpolation was used to indicate the maximum Reynolds number of the remaining sections, leading to Equation 8.18. This was done to avoid excessive Reynolds numbers, which would lead to high chord lengths and invalidate the aerodynamic data. Specifically, the data of the double-edged plate airfoil, which was analysed by Koning et al. [6] up to Re = 30 351. Moreover, the Reynolds number range for a Mars rotor airfoil is between 10 000 and 30 000 [22].

$$\mathrm{Re}(\tilde{r}) \leq 19565.2\tilde{r} + 10434.8 \tag{8.18}$$

The solidity σ of the rotor was limited to 0.20, to minimise the weight of the rotor and limit the hover power. The blade loading $\frac{C_T}{\sigma}$ was restricted to a maximum value 0.16, as limited by stall [21]. A constraint was added, such that the induced and profile power were strictly positive. Lastly, to have a sufficient thrust-to-weight factor for the controllability of the GNC subsystem, a factor of 1.3 was applied to the total weight of the drone. Following this constraint, the thrust each rotor has to provide is described in Equation 8.19:

$$T \geq \frac{1.3mg}{6} \tag{8.19}$$

where m is the total mass of the drone and g is the gravitational acceleration on Mars. The weight is divided by six since this gives the required thrust per rotor, assuming each rotor provides an equal amount of thrust.

Objective and Inputs

Next, the inputs and the objective function of the optimisation were investigated. Since other subsystems require propulsive power as input and power is the limiting factor during their sizing process, it was decided to minimise the total required power of the propulsion subsystem. Due to the tool's high variability, the non-dimensional chord and pitch parameters were used as variables to iterate over, creating a seven-dimensional space. This left the number of blades, rotor radius, and mass as input parameters for iteration. The chord and pitch parameters are independent values, as discussed previously in Section 8.2.3

Optimisation Algorithm

With the optimisation procedure set up, an optimisation algorithm could be chosen. Since this procedure is a multivariate problem requiring finding the global minimum of the objective function, the differential evolution (DE) algorithm was found to be the most applicable. This method is part of a series of evolutionary algorithms and is stochastic. It, therefore, uses no gradient methods to find minima. The algorithm is based on four main phases: initialisation, mutation, crossover and selection. The initialisation phase occurs only at the beginning, whereas the other three phases are repeatedly executed during the DE's search process within the seven-dimensional solution space [28]. Due to its robustness, efficiency and easy implementation, this algorithm was deemed the most suitable for this procedure [29]. Ahmad et al. [28] suggest using a population size of 100, and a crossover value of 0.5 as the parameter settings for various research domains, thereby providing more diverse candidate solutions and improve the procedure of finding the global minimum. During the set-up of the DE optimiser, these values were considered, as they provide a solid baseline for the optimisation process.

8.4. Results

The final blade geometry and propulsion system layout followed from the optimisation tool and the final iteration with the other subsystems. The results are listed in Table 8.3. During the iterations, it was observed that the root chord length was highly variable and rather random. After further inspection, it was concluded that the root chord had little influence on the overall performance of the rotor. The length of the root chord was therefore changed accordingly, such that it complies with structural and weight requirements set by the other departments, while still meeting the optimisation constraints. Moreover, two rotor blades per rotor were found to be insufficient, as no feasible configurations were found by the optimiser at the considered masses. Three blades were therefore considered for the final design; dimensional limitations and the need for a folding mechanism warranted the minimum possible number of blades.

A root pitch angle of 15.6° and a tip pitch angle of 10.1° was observed. The higher pitch angle at the tip of blade can be related to the thrust constraint, which requires a significant thrust output from each rotor.

To define the overall (hovering) efficiency of the rotor, the figure of merit (FM) can be determined. This metric compares the rotor performance with the ideal rotor performance [7]. It follows from Equation 8.20:

$$FM = \frac{C_T^{3/2}/\sqrt{2}}{C_P} \tag{8.20}$$

where C_T and C_P are the thrust and power coefficients, respectively, of the rotor. From the optimised geometry, a figure of merit of 0.65 was found, approximately 7 % higher than Ingenuity's rotor at the same thrust coefficient [21].

Table 8.3: Rotor results

Optimised blade model inputs

Input	Value	Unit
N	3	-
R	1.2	m
Airfoil($\tilde{r}_0$)	*Diamond*	-
Airfoil($\tilde{r}_1$)	*Triangular*	-
Airfoil($\tilde{r}_2$)	*Double-edged plate*	-
Airfoil($\tilde{r}_3$)	*Double-edged plate*	-
$\tilde{c}(\tilde{r}_0)$	0.16	-
$\tilde{c}(\tilde{r}_1)$	0.2315	-
$\tilde{c}(\tilde{r}_2)$	0.1637	-
$\tilde{c}(\tilde{r}_3)$	0.1452	-
$\theta(\tilde{r}_0)$	0.2715	rad
$\theta(\tilde{r}_3)$	0.1754	rad
$\mathrm{d}\theta/\mathrm{d}\tilde{r}(\tilde{r}_0)$	-0.1725	rad

Key rotor characteristics

Parameter	Symbol	Value	Unit
Number of rotors	N_{rot}	6	-
Rotor disk area	A	4.524	m^2
Disk loading	$(T/g)/A$	2.33	$\mathrm{kg\,m^{-2}}$
Blade aspect ratio	AR	5.86	-
Rotor solidity	σ	0.163	-
Blade loading coeff.	C_T/σ	0.127	-
Mean lift-to-drag ratio	c_l/c_d	14.7	-
Max. Reynolds number	Re	29004	-
Max. rotor speed	Ω	1443	rpm
Max. thrust	T	39.1	N
Max. induced power	P_i	746	W
Max. profile power	P_o	362	W
Max. rotor power	P	1108	W

Table 8.3 displays the optimised blade model parameters and the key rotor parameters after inputting these optimised inputs into the model. It is important to note that the maximum values in the output table correspond to a thrust-to-weight ratio of 1.3, and the values are per rotor disk. The rotor power values do not account for motor efficiency. These values can be non-dimensionalised, and from there, the coefficients can be used to calculate the required rotor speed for a submaximal thrust (e.g. hover), which is used for performance analysis.

8.5. Motor Selection

The next step for the propulsion subsystem was to select a rotor motor, turning battery power into the rotation of the blades. It was decided to select an off-the-shelf motor; despite potentially incurring costs, building a motor in-house would require additional development time. The properties were based on the rotor output table in Section 8.4, particularly the maximum of 1443rpm. Converting this to SI units and using $P = Q\Omega$ where Q is torque, the required torque is calculated to be 7.33 N m. Taking the maximum power of 1108 W, these three parameters are used to select a motor.

The chosen motor was the Plettenberg NOVA 1 motor[2] . This motor has a peak power of 2 kW and peak torque of 2.4 N m, or a maximum rotational speed of 15 000rpm in stock conditions. However, Plettenberg allows for the request of customised motors within the appropriate constraints. Particularly, an increase in the number of coils in the motor armature would allow an increase in the peak torque to 8 N m with a corresponding maximum rotational speed reduction to of 4500rpm at the same peak power, which is still well above the required rotational speed. This is a more mass-efficient approach than using a gearbox, as the required gear ratio is small and does not warrant a gearbox. The mass of the motor is 375 g, but a 10 % contingency is applied due to the modifications.

The motor has an efficiency of over 90 %, but just 90% is assumed. This means that for each rotor, the maximum motor power required is 1231 W. The heat loss, corresponding to the efficiency loss of the motor, is thus the portion of this power that does not go to the rotors, equal to 123.1 W per motor. This is a conservative assumption and is used for the thermal control system. Additionally, the maximum operational temperature of the motor, as stated in its manual, is 100 °C, or 373.15 K.

[2]URL: https://plettenbergmotors.com/product/nova-1-en/ [cited on 18 June 2024]

8.6. Verification and Validation

To assess the reliability and accuracy of the design tool, verification and validation procedures were followed. Various verification and validation procedures are therefore discussed in this section, to assess the validity of the developed design tool.

Verification

Verification of the main blade model tool was performed through numerous tests. A sample dataset, consisting of the rotor radius, number of blades, radial stations, chord parameters and pitch parameters was first generated. Using these inputs, a test was written that checked if the properties are correctly initialised by the model. Next, arbitrary atmospheric conditions and tip Mach number were assumed, which checks if the model correctly calculates and assigns the attributes speed of sound, tip speed and Reynolds number of each rotor. Another test was written that checks if the thrust and induced power rotor are correctly calculated and assigned. This test was initialised using arbitrary values for the thrust coefficient, rotor area, and tip speed. Lastly, the interpolated lift and drag curves were visually examined against the aerodynamic input data of the airfoils, to check for any deviations between the curves. After running the tests, no errors or discrepancies were found.

Sensitivity analyses were also conducted to assess the influence of input parameters on the output of the model. Extreme values were considered, such as a rotor radius of zero or zero rotor blades. Other tests involved varying the pitch and chord parameters to verify their relation with expected geometric changes. For instance, increasing the chord length at an arbitrary station should increase the aspect ratio of the blade. The analyses revealed no conflicting results in the model's predictions.

The optimisation tool was also verified by manually trying numerous blade configurations, to optimise the rotor blade performance and minimise the required power by hand. Despite extensive testing, it was concluded that no solutions surpassed the optimised solution identified by the algorithm, without violating the constraints that were discussed in Section 8.3.

Validation

To validate the design tool, the Mars Science Helicopter (MSH) hexacopter design inputs were considered. The blade geometry, including chord, twist and airfoils, is available in NASA's MSH Conceptual Design [21]. For brevity, this data is not listed in this report. The only missing data point is the airfoil curves for the diamond airfoil at 25% of the blade. Data for the triangular airfoil at this point is used as an approximation, due to similar Reynolds numbers. Environmental parameters were adjusted in the model to match those used for NASA's site. Taking these parameters are model inputs, the generated outputs are compared with those in the MSH paper. Besides solidity, which serves to verify the basic planform dimension calculation, other outputs which are exclusively geometric (e.g. aspect ratio) are not compared, since they are entirely equivalent. Due to the limited amount of information from NASA, this meant only three additional parameters were available.

Table 8.4: Validation of the blade model with NASA's Mars Science Helicopter design [21]

Output	Symbol	NASA Value	Model Value	Unit	Deviation
Blade loading coeff.	C_T/σ	0.115	0.116	—	0.87 %
Disk loading	$(T/g)/A$	2.24	2.57	$\mathrm{kg\,m^{-2}}$	14.7 %
Rotor solidity	σ	0.181	0.181	—	0 %
Rotor power	P	336	339	W	0.89 %

Table 8.4 compares the model outputs to NASA's data. Solidity matches exactly, meaning the geometrical definition of the planform by the model is fully accurate. The variations in blade loading coefficient and rotor power are below 1 %, well within a threshold to be considered validated; it the model is very accurate in estimating hovering performance and efficiency. The only major discrepancy is in the disk loading. The discrepancy may be attributed to the missing airfoil data point, but this is unlikely as it would have resulted in a larger deviation for C_T/σ and power. Instead, it is likely due to NASA's disk loading figure being exclusively based on the design weight of the hexacopter; on the other hand, the blade model used in this report calculates disk loading from the maximum thrust generated by the rotor blade, which can exceed the weight due to margins. NASA does not apply a margin on thrust in the disk loading. Given that NASA's values are from the validated NDARC design tool [30], and all significant discrepancies can be addressed, the model is both internally and externally consistent and can be considered validated for optimisation.

9 Electrical Power System

***Authors**: Florian*

The electrical power system (EPS) is a critical subsystem for the Martian Drone and is responsible for providing a reliable power supply to the various onboard systems. The harsh and variable environmental conditions on Mars present unique challenges for power generation, storage, and distribution systems that must be addressed. This chapter outlines the design methodology for the EPS, component selection, and system architecture. Emphasis is placed on finding lightweight solutions that provide a robust and efficient design to meet stakeholder requirements. Redundancy and fault tolerance are incorporated to enhance the system's reliability and ensure a successful mission.

This chapter highlights the main functions of the EPS, the driving and key requirements for the design and the selected power generation and storage concepts in Section 9.1. Additionally, the challenges relevant to the chosen EPS concept encountered in the Martian environment are discussed in Section 9.2. The design method is presented in Section 9.3. The design method describes the construction of a power usage profile, reflecting the power requirements of the drone's subsystems throughout a typical mission. From this profile, the design of the power generation, storage and distribution system architectures follow. The method for verifying and validating the design process is presented in Section 9.4. Finally, the results are presented along with a performance analysis of the EPS in Section 9.5.

9.1. Requirements

In this section, the basis for designing the EPS is provided by identifying the primary functions that must be fulfilled and formulating the design's driving and key requirements. Once these requirements are established, the selected power generation and storage concepts is discussed, paying particular attention to their advantages over others.

Primary Functions

The functional breakdown illustrated in Figure 9.1 provides an insight into the primary functions that this subsystem must fulfil.

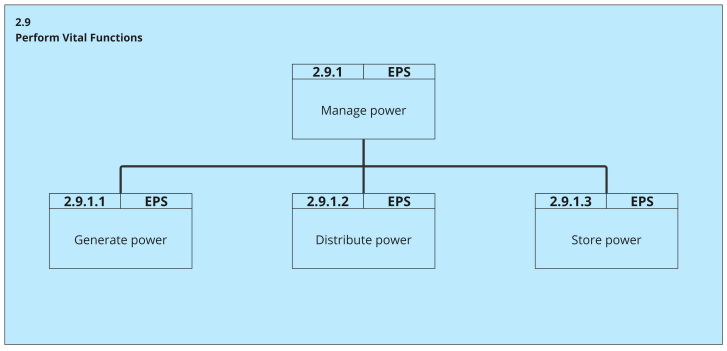

Figure 9.1: Functional breakdown structure of the EPS

Requirements

In Table 9.1, the key and driving requirements for the design of the EPS are presented. For the sake of readability, the other requirements, though necessary for the final EPS design to comply with, are not included as they are not directly relevant to the primary design considerations of the EPS.

Table 9.1: Requirements for the EPS design. Verification of these requirements falls under the responsibility of the power lead.

ID	Requirement	Verification Method
EPS-SYS-02-01-I	The power system shall generate at least 89 W of average power at yearly average solar flux conditions, the average power consumption over a two-day mission	Test
EPS-SYS-03-I	The power system shall be able to store at least 2374 W h of energy, the energy required for 30 minutes of flight endurance	Demonstration
EPS-SYS-06-I	The power distribution system shall be designed to provide a peak power of 7387 W, the power usage when the drone's six rotors operate at a T/W of 1.3	Analysis, Test
EPS-SYS-07	The power system shall generate power from a renewable source	Demonstration
EPS-SYS-10-02-I	The power distribution system shall have no single point of failure (SPF)	Inspection
EPS-SYS-11-I	The solar arrays shall provide the design average power of 89W at yearly average solar flux conditions with one inoperative string	Test
EPS-SYS-13-I	The battery shall be capable of operating at temperatures between −20 °C and 40 °C	Test
EPS-SYS-14-I	The power system shall have a reduced power mode using a maximum of 30 W, to be activated in case of dust storms	Test
EPS-SYS-16	The power system shall be designed such that the drone may charge on a 15° incline, the maximum slope on 94 % of the Eberswalde crater	Analysis
EPS-SYS-17	The power system shall be able to store at least 2374 W h of energy under one string inoperative conditions	Test

Selected Concepts

To address the power generation function of the EPS, photovoltaic (PV) solar panels were selected as the most optimal concept given the mission requirements. A radiothermal isotope generator (RTG) concept was initially considered but was ultimately rejected due to the low specific power, given that minimizing mass is of primary importance to the design of the EPS. Indeed, RTGs only provide up 10 W kg^{-1} compared to 300 W kg^{-1} for PV panels [31]. Moreover, RTGs rely on non-renewable energy sources, which is a violation of the stakeholder requirements.

For the power storage function, Lithium-ion (Li-ion) batteries were selected. Lithium-polymer (Li-poly) batteries were also initially considered due to their high discharge rate capabilities. However, given the 30-minute flight profile and allowing for peak power spikes, a maximum discharge rate of around 3C is sufficient. Li-ion batteries offer high specific energy (up to 265 W h kg^{-1}), a high Technology Readiness Level (TRL) due to extensive use in the space industry, and a cycle rating of up to 5000 charging cycles[31]. An important consideration is Li-ion batteries' relatively restricted operational temperature range, which is discussed in Chapter 10.

9.2. Environmental Challenges

The Martian environment presents significant challenges for the operation of the EPS. To achieve a high-fidelity design, it is crucial to accurately model the impact of these environmental factors on the performance of the various components of the EPS, including the solar arrays and batteries, and to identify where design margins should be taken. In this section, the primary environmental considerations are discussed, and their impact is quantified.

Solar Irradiance

The solar irradiance on Mars is lower than on Earth since Mars is further away from the Sun. Additionally, since the design concerns a vehicle operating close to the surface and not in orbit around the planet, the effect of the angle of incidence between the surface of the solar array and the solar radiation has to be considered. It was possible to obtain the incident solar flux on the horizontal surface on Mars through the Martian Climate Database[4]. This tool provides information about the solar flux value for the previously selected landing location, with an hourly resolution over an entire year, as seen in Figure 9.2.

As can be observed from the heatmap of Figure 9.2, the solar flux greatly varies throughout the day and the year. For this reason, the data in its default format is not particularly useful for sizing the solar arrays. Instead, some further processing of the data is performed. In Figure 9.3, the average solar flux per day is plotted over an entire year. It can be seen that the average solar flux fluctuates between 80 W m^{-2} to 210 W m^{-2}. Choosing either of those for the sizing of the solar array would lead to either over- or under-sizing the solar array. Instead, the yearly harmonic average is calculated and used to determine the area of the array.

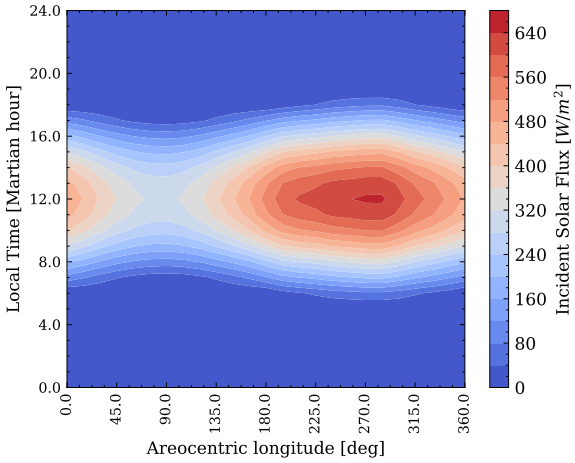

Figure 9.2: Incident solar flux on the horizontal surface over the year

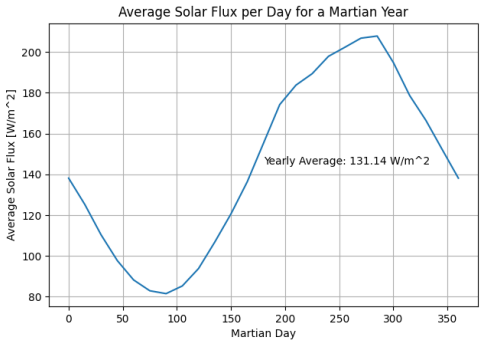

Figure 9.3: Daily average solar flux over the year

Dusty Environment

A characteristic of the Martian surface is the abundant presence of dust. Dust particles can hinder the performance of the solar arrays, utilising three different mechanisms, each of which is discussed here. The first mechanism is the reduction of solar flux reaching the solar arrays due to airborne dust in the atmosphere. According to the Martian Climate Database [4], this can only occur during the dust-storm period of the year and has an approximate occurrence frequency of 3 years[1] . The effect of the dust storm can be simulated through the MCD tool, however, since the drone is not intended to operate through extreme weather conditions it does not make sense to use extreme dust conditions for the sizing of the array. Research is currently being done on the prediction of these extreme events, for now, it can be assumed that the occurrence of global and local dust storms can be predicted to a sufficient level of confidence such that the drone may prepare for such events by temporarily halting scientific operations and focus on recharging its batteries[32].

The second consideration is the accumulation of dust on the surface of the solar panels which can limit the area exposed to incident solar flux. This mechanism is favoured due to the slightly electrostatic nature of Martian dust, which causes it to stick more easily to the solar array surface[2] . This issue is of major concern: data from the Pathfinder mission demonstrates that its solar array performance degraded at the extremely high rate of 0.28 % per sol due to dust accumulation, extrapolating this over a two-year mission means that less than one-quarter of the performance is expected to remain at EOL[33]. This is unacceptable and thus the issue must be actively mitigated by performing regular dust removal operations. The concept for clearing the drone's solar arrays from dust is to utilise the downwash from the rotor blades to blow the dust away. Analysis of solar array performance data from the Pathfinder mission suggests that 'significant clearing of dust occurred with wind speeds above $35\,\mathrm{m\,s^{-1}}$'[34]. The downwash produced at the blade tips reaches the order of $50\,\mathrm{m\,s^{-1}}$ during flight, the placement of the solar arrays must be such that the downwash velocity over the panels is maximized. However, upon landing, a significant amount of dust is expected to be uplifted into airborne particles, as demonstrated by Lemmon et al.[35] in their study of high-speed imaging data from the Perseverance rover of Ingenuity during takeoff and landing. To account for uncleared dust in flight and the settlement of this airborne dust post-landing, it is considered that the dust could cover up to 10% of the available solar array area.

The last consideration in terms of dust is the abrasion of the solar cells, leading to accelerated degradation of the performance of the solar arrays. Data from the Opportunity mission suggests that the solar cell performance degraded by 9.4% over a mission time of 4.9 Martian years (or 1% per Earth year) due to dust abrasion[36]. Further development of the EPS in the detailed design phase could look into the feasibility of using cover glass to limit cell degradation.

Temperature

As can be seen in the temperature distribution for the Eberswalde crater presented in Figure 9.4, the temperature at the surface during power generation periods is expected to lie in the range of $-100\,^{\circ}\mathrm{C}$ to $0\,^{\circ}\mathrm{C}$. Solar arrays

[1]URL: https://www.powerandresources.com/blog/solar-power-is-challenging-on-mars [cited on 21 May 2024]
[2]URL: https://www.nasa.gov/solar-system/the-fact-and-fiction-of-martian-dust-storms/ [cited on June 12 2024]

operate most efficiently at low temperatures, so it is assumed that the solar cell efficiency will not be degraded due to the Martian temperature environment. On the other hand, low temperatures are a primary consideration for the design of the batteries, as they must be kept in a range of $-20\,°C$ to $40\,°C$ at all times. This aspect is be discussed in Chapter 10

Electromagnetic Spectrum Shift

The solar irradiance spectrum on Mars is different than on Earth. This results from light being filtered differently by the gasses and dust in the Martian atmosphere. According to Landis et al., the scattered light reaching the Martian surface features more long-wavelength "red" light and less short-wavelength "blue" light[37]. This can impact solar cell efficiency, as most of the documentation behind solar cells is based on the AM0 spectrum or zero atmospheric light spectrum.

Radiation

Although Mars lacks a magnetosphere, the Martian atmosphere provides some shielding from radiation, with the radiation levels on the surface in the range of $240\,\text{mSv yr}^{-1}$ to $300\,\text{mSv yr}^{-1}$, which is lower than in typical LEO orbits [38]. At this level of radiation, space-qualified solar cells will not degrade rapidly, and thus a degradation rate due to radiation of 1% per year will be considered [33].

Surface Topography

Finally, the hilly topography of the Eberswalde crater should be taken into account, as the drone will likely not receive solar flux from an ideal angle when recharging after having collected a sample on an inclined surface. According to the MCD, 94% of the Eberswalde crater has slopes of at most 15° incline, as displayed in Figure 9.5[4]. The solar arrays are sized considering the drone may recharge on a slope up to 15°.

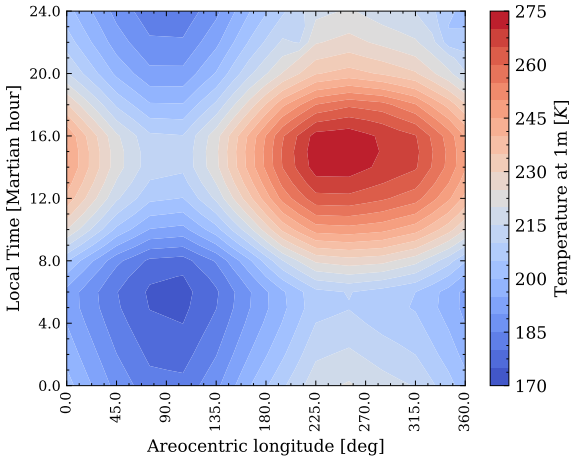

Figure 9.4: Daily temperature distribution throughout the Martian year

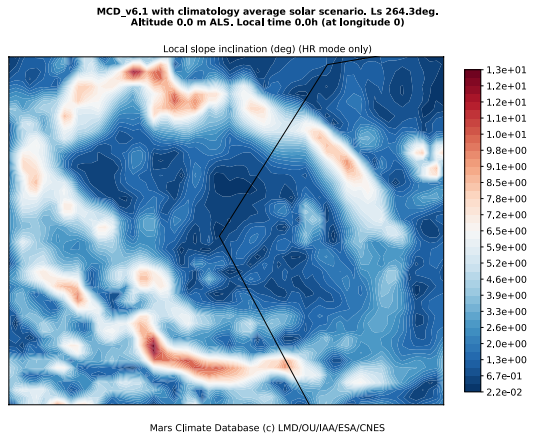

Figure 9.5: Slope angle in deg along the Eberswalde crater (24 °S to 23.5 °S and 326.6 °E to 327.1 °E)[4]

9.3. Methodology

In this section, the design method for the EPS is outlined and justified. First, a power usage profile is constructed for the given mission profile, considering the power usage from the drone's subsystems. Then, the solar array architecture is designed to ensure average power can be generated for this power profile. The battery is then sized to store energy to perform the flight and for night power usage. Finally, the power management and distribution system is designed, emphasising power delivery to the most power-demanding subsystem, the propulsion subsystem.

Power Usage Profile

To design the EPS for the drone, it is essential first to establish the power usage profile throughout a typical mission. The power profile is based on the two-day return mission presented in Chapter 7, however since this profile was not fully established at the time of finalising the EPS design, the profile presented in this section deviates slightly from it while remaining conservative in terms of total energy requirement. On the first day,

the drone will fly to a designated area, conduct scanning operations, and acquire a sample. It will then land, recharge and fly back to the Martian ground station on the second day. In Table 9.2, all power usage states encountered over the mission profile are listed. Note that on the second day, the flight is shorter since the drone can return straight to the ground station and scanning operations are not required.

As discussed in Chapter 10, the thermal power required to keep the battery within its operational temperature range fluctuates both throughout the day and year, depending on the external temperature. Sizing the solar arrays based on the worst-case thermal power usage during winter would result in an overdesigned system. Therefore, to construct the power usage profile for sizing the solar arrays, a continuous power requirement for the TCS of 20 W (the power required on an average day in terms of temperature) is be assumed. In Section 9.5, the performance of the solar arrays during winter operations is evaluated by analysing the battery charge time under conditions of variable thermal power demand and solar flux availability to highlight the implications of this design decision.

The power usage states presented in Table 9.2 were plotted over the mission duration of two days, and the power profiles during scanning and sample return flights were extracted as illustrated in Figure 9.6 and Figure 9.7 respectively. The power profiles for the two flights are plotted relative to their takeoff times. The moment during the day the flight operations are carried out is not of importance to the sizing of the solar arrays; it has major implications for the power storage system. This section discusses these implications, and the optimal moment to perform the flight is presented.

Once this power profile was developed, the total energy consumption per day was calculated by integrating the power usage over the entire two-day mission duration and dividing by two. The average power used over the mission was also obtained by dividing the daily energy consumption by the length of one day. These values were evaluated at 2198 W h and 89.12 W, respectively, and are important input values for the design of the solar arrays.

Table 9.2: Power usage states

Mission phase	**Active subsystems**	**Power usage** [W]	**Duration** [s]
Standby	TCS	20	Permanently
Takeoff	PRO, GNC, COM	5736.5	45
Cruise	PRO, GNC, COM	4322.5	1000
Scanning	PRO, GNC, COM, PLD	4332.5	600
Landing	PRO, GNC, COM	5727	45
Sample collection	GNC, COM, PLD	89.5	120

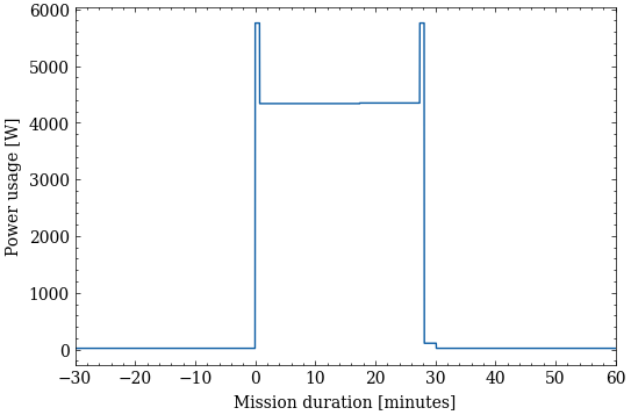

Figure 9.6: Power usage profile for a typical scanning flight

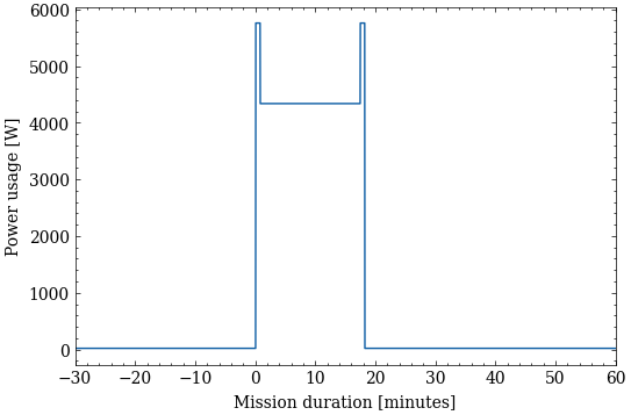

Figure 9.7: Power usage profile for a typical sample return flight

Power Generation

In this section, the design method for the solar arrays will be presented. First, the design average power that the solar arrays are expected to generate was calculated from the average power usage. Then, the solar arrays were sized to provide this design average power at the yearly harmonic average solar flux conditions, as discussed in Section 9.2.

According to the power profile, an average of 89 W will be consumed over a typical two-day mission. The design average power (the power that the solar arrays must generate such that the EPS can provide the 89 W) can be obtained using Equation 9.1, assuming all power transits through the battery and the harness. As will be explained in the design method for power storage and power management & distribution, the battery and harness efficiencies were evaluated at 0.99 and 0.979 respectively. In reality, a fraction of this power will be used directly and will not have to be stored in the battery, so this is a slightly conservative estimate.

$$P_{design} = \frac{P_{consumed}}{\eta_{battery} \cdot \eta_{harness}} \tag{9.1}$$

P_{design} was evaluated at 92 W and corresponds to the power that must be generated given average yearly solar flux at EOL conditions, when the solar cells will have been degraded by external factors such as dust abrasion and radiation. From this, the power that must be generated at BOL conditions can be obtained using Equation 9.2[31]. As discussed in Section 9.2, a degradation rate of δ=2% per year will be taken to account for both dust abrasion and radiation over a mission lifetime of 2 years

$$P_{BOL} = \frac{P_{design}}{(1-\delta)^{t_{life}}} \tag{9.2}$$

Based on the power that must be generated at BOL, evaluated at 95.7 W, the reference array area (ie. the required active solar cell area) can be sized using Equation 9.3[31]. As explained in Section 9.2, the average solar flux of 131.14 W m^{-2} will be taken as the design point such that the array is not overdesigned. According to the State-of-the-Art of small spacecraft technology report by NASA[3] , the Quadruple Junction GaAs Solar Cell from Azur Space is one of the best performing, currently available solar cell technologies, and were thus selected for the design[4] . These solar cells have an efficiency of 32% at nominal conditions. As discussed in Section 9.2, this efficiency will be degraded slightly under Martian spectrum conditions, however this effect is difficult to quantify. It will be assumed that advances in cell efficiencies by the second half of 2028 when the Engineering Model (EM) will enter production, will outweigh this effect. The active area factor AF, the proportion of the array area not expected to be covered with dust, is set to 0.9 as previously discussed. The design incidence angle θ is set to 15° to account for the expected topography.

$$A_{ref} = \frac{P_{BOL}}{S \cdot cos(\theta) \cdot \eta_{cell} \cdot AF} \tag{9.3}$$

The array reference area was thus evaluated at 2.62 m^2. From this, the array architecture was defined based on the desired bus voltage using Equation 9.4. The selected solar cells have an area of 30.18 cm^2 and a peak power voltage of 3.025 V. The bus voltage is set to 60 V as this is the maximum voltage of the propulsion system's motors. Operating the motors at high voltage is ideal for reducing power losses in the cables. Designing the solar arrays to operate at 60 V will also eliminate the need to upscale the voltage provided to the motors, avoiding additional power losses.

$$\begin{aligned} n_{cells} &= \frac{A_{ref}}{A_{cell}} \\ n_{cells\,per\,string} &= \frac{V_{bus}}{V_{cell}} \\ n_{strings} &= \frac{n_{cells}}{n_{cells\,per\,string}} \end{aligned} \tag{9.4}$$

To implement robustness in the design, the solar arrays shall provide the design average power under one inoperative string conditions as stated in the EPS requirements. The number of strings is thus rounded up, and one extra string is added on top of that. Finally, the actual array area was calculated, along with the mass and cost of the array assembly using Equation 9.5. A packing factor of 0.9 was used, which is typical for rectangular cells[5] , along with a specific density ρ_{array} = 2 kg m^{-2} (which is the value used by the Mars Science Helicopter

[3]URL: https://www.nasa.gov/smallsat-institute/sst-soa/ [cited on 21 May 2024]
[4]URL: https://satsearch.co/products/azur-space-qj-solar-cell-4g32c-advanced [cited on 14 June 2024]
[5]URL: https://sinovoltaics.com/learning-center/basics/packing-density/ [cited on 13 June 2024]

design[21]) and specific cost for GaAS solar arrays of C =116 k€ m^{-2}[39]. This resulted in an array architecture of 900 cells in a 20S45P configuration, for a total area of 3.02 m^2, a mass of 6.04 kg and manufacturing cost of 350 k€.

$$\begin{aligned} A_{array} &= n_{strings} \cdot n_{cells\,per\,string} \cdot A_{cell} \cdot PF \\ M_{array} &= \rho_{array} \cdot A_{array} \\ C_{array} &= C \cdot A_{array} \end{aligned} \tag{9.5}$$

Power Storage

To provide power during eclipse periods and at times when power demand exceeds the power generated by the solar arrays (typically during flight), the EPS must be equipped with appropriately sized batteries. The method used for designing the battery begins with the power usage profile presented earlier in this section. The net power profile could be constructed at all times by subtracting the power usage profile from the power generation profile throughout the two-day mission. An advantage of designing the power storage system from the net power profile is that it accounts for power generated during flight, leading to a more accurate representation of the system's needs. A positive net power value indicates a surplus of generated power, which can be used to charge the batteries, while a negative net power value indicates that power must be supplied to the drone from the batteries. Performing a cumulative integral of the net power profile gives the variation of the system's energy state from a reference point t=0. To translate this into the State-of-Charge (SOC) of the battery at any point in time, the energy state must be shifted up by the minimum value of the energy state, as described in Equation 9.6.

$$\begin{aligned} SOC(t) &= SOC(t=0) + \int_0^t P_{net}(\tau) d\tau \\ SOC(t=0) &= -\int_0^{t_{min}} P_{net}(\tau) d\tau \end{aligned} \tag{9.6}$$

The maximum SOC of the battery corresponds to the minimum required energy storage capacity so that the full variations in the drone's energy state over the two-day mission can be covered. The required battery capacity was obtained using Equation 9.7, applying an EOL capacity factor of 90%, per research by Preger et al.[40] on degradation rates of LiFePO cells. An allowable Depth-of-Discharge (DoD) of 90% was also added to ensure the rated peak discharge rates are attainable throughout the flight and to limit the degradation of the cells.

$$C_{battery} = \frac{SOC_{max}}{DoD \cdot CF_{EOL}} \tag{9.7}$$

The SOC profile for the drone using yearly average solar flux data is provided in Figure 9.8, with the most energy-intensive flight, the scanning flight, performed at 12:00 local time. It can be seen that this flight utilizes the full depth of discharge under beginning-of-life (BOL) conditions, proving that the battery is not oversized. This optimal performance is achievable only when the flight occurs between 10:00 and 14:00 local solar time. Flights outside this time range require a larger battery because the drone does not have enough time to recharge the battery before the flight and must enter an eclipse with more stored energy. Note as well that the SOC of the battery returns to 60% after the two-mission, this confirms that the arrays were sized appropriately as they were designed to provide a zero net energy state over a two-day mission at yearly average solar flux conditions.

Similarly to what was done for the solar array architecture, the number of cells per string and number of strings was determined using Equation 9.8. To design for failure of one battery string, the number of strings was rounded up and one extra string was added. Due to their excellent energy density of 260 W h kg^{-1}, LG's Lithium-ion INR 21700 M50LT [6] presented in NASA's power state-of-the-art report were selected[33].
For a 60 V bus and a cell voltage of 3.6 V, the optimal battery architecture has 153 cells in a 17S9P configuration, for a total mass of 10.25 kg and an off-the-shelf cost of 37 k€ [7] .

[6] URL: https://f.hubspotusercontent10.net/hubfs/6584819/Cell%20Spec%20Sheets/LG/Lithium%20Ion%20LG%20INR%2021700%20M50LT%202021-LSD-MBD-b00002_21700_M50LT_PS_Promotion_V1.pdf [cited on 16 June 2024]

[7] URL: https://www.tenergy.com/30292 [cited on 18 June 2024]

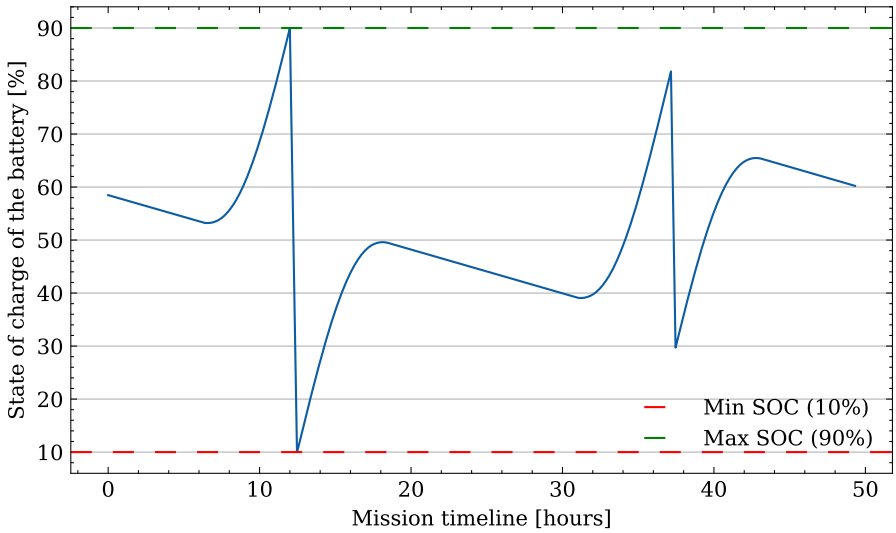

Figure 9.8: State of Charge of the battery over a two-day mission for a flight performed at 12:00 local at yearly average solar flux conditions

$$n_{cells\,per\,string} = \frac{V_{bus}}{V_{cell}}$$
$$n_{strings} = \frac{E_{battery}}{E_{string}} = \frac{E_{battery}}{n_{cells\_series} \cdot C_{cell} \cdot V_{cell}} \tag{9.8}$$

Finally, the maximum required charge and discharge rates were calculated to ensure the suitability of the selected cells. The battery may charge at a rate of up to 0.12C, compared to the selected cells' rating of up to 0.7C, within the acceptable limits for the chosen cells with some design margin. Under normal takeoff and landing operations, the battery may experience discharge rates of up to 2.4C, while the selected cells are rated for up to 3C. However, under the extreme case where 1.3 T/W conditions would be required on all rotors simultaneously, the peak discharge rate may reach up to 3.1C, depending on the power generated by the solar array at that moment, so this is an important risk to take into account for further development of the EPS. Furthermore, the 3C maximum discharge rating of the batteries is under 3.6 V conditions while Li-ion batteries typically suffer from a voltage drop below 20% SOC, as can be seen in Figure 9.9[8] . This means that a 3C discharge rate may damage the battery or may not be attainable at all during the landing sequence. The need for different battery technology or capacitors to provide burst energy boosts should be studied further, as a potential solution to relieve stress on the batteries and increase their reliability.

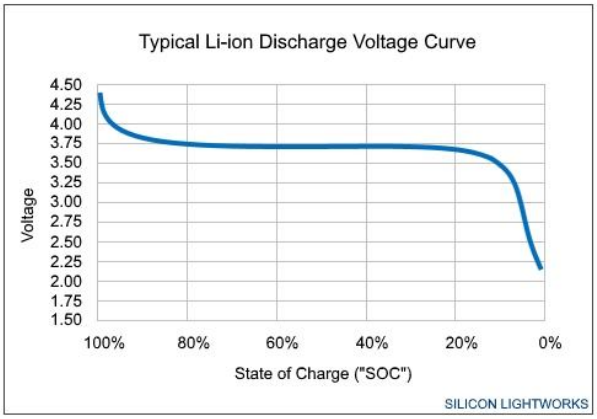

Figure 9.9: Discharge voltage as a function of SOC for typical Li-ion cells[8]

The structure of the solar array and battery sizing tools developed from these equations is presented in the form of a flow chart in Figure 9.10. A summary of the solar array and sizing tool inputs is also provided in Table 9.3.

Power Management & Distribution

Regarding power management, the main functions that must be fulfilled are to control the operation of the solar arrays, control the charging and discharging of the battery, control the power delivered to the motors and control the voltage supplied to the low-voltage systems. The power management and distribution architecture

[8]URL: https://siliconlightworks.com/li-ion-voltage [cited on 18 June 2024]

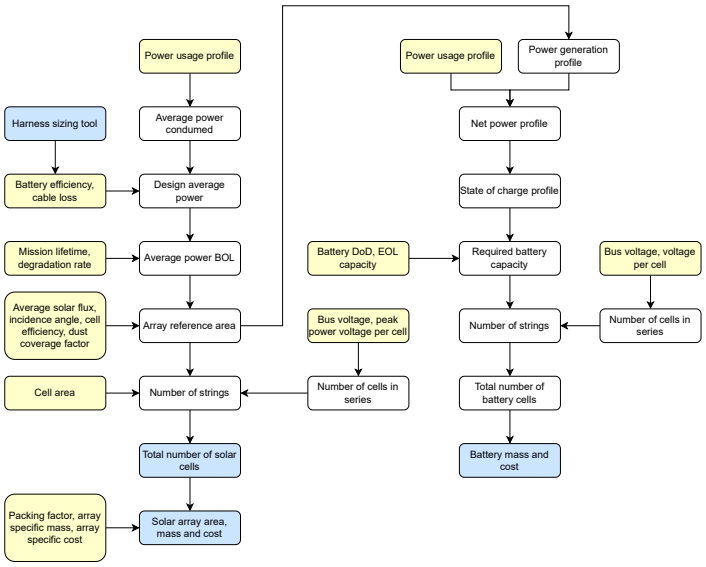

Figure 9.10: Flowchart of the EPS design tool

Table 9.3: Power generation and storage sizing tool design inputs

Input solar array sizing	**Value**	**Unit**
Average power consumed	89.21	W
Battery efficiency $\eta_{battery}$	0.99	-
Harness efficiency $\eta_{harness}$	0.979	-
Solar cell efficiency η_{cell}	0.32	-
Degradation rate δ	2	% per year
Mission lifetime t_{life}	2	Years
Bus voltage V_{bus}	60	V
Design incidence angle θ	15	deg
Average solar flux S	131.14	$\mathrm{W\,m^{-2}}$
Active area factor AF	0.9	-
Packing factor PF	0.9	-
Solar cell peak power voltage V_{cell}	3.025	V
Solar cell area A_{cell}	30.18	$\mathrm{cm^2}$
Solar array specific density ρ_{array}	2	$\mathrm{kg\,m^{-2}}$
Solar array specific cost C	116	$\mathrm{k€\,m^{-2}}$

Input battery sizing	**Value**	**Unit**
Depth of discharge DoD	90	%
EOL capacity C_{EOL}	90	%
Battery cell voltage V_{cell}	3.6	V
Battery cell mass m_{cell}	67.5	g
Battery max discharge rate	3	C
Battery max charge rate	0.7	C

can best be visualised with the means of the electric block diagram provided in Section 16.3.

A maximum power point tracker (MPPT) will control the solar arrays to ensure that they operate at maximum efficiency despite varying solar flux and temperature conditions. Space-certified power conditioning and distribution units (PCDUs) that can fulfil the high power delivery and voltage requirements of the Martian Drone are not readily available. A PCDU will likely have to be designed in-house to further develop this mission. For now, a mass of 2 kg and cost of 300 k€ is allocated to the PCDU based on commercially available PCDUs for small to medium satellites[9] . Advances in this aspect are likely in the near future due to the development of lightweight PCDU utilizing GaN technology[10] .

Regarding power delivery, the harness for the Martian drone was sized. The harness is composed of the following wired connections:

- Solar array to the PCDU
- PCDU to the battery
- PCDU to the propulsion system's motors
- PCDU to all other power users

[9]URL: https://www.airbus.com/sites/g/files/jlcbta136/files/2022-02/Datasheet-PureLine_Pearl_V2_2022.pdf [cited on 16 June 2024]
[10]URL: https://nebula.esa.int/content/gan-based-pcdu-eo-missions-based-recurrent-platforms [cited on 17 June 2024]

The harness size method focuses on the cables delivering power to the propulsion system. Due to the large power draw of the motors and their relative position from the centre of the bus where the battery and PCDU will be located, the propulsion system wires are expected to make up most of the drone's harness mass. To account for spikes in power draw when all rotors must provide the drone with a T/W of 1.3, the harness must be sized to provide a total power of 7387 W as per the requirements. From the peak power, the operating voltage of 60 V and applying a 10% safety margin, the maximum current drawn by each motor was calculated to be 22.16 A using Equation 9.9.

$$I_{max} = \frac{P_{max}}{\mathrm{V}} \tag{9.9}$$

Based on the expected maximum current, it was decided to use three AWG12 cables, each capable of delivering up to 9.3 A [11] . To design for redundancy, one extra wire was added in each arm such that the maximum power can still be delivered to each motor in case of failure of one wire. Given that DC power must be delivered, a set of return cables must also be present, bringing the total to 8 wires per motor. The wires for the propulsion system must deliver power from the PCDU located near the centre of the bus to the extremities of the drone's arms over a length of 2.46 m. The AWG chart specifies that the cross-sectional area of gauge 12 wires is 3.2 mm^2. Aluminium wiring was selected over copper for its superior conductivity-to-weight ratio, thus given the density of aluminium of 2700 $\mathrm{kg\,m}^{-3}$, the mass of the cable harness for the propulsion system's six motors was estimated at 1.02 kg using Equation 9.10.

$$M_{propulsion\_harness} = \rho_{aluminium} \cdot A_{AWG12} \cdot l_{cable} \cdot n_{wires} \cdot n_{motors} \tag{9.10}$$

For the other parts of the cable harness, only an order of magnitude estimate could be carried out since the exact architecture of the drone and the placement of its components was still uncertain. From the array to the PCDU, the maximum power expected will occur at solar flux maximum of 650 $\mathrm{W\,m}^{-2}$. Using the previously discussed solar array design tool, the maximum power generated by the arrays at this flux is ~500 W. Using Equation 9.9, the maximum current corresponding to this power is 8.3 A. According to the AWG chart, gauge 12 should be selected. Over a length of 10 cm (or half of the bus) and accounting for one set of redundant wires, an upper estimate of the mass of these wires is 0.1 kg each. From the battery to the PCDU, although the maximum power to be delivered is in the order of 7500 W when the battery operates at the maximum discharge rate, the distance is very short as both will be located near the centre of the bus. A conservative estimate for the mass of this part of the harness is in the order of 0.1 kg. Finally, the rest of the harness composed of the wires from the PCDU to all other power drawing systems (including the drone's sensors, payload instruments, avionics and thermal control system) was estimated at 0.5 kg, bringing the total harness mass to 1.82 kg.

The power losses in the EPS harness were also estimated. The first step was to calculate the resistance in the propulsion system cables. With the resistivity of aluminium of $2.62 \times 10^{-8}\,\Omega\,\mathrm{m}$, a length of twice 2.46 m and a cross-sectional area of gauge 12 wires of 2.62 mm^2, the resistance of each cable was estimated using Equation 9.11.

With each cable carrying 7.3 A at peak power conditions and a resistance of 0.0498 Ω. The power loss of the propulsion system was then calculated using Equation 9.11, giving a total power loss of 2.72 W or 0.6%. Since minimal voltage transformations are required for the propulsion system, power losses of the PCDU are expected to be minimal and were estimated to be up to 1% [9]. Finally, the rest of the harness was estimated to add 0.5% power loss, assuming the power losses can be scaled down according to the relative cable masses, bringing the total harness loss to 2.1%.

$$R = \rho \frac{l}{\mathrm{A}} \qquad\qquad P_{loss} = I^2 R \tag{9.11}$$

[11] URL: https://www.calmont.com/wp-content/uploads/calmont-eng-wire-gauge.pdf [cited on 12 June 2024]

9.4. Verification and Validation

This section describes the verification and validation strategy for the EPS design. In particular, the different testing regimes that will take place at the engineering, qualification and flight model stages are expanded on.

Regarding the verification process of the EPS design models presented in this report, extensive code verification was not necessary as the models were built on simple equations. However, the correct implementation of these equations was verified by simple unit testing during and after the development of these models. Intermediate and final results were printed or plotted to judge the validity of the outputs.

On the other hand, model validation will require extensive testing, beginning with producing an engineering model. The objective of the engineering model is to confirm that the design and simulation models accurately reflect the system's performance in the Martian environment. After each component of the EPS has undergone a series of performance tests, they will be integrated into the subsystem and tested together. As a key element of the EPS, performance testing will be done on the power supply to the motors through load testing. The solar flux conditions on Mars will be simulated to verify that the solar arrays provide the expected power to the system. The battery will be tested in a temperature environment on Mars to ensure it meets the expected efficiencies and discharge rates. Integrating the EPS with the rest of the drone's avionics hardware will allow the building of an avionics bench for functional and performance verification and validation of the drone's software and operational procedures.

Next, the EPS will be tested using a qualification model (QM). This set of tests will focus on stress testing the system. This includes exposing the model to simulated Martian dust and dust storm conditions, extreme temperature variations, and vibrational tests to simulate launch and entry loads. The batteries will undergo deep cycle testing to determine their long-term performance and thermal cycling to simulate Martian day-night temperature fluctuation.

Finally, the EPS will be integrated into the flight model (FM) and undergo acceptance testing to pass the Flight Readiness Review (FRR). In particular, the solar arrays will undergo integration testing to ensure they work seamlessly with the drone's other subsystems. The batteries on the FM will undergo testing to ensure they meet capacity and power delivery requirements as expected.

9.5. Results

In this section, the results of the EPS design are presented, along with a performance analysis of the design. The solar array, battery and power delivery architectures are presented, along with the subsystem's mass and cost breakdown in Table 9.4.

Table 9.4: EPS architecture

EPS architecture parameters	**Values**	**Units**
Solar array area	3.02	m^2
Solar array configuration	*20S45P*	-
Solar cell type	*Azur Space QJ Solar Cell 4G32C - Advanced*	-
Solar array mass	6.04	kg
% of year when t_{charge} < 1 sol at EOL	54	%
% of year when t_{charge} < 2 sols at EOL	83	%
Battery cell type	*LG Lithium-ion INR 21700 M50LT*	-
Battery mass	10.25	kg
Battery configuration	*17S9P*	-
Battery voltage	60	V
Battery capacity	2375	W h
Cable type for propulsion	*Triple AWG12 cabling*	-
Harness and PCDU mass	3.82	kg
Harness loss	2.1	%
EPS total mass	20.11	kg
EPS total cost (Flight Model)	687	k€, FY2024

Performance Analysis

In this section, the EPS performance is discussed, emphasising the drone's charge time throughout the year. To perform this analysis, the time required to generate the energy consumed during a typical scanning flight was determined throughout the year using a variable solar flux distribution provided by the Mars Climate Database as well as a variable thermal power required to keep the battery heated, as these two parameters have a major influence on the charge time[4]. As mentioned in Chapter 10, the average power usage for the thermal control system varies from 10 W in summer up to 25 W in winter. On the other hand, the daily average solar flux varies from 80 W m^{-2} in winter to 210 W m^{-2} in summer, as mentioned in Section 9.2.

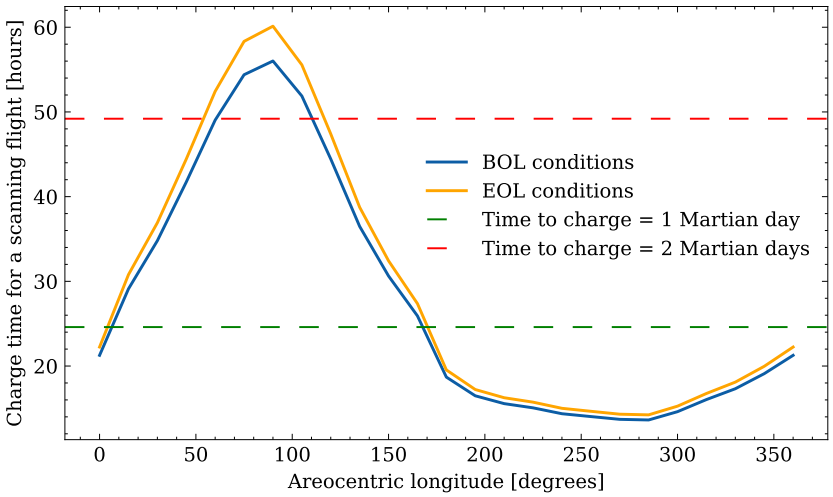

Figure 9.11: Charge time distribution throughout the Martian year considering variable thermal power usage to heat the battery and solar flux availability

As can be seen in Figure 9.11, the charge time variation is large throughout the year, ranging from 14 to 60 hours at EOL conditions. Analysing this data further, it can be seen that the charge time to replenish the required flight energy is below 1 sol for 56% of the year and below 2 sols for 87% of the year for BOL conditions. At EOL conditions, these values go down to 54% and 83% respectively.

Based on this analysis, it is feasible to fly at all times of the Martian year from a power availability perspective, although the charge time is longer in the winter. Another option that should be considered is to reduce the endurance requirement during winter and perform shorter flights. If the endurance requirement is reduced to 20 min, the flight energy would reduce to 1400 W h with the current design. This would mean that the charge time exceeds 1 sol for only 32% of the year and never exceeds 2 sols, as can be seen in Figure 9.12.

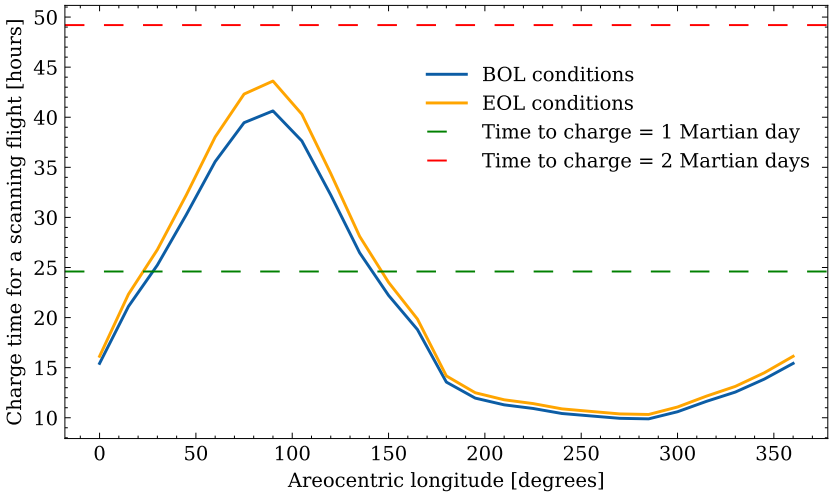

Figure 9.12: Charge time distribution throughout the Martian year considering variable thermal power usage to heat the battery and solar flux availability for a 20 min flight profile

10 Thermal Control System

***Authors**: Sebastien*

The thermal control system (TCS) is a key system for the Martian Drone. Its primary function is maintaining each drone system's temperature within the operational or survival range. Operations on Mars' surface present many challenges due to its extreme temperature fluctuations and thin atmosphere. In this chapter, methods to address these challenges are presented, as well as the resulting preliminary design of the TCS. Although only the motor and the battery TCS design are fully developed for this phase of development, the same method can be applied to the design of other TCSs.

Firstly, in Section 10.1, the primary systems that need a thermal system are presented with the respective requirements for the TCS. Hereafter, in Section 10.2, the method to develop this system is presented, followed by the verification and validation steps taken for the created code in Section 10.3. Lastly, the results from the analysis for the TCS and its design are presented in Section 10.4.

10.1. Requirements

As noted, the Martian atmosphere presents challenges for thermal design. These thermal challenges are similar to those of a satellite as little thermal convection occurs on Mars [1] . As limited time is available to develop the TCS for all drone systems during this project, the limiting cases are studied. For these cases, the following is considered.

Satellite design and design of the past Martian vehicles dictates that the electrical system is one of the primary systems that require precise temperature control [31]. Namely, the battery and electrical boards are sensitive to temperature fluctuations and thus require thermal systems in most instances. It is important to note that in most cases, the electrical components must be heated due to their high relative operational temperatures. Solar arrays should also be maintained within a certain temperature range; however, this range is not limiting for the design, as illustrated in Table 10.1, and thus the TCS for the solar arrays is not designed for the preliminary design. The requirements for the electrical components are subsets of TCS-SYS-01-09-I: "The TCS shall maintain the EPS within its operational temperature range," and are illustrated in the table.

One of the main challenges in designing rotorcraft for Mars, as demonstrated by existing models [21], is effectively managing the temperature of the helicopter. The lack of advanced cooling methods in Ingenuity resulted in motor overheating, which ultimately limited its performance and flight time of 7 min [2] . As previously noted, this challenge is imposed as little thermal convection occurs in the thin Martian atmosphere. Additionally, in Section 8.2, it is noted that the propulsion system generates a large amount of heat. Thus, the motors for the propulsion system also require a TCS. In Section 8.5, it is described that the NOVA-1 has been selected for the preliminary design. This motor has a maximum temperature of 100 °C. F. Acquaviva also uses this maximum temperature in his Master's Thesis on Martian Drone thermal design [41]. The resulting requirement, TCS-SYS-01-07-01, is presented in Table 10.1.

Lastly, the requirements related to the payload systems, the navigation sensors and the communications system are also presented in Table 10.1. These requirements are crucial for future design; however, as previously noted, they are not limiting for the design, and thus, the TCS for these systems has not been designed.

From these requirements in Table 10.1, the TCS for the motor, battery, and surrounding electrical boards are developed for the preliminary design. Two TCS shall be developed; one to maintain the temperature of the battery and surrounding electronics in the range of -20 °C to 40 °C, and another for the propulsion motors so as not to exceed 90 °C. A margin of safety is taken to ensure the system can better operate during the demanding power of descent and as recommended by Dr I. Uriol Balbin [3] .

[1] URL: https://marspedia.org/Cooling [cited on 27 May 2024]
[2] URL: https://x.com/NASAJPL/status/1412092497552019458 [cited on 16 June 2024]
[3] Communication with Dr I. Uriol Balbin, dd. 5 June 2024

Table 10.1: Driving requirements for the TCS design. All requirements can be traced to GE-SYS-05, and the verification lead is the TCS Lead.

ID	Requirement	Verification Method
TCS-SYS-01-04-01-I	The TCS shall maintain the payload sensors within their operational temperature range	Demonstration
TCS-SYS-01-06-01	The TCS shall maintain the antenna's temperature between −100 °C and 100 °C [31]	Demonstration
TCS-SYS-01-07-01	The TCS shall maintain the propeller motor's operational temperature between −40 °C(TBC) and 100 °C	Demonstration
TCS-SYS-01-08-01	The TCS shall maintain the flight computer's temperature between −40 °C and 75 °C [31]	Demonstration
TCS-SYS-01-08-02	The TCS shall maintain the flight computer's temperature during operations between −20 °C and 60 °C [31]	Demonstration
TCS-SYS-01-09-01	The TCS shall maintain the battery's temperature between −20 °C and 40 °C [31, 42]	Demonstration
TCS-SYS-01-09-02	The TCS shall maintain the solar array's temperature between −200 °C and 130 °C [31]	Demonstration
TCS-SYS-01-09-03	The TCS shall maintain the power conditioning and distribution unit's temperature between −20 °C and 60 °C [31]	Demonstration

10.2. Methodology

This section describes the TCS design method. First, the global heat balance is presented, describing the various types of heating sources in the Martian atmosphere in Section 10.2.1. Following, the time-dependent analysis method is described in Section 10.2.2. Additionally, the specifics for the motor and battery TCS analysis method are described in Sections 10.2.3 and 10.2.4.

10.2.1. Thermal Balance

The primary thermal analysis method uses a heat rate balance, where the heat rate coming into the system equals the heat rate going out, depicted in Equation 10.1 [43]:

$$\dot{Q}_{in}^{ext} + \dot{Q}_{in}^{int} - \dot{Q}_{conv} = \dot{Q}_{out} \tag{10.1}$$

where the external heat input rate is the sum of the solar radiation, albedo, black body radiation and conduction: $\dot{Q}_{in}^{ext} = \dot{Q}_{sun} + \dot{Q}_{albedo} + \dot{Q}_{IR} - \dot{Q}_{cond}$. If the system is in thermal equilibrium, both sides of the thermal balance equation are equal. Following, all heat rates are defined.

Solar Radiation

Solar radiation is the radiation received from the sun at a distance. The resulting solar flux, or solar irradiance, can be calculated using: $I_s = \frac{P_s}{4\pi d^2}$, where P_s is the total solar power and d the distance to Mars. However, for the development of the TCS, the MCD was used to gather the solar irradiance, which provides the solar radiation along the year as presented in Figure 9.2. To calculate the resulting heat rate, Equation 10.2 is used :

$$\dot{Q}_{sun} = \alpha_{sys} I_s A_{top} F_{s/d} \tag{10.2}$$

where α represents the absorptivity of the top surface of the drone and $F_{s/d}$ the view factor between the solar radiation and system, thus the Martian Drone's top surface. In the case of solar radiation, the view factor is equal to 1 [43].

Albedo

The albedo radiation is the radiation caused by reflected solar radiation from the surface or atmosphere of a planet. The heat rate caused by albedo is calculated using Equation 10.3:

$$\dot{Q}_{albedo} = b\alpha_{sys} I_s A_{top} F_{s/d} \tag{10.3}$$

where b is the albedo. "For Mars, it varies from a maximum of 0.4 in dust-covered surface regions to a minimum of 0.15 in regions with volcanic rock basalt on the surface." [43] For the Eberswalde crater, the albedo is lower due to the low altitude from the areoid and rock composition, ranging between 0.13 and 0.25 [5], and thus a value of 0.2 is used as average. Similarly to the solar radiation, Figure 9.2 is used for the solar flux.

Black-Body Planetary Radiation
All celestial bodies with a certain temperature radiate heat away in the IR spectrum. The thermal flux is calculated with: $J_p = \sigma \epsilon_{Mars} T_{eff}^4$, where ϵ_{Mars} represents the emissivity of Mars, and T_{eff} the effective black body temperature [31]. For Mars, the effective temperature is 209.8 K [4] , however the average thermal IR flux can be gathered from the MCD, resulting in ~70 W m^{-2}. The resulting heat rate by IR radiation from Mars is computed with Equation 10.4 [43]:

$$\dot{Q}_{IR} = \sigma J_p A_{top} F_{s/d} \tag{10.4}$$

Conduction
Thermal conduction is the transfer of heat between objects in direct physical contact. Conduction is computed using Equation 10.5:

$$\dot{Q}_{cond} = \frac{k A_{total}}{t} (T_{sys} - T_{atm}) \tag{10.5}$$

where k is the material's thermal conductivity and t is its thickness. Conductivity is an important factor in developing insulation for the subsystem and is also the primary factor in heat distribution throughout the drone.

Internal Heat Input
The internal heat input rate is defined by the heat generated by the system's components. The primary factors that may cause internal heating are inefficiencies of certain subsystems or intended heating by, for example, heaters. Inefficiencies inherent to various subsystems are caused by the conversion of energy types, which will inevitably generate heat. This can be, for example, the conversion of electrical energy in the battery to mechanical energy in the motors. Heaters are critical components in maintaining the operational temperature of systems on Mars due to the low temperatures reached, −60 °C, as illustrated in Figure 9.4.

Convection
The final heat input rate is the convection heat rate. As mentioned before, due to the thin atmosphere on Mars, convection is limited. Convection differs from conduction, which involves the transfer of heat between solid objects in contact, while convection involves the transfer of heat to gases and fluids. Convection heat transfer is calculated using Equation 10.6:

$$\dot{Q}_{conv} = h A_{total} (T_{sys} - T_{atm}) \tag{10.6}$$

where h is the heat transfer coefficient. From the Phoenix Mars Lander mission, a natural heat transfer coefficient of 0.15 was computed [44]. Natural heat transfer is when wind speed is at 0 m s^{-1}. Forced convection occurs with a large wind speed or induced airflow. Forced convection is expanded on in Section 10.2.3.

Heat Output Rate
The heat output rate is the heat that leaves the system due to radiation. This is computed using Equation 10.7 [43]:

$$\dot{Q}_{out} = F_{d/e} \sigma \epsilon_{sys} A_{total} (T_{sys}^4 - T_{atm}^4) \tag{10.7}$$

where $F_{d/e}$ is the view factor between the system and the environment. This factor can be estimated and is further expanded in Section 10.2.3.

10.2.2. Time Dependant Analysis Method

The steps described in Section 10.2.1 provide a power and heat rate balance. However, as the environmental parameters in the Martian atmosphere are time-dependent, and thus the temperature gradient also has to be analysed. The rate of heat transfer is calculated using Equation 10.8:

$$m C_P \frac{dT}{dt} = P_{in} \tag{10.8}$$

where m is the mass of the system, C_P the specific heat capacity, dT/dt the rate of change of the temperature and P_{in} the power going into the system, also equal to $P_{in} = \dot{Q}_{in}^{ext} + \dot{Q}_{in}^{int} - \dot{Q}_{conv} - \dot{Q}_{out}$.

[4] URL: https://nssdc.gsfc.nasa.gov/planetary/factsheet/marsfact.html [cited on 5 Jun 2024]

10.2.3. Motor Thermal Design Methodology

A significant constraint of the rotorcraft design, as evidenced by existing models [21], is thermal control of the helicopter. Ingenuity had no advanced cooling methods; motor overheating limited its performance. Similarly, without cooling fins, the rotor would overheat in ~8 min, as illustrated in Figure 10.3. NASA suggested two options for future projects: a phase-change material (PCM) heat sink and a cooling fin system, which uses the rotor downwash to create forced convection. The cooling fins have been selected for this design as PCM can not be easily designed with current knowledge. The primary two factors important for radiator and convection fins are the area and the heat transfer coefficient. Additionally, the view factor also affects the performance of the fins.

Cooling Fin Heat Transfer Coefficient

The heat transfer coefficient can be estimated using mathematical correlations of flow geometries. Empirical correlations have been developed for various geometries of surfaces for natural and forced convection.

To estimate the heat transfer coefficient, Equation 10.9 is used [45]:

$$h = \frac{\mathrm{Nu} k_{atm}}{L} \tag{10.9}$$

where Nu is the Nusselt number and k_{atm} is the thermal conductivity of the Martian atmosphere. The thermal conductivity for the Martian atmosphere is assumed to be equal to that of pure CO_2 gas, namely $14.7 \times 10^{-3}\,\mathrm{W\,m^{-1}\,K^{-1}}$ [5] . Furthermore, the Nusselt number is estimated using empirical relation in Equation 10.10:

$$\mathrm{Nu} = C\,\mathrm{Re}_L^m\,\mathrm{Pr}^n \tag{10.10}$$

where Re is the Reynolds number along the fin and Pr, the Prandtl number. C, m and n are the results of empirical relations. The Reynolds number, $\mathrm{Re} = \frac{\rho v L}{\mu}$, is calculated from the downwash velocity v, and the dynamic viscosity of the atmosphere μ. Similarly, the Prandtl number, $\mathrm{Pr} = \frac{\nu}{\alpha}$, is calculated from the kinematic viscosity and the atmospheric thermal diffusivity $\alpha = \frac{k_{atm}}{\rho_{atm} C_{p,\,atm}}$.

Fin View Factor

The view factor for angled plates is a major contributor to the heat output rate. As heat is radiated away, nearby fins can capture the energy again, resulting in the energy not being radiated away from the system. While an accurate estimation of this factor is dependent on many factors, simplification can be made. An initial estimate can be performed by calculating the Gebhart factor. This factor considered the effect of captured heat from one fin to another, including reflection, and was recommended by Dr I. Uriol Balbin for initial estimates [6] .

The view factor between each cooling fin, F_{ij}, has to be calculated first. This factor is calculated using Equation 10.11 [45]:

$$F_{ij} = 1 - \sin\theta/2 \tag{10.11}$$

where θ is the angle between the radiator fins. As all fins are the same dimensions, $F_{ij} = F_{ji}$. Using this, the Gebhart factor, B_{ij} can be estimated with an iterative loop using Equation 10.12 [7] :

$$\begin{aligned} B_{12} &= F_{12}\epsilon + (1-\epsilon)F_{12}B_{22} \\ B_{22} &= (1-\epsilon)F_{21}B_{21} \end{aligned} \tag{10.12}$$

where ϵ is the emissivity of the fins. It is important to note that this Gebhart factor provides the view factor between the fins. However, the view factor from the fins to the environment is required for the analysis; thus, $F_{d/e} = 1 - B_{ij}$.

[5] URL: https://www.engineeringtoolbox.com/carbon-dioxide-thermal-conductivity-temperature-pressure-d_2019.html [cited on 5 Jun 2024]

[6] Communication with Dr I. Uriol Balbin, dd. 5 June 2024

[7] URL: https://www.dspe.nl/knowledge/thermomechanics/chapter-2-in-depth/2-4-thermal-radiation/2-4-3-gebhart-method/ [cited on 7 Jun 2024]

Motor Coating

Lastly, the coating of the fins can have a major effect on its performance. The primary goal of the fins is to radiate as much as possible; thus, a high emissivity is required. As described in a later section, Section 10.4, the absorptivity plays less of a role due to the negligible top area of the fins. White coatings result in the highest emissivity, >0.90 [8] .

10.2.4. Battery Thermal Design Methodology

Unlike the motor, the battery is required to be heated due to its restrictive temperature range. Methods could entail insulation to ensure the battery does not go beyond the survival temperature range and heaters to provide the extra heat necessary.

Heater

While many methods exist to heat systems, the primary method of heating used for batteries is heating foils [9] . These foils produce heat by passing a current through a resistor. The required heat power is first gathered to develop a heater, and a 25 % margin is applied [10] . Then, the average heater area density is computed using: $\rho = P_{heater}/A$. Based on this density, a heater type is selected.

Battery Coating

Lastly, similarly to the motor, the coating of the battery can have a major effect on its performance. The primary goal of the battery is to radiate as little heat as possible and to capture as much as possible; thus, a low emissivity and high absorptivity are required, resulting in a large absorption-to-emittance ratio. Electroplated gold or copper provide a large absorption-to-emittance ratio, 7.5 to 10 [11] .

10.3. Verification and Validation

Verification and validation of the method are crucial to ensuring the correct results. This section describes the V&V steps for the TCS model. It is important to note that the model was unit-tested.

The TCS model was verified in two phases. First, the model was verified without insulation and heater fins with the model for perseverance [43]. This provided a robust base code for new items to be appended. The resulting equilibrium temperature for the same input parameters as the perseverance design was 331.762 K in the hot case and 261.286 K in the cold case. The model by G. Quattrocchi returned results of 331.738 K and 262.331 K, respectively. The developed model thus has an error 0.01 % and 0.40 % respectively. This is deemed accurate enough for further analysis.

Following the verification of the general equations, the tool for the battery thermal tools was verified. Thermal analysis of the Ingenuity's battery TCS has been done previously by S. Cappucci. [42]. Similar to the results produced by the battery TCS model, the Ingenuity TCS maintained the battery with a layer of insulation within the temperature range. This report also presented Validation data and complied with S. Cappucci's results. Only visual verification and validation were performed as insufficient data has been shared to perform more detailed verification and validation.

It is similar to the TCS for the heating fins. Only visual V&V was performed due to the limited amount of data available. From F. Acquaviva [41], similar data was produced to develop heating fins. While similar blades were produced, only factors such as the Nusselt number and heat transfer coefficient were inspected and verified, lying in the same order of magnitude. More detailed verification could not be performed with limited access to sources and time.

It is important to note that proper tool validation is required before full production of any TCS. This is a major recommendation for the future phases of the development of the Martian Drone.

10.4. Results

This section provides the results using the method described in Section 10.2. In Section 10.4.1, the motor fin TCS design results are presented. Similarly, the battery TCS design is presented in Section 10.4.2. Lastly, the results

[8] URL: https://www.design1st.com/Design-Resource-Library/engineering_data/ThermalEmissivityValues.pdf [cited on 4 Jun 2023]
[9] Communication with Dr I. Uriol Balbin, dd. 5 June 2024
[10] URL: https://www.tempco.com/Tempco/Resources/09-Flexible-Resources/KaptonCatalogPages.pdf [cited on 19 June 2024]
[11] URL: https://apps.dtic.mil/sti/tr/pdf/ADA305864.pdf [cited on 18 Jun 2023]

of the total system are provided in Section 10.4.3, including margins for systems that are not designed.

10.4.1. Motor TCS Results

For the motor fin design, the fin dimensions were developed first. With various fin parameters, integer optimisation on the fin amount was consequently performed. Subsequently, the fin efficiency and fin flow parameters were calculated. Lastly, the heat balance resulted in the temperature over time plot. The primary objective of the optimisation is to minimise the mass while complying with the motor's temperature requirement.

The analysis resulted in the dimensions presented in Figure 10.2. Figure 10.1 illustrates the parameters. It is important to note that θ is the angle of the fins concerning the length. Angling the blades increases the total surface area, which improves the total radiative and convective cooling performance. Additionally, N is the number of fins. The motor fins are made from the same material as the motor casing, which is Al-6063-T5. This common material is frequently used for heating fins in satellites [12] . This aluminum alloy has a density ρ of 2700 kg m^{-3}, a specific heat capacity C_P of 900 J kg^{-1} K^{-1} and a thermal conductivity k of 209 W m^{-1} K^{-1} [13] . The total mass of all six fin assemblies for the motors equals 4.029 kg.

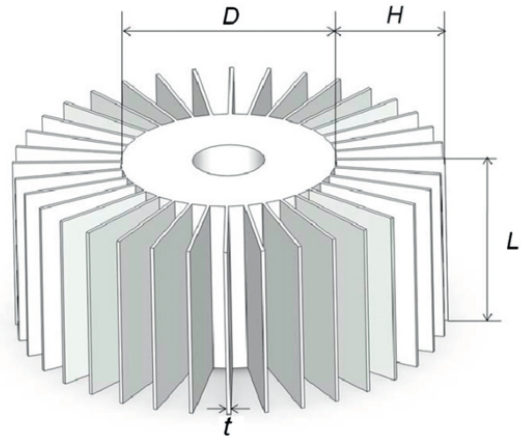

Figure 10.1: Illustration of cooling fins with geometrical parameters [46].

Figure 10.2: Resulting fin geometry parameters and mass from TCS analysis.

Parameter	Dimension	Unit
L_{fin}	6.28	cm
H_{fin}	15	cm
t_{fin}	2.2	mm
θ	35.7	deg
m_{fin}	671	g
N_{fin}	12	-

The flow parameters and fin efficiency are calculated from the developed parameters. Firstly, the dynamic viscosity of the atmosphere $\mu = 1.377 \times 10^{-5}$ N s m^{-2} and the density $\rho = 0.0127$ kg m^{-3} at the flight altitude of 100 m in the limiting case: the warmest sol. The Pr is calculated from the environmental parameters, resulting in Pr = 0.77. From the inflow determined in Chapter 8, the downwash can be calculated with $v = \lambda_i V_t$, resulting in an average downwash of ~15 m/s. Along with the H_{fin}, the resulting average Re = 0.870×10^4. For thin plates with Pr $\geq$ 0.6, Equation 10.10 results in Nu = $0.664 \mathrm{Re}_L^{1/2} \mathrm{Pr}^{1/3}$ [45, Eq. 7.30]. This results in Nu = 17.98 and with Equation 10.9, $h = 4.21$ W m^{-2} K^{-1}. This is in the same order of magnitude as F. Acquaviva's work, which serves as a verification and validation of the value [41].

It is important to note that the fin is not entirely efficient across the total area. Therefore, fin efficiency is calculated using $\eta = \frac{(hpkA_c)^{0.5}}{hA_f} \frac{\tanh\left(\sqrt{\frac{hp}{kA_c}}H\right) + \left(h/\sqrt{\frac{hp}{kA_c}}k\right)}{1 + \left(h/\sqrt{\frac{hp}{kA_c}}k\right)\tanh\left(\sqrt{\frac{hp}{kA_c}}H\right)}$ [46], where A_f is the fin area, A_c the cross-sectional area, p is the perimeter, and k is the thermal conductivity of the fin. The equation is a function of the geometry and fin flow parameters, resulting in $\eta = 0.877$. The total area thus becomes $A_{total} = h(\eta N_{fin} A_f + A_{unfinned})$.

Additionally, as previously mentioned, a coating is necessary to increase the emissivity of the fins. The emissivity for the fins is 0.92, and the absorptivity is 0.2 based on white paint coating: GSFC White Paint NS43-C [14] . Lastly, from Chapter 8, the resulting power per motor for take-off and cruise is 5682 W and 4262 W, respectively. This, with an efficiency of 90 %, 10 % goes to heat. However, it was recommended to take a large margin, resulting in a final thermal factor of 20 %. For six motors, this results in 189.4 W and 142.05 W for take-off and cruise,

[12] URL: https://clintonaluminum.com/best-aluminum-alloys-for-heat-transfer/ [cited on 12 Jun 2024]
[13] URL: https://asm.matweb.com/search/SpecificMaterial.asp?bassnum=MA6063T5 [cited on 5 Jun 2024]
[14] URL: https://www.design1st.com/Design-Resource-Library/engineering_data/ThermalEmissivityValues.pdf [cited on 4 Jun 2023]

respectively, per motor.

Combining the parameters described and the method outlined in Section 10.2 and the mission phases from Table 9.2, the time-dependent plot of the temperature profile for the motor is generated and presented in Figure 10.3. The graph has four phases: take-off, cruise, landing and standby.

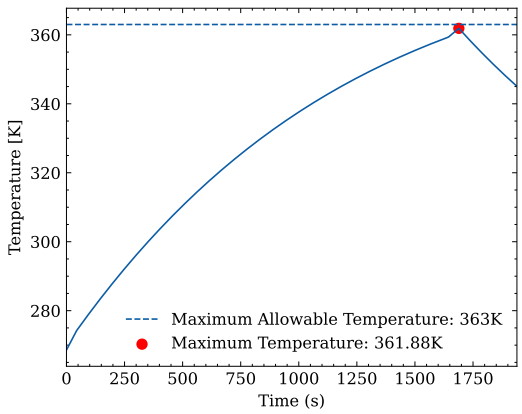

(a) Motor temperature with cooling fins, reaching a maximum temperature of 362 K.

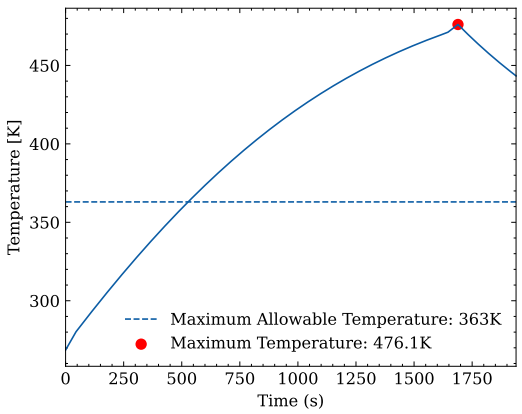

(b) Motor temperature without cooling fins, reaching a maximum temperature of 476 K.

Figure 10.3: Motor temperature during the hottest sol at the Eberswalde Crater (Areocentric longitude at 255°) with and without cooling fins.

10.4.2. Battery TCS Results

The insulator dimensions and the necessary heater power were developed for the battery TCS design. The primary objective of the development process for the battery design is to minimise the insulator mass and reduce the heater power usage.

Various insulators, including MLI, aerogel and cork, were investigated. While MLI is more efficient, it "is not very effective in the presence of a gas [31, p. 695]." Aerogel is very brittle and thus was also not considered. Cork was thus selected for insulation material, which has a thermal conductivity of 0.035 [15] . Additionally, a layer of air was also added as an insulator. This was also done for Ingenuity [42].

The battery insulation is also coated with electroplated gold due to its low emissivity, 0.03, and relative high absorptivity, 0.23.

Lastly, just resorting to insulation is insufficient; thus, heaters are required, as illustrated in Figure 10.4. A heating film is a common standard for satellite battery heating and was used in ingenuity [42]. From analysis, it was devised that up to 25 W of heating power is required for the battery. Using the method devised in Section 10.2.4, a maximum heat power of P_{heater} = 31.25 W including the 25 % margin, is required [16] . Using half of the area of the battery of 530 cm^2, as done with Ingenuity, one requires a power density of 0.06 W cm^{-2} = 0.38 W in^{-2}. Additionally, the power system has a maximum 60 V line for the heater, as noted in Chapter 9. Following this, Kapton heaters are the most feasible solution [17] . For a total area of 530 cm^2, and a mass density of 0.05 g cm^{-2} [18] , results in a mass of 26.5 grams.

The battery temperature for the hottest and coldest sols with and without heaters are illustrated in Figures 10.4a and 10.4b. A control loop was also devised for lower power usage, an industry standard for satellites and planetary vehicles. This control loop turns the heater on if the temperature reaches below a certain threshold. A major recommendation is to improve the design of this control loop in future iterations.

[15] URL: https://www.nuclear-power.com/nuclear-engineering/heat-transfer/heat-losses/insulation-materials/thermal-conductivity-of-cork-insulation/ [cited on 7 June 2024]

[16] URL: https://www.tempco.com/Tempco/Resources/09-Flexible-Resources/KaptonCatalogPages.pdf [cited on 17 June 2024]

[17] URL: https://www.nasa.gov/smallsat-institute/sst-soa/thermal-control/#7.3.1 [cited on 17 June 2024]

[18] URL: https://www.tempco.com/Tempco/Resources/Engineering-Data/Specifications-and-Tolerances/Kapton-Heater-Specifications-and-Tolerances.htm [cited on 17 June 2024]

Table 10.2: Battery heater and insulation parameters.

Parameter	Dimension	Unit
t_{ins}	1	cm
k_{ins}	0.035	$W\,m^{-1}\,K^{-1}$
t_{air}	1.5	cm
k_{air}	0.0209	$W\,m^{-1}\,K^{-1}$
$m_{insulator}$	297	g
$m_{insulator}$	27	g
P_{heater}	10 to 25	W

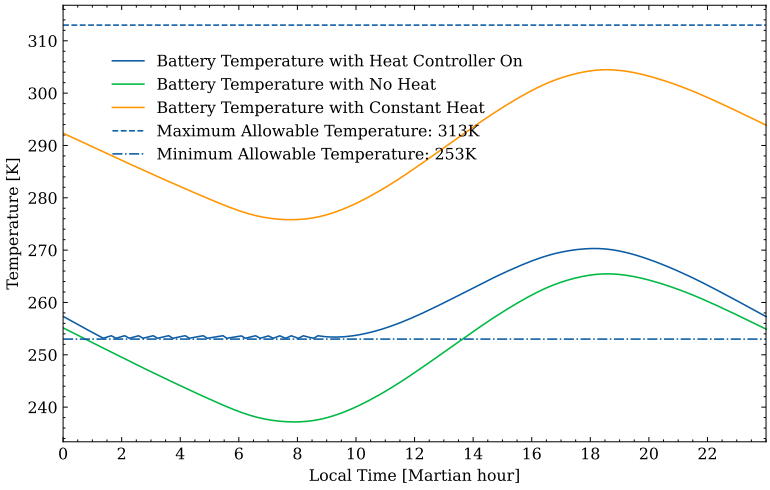

(a) Battery temperature during the hottest sol (Areocentric longitude at 255°). Heat controller on requires 7 W on average and 15 W peak. Constant heat is set at 15 W.

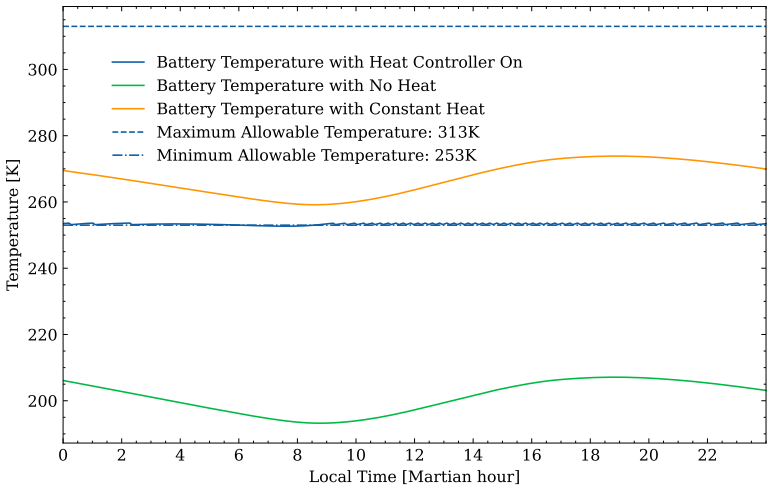

(b) Battery temperature during the coldest sol (Areocentric longitude at 101°) Heat controller on requires 15 W on average and 30 W peak. Constant heat is set at 25 W.

Figure 10.4: Battery temperature at extreme temperatures throughout the Martian year.

10.4.3. Total TCS Results

The TCS for the motor and the battery has been designed, resulting in a total mass of 4.35 kg. However, other systems, such as the antennae, payload motor and sensors, also require a TCS. All these systems are assumed to require a TCS similar to the battery heater, and these systems will be developed in future phases. Additionally, systems such as the thermal management board and thermocouples must be developed. To ensure these systems are taken into account, a 30 % margin is added to the total mass of the system, resulting in a total mass of 5.65 kg.

As noted, a total power of 10 W to 25 W is required for the battery heating. Adding a 30 % margin to the power and the 25 % for heating loss, results in a total power required of 16.25 W to 40.63 W, averaging at ~25 W.

11 Guidance, Navigation and Control

***Authors**: Li, Raf*

In this chapter, the design of the Guidance, Navigation and Control (GNC) subsystem are discussed in detail. This system plays a pivotal role in the success of the mission, as it determines whether the drone can perform mission sequences and operate autonomously. First, in Section 11.1, the requirements driving the design of the GNC subsystem are presented to the reader. Subsequently, the methodology and theory used to size the subsystem are detailed in Section 11.2. The V&V procedures to be carried out for the drone are determined in Section 11.3. Finally, in Section 11.4, the subsystem sizing are be provided and discussed in detail.

11.1. Requirements

***Author**: Li*

Stemming from the requirements derived during earlier stages in the design, the GNC subsystem shall be able to comply with the following items:

Table 11.1: GNC requirements. The verification lead for all is the S&C lead, except for GNC-SYS-02, where it is the GNC lead.

ID	Requirement	Verification Method
GNC-SYS-01	The Martian Drone shall have a control system	Demonstration
GNC-SYS-01-01	The control system shall provide attitude control	Demonstration
GNC-SYS-01-02	The control system shall provide lateral control	Demonstration
GNC-SYS-01-03	The control system shall provide directional control	Demonstration
GNC-SYS-01-04-I	The control system shall provide altitude control	Demonstration
GNC-SYS-01-05	The control system shall allow for manoeuvring of the Martian Drone	Demonstration
GNC-SYS-02	The Martian Drone shall execute a flight plan autonomously	Demonstration
GNC-SYS-02-01	The Martian Drone shall be able to take off autonomously	Demonstration
GNC-SYS-02-02	The Martian Drone shall be able to land autonomously	Demonstration
GNC-SYS-02-02-01	The Martian Drone shall be able to control the descent rate to within $0.1\,\mathrm{m\,s^{-1}}$	Demonstration
GNC-SYS-02-02-02	The Martian Drone shall be able to land within $0.377\,\mathrm{m\,s^{-1}}$ of a target	Demonstration
GNC-SYS-03-I	The GNC system shall enable the Martian Drone to navigate safely and autonomously	Demonstration
GNC-SYS-03-01-I	The GNC system shall be capable of autonomously detecting terrain variation	Demonstration
GNC-SYS-03-02-I	The GNC system shall be capable of autonomously avoiding terrain variation	Demonstration
GNC-SYS-04-I	The GNC system shall be able to determine the system's attitude accurately	Demonstration
GNC-SYS-05-I	The GNC system shall be able to determine the system's location accurately	Demonstration
GNC-SYS-06-I	The GNC system shall be able to determine the system's velocity accurately	Demonstration
GNC-SYS-07-I	The GNC system shall be able to determine the system's acceleration accurately	Demonstration
GNC-SYS-08-I	The GNC system shall be able to determine the system's angular rates accurately	Demonstration

For the sake of brevity, only the most critical requirements for the GNC subsystem are presented. These have the most significant impact on the drone's controllability and autonomous navigation capabilities, and thus drive the design of the GNC subsystem. Some of the requirements have been updated further into the design process, denoted by Roman numerals. In the following sections, the method to design a subsystem that fulfils these requirements are presented, along with the final subsystem sizing results.

11.2. Methodology

In this section, the methodology and theory used to determine the architecture and design of the GNC subsystem are presented to the reader. Section 11.2.1 details the guidance and navigation aspect of the subsystem, providing an overview of the sensors and algorithms that will enable the drone to navigate autonomously. Section 11.2.2 discusses the controllability of the hexacopter using a dynamic model, along with a flight controller design.

11.2.1. Guidance and Navigation

Author: Li

For autonomous navigation, the drone shall be able to locate itself in space so that the flight controller can command the appropriate inputs to the thrusters. There are multiple ways to achieve this, and extensive literature research was carried out to determine the system architecture. The harsh environment of Mars, coupled with the lack of a Global Navigation Satellite System (GNSS), makes autonomous navigation on the Red Planet a particularly challenging task.

From literature [47] [48], it was seen that a common approach to GNSS-constrained navigation is to use multiple odometry sensors, fuse their measurements and estimate the pose using different algorithms to minimize inaccuracies caused by noisy sensor data. Some examples of unmanned air vehicles include Visual-Inertial Odometry (VIO) and Lidar-Inertial Odometry (LIO), based respectively on camera images and lidar point clouds. These approaches typically use pre-mapped landmarks, allowing the vehicle to obtain the ground truth of its position using only one image from the sensors. This is, however, infeasible on Mars due to the low resolution of mapped landmarks, as they are generated from a long distance via planetary orbiters [49].

NASA's Ingenuity used a velocimetry-based VIO approach [49] due to power limitations, both from a computational and energy perspective. This allows for a lower order filter compared to lidar approaches, which in turn reduces the memory and computational required by orders of magnitude. Despite the high robustness of the proposed algorithm, which makes use of the approach taken by NASA still suffered from long-term drift in position and heading despite the high robustness proven in the flight tests. For Ingenuity, such an approach was acceptable due to the short range and endurance of the mission. The Martian Drone will be subjected to substantially harsher mission environments, leading to the need for a more robust state estimation algorithm.

LVI-SAM Algorithm

Extensive literature research was carried out in order to select the optimal state estimation algorithms for the Martian Drone. It was decided that a SLAM (Simultaneous Localization And Mapping) approach would be taken, as it also enables the system to produce valuable, high-resolution mappings of the Martian surface, which adds further scientific value to the mission. Shan et al. proposed a state-estimation framework which combines VIO and LIO in a tightly coupled manner, named LVI-SAM (Lidar-Visual-Inertial odometry via Smoothing And Mapping) [8]. This algorithm successfully achieves real-time state estimation and mapping with high accuracy and robustness. The framework is built on a factor graph and composed of two primary sub-systems: the Visual-Inertial System (VIS), and the Lidar-Inertial System (LIS). The top-level implementation of the framework can be seen in Figure 11.1.

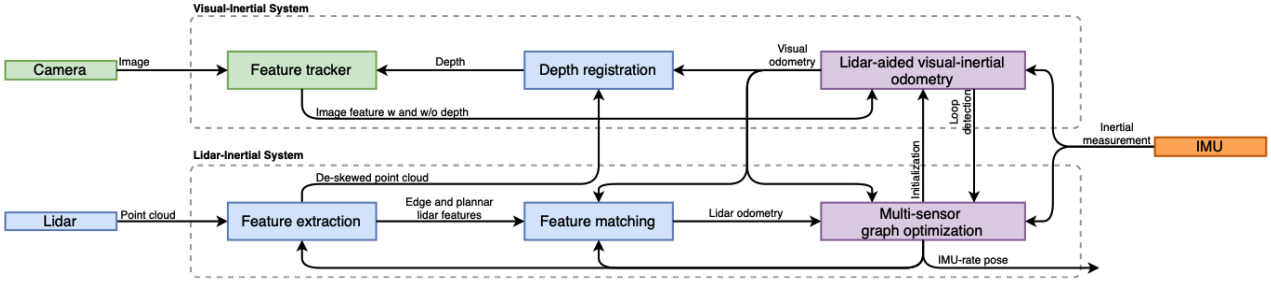

Figure 11.1: System structure of LVI-SAM [8]

The detailed implementation of the algorithm can be seen in the original publication [8], and is left out of this report for the sake of brevity. The main advantages of this framework are highlighted below, taking into account the mission profile and objective of the drone:

High robustness: The two subsystems can function independently if the other fails during operation, or not enough features are extracted from the relevant sensors. This provides a high-level of robustness which is critical for an autonomous Martian mission.

High precision: LVI-SAM can achieve virtually drift-less state estimation across a long distance if loop-closure is exploited during operations. Loop-closure refers to the recognition of a previously visited location and the correction of accumulated drift of the drone using this information. Even if no previous features are recognized, the system is still precise enough to follow the trajectory with limited inaccuracies. In Figure 11.2, an example trajectory is illustrated comparing the performance of LVI-SAM with and without loop-closure. For the drone, loop closure is assumed to be present during operations, as the mission consists of flying out to a designated area and then flying back following a similar path. This will ensure autonomous, drift-less navigation over a long range without relying on GNSS, which is foundational to the success of the mission.

Effectiveness in feature-less environments: LIO systems often rely heavily on feature-rich environments to accurately map the vehicle's surroundings. Due to the lack of vegetation and scarcity of other feature-rich landmarks on the Martian surface, navigation based on pure LIO approaches becomes significantly challenging. Nonetheless, LVI-SAM has proven to be highly effective even in these scenarios, as the paths illustrated in Figure 11.2 were generated on a flat, feature-poor baseball field, which severely limits the performance of the LIS subsystem.

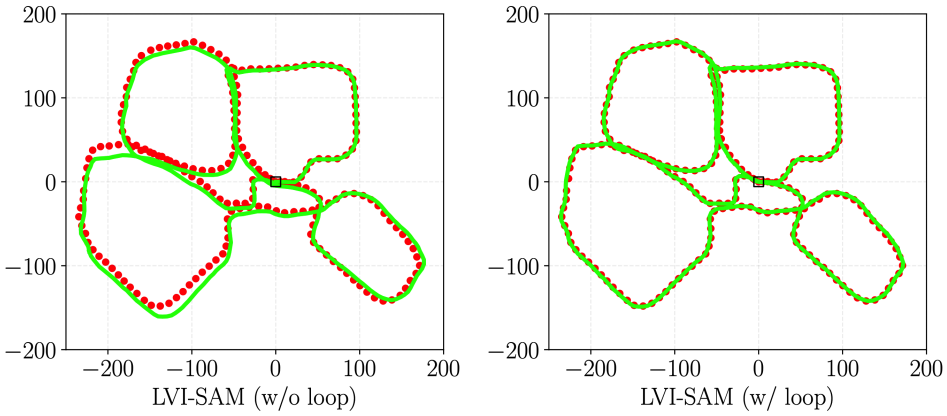

Figure 11.2: LVI-SAM position estimations (Green) overlayed on GNSS ground truth (Red). X-Y axes are given in meters. [8]

Considering all of the aforementioned factors, the LVI-SAM algorithm is used to estimate the state of the Martian Drone during mission operations.

Absolute Positioning

Despite the high robustness and precision of the LVI-SAM algorithm, drift is still inevitably bound to happen over a longer period of time. To prevent this issue from causing critical impacts on the mission, the GNC system shall still be capable of periodically determining the drone's absolute position on Mars. After careful consideration and extensive literature research, three potential options to obtain global positioning have been proposed, each with its advantages and constraints.

The first option would be deploying a full-fledged GNSS constellation along with the mission. Molli et al.[50] proposed a SmallSat GNSS system comprised of one 12U mothercraft and four 6U daughtercrafts. These SmallSats could potentially be brought along with the mission to Mars orbit, due to their small size and the large payload capacity of the selected launcher of the mission (Ariane 6). These SmallSats are put in polar orbit, with two possible configurations, corresponding to an orbital period of 0.5 sols and 0.25 sols, respectively. The second orbital configuration was chosen due to its advantageous positioning concerning the Eberswalde crater, which is located at (23.90 °S, −26.74 °E). The ground tracks of the constellation over four orbital periods (which corresponds to 1 sol) are illustrated in Figure 11.3.

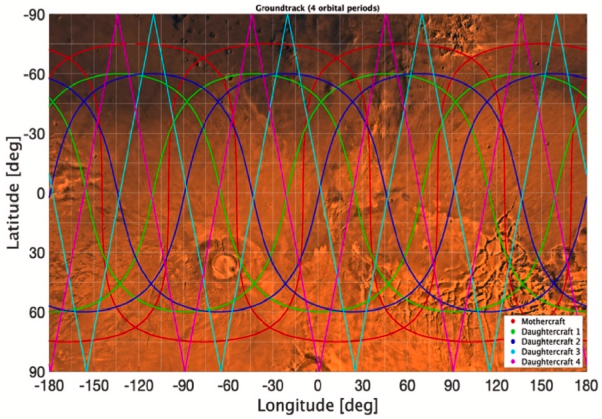

Figure 11.3: Ground track of the proposed GNSS constellation over 4 orbital periods [50]

As can be seen from Figure 11.3, over 1 sol, there will always be at least three crafts of the constellation passing near the Eberswalde crater, allowing the Martian Drone to calibrate its absolute position once every sol. As discussed in the previous section, this option is the most reliable and provides a fully robust positioning system on Mars when paired with an autonomous odometry algorithm. Nonetheless, it brings significant drawbacks in terms of mission cost and complexity.

An alternative option would be the usage of ground-based radio beacons, which would be deployed in parallel to the ground station. These suffer from limited range [13], having an effective range of only up to 4.4 km, but provide a reliable way of determining absolute position within the communication range. This constraint does not have critical impacts on the mission, due to the higher precision with loop-closure of the odometry navigation framework, meaning the drone would be able to travel back following the same path with high accuracy. These add relatively less mission complexity and cost to the system compared to the first option. However, they would need to be sized to fit inside the aeroshell along with the ground station and the drone, adding additional constraints to the design.
A similar but more minimal solution is also considered for global positioning. For this, the drone would simply communicate multiple times from different positions with the ground station when it is within communication range. This would effectively serve as a triangulation procedure to obtain an estimated position. The system selection is left for future work, in which a detailed trade-off between the different options will be performed. For the scope of the project, LVI-SAM is considered to provide the drone with sufficiently accurate global pose estimation, and periodic calibrations can be performed after each mission cycle near the ground station.

In parallel with the global position estimation, the drone shall also be able to correct and determine the ground truth of its heading. Due to the low power and weight requirements, a sun sensor will be used for this purpose. During the day, it will be able to provide the drone with the absolute heading given the sun's position. This method will not be effective during nighttime, but it will not become an issue since the drone will be stationary.

11.2.2. Control

***Authors**: Raf, Li*

This section discusses the design of a basic flight controller for the system and the drone's controllability. A nonlinear dynamic model of the hexacopter was simulated in Python to discuss the drone's controllability. Furthermore, a flight computer has been developed as well.

Model

The following body reference frame ($\mathcal{R}_B$) definition of the hexacopter is used, as illustrated in Figure 11.4:

$\mathcal{R}_B$ is related to the inertial reference frame $\mathcal{R}_I$ via the following transformation matrix, in which ϕ, θ and ψ are the Euler rotation angles around x, y and z axes respectively:

$$\mathcal{T}_B^I = \begin{bmatrix} \cos\theta\cos\psi & \cos\psi\sin\theta\sin\phi - \sin\psi\cos\phi & \cos\psi\sin\theta\cos\phi + \sin\psi\sin\phi \\ \sin\psi\cos\theta & \sin\theta\sin\psi\sin\phi + \cos\psi\cos\phi & \cos\phi\sin\psi\sin\theta - \cos\psi\sin\phi \\ -\sin\theta & \sin\phi\cos\theta & \cos\theta\cos\phi \end{bmatrix} \tag{11.1}$$

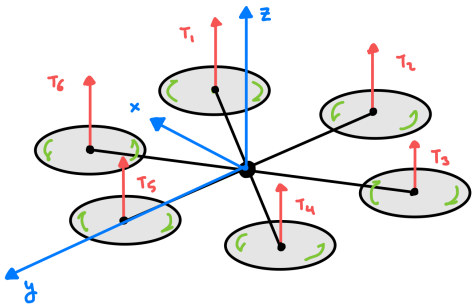

Figure 11.4: Body reference frame $\mathcal{R}_B$ of the hexacopter dynamic model

The total propulsive thrust T and moments M_x, M_y, M_z applied to the hexacopter can be related directly to each propeller's rotational speed, denoted by Ω_i. This can be represented as a simple linear mapping of form $\bar{\mathcal{F}} = A\bar{\Omega}$, where $\bar{\mathcal{F}}$ is the vector containing the propulsive thrust and moments and $\bar{\Omega}$ is the vector containing the propeller speeds. This linear mapping is expanded in Equation 11.2, which takes into account the position of each propeller with respect to the origin of $\mathcal{R}_B$.

$$\begin{bmatrix} T \\ M_x \\ M_y \\ M_z \end{bmatrix} = \begin{bmatrix} b & b & b & b & b & b \\ -\frac{bl}{2} & -bl & -\frac{bl}{2} & \frac{bl}{2} & bl & \frac{bl}{2} \\ -\frac{bl\sqrt{3}}{2} & 0 & \frac{bl\sqrt{3}}{2} & \frac{bl\sqrt{3}}{2} & 0 & -\frac{bl\sqrt{3}}{2} \\ -d & d & -d & d & -d & d \end{bmatrix} \begin{bmatrix} \Omega_1^2 \\ \Omega_2^2 \\ \Omega_3^2 \\ \Omega_4^2 \\ \Omega_5^2 \\ \Omega_6^2 \end{bmatrix} \tag{11.2}$$

$$\begin{cases} b = C_T \rho r_p^4 \pi \\ d = C_Q \rho r_p^5 \pi \end{cases} \tag{11.3}$$

In which l is the length of the arm, whereas b and d are related to the propeller radius r_p thrust coefficient C_T, torque coefficient C_Q and aerodynamic density ρ.

Having taken these definitions into account, the dynamics of the system can be fully modelled with Equation 11.4. The detailed derivation of this set of equations is given in Kattupalli and Abraham[51] and is left out of this report for the sake of brevity:

$$\begin{cases} \ddot{\phi}_d = \dfrac{J_{yy} - J_{zz}}{J_{xx}} \dot{\theta}\dot{\psi} + \dfrac{-(J_r)}{J_{xx}} \Omega_r \dot{\theta} + \dfrac{l}{J_{xx}} M_x \\ \ddot{\theta}_d = \dfrac{J_{zz} - J_{xx}}{J_{yy}} \dot{\phi}\dot{\psi} + \dfrac{J_r - J_{xx}}{J_{yy}} \dot{\phi}^2 + \Omega_r \dot{\phi} + \dfrac{l}{J_{yy}} M_y \\ \ddot{\psi}_d = \dfrac{J_{xx} - J_{yy}}{J_{zz}} \dot{\phi}\dot{\theta} + \dfrac{l}{J_{zz}} M_z \\ \ddot{x}_d = \dfrac{l}{m} (\cos\phi \cos\psi \sin\theta + \sin\phi \sin\psi) \\ \ddot{y}_d = \dfrac{l}{m} (\cos\phi \sin\theta \sin\psi - \sin\phi \cos\psi) \\ \ddot{z}_d = \dfrac{\cos\phi \cos\theta}{m} T - g \end{cases} \tag{11.4}$$

$$\frac{(\Omega_i)^2}{(\Omega_i^*)^2} = \frac{\omega_n^2}{s^2 + 2\zeta\omega_n s + \omega_n^2} \tag{11.5}$$

Equation 11.4 defines the hexacopter dynamics in all 6 degrees of freedom (DOF) and relates them to the actuator inputs, which allows for a comprehensive understanding and modelling of the drone. In the set of equations, J_{xx}, J_{yy}, J_{zz} stand for the mass moments of inertia of the drone around the respective axes. For simplicity, it has been assumed that the drone will be axis-symmetrical. J_r stands for the propeller moment of inertia, and $\Omega_r = -\Omega_1 + \Omega_2 - \Omega_3 + \Omega_4 - \Omega_5 + \Omega_6$. In order to account for the non-instantaneous response of the motors, a second-order lag-response model is implemented. Note that this is not the actual response of the motors used, but rather a generalized approach to simulate the response of motors of such scale as deemed realistic by the team. The transfer function for this is given by Equation 11.5, where Ω_i^* is the targeted rotational speed, $\omega_n \approx 15\,\mathrm{rad\,s^{-1}}$ and $\zeta = 1.05$ is the damping ratio.

Note that at this design stage, the effects of aerodynamic drag on the main body have been neglected due to the

limited information. This assumption is considered to have negligible impacts on the discussion results due to the low density on Mars and the relatively small dimensions of the drone body. Nonetheless, to demonstrate that the drone can still be controllable in environments with harsh, disturbances in the drone dynamics due to turbulence are still modelled. The subscript d in Equation 11.4 indicates that the given accelerations are related to the dynamic model, whereas later on, the subscript T denotes the terms related to disturbances.

A method based on the Wiener process is used to model the disturbances, adding extra terms to the second derivatives of each DOF. This approach is taken as no existing disturbance models apply to the specific set of equations given in Equation 11.4. A stochastic process is defined such that the magnitude of the disturbance is always smaller or equal to 1, whereas the derivative is equal to $\mathcal{K}$ times the derivative of the Wiener process, except when this would cross the magnitude constraint, in which case it is 0 when this would leave the bounds:

$$d\xi_t = \begin{cases} 0 & \text{if } \xi_t = 1 \wedge dW_t > 0 \\ 0 & \text{if } \xi_t = -1 \wedge dW_t < 0 \\ \mathcal{K} \cdot dW_t & \text{otherwise} \end{cases} \qquad \begin{matrix} \mathcal{K} = 1.25 \\ dW_t = N_t dt \end{matrix} \tag{11.6}$$

Where N_t is the continuous Gaussian white noise process with 0 mean and variance 1 [52]. For each of the 6 DOFs an independent Wiener process exists such that the second derivatives of each can be defined as:

$$\begin{cases} \ddot{\phi}_T = \lambda_h c_\phi \xi_t, & c_\phi = 0.3 \\ \ddot{\theta}_T = \lambda_h c_\theta \xi_t, & c_\theta = 0.3 \\ \ddot{\psi}_T = \lambda_h c_\psi \xi_t, & c_\psi = 0.2 \\ \ddot{x}_T = \lambda_h c_x \xi_t, & c_x = 0.15 \\ \ddot{y}_T = \lambda_h c_y \xi_t, & c_y = 0.15 \\ \ddot{z}_T = \lambda_h c_z \xi_t, & c_z = 0.2 \end{cases} \qquad \lambda_h = \begin{cases} 0.9 \left(\frac{z}{100\,\mathrm{m}}\right)^{\frac{3}{2}} + 0.1 & \text{if } 0\,\mathrm{m} \leq z \leq 100\,\mathrm{m} \\ 1 & \text{if } z > 100\,\mathrm{m} \end{cases} \tag{11.7}$$

Note that the constants c_i and $\mathcal{K}$ are arbitrarily chosen, as no detailed aerodynamic or atmospheric analysis has been performed at this stage. The factor λ_h was included to account for variations in atmospheric density and disturbances and is given as a function of altitude. For future work, a more detailed turbulence model incorporating the actual drag model of the hexacopter main body is recommended for more accurate results. For this project's scope, the turbulence model is deemed sufficient to prove the robustness and controllability of the drone even with the presence of external disturbances. The total second derivatives are subsequently derived by summing the terms stemming from Equation 11.4 and Equation 11.7.

Architecture

To effectively control the drone, the flight situation first has to be determined. This is performed by reviewing a list of checks, each with its priority if flagged. The list of priorities and associated targets for the Martian Drone control system to meet is as stated in Table 11.2 based on each control mode. At this stage, the control loop and constrained weighting set for the drone are also selected, which is stated in Table 11.2 and further divulged in Section 11.2.2 and table 11.4.

Table 11.2: List of control models and triggers, ordered by priority from top to bottom

Mode	Triggered by	Control loop	Dynamics target	Constrained weight set
Attitude recovery	$\lvert\phi\rvert > 45° \vee \lvert\theta\rvert > 45°$	1	$z^* = 100\,\mathrm{m}$, $\phi^* = 0°$, $\theta^* = 0°$, $\psi^* = 0°$	$\bar{w}_3$
Landing	$r < 5\,\mathrm{m} \wedge \left\lvert(\dot{x}, \dot{y})\right\rvert < 1\,\mathrm{m\,s^{-1}}$	3	$\dot{z}^* = \begin{cases} -0.3, & z < 12.5\,\mathrm{m} \\ -8, & z \geq 12.5\,\mathrm{m} \end{cases}$, $x^* = x_{\text{target}}$, $y^* = y_{\text{target}}$, $\psi^* = \psi_{\text{target}}$	$\bar{w}_2$
Maximum climb	$z < 20\,\mathrm{m}$	1	$z^* = 100\,\mathrm{m}$, $\phi^* = 0°$, $\theta^* = 0°$, $\psi^* = 0°$	$\bar{w}_2$
Altitude recovery	$z < 80\,\mathrm{m}$	2	$z^* = 100\,\mathrm{m}$, $\psi^* = 0°$, $\left\lvert(\dot{x}^*, \dot{y}^*)\right\rvert = 30\,\mathrm{m\,s^{-1}}$	$\bar{w}_2$
Closing in	$r < 125\,\mathrm{m}$	2	$z^* = 100\,\mathrm{m}$, $\psi^* = 0°$, $\left\lvert(\dot{x}^*, \dot{y}^*)\right\rvert = 3\,\mathrm{m\,s^{-1}}$	$\bar{w}_1$
Nominal flight	No other active mode	2	$z^* = 100\,\mathrm{m}$, $\psi^* = 0°$, $\left\lvert(\dot{x}^*, \dot{y}^*)\right\rvert = 30\,\mathrm{m\,s^{-1}}$	$\bar{w}_1$

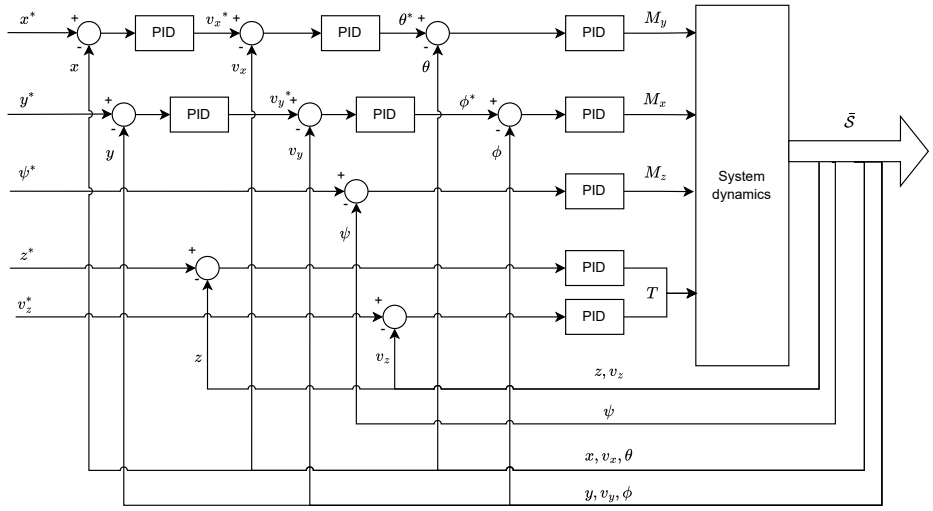

Figure 11.5: Cascaded PID architecture

The flight computer serves as a higher-level controller for the drone, whereas the control inputs is fully determined by a cascaded PID-like (Positional, Integral, Derivative Controller) control loop. The full cascaded PID loop is presented in Figure 11.5. The PIDs also include an anti-windup parameter.

For a given state $\bar{\mathcal{S}}$ and a flight computer mode, the system states will be put through a series of PID controllers to determine the required system inputs. Note that not all PID control loops illustrated in Figure 11.5 are active at all times. The combination of PID sets and flight computer modes are presented in Section 11.2.2. This table has the target selected by the flight computer as the leftmost of each input, and each arrow represents a PID as depicted in Figure 11.5.

Table 11.3: Active PIDs per selected control loop

Control loop	T	$\mathbf{M_x}$	$\mathbf{M_y}$	$\mathbf{M_z}$
1	$z^* \rightarrow T$	$\phi^* \rightarrow M_x$	$\theta^* \rightarrow M_y$	$\psi^* \rightarrow M_z$
2	$z^* \rightarrow T$	$v_x^* \rightarrow \phi^* \rightarrow M_x$	$v_y^* \rightarrow \theta^* \rightarrow M_y$	$\psi^* \rightarrow M_z$
3	$v_z^* \rightarrow T$	$x^* \rightarrow v_x^* \rightarrow \phi^* \rightarrow M_x$	$y^* \rightarrow v_y^* \rightarrow \theta^* \rightarrow M_y$	$\psi^* \rightarrow M_z$

The desired inputs are given directly as moments and total thrust, which can raise issues in terms of actuator saturation since there might not be a set of motor input values which can be mapped to all four desired system inputs following Equation 11.2. To solve this, for a given set of desired system inputs ($M_{x,y,z}, T$) a weighted linear least-squares solution to Equation 11.2 is found, in which the motor speeds are constrained to $\Omega_{idle} \leq \Omega_i \leq \Omega_{max}$, with thrust to weight: $0.7 < \frac{T}{W} < 1.3$. This ensures that the individual motor inputs are not saturated, and the thruster combination leads to a set of system inputs that match the desired inputs as closely as possible within constraints. Thus, the minimised cost function, f, in weighted linearly constrained least squares is:

$$\begin{aligned} f\left(\bar{\Omega}^*\right) &= \left|W\left(A\bar{\Omega}^* - \bar{\mathcal{F}}\right)\right|_2, \\ \Omega_{idle} \leq \Omega_i^* &\leq \Omega_{max}, \quad \forall \Omega_i^* \in \bar{\Omega}^* \end{aligned} \tag{11.8}$$

The weight matrix can be found by $W = I\bar{w}_i$, where $\bar{w}_i$ is the vector which corresponds to the i-th weight set and I is the identity matrix. The weight vectors $\bar{w}_i$ can be found in Table 11.4:

The results of the manual PID tuning are as in Table 11.5. The $x^* \rightarrow v_x^*$ and $y^* \rightarrow v_y^*$ have an output magnitude capped to $0.3\,\mathrm{m\,s^{-1}}$, and $v_x^* \rightarrow \phi^*$ and $v_y^* \rightarrow \theta^*$ have an output magnitude capped to 0.67 rad. Furthermore, PIDs controlling thrusts and moments indicate a thrust to weight and moment to weight, respectively; other PID values are in metric or radians, where applicable.

Table 11.4: Least squares weighting sets

Constrained weighting set	Weight vector
$\bar{w}_1$	$[9,5,5,3]^T$
$\bar{w}_2$	$[10,5,5,3]^T$
$\bar{w}_3$	$[2,5,5,3]^T$

Table 11.5: Gains and limits of every PID in the control loop

PID	K_P	K_I	K_D	wind-up limit
$\phi^* \rightarrow M_x$	1.4	0.13	2.2	0.3
$\theta^* \rightarrow M_y$	1.4	0.13	2.2	0.3
$\psi^* \rightarrow M_z$	0.5	0.1	1.3	0.6
$x^* \rightarrow v_x^*$	0.3	0.0002	0.35	5
$y^* \rightarrow v_y^*$	0.3	0.0002	0.35	5
$z^* \rightarrow T$	0.7	0.3	3.0	2
$v_x^* \rightarrow \phi^*$	0.1	0.009	0.2	7
$v_y^* \rightarrow \theta^*$	0.1	0.009	0.2	7
$v_z^* \rightarrow T$	10	0.016	4	20

11.3. Verification and Validation

***Author**: Li*

Due to the design methodology's qualitative nature, no V&V procedures were carried out for the guidance and navigation section of the GNC subsystem. To validate and verify the subsystem, demonstration tests are carried out using the selected sensors to certify the final design.

For the hexacopter model, many unit tests were written to ensure that the individual parts were correctly implemented. System tests via inspection were carried out for the dynamic model by giving arbitrary control inputs to the hexacopter and checking that the model outputs were as expected. Validation was not performed for this section of the code, due to the limited amount of real-life data or high-fidelity models. For future work, the designed control system could be implemented in a real drone and validation would be performed by checking the hexacopter states from the model output against sensor data.

11.4. Results

The results of the GNC system sizing and characterization are provided in the following section. First, the final selected sensors to enable onboard autonomous navigation is presented, followed by detailed plots discussing the drone's controllability.

11.4.1. Sensor Selection

***Author**: Li*

In Section 11.2.1, the specific navigation algorithm to be used to determine the states of the vehicle is provided. In this section, an overview of the specific sensors composing the GNC system are described, along with other required components needed for the system's proper functioning. The odometry sensors are as follows:

Fisheye camera This will provide the required image for the LVI-SAM algorithm. A high-resolution black-and-white camera with a fisheye lens was selected to maximize the FOV and facilitate feature extraction with minimal cameras.

Lidar The lidar sensor will provide the point clouds required for the LVI-SAM algorithm and enable real-time 3D surface mapping of Mars.

Inertial Measurement Unit (IMU) Fundamental for autonomous navigation, this sensor will provide the drone's angular rates and linear accelerations at a high refresh rate.

Inclinometer Provides the absolute rotation of the drone when landed, fundamental for takeoff and landing operations.

Sun sensor Provides the drone with absolute heading during the day.

Note that the communication antennae for GNSS calibration is not included, as it will be handled by the communication subsystem. In addition to the aforementioned sensors, the following components are required to process and store the data generated by the odometry sensors (as well as payload sensors when applicable):

Onboard computer LVI-SAM requires high computational power due to the complexity of the algorithm and the large amount of data to be processed. Furthermore, the onboard computer (OBC) will handle all other avionics components, including payload, communications, power management, and flight controls. Thus, powerful and computationally efficient boards capable of visual data processing and AI applications were considered for the Martian Drone.

Data storage device The drone will need to store the features from locations it has traversed through before to perform loop-closure on the newly acquired sensor data. The storage device has been selected such that the features generated over one mission cycle can be fully stored. After each mission cycle, this data will be sent to the ground station and deleted from the drone's memory. This data can be fetched at any moment from the ground station, providing features generated from previous mission cycles.

The final selected components are provided in Table 11.6.

Table 11.6: Component list for the GNC subsystem

Sensor type	Model	Mass [kg]	Power [W]	Data Rate [Mbit s^{-1}]	Note	Dimensions [m]	Cost [€]
Sun Sensor	Aquila Sun Sensor [1]	0.037	0.15	0.0008	-	0.034 × 0.040 × 0.020	11 215
IMU	InvenSense IIM-46230 [2]	0.016	0.144	0.0144	Two are included for redundancy	0.023 × 0.023 × 0.0085	790
Inclinometer	Murata SCA100T [3]	0.0012	0.02	0.0002	-	0.016 × 0.011 × 0.005	166
OBC	Nvidia Jetson AGX Xavier 64GB [4]	0.28	15	1092000	Data rate is data handling rate Two are included for redundancy	0.1 × 0.087 × 0.005	3100
Lidar	Velodyne Puck [5]	0.49	12	57.6	Dimensions are diameter x length	0.103 x 0.073	3700
Laser rangefinder	Lightware LW20-C IP67 [6]	0.02	0.715	0.01552	-	0.0195 x 0.0302 x 0.035	350
Fisheye camera	Intel RealSense T265 [7]	0.06	1.5	162.8	Data rate assumed streaming Two are included for redundancy	0.108 × 0.0245 × 0.0125	880
Storage device	Exascend PR4 NVMe 15.36TB [8]	0.01	7.5	28000	Data rate is data upload rate	0.1 × 0.07 × 0.007	5000

11.4.2. Control

***Author**: Raf*

The model and flight computer, as found in Section 11.2.2, are simulated at different speeds: the flight computer has a polling rate of 50 Hz, and the model is simulated with a time step $\Delta t = 1$ ms. From convergence analysis, this was found to be sufficient.

The control system is tuned to achieve both landing accuracy and short take-off and landing time while remaining stable under turbulence. To verify whether the times of the flight profile are achievable, a short flight is analysed. For this, the position and altitude throughout time are used, as well as the velocity during landing. Figures 11.6 and 11.7 illustrate a climbing time of 20 s is possible, along with a descent of 45 s, while having a touchdown velocity of $-0.3\,\mathrm{m\,s^{-1}}$ and with an accuracy of $0.01\,\mathrm{m\,s^{-1}}$. This proves that the flight profile found in Section 7.3 is barely possible when taking into account that the flight profile has two separate descents totalling 50 s. To verify stability, the drone must be stable at all angles, horizontal velocities, and altitudes. Figures 11.6 to 11.8 illustrate the control system correcting deviations from the targeted values, proving both stability and controllability. Furthermore, using the spectrogram in Figure 11.11, the Controller-Induced Vibration (CIV) can be analysed. This shows an induced vibration of 5 N at 3.25 Hz during the landing phase. This is analysed further in Section 14.2.6.

The log plot of the distance from the target over time is depicted in Figure 11.9, which illustrates a steady convergence, especially close to landing, for landing accuracy. The landing distance was computed 1000 times, providing the histogram and kernel density estimation as in Figure 11.10. This illustrates that in almost all cases the drone lands within accuracy requirements for the robotic arm, as specified in Section 15.5. More specifically the drone landed with $r_f < 0.10$ m in more than 99 % of the cases, where r_f is the landing distance and always has $r_f < 0.20$ m.

[1] URL: https://www.newspacesystems.com/wp-content/uploads/2023/08/Aquila-SUN-SENSORS.pdf [cited on 18 June 2024]
[2] URL: https://invensense.tdk.com/products/smartindustrial/iim-46230/ [cited on 18 June 2024]
[3] URL: https://nl.mouser.com/ProductDetail/Murata-Electronics/SCA100T-D02-6?qs=qUsL5DZkYVoJ8j9QccGmeQ%3D%3D [cited on 18 June 2024]
[4] URL: https://www.nvidia.com/en-us/autonomous-machines/embedded-systems/jetson-agx-xavier/ [cited on 18 June 2024]
[5] URL: https://velodynelidar.com/products/puck/ [cited on 18 June 2024]
[6] URL: https://lightwarelidar.com/shop/lw20-c-100-m/ [cited on 18 June 2024]
[7] URL: https://www.intelrealsense.com/visual-inertial-tracking-case-study/ [cited on 18 June 2024]
[8] URL: https://exascend.com/product-category/pcie-gen-4/pr4/ [cited on 18 June 2024]

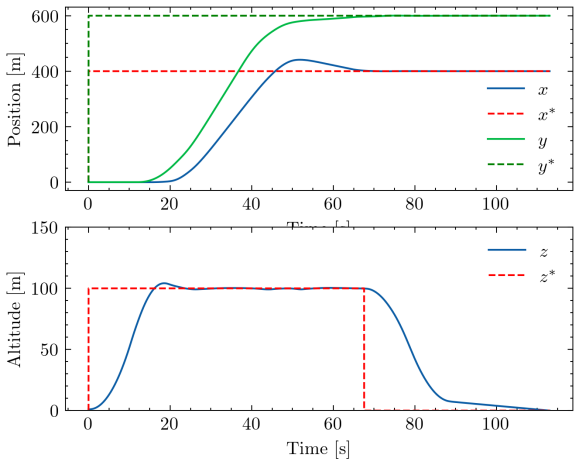

Figure 11.6: Altitude and position in a flight

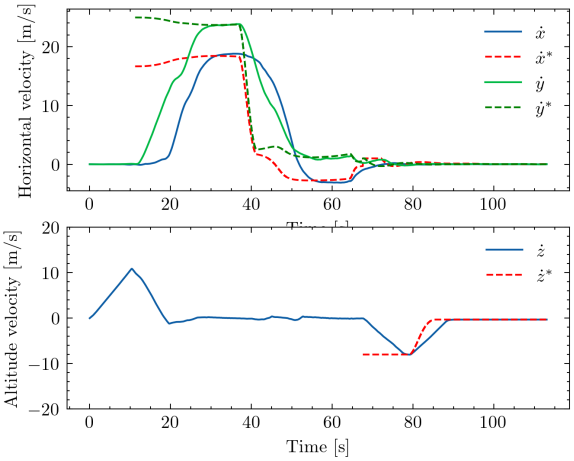

Figure 11.7: Horizontal and vertical velocity in a flight

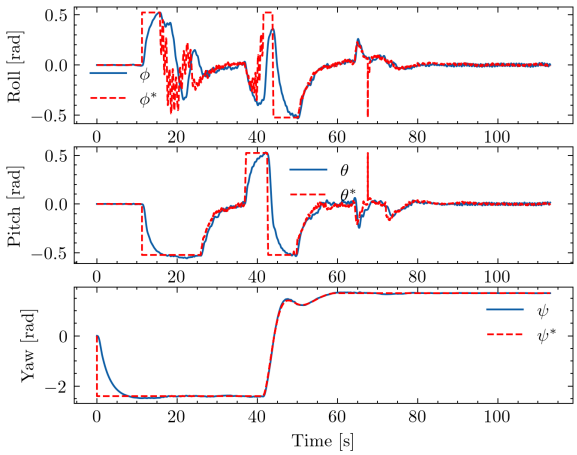

Figure 11.8: Flight angles in flight

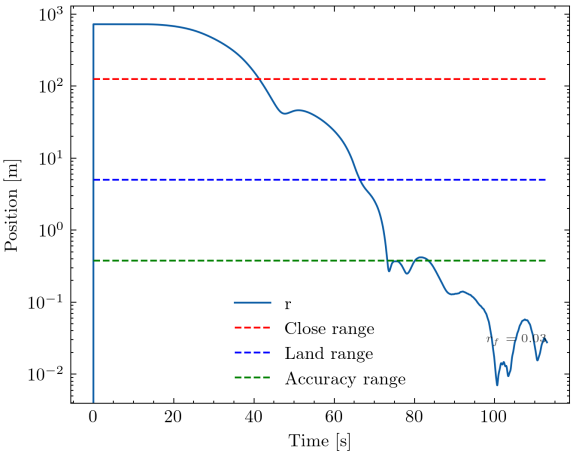

Figure 11.9: Radial distance in flight

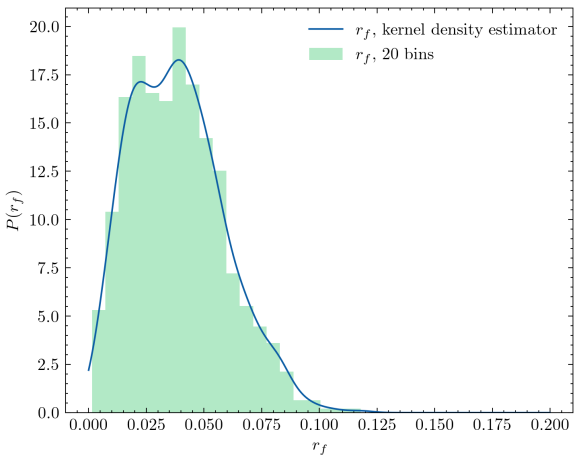

Figure 11.10: Histogram and KDE of landing distance from target

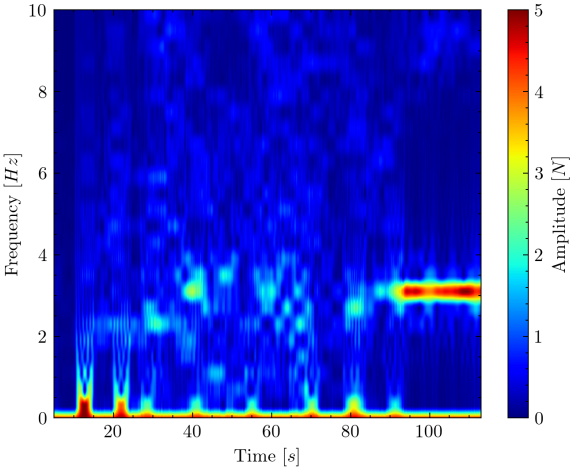

Figure 11.11: Thruster spectrogram

12 Payload Instrumentation

***Authors**: Diede*

The mission of our drone is to identify and acquire rocks on Mars, this makes the payload system an essential component for our mission. Without the payload, the drone would be no more than a technology demonstrator flying on Mars. In this chapter the design of the payload scanning and analysis subsystem is expanded upon, the grabbing arm design is discussed in Chapter 15.

First the requirements for the payload system are shown in Section 12.1, afterwards the methodology for designing the payload system is discussed in Section 12.2, the results are then shown and discussed in Section 12.3 and lastly the verification and validation of the design method is discussed in Section 12.4

12.1. Requirements

Stemming from the requirements derived during earlier stages in the design process, the payload subsystem shall comply with the following set of subsystem requirements:

Table 12.1: Relevant requirements for the Scanning Payload design, verification lead for all requirements is the Payload lead

ID	Requirement	Verification Method
PLD-SYS-04	The payload system shall be able to scan an area for suitable rock collection	Demonstration
PLD-SYS-04-01	The payload system shall be able to scan an area of 1 km^2 at a scan altitude of 75 m	Testing
PLD-SYS-04-03	The payload system shall be able to scan the area with a resolution of at least 5 cm at a scan altitude of 75 m	Demonstration, Analysis
PLD-SYS-04-04	The payload system shall be able to scan within an altitude range of 10 and 100 m	Analysis
PLD-SYS-06	The payload system shall be able to distinguish between different types of Martian rocks	Demonstration
PLD-SYS-06-01	The payload system shall be able to estimate the chemical composition of rocks	Demonstration
PLD-SYS-07	The payload system shall be able to identify the shape of the Martian rocks	Demonstration
PLD-SYS-07-01	The payload system shall be able to measure the dimensions of the Martian rock	Demonstration
PLD-SYS-07-02	The payload system shall be able to estimate the mass of the Martian rock	Demonstration
PLD-SYS-08	The accuracy of the rock identification algorithm shall improve over the operational lifetime	Demonstration
PLD-SYS-08-01	The rock identification algorithm shall be trained with feedback data provided from Earth on the relevance of previously collected and analysed samples	Demonstration

12.2. Methodology

In this section, the method for the scanning payload analysis is described. Firstly the selection for the spectrometer and camera are discussed in Section 12.2.1 and Section 12.2.2 respectively, the rock identification algorithm is then discussed in Section 12.2.3 and lastly the scanning performance is discussed in Section 12.2.4.

12.2.1. Spectrometer Selection

To perform a preliminary analysis on the rock sample, a spectrometer on the underside of the drone is needed. One of the most common ranges of the electromagnetic spectrum that is used for remote mineral analysis is the Visual and Near-Infra Red (VNIR) wavelength range (0.5 µm to 3.65 µm). As a basis for the spectrometer on the drone, multiple flight-proven spectrometers that operate in this range were compared, see Table 12.2. From these, the MicrOmega spectrometer was chosen since it was the lightest and least power-consuming. A cost could not be found for this specific spectrometer but is estimated to be in the order of €30 000. Since the sample will be underneath the drone, an artificial light source is needed to illuminate the sample, Tungsten-Halogen

[1] URL: https://science.nasa.gov/mission/mars-2020-perseverance/science-instruments/ [cited on 19 June 2024]

Table 12.2: A selection of flight-proven VNIR spectrometers namely LMS[53], SuperCam[1] , MicrOmega[12]

Model	Mass	Power
LMS (Chang'e 5&6)	5.6 kg	16 W
SuperCam (Perseverance)	5 kg	17.9 W
MicrOmega (Hayabusa 2, ExoMars)	1.8 kg	5 W

lamps are a good light source for this, since they produce white light. So additionally a light source was selected, see Table 12.3. Additionally, a UV light will be added, since UV-light can be very useful in rock identification, this one is very small and has low power usage, so it will be best to use it during nighttime.

Table 12.3: Tungsten-Halogen light source specifications [2] and UV-light specifications [3]

Model	Mass	Power	Cost
ThorLabs SLS201L	1 kg	9 W	€1090
UV light	0.1 kg	4 W	€20

12.2.2. Camera Selection

Before rock samples can be collected, they first need to be identified from altitude. To do this, cameras are needed that can scan an area at a high enough resolution to distinguish small objects such as rocks. Additionally, it can be valuable to get already some first idea of the chemical composition of the rock sample; this can be accomplished using a multispectral camera. A multispectral camera has filters that allow it to look at the light at specific wavelengths, usually within the visual and near-infrared spectrum [4] . From McKeown and Rice[9], four wavelengths were identified that are characteristic for some of the minerals that have been identified in the Eberswalde crater, these wavelengths are: 1.0 µm, 1.4 µm, 1.9 µm and 2.0 µm. The mass and power for the selected cameras can be seen in Table 12.4. These specific cameras were chosen as a baseline given their

Table 12.4: Mass and power for the selected RGB camera[5] [6] and multispectral camera[7] [8]

Type	Mass	Power	Cost
RGB Camera	0.14 kg	3 W	€1358
Multispectral Camera	0.26 kg	4 W	€6815

relatively low mass and power consumption, and their high performance. The actual camera will be designed in-house, during the later phases of the design process. These cameras, however, provide a good first indication and ideally put an upper limit on mass and power and a lower limit on the performance of the camera systems onboard the drone.

12.2.3. Rock Detection Algorithm

In order to process the visual data from the cameras and detect visual features on the ground, a rock detection algorithm needs to be used on board the drone, which can be seen in Figure 12.1. The potential for using algorithms to distinguish between different terrain types has already been proven using the camera on board Perserverance[9] . Although this AI was not yet perfect, it showed the potential for using machine learning for this type of identification, especially if more data is available. For our drone, much more data will be available, given that our drone will use an RGB camera supported by a multispectral camera. This first algorithm will be used to identify different types of terrain and soil from high altitude, in order to find the most interesting area(s) in the search area. When the smaller area is being scanned, the rock identification algorithm will identify individual rocks and determine their size and the type of rock. Algorithms for rock identification on Mars have been researched for some time since they are very useful for hazard avoidance[10]; however, trying to identify the lithology of rocks using algorithms has only become possible in the last years. One promising type of algorithm is single shot detection (SSD) algorithms since they are capable of performing real-time identification and

[2]URL: https://www.thorlabs.com/thorproduct.cfm?partnumber=SLS201L/M [cited on 14 June 2024]

[3]URL: https://www.bol.com/nl/nl/p/draagbare-blacklight-draagbare-blacklight-uv-lamp-met-led-zaklamp-vals-geld-detector-geocaching/9200000036383815/?referrer=socialshare_pdp_www [cited on 19 June 2024]

[4]URL: https://spectraldevices.com/collections/snapshot-multispectral-cameras [cited on 17 June 2024]

[5]URL: https://www.edmundoptics.eu/p/bfs-u3-50s4c-c-usb-31-blackflyr-s-color-camera/49878/ [cited on 17 June 2024]

[6]URL: https://www.edmundoptics.eu/f/c-series-fixed-focal-length-lenses/13679/ [cited on 17 June 2024]

[7]URL: https://spectraldevices.com/products/custom-camera [cited on 17 June 2024]

[8]URL: https://www.edmundoptics.eu/p/8mm-focal-length-lens-1quot-sensor-format/17859/ [cited on 17 June 2024]

[9]URL: https://www.zooniverse.org/projects/hiro-ono/ai4mars/about/results [cited on 17 June 2024]

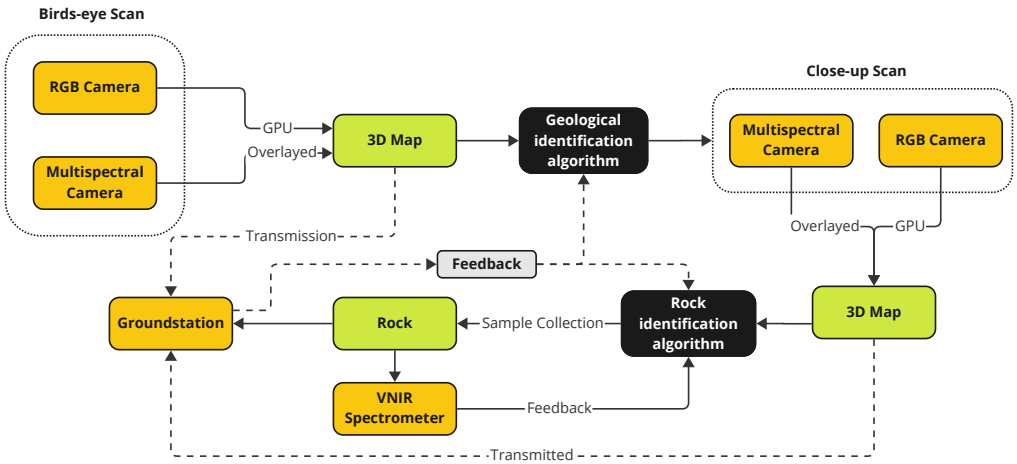

Figure 12.1: Flow diagram showing the general flow of the role of the rock detection algorithms within the mission profile.

localization of rocks within images[11], the exact purpose of our algorithm. The SSD developed by Zhenlong et al.[10] was able to achieve an accuracy up to 98.4 %. A similar algorithm could likely also be used on Mars, using images of previously identified rocks by current rovers, and since the geological features on Mars also exist on Earth, it might even be possible to train it on Earth as well.

12.2.4. Scanning Performance

In order to verify that the selected camera is actually performing as intended, the scanning path needs to be analysed. One important parameter to determine the spatial resolution of a camera is the Ground Sampling Distance (GSD), which can be calculated using:

$$GSD\ [mm] = \frac{w \cdot h}{FL \cdot rx} \cdot 1000 \tag{12.1}$$

Where w is the sensor width, h the scanning altitude, FL the focal length and rx the resolution in the sensor width direction, lastly the factor of 1000 is added to convert the GSD into mm. GSD determines the limitation on spatial resolution due to sampling. Another important parameter to keep in mind is the motion blur caused by the movement of the drone, this should always be lower than other distortions (in this case GSD), such that the images are sharp. It can be calculated using:

$$Motion\ Blur\ [mm] = V \cdot t_{exp} \cdot 1000 \tag{12.2}$$

Where t_{exp} is the exposure time of the camera.
Additionally it is important to quantify the scanning time, since this is determined by the flight profile, and this time should not be exceeded. This is calculated using:

$$t_{scan} = \frac{l_{area} N_{scan\_lines}}{V} \tag{12.3}$$

Where N_{scan_lines} is calculated using:

$$N_{scan\_lines} = \left\lceil 2 \cdot \frac{w_{area}}{w_{scan}} \right\rceil \tag{12.4}$$

Here w_{area}, the width of the scanning area, is equal to l_{area}, and w_scan is the width of the scanner, determined from the angular field of view of the camera, the factor 2 is added to make sure that there all areas are covered from two different horizontal positions. The $\lceil\ \rceil$ denotes a ceiling function, a functions that rounds the input up to the closest integer above it, this was used since it does not make sense to have a fractional number of scanning lines, as in reality this has to be an integer.

12.3. Results

Using the method described above, the selected cameras were analysed to determine if they perform sufficiently for the purposes of our mission. Two different scanning 'modes' were determined:

- Bird-eye: h = 75 m; V = 38 m s^{-1}; A_{scan} = 1 km^2
- Close-up: h = 10 m; V = 2.5 m s^{-1}; A_{scan} = 30 m^2

Using these parameters, combined with the selected cameras, the performance was analysed in Table 12.5.

Table 12.5: Performance RGB and multispectral camera

	Birds-eye		**Close-up**	
	RGB	*Multispectral*	*RGB*	*Multispectral*
GSD	45.7 mm	188 mm	6.09 mm	25.0 mm
Motion Blur	0.38 mm	0.84 mm	0.025 mm	0.055 mm
t_{scan}	289 s	421 s	36.0 s	48.0 s

Although it is difficult to confidently say that this level of performance will be adequate for the algorithm, it is assumed that this will be the case. The current resolution is sufficient since every point will be photographed at least twice; the images can be overlapped to increase the resolution of the mapping[54]. Next to this, the camera can be further developed to optimize its optical parameters for this mission.

12.4. Verification and Validation

To verify the calculations on the scanning payload, all equations that were used were seperately verified by performing the calculations by hand. Through this it was shown that the implementation of the formulas was done well.

In order to validate the code, data was taken from an existing drone, and fed through the program. The selected camera was that of the DJI Mavic 3M[10] , the used data was can be seen in Table 12.6. This camera was considered for use on the drone system, since it also included a multispectral camera, however no power and mass data were available for this camera system so it had to be discarded.

The value is calculated by plugging these variables into Equation 12.1. The resulting GSD was 58.2 mm, and the quoted GSD by DJI was 57.3 mm, the small difference can likely be explained by slight differences in the actual values used by DJI. This allows for the calculations performed for the GSD to be validated.

Table 12.6: Scanning parameters for validation

Parameter	h_{scan}	V_{scan}	A_{scan}	rx_{hor}	w	FL
Value	217 m	15 m s^{-1}	200 ha	5280 px	17.4 mm	12.29 mm

[10]URL: https://ag.dji.com/mavic-3-m [cited on 18 June 2024]

13 Communications

***Authors**: Diede*

Although the drone is capable of autonomous operations, the drone still needs to be able to communicate with Earth through the ground station. For this a communication system is necessary. The requirements that the communication system needs to comply with are shown in Section 13.1. In order to size the communication system, the data budget was calculated using the method from Section 13.2.1, and afterwards, the link budget was made using the method from Section 13.2.2. The results from these calculations are presented and discussed in Section 13.3, the verification of which is briefly discussed in Section 13.4.

13.1. Requirements

Stemming from the requirements derived during earlier stages in the design process, the communication subsystem shall comply with the following subsystem requirements:

Table 13.1: Driving requirements for the scanning payload design

ID	Requirement	Verification Method
COM-SYS-01	The communication system shall have a mass of at most 2.9 kg (TBC)	Inspection
COM-SYS-02	The communication system shall use at most 2100 W (TBC) of power	Demonstration, Testing
COM-SYS-03	The communication shall communicate with a ground station	Demonstration
COM-SYS-03-04	The communication systems shall have a downlink data rate of at least 10.1 Mbit s^{-1}	Testing
COM-SYS-03-05	The communication system shall have a signal-to-noise ratio of at least 1.01×10^9	Analysis

13.2. Methodology

This section expands on the method for the communication subsystem design. First, it explains how the data rate was calculated, and second, how the actual link budget was established.

13.2.1. Data Budget

To size the communication system, it is important to determine the data rate that the communication system will need to be able to handle. This is subdivided into the scientific data generated (mainly during the scanning phase) and the data generated by the GNC subsystem, with an additional factor to allow for any extra data that will have to be sent in the downlink. The assumption has been made that the uplink data rate is negligible for the sizing since the data rate, in this case, will be lower, and it will occur separately from the downlink. Therefore, this section only focuses on the downlink data rate.
The scanning data rate was calculated based on real-time communication, which is not what will occur during the mission, but it is a conservative assumption since, during the mission, the data is further compressed. The data rate for scanning is calculated using the formula:

$$DR_{scanning} = \frac{b_{px} N_{pxls} N_{pics}}{T_{transmission} CF} \tag{13.1}$$

Where b_{px} is the number of bits per pixel, N_{pxls} is the total amount of pixels per image, and N_{pics} is the number of pictures taken, determined from the scanning path. For the data generated from the GNC subsystem, the data rate was calculated using:

$$DR_{GNC} = \frac{DR_{gen} t_{mission}}{t_{transmission} CF} \tag{13.2}$$

Where DR_{gen} is the data rate at which data is generated by the GNC subsystem, $t_{mission}$ is the time of the mission (assumed to be the endurance time of 30 min), and $t_{mission}$ the mission time.

13.2.2. Link Budget

At first, the link budget was calculated using the equation for the received power-to-noise ratio:

$$\frac{C}{N_0} = P_t G_t \left(\frac{\lambda}{4\pi r}\right)^2 \frac{1}{L_a} \frac{G_r}{T_s} \frac{1}{k_b} \tag{13.3}$$

Here the factor of $\left(\frac{\lambda}{4\pi r}\right)^2$ was used for the propagation loss of the communication. Later it was discovered by Chahat et al.[13] that beyond a certain range determined by:

$$r \leq \frac{43}{{f_{MHz}}^{1/3}} \tag{13.4}$$

diffraction starts to occur, and communication becomes no longer feasible[13], using a UHF frequency of 914 MHz the maximum range is 4.4 km. This also means that the requirement STK-USER-07 cannot be complied with, as this has now been found to be infeasible. Instead of real-time communication, relevant data will be stored and transmitted to the ground station when the drone is within the communication range of 4.4 km A different way to calculate the propagation loss for ground-to-ground communication loss was also found in the same paper:

$$L_{FG}[\text{dB}] = -20\log_{10}(h_t h_r) + 40\log_{10}(r) \tag{13.5}$$

Here h_t is the altitude of the transmitting antenna (drone), h_r of the receiving antenna (ground station), and r is the distance between the drone and ground station. Since this formula is in decibels, it is necessary to convert it back out of decibels by applying the inverse formula: $x = 10^{x(\text{dB})/10}$. This meant that the new formula that was used was:

$$\frac{C}{N_0} = \frac{P_t G_t G_r}{L_{FG} L_a T_s k_b} \tag{13.6}$$

13.3. Results

First the data budget was determined from the previously discussed equations, next to this the data generated by the spectrometer was taken into account using the data per sample figure found from Leroi et al.[12]. For all data, a transmission time of 30 s was used, and from this, the data budget, as presented in Table 13.2, was generated.

Table 13.2: Data Budget

Data source	Data Rate
Scanning	4.64 Mbit s^{-1}
Sensor data	2.64 Mbit s^{-1}
Spectrometer	2.08 Mbit s^{-1}
Other	0.728 Mbit s^{-1}
Total	10.1 Mbit s^{-1}

Using the total data rate, the fact that $\frac{E_b}{N_0} \approx 100$ and the relation: $E_b = C/DR$ [31], a required power-to-noise ratio was determined of 1.01×10^9 . For the sizing of the communication system, the power required is of the most interest, so Equation 13.6 was rewritten to:

$$P_t = \frac{\frac{C}{N_0} L_{FG} L_a T_s k_b}{G_t G_r} \tag{13.7}$$

To see how the range then changes with respect to distance Figure 13.1 was created. From this figure, it can be seen that the required is very low, which is due to the low range and the low attenuation that occurs on Mars[1] . The parameters for the link budget that were used for Figure 13.1 can be found in Figure 13.2.

From the variables in Figure 13.2 and Figure 13.1 the required power at the maximum range of 4.4 km was found to be 0.29 W. Given the low power requirement, there was no need to increase the gains on the transmitter and receiver end, so it was decided that a monopole antenna would suffice for the drone communication. To

[1]URL: https://descanso.jpl.nasa.gov/propagation/mars/MarsPub_sec4.pdf [cited on 18 June 2024]

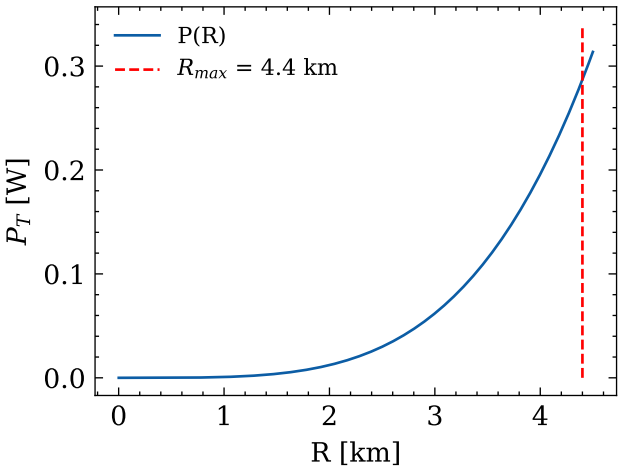

Figure 13.1: Required transmission power [W] as a function of Range [km], illustrating the maximum communication range of 4.4 km

Figure 13.2: Link budget parameters

Parameter	Values	Unit
$\frac{C}{N_0}$	1.01×10^9	-
G_t	1	-
f	914	MHz
G_r	1	-
L_a	1.00	-
T_s	550	K
R	[0 , 4.4]	km

size such an antenna it can be assumed that it should be at least a quarter of the wavelength of the signal. Given that $\lambda = c/f$, we get $l = \lambda/4$ =8.2 cm which was decided to be rounded up to 15 cm to estimate the mass conservatively. The mass was estimated to be ±210 g, using a density range from 7.87 g cm^{-3} to 8.07 g cm^{-3}, which corresponds to stainless steel[2] .

13.4. Verification and Validation

In order to verify the calculations, unit tests were performed to verify the implementation of the used formulas. To ensure that the performed calculation worked as expected, all calculations were double-checked by verifying the outcome of the equation with a hand calculation for one of the performed calculations, to ensure they would match. All these steps were passed by the program, and it was thus deemed verified.
Since the used equations were standard equations, the verification was deemed enough to also validate the program for the use cases in this report.

[2]URL: https://www.azom.com/properties.aspx?ArticleID=863 [cited on 19 June 2024]

14 Structures and Materials

***Authors**: Dionysis, Vini, Maurits*

In this section, the structural design of the system is developed. First, the requirements driving the structure are listed in Section 14.1. Afterwards, in Section 14.2, the methods behind the sizing of the various structures and the aspects of consideration are discussed. These include, among others, the tools used for optimization, the approach to material selection and other component-specific considerations. In Section 14.3, the resulting geometries of the designed components are presented. Finally, in Section 14.4, a brief discussion is provided regarding the verification and validation of the tools and the design.

14.1. Requirements

In Table 14.1, a set of important requirements that were vital for the structural are listed, along with their respective verification methods

Table 14.1: Requirements for the structural design

ID	Requirement	Verification Method
STR-SYS-01	The structure shall have a mass of at most 29.7 kg	Inspection
STR-SYS-02	The structure shall withstand the loads during operation	Demonstration
STR-SYS-02-05	The structure shall provide load paths	Analysis, Demonstration
STR-SYS-03	The spacecraft structure shall maintain structural stability during operations	Demonstration
STR-SYS-03-01	The spacecraft structure shall not deform plastically during operations	Demonstration
STR-SYS-03-02	The spacecraft structure shall not impede the functionality of other sections if deformed elastically	Demonstration
STR-SYS-08	The structure shall fit within the Mars 2020 aeroshell in a folded configuration	Analysis, Demonstration
STR-SYS-05	The shell shall shield the internal systems from the environment	Demonstration
STR-SYS-15	The bus shall provide mounting points for all hardware	Demonstration
STR-SYS-07	The structure shall withstand the loads during landing	Demonstration
STR-SYS-12	The landing structure shall absorb the impact created during the landing of the drone	Test
STR-SYS-13	The landing structure shall accommodate landing on a surface with a slope up to 15 degrees	Demonstration
STR-SYS-14	The landing structure shall accommodate take-off on a surface with a slope up to 15 degrees	Demonstration
STR-SYS-09	The rotor arms shall withstand the loads exerted by the rotor	Test
STR-SYS-11	The rotor arms shall not deflect more than 0.005 m	Test

14.2. Methodology

In this section, the design of the drone's structure is discussed. First, in Section 14.2.1, the general layout of the vehicle's structure and the sizing approach are presented. At this point, it is clarified what aspects of the structure are vital to the design. In Section 14.2.7, the relevant structural parts of the assembly are sized and optimized using the developed design tools. In Section 14.2.8, the methodology behind selecting suitable materials for each system part is elaborated upon.

14.2.1. Drone Structure Layout

The first step in the design process consisted of identifying the different structural components constituting the drone structure. The drone has been divided into three structural components. These are the bus, rotor arms

and landing struts. The bus is the main structure of the drone, hosting the payload and other subsystems. The rotor arms are the connection point between the bus and the rotors, while the landing struts are the structural connection between the ground and the bus. An overview of the components can be seen in Figure 14.1.

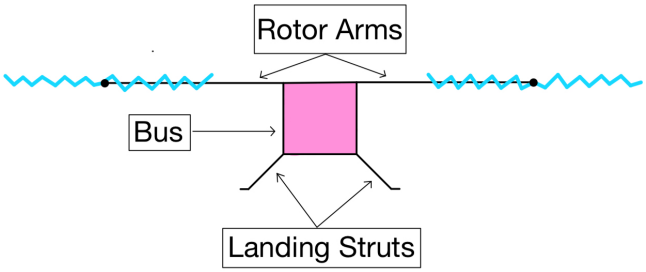

Figure 14.1: Drone structural overview

14.2.2. Sizing

At this stage, it is also important to identify the dependencies of the structure on other subsystems and the performance characteristics of the drone, which flows toward the initial sizing of the different structural elements.

Rotor Arms

The design of the rotor arms is driven by the propulsion system, as the rotor disks must be arranged such that they do not interfere with each other with an acceptable clearance and may not deflect more than a set value. The circular placement of the rotors around the bus structure, depicted in Figure 14.2, made it possible to calculate the arm length using Equation 14.1.

$$L_{\text{arm}} = \frac{D_{\text{centers}}}{2 \cdot \sin\left(\frac{\pi}{n_{\text{rotors}}}\right)} - R_{\text{bus}} \tag{14.1}$$

,where D_{centers} is the distance between two rotor centers evaluated using Equation 14.2, n_{rotors} is the number of rotors and R_{bus} is the radius of the bus.

$$D_{\text{centers}} = 2 \cdot R_{\text{rotor}} + \text{clearance} \tag{14.2}$$

where R_{rotor} is the radius of the rotor blades and clearance is the required clearance between two rotors. Using a Python script, it was possible to iteratively obtain the arm length based on the propulsion system's dimensions and the bus which was assumed to be cylindrical. The top view of the vehicle is also being generated for verification purposes and can be seen in Figure 14.2.

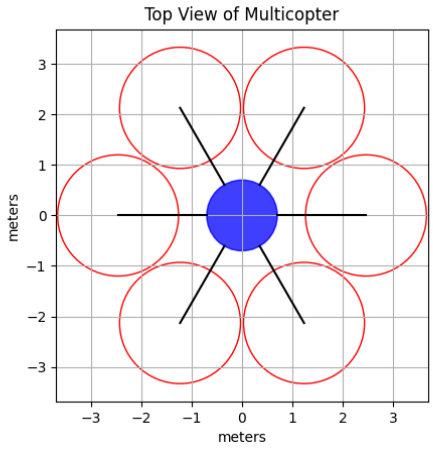

Figure 14.2: The top view of the Martian Drone as generated by the sizing script

Bus

As previously mentioned the drone bus is responsible for housing the battery and other electronics, creating attachment points for the rotor arms, and facilitating the placement of a solar array on top. However, as explained in Chapter 11 and Chapter 9, the electronic components to be placed inside the bus together with the required thermal management systems occupy a small volume. On the other hand, the radius of the bus directly affects the arm length. Since a smaller arm results in less weight and deformation, a middle ground had to be established for the radius of the bus. A larger bus also benefits the placement of the solar array, and it has thus been assumed for the sizing of the bus that 50% of the solar panel shall be supported by the bus. The bus radius can then be calculated using Equation 14.3.

$$R_{\text{bus}} = \sqrt{\frac{A_{\text{solar}} \cdot 0.5}{\pi}} \tag{14.3}$$

, where A_{solar} is the total solar panel area.

Landing Struts

The landing strut sizing is driven by requirement STR-SYS-13, which entails the landing on a sloped surface. While landing on a slope the landing struts need to ensure that the drone does not tip nor that the rotor blades touch the ground. In the case of tipping, the line of action of the drone weight can not surpass the contact point between the strut and the ground, this can be visualised in Figure 14.3. Thus the required strut width can be calculated using Equation 14.4 .

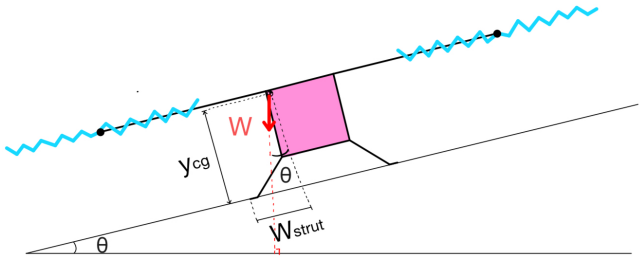

Figure 14.3: Tipping scenario on inclined surfaces

$$W_{\text{strut}} = \frac{\tan\left(\theta_{\text{slope}}\right) \cdot y_{\text{cg}}}{\cos 30} \tag{14.4}$$

, where θ_{slope} is the slope angle and y_{cg} is the distance from the ground to the centre of gravity. It is also assumed that the centre of gravity is located at the highest point in the structure, such that all centre of gravity locations are being designed for. In the case of landing on a slope, the struts need to extend a certain distance, such that the rotor blades do not come into contact with the ground while performing the landing manoeuvrer. This entails that the distance d between the tip of the rotor blade and the ground needs to be larger than zero, as can be visualized in Figure 14.4. The required strut width can be calculated using Equation 14.5.

$$W_{\text{strut}} = \frac{\frac{y_{\text{cg}}}{\tan\left(\theta_{\text{slope}}\right)} + L_{\text{Arm}} + R_{\text{rotor}}}{\cos 30} \tag{14.5}$$

,where L_{arm} is the length of the rotor arm, and R_{rotor} is the length of the rotor blade. As the landing struts

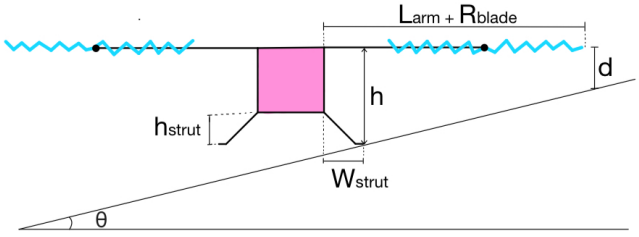

Figure 14.4: Landing manoeuvre

are positioned at the edges of a hexagonal structure, the required width needs to be divided by cos(30) to incorporate this design aspect. The total length of the strut is then evaluated using Equation 14.6.

$$L_{\text{strut}} = \sqrt{2W_{\text{strut}}^2 + h_{\text{strut}}^2} \tag{14.6}$$

where h_{strut} is the height of the strut.

14.2.3. Loading

In order to distinguish the type of loading for each structure, it is important first to create a Free Body Diagram containing all loads. In Figure 14.5a, Figure 14.5b, Figure 14.6 and Figure 14.5c the FBDs for the Rotor Arm, the Landing Strut, the Bus and the Rotor Blade can be seen respectively.

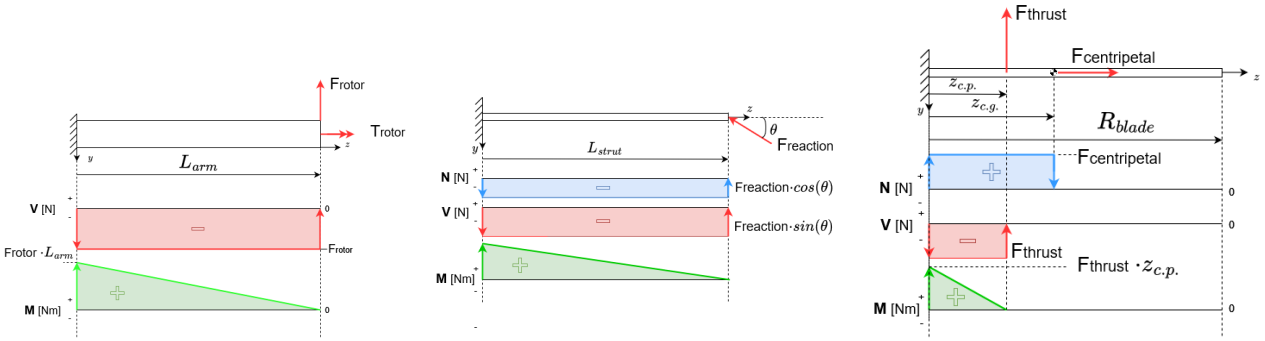

(a) Loading diagram of the rotor arm **(b)** Loading diagram of the landing strut **(c)** Loading diagram of the rotor blade

Figure 14.5: Loading diagrams

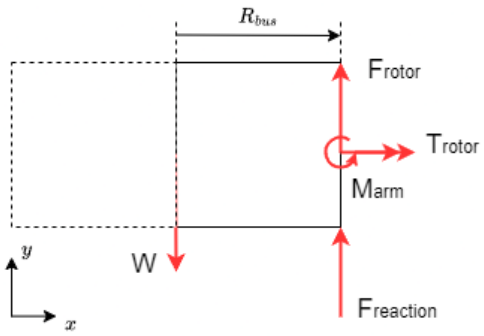

Figure 14.6: FBD of the bus

Based on the FBDs, the loading scenarios for each structure can be analysed.

- **Rotor Arms**
  The vertical force F_{rotor} at the tip of the arm is the resultant force of the thrust produced by the rotor blade. It causes the arm to bend upwards, around the x-axis. Additionally, an imbalance in the thrust distribution of the rotor disk, due to the advancing side of the blade experiencing a higher flow velocity, causes a torsional moment around the z-axis. Since there was no exact information regarding the torsional moment created by the rotor disk, a conservative assumption had to be made. It was assumed that at the most extreme situation, where the arm is aligned to the incoming airflow, the advancing half part of the rotor disk creates 50% more lift than the receding part. Additionally, it is assumed that the resultant of the thrust occurs at 75% of the blade radius. The torsional moment created by this imbalance can be calculated through Equation 14.7.

$$T_{\text{rotor}} = (F_{\text{adv}} - F_{\text{rec}}) \cdot 0.75 \cdot R = \frac{T_{\text{rotor}}}{5} \cdot 0.75 \cdot r \tag{14.7}$$

- **Landing Struts**
  The Landing Struts have to support the weight of the drone. The limiting condition for this occurs when the drone is tipping or performing a landing manoeuvre on a slope, at which point it is assumed that

two landing struts carry the total weight of the drone. By dividing the force into the axial and lateral components along the z- and y-axes, it can be seen that the beam is subjected to a compressive axial force and a lateral force, causing a bending moment about the x-axis.

- **Bus**
  The bus experiences the forces applied to it through the attached structures. The forces create concentration stresses at the attachment points. The objective is to size the thickness of the plate so that the stress does not cause the material to yield.
- **Rotor Blades**
  The rotor blades experience thrust and centripetal forces due to angular velocity. These forces cause bending and tension along the structure of the blade. As it is impossible to analyse the exact distribution of force over the rotor blades, it is assumed that the forces are applied as point forces through the structure's centre of gravity and the centre of pressure, respectively. Furthermore, the rotor blade is modelled as a thin, hollow rectangular beam. In reality, the geometry of the beam is quite complex and detailed Finite Element Method models should be created during the future development of the project

Further analysing the loads applied to the structures, the following load diagrams can be produced, as seen in Section 14.2.3

Simplifying the loading scenarios makes it easy to obtain the stresses and deformations with the following formulas.

- **Strain**
  A normal force applied to a beam causes it to elongate by distance δ which can be calculated through Equation 14.8.
  $$\delta = \frac{N \cdot L}{A \cdot E} \tag{14.8}$$
  The stress under this mode can be calculated through Equation 14.9
  $$\sigma = \frac{N}{A} \tag{14.9}$$
  where N is the normal force applied to the structure, L is the length of the structure, A the cross-sectional area and E the material's elastic modulus.
- **Torsional Deformation**
  The torsional deformation ϕ of a beam subjected to a torsional moment can be calculated through Equation 14.10.
  $$\phi = \frac{T \cdot L}{G \cdot J} \tag{14.10}$$
  where T is the torsional moment applied to the structure, G is the torsional stiffness of the material and J is the polar moment of inertia of the cross-section. The shear stress caused by the torsional force at a certain location on the cross-section can be calculated through Equation 14.11.
  $$\tau = \frac{T \cdot \rho}{J} \tag{14.11}$$
  where ρ is the distance from the centre of the shaft at the location of interest and J is the polar moment of inertia of the cross-section.
- **Bending Deformation**
  The deflection caused by a bending force applied at the tip of a cantilever beam is given by Equation 14.12[55].
  $$\delta = \frac{F \cdot L^3}{3 \cdot E \cdot I} \tag{14.12}$$
  where F is the force applied to the structure and I is the moment of inertia of the cross-section about the bending axis. The shear stress created by the force due to bending is given by Equation 14.13.
  $$\sigma = \frac{M \cdot y}{I} \tag{14.13}$$

where M is the moment caused by the force F at the root of the beam and y is the distance from the neutral axis.

- **Column Buckling** The critical compressive load under which a column buckles can be calculated through Equation 14.14 [56].

$$P_{crit} = \frac{n \cdot \pi^2 \cdot E \cdot I}{L^2} \tag{14.14}$$

where n is a parameter dependent on the boundary conditions of the structure. For a cantilever beam with an axial compressive force applied at its tip it has a value of 0.25.

14.2.4. Safety Factors

While sizing the structures, it is important to use the correct safety factors to ensure confidence in the design. The safety factors have been derived from NASA's *Structural Design and Test Factors of Safety for Spaceflight Hardware* technical standards [57]. According to those, the following safety factors have been used:

- **Yield design of metallic structures**: 1.25
- **Yield design of beryllium structures**: 1.4
- **Qualification factor of composite uniform materials**: 1.4

14.2.5. Pin Connections

Due to the limited dimensions of the Mars 2020 Aeroshell [20], which is the currently most suitable option to transfer the vehicle, a number of parts shall be folded into a stowed configuration. This can be performed with the use of lug hinges. For this reason, the effect of pin joints to stress shall be investigated. The general layout of a lug can be seen in Figure 14.7.

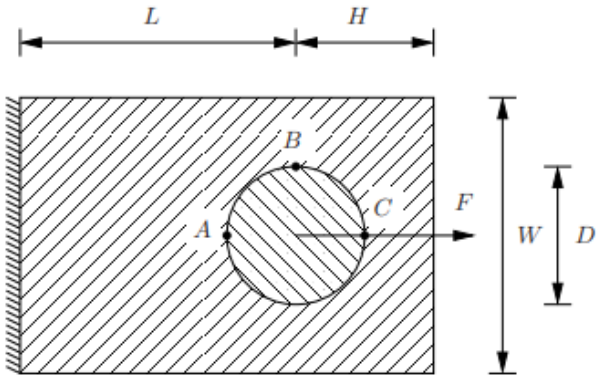

Figure 14.7: Dimensions of a lug with a circular pin [58]

The nominal stress created by a force F applied at such a joint can be calculated through Equation 14.15.

$$\sigma^n_{\text{nom}} = \frac{F}{(W - D) \cdot T} \tag{14.15}$$

where T is the thickness of the lug. The maximum principal stress in the section due to the load concentration can be calculated through Equation 14.16.

$$K^n_t = \frac{\sigma_{\text{max}}}{\sigma^n_{\text{nom}}} \tag{14.16}$$

where K^n_t is the experimentally obtained stress concentration factor which can be obtained through Figure 14.8.

14.2.6. Vibrations

As occurring vibrations during nominal operations may harm the structure's integrity, it is important to evaluate the natural frequencies of the structural components. It is assumed that the structural elements are supported during launch and reentry, and thus only the vibrations resulting from the rotation of the rotor blades are being analysed. As the bus and the landing struts are located far from the rotors, the vibrational effects are assumed to be negligible at these points. From Chapter 8 it follows that the motor operates in a rpm range of 0 to 1443, or 0 Hz to 24.05 Hz. From Figure 11.11 it follows that the control-induced oscillation has a maximum frequency of

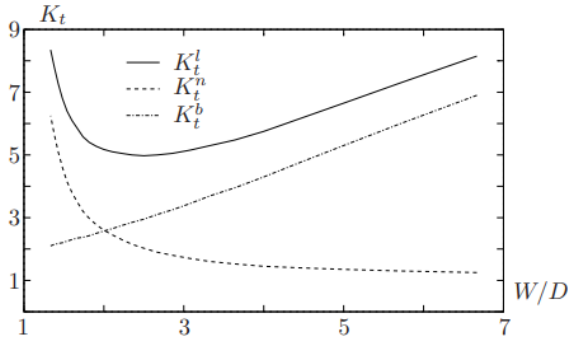

Figure 14.8: The stress concentration factors with respect to the ratio of W/D [58]

3.25 Hz, thus the rotor arm natural frequency needs to be far from this value. The rotor blades can be modeled by a uniformly distributed beam, and their natural frequency can be evaluated using Equation 14.17 [59].

$$f_{\text{nat}} = 0.560\sqrt{\frac{E \cdot I_{xx}}{m_{\text{blade}} \cdot R_{\text{blade}}^3}} \tag{14.17}$$

As the rotor arms are uniformly distributed beams with a point pass at the tip, their natural frequency can be evaluated using Equation 14.18 [59].

$$f_{\text{nat}} = 0.276\sqrt{\frac{E \cdot I_{xx}}{m_{blade} \cdot L_{\text{arm}}^3 + 0.236 \cdot m_{\text{arm}} \cdot L_{\text{arm}}^3}} \tag{14.18}$$

In addition to the manual calculations, FEM Modal analysis will be used to determine the natural frequencies for the different vibrational modes, and the participation factors corresponding to different types of excitations.

14.2.7. Design Tools

For structural design and optimization, several design tools have been developed around a beam analysis class. The class is responsible for the creation of a beam object and the assignment of all properties relevant to the analysis, such as the mass and the moments of inertia. These properties are then used to compute the resulting deformations and stresses on the beam. A flow chart for the beam class can be seen in Figure 14.9.

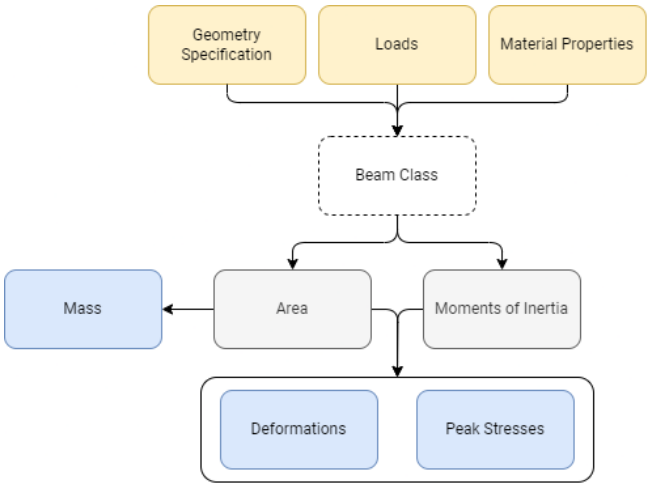

Figure 14.9: Flow chart of the beam class

Cross-Section Design Space

The first tool concerns the selection of a suitable cross-section for the beam-like elements of the structure, such as the rotor arms and the landing struts. For such structures, the objective is to minimize mass, deflection, and angular deflection. For this purpose, a Python script tool was created, capable of providing the design space for

different types of cross-sections. A flow chart for the cross-section tool is presented in Figure 14.10.

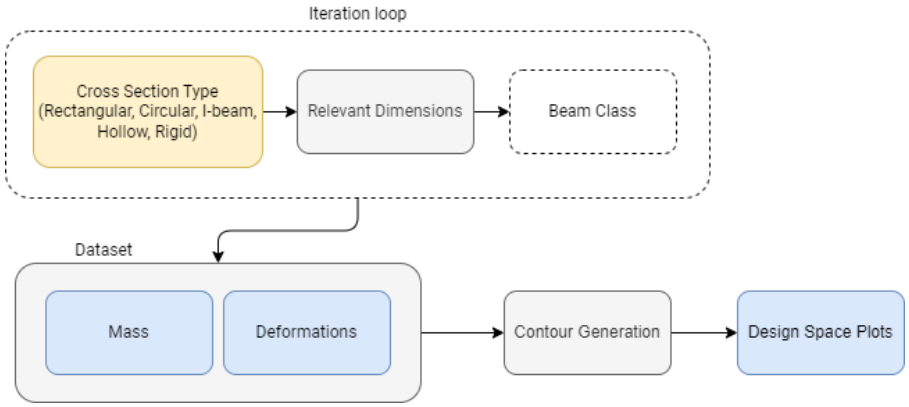

Figure 14.10: Flow chart of the cross-section tool

As seen in Figure 14.10, the tool takes as input the five types of cross-section geometry, rigid and hollow rectangle and circle, and I-beam. For each type of cross-section, the tool iterates through all the relevant dimensions, such as height, width, thickness, or web and flange thickness for rectangular cross-sections and radius and thickness for circular cross-sections, and stores the mass, directional, and angular deformation for each configuration. Some upper limits for mass and deformation are established to eliminate unrealistic options. Plotting the contour assumed by all the generated data points makes it possible to obtain the design space for all cross-section types regarding mass and deflection. This provides an idea about the mechanical capabilities and limits of each cross-section. The Deflection-Mass and Angular Deflection-Mass plots, which are relevant for this situation, can be seen in Figure 14.11a and Figure 14.11b respectively.

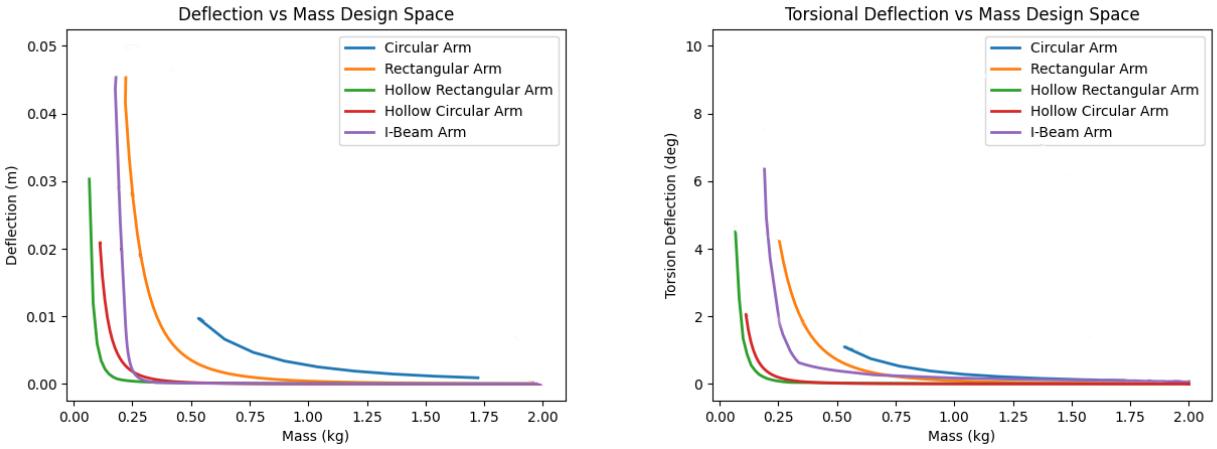

(a) Deflection-mass design space for all cross-sections

(b) Angular deflection-mass design space for all cross-sections

Figure 14.11: Design spaces for different cross-sections

The objective is to select the cross-section with the lowest limits, which means that both parameters can be minimized effectively.

Cross Section Optimization

After the cross-section type has been selected, an optimization tool has been developed further to specify the exact geometry and material of the beam. The functional flow diagram of this tool can be seen in Figure 14.12.

As can be seen in the diagram, the tool uses as input the selected cross-section, the loads applied to the beam, a range of suitable materials, which is explained further in Section 14.2.8, as well as the performance requirements for the structure. The material and geometry are iterated with sufficient resolution, resulting in a data frame of feasible configurations. Feasible configurations are defined as all configurations that adhere to a maximum weight and deflection value while not exceeding the material yield strength within an appropriately selected safety margin [57]. To select between the available configurations, a weighted trade-off is performed with respect

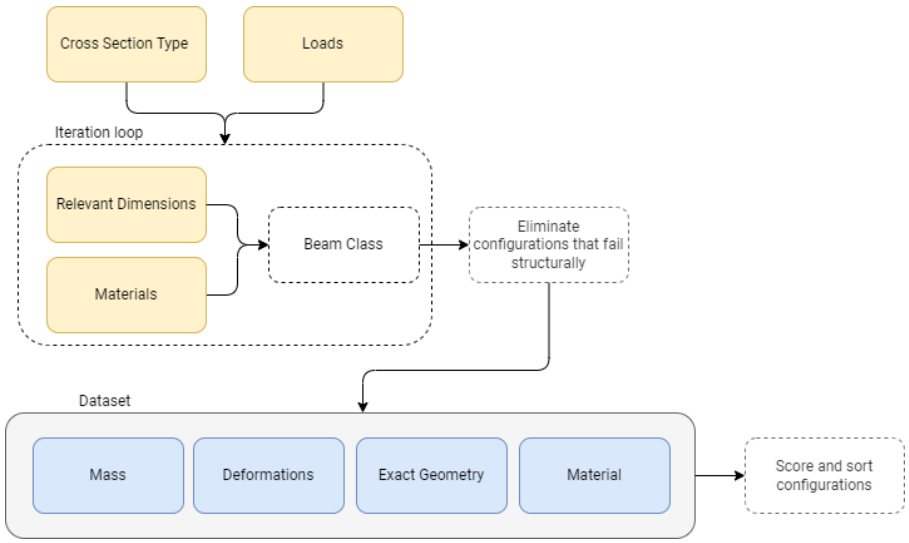

Figure 14.12: Functional flow diagram for the beam optimization tool

to the structure's weight, the values of directional and torsional deformation of the structure and the material's embodied energy. After specifying the corresponding weights, the tool outputs the winning configuration.

14.2.8. Material Selection

For the propeller arm, landing struts and drone bus the Ansys Granta EduPack software with the aerospace materials database was used to select the most optimal materials. Within the software, three charts were created to analyze important material indices. Firstly, the material yield strength was plotted against the density. This chart allows for material selection primarily focused on lightweight, high-strength materials which can carry greater forces without failure. Secondly, a similar chart was made for Young's modulus against density, to analyse lightweight, high stiffness materials, that limit deflection. Lastly, a plot of the embodied energy vs the CO_2 production was created to take environmental sustainability into account, in the case of tiebreakers.

Furthermore, limits were set on both the yield strength and Young's modulus to exclude any unsuitable materials based on the requirements. With all this setup, material indices were chosen and maximized to optimize the structure of the drone. An example of such a plot can be found in Section 14.2.8, which shows the plot of the Young's modulus against the density, has limits set on the Young's modulus and yield strength and is optimizing for $\sqrt{E}/\rho$.

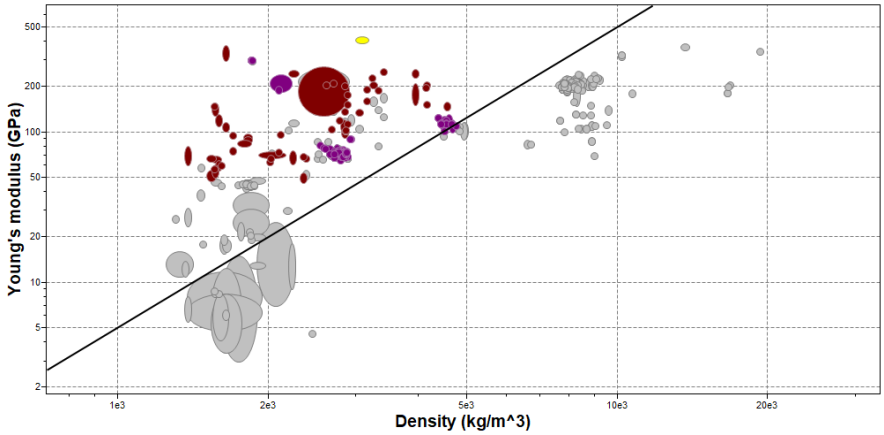

Figure 14.13: Example of a material selection chart, for Young's modulus against density. Limits are set on the Young's modulus ($\geq$ 100 GPa), and the yield strength ($\geq$ 100 MPa), and is optimizing for $\sqrt{E}/\rho$ depicted by the straight black line

Propeller Arms and Landing Struts

To start the material selection limits were imposed on the Young's modulus and yield strength according to the desired performance. After imposing these limits there were still a lot of feasible materials available. Therefore

the team set out to maximise the specific stiffness. Since the propeller arms and landing struts are beams or struts, this means that $\sqrt{E}/\rho$ [60, p.418] had to be maximised. The four optimal materials found through this method are summarized in Table 14.2 below. These materials were fed back into the optimizer tool to find the best cross-section and material combination. From this, it was found that Beryllium was optimal for lightweight beams, regardless of its high embodied energy.

Table 14.2: Final material selection optimized for lightweight beams and shafts

Material	Density [kgm^{-3}]	Young's modulus [GPa]	Yield Strength [MPa]	Embodied Energy [MJkg^{-1}]	Price [€kg^{-1}]
SiC/SiC fiber, 35-45Vf, QI laminate	2300 – 2900	179 – 259	208 – 249	132 – 146	2900 – 5120
Alumino silicate/Nextel 720. QI laminate	2450 – 2600	133 – 139	67.9 – 68.8	34.8 – 38.4	4930 – 5900
Beryllium, grade SR-200, sheet, 0.5 mm to 6.35 mm thick	1840 – 1860	290 – 315	340 – 450	6080 – 6700	571

Drone Bus and Rotor Blade

The material selection for the drone bus and rotor blade was a little more arbitrary. Since the forces acting on the section were not entirely known and difficult to model, the team set out to maximize both the specific stiffness and specific strength to ensure the best material was selected. The material indices to maximize are given as $\sqrt[3]{E}/\rho$ [60, p.418] for the stiffness and $\sqrt{\sigma_f}/\rho$ [60, p.420] for the strength since both systems can be modelled as flat plates. This analysis found that Cyanate ester/HM carbon fibre, UD prepreg, and QI lay-up were the best-performing materials in both indices. It has to be noted that other composites did show a better specific performance but did not have the quasi-isotropic property. These were excluded as they would not perform sufficiently well in a direction perpendicular to the fibres. The properties of the selected composite can be seen in Table 14.3.

Table 14.3: Cyanate ester/high modulus carbon fiber properties

Property	Values	Unit
Density	1620 – 1670	kg m^{-3}
Young's Modulus	101 – 115	GPa
Yield Strength	607 – 738	MPa
Embodied Energy	725 – 799	MJ kg^{-1}
Price	196 –219	€ kg^{-1}

14.3. Results

In this section, the design for each structural component is elaborated, and the final results are presented. All inputs have been taken from the last performed iteration.

14.3.1. Rotor Arms

The first value, determined in the design of the rotor arms, was the arm length. From Chapter 8, it follows that the blades shall have a radius of 1.2 m, a clearance of 5 % of the blade radius, and produce a maximum thrust of 45.14 N. On top of that, a safety factor of 1.5 was used, resulting in a value of 67.71 which was used for sizing. Using Equation 14.7, T_{rotor} was calculated to be 12.63 N m

In the bus design section, it was determined that the optimal bus radius was 0.7 m. Plugging these values into Equation 14.2 and Equation 14.1, results in a required length of 1.76 m. As shown earlier through the loading diagram of the rotor arm, the beam is subjected to a torsional and a transverse force at the tip. These result in the following reactions at the root:

- A bending moment

$$M = F_{\text{rotor}} \cdot L_{\text{arm}}$$

- A shear force

$$V = F_{\text{thrust}}$$

- A torsional moment around the axis through the beam

$$T = T_{\text{rotor}}$$

From the design space created by the cross-sectional design space tool, as seen in Figure 14.11a and Figure 14.11b, it was determined that a hollow rectangular cross-section performs best for both deflections caused by bending and angular deflection. Therefore, a hollow rectangular cross-section is selected and optimized for the rotor arm.

In this case, the optimization software creates a beam with length 1.76 m. The parameters related to the cross-section to be iterated are the inner and outer height, as well as the inner and outer width. The material is iterated on, ranging between the two Beryllium alloys and the two Composites described in Section 14.2.8. The script checks the deformations for each cross-section iteration and material combination and ensures that the maximum normal and shear stresses which occur at the root of the arm do not cause the material to yield when multiplied with a safety factor of 1.5. The optimization process resulted in a final cross-section, with a wall thickness of 1 mm, an outer width of 4 cm and an outer height of 6 cm. Out of the four potential materials, beryllium offered the lightest beam, with a total mass of 0.638 176 kg. Applying Equation (14.18) results in a natural frequency of 16.32 Hz, exceeding the control induced oscillation of 3.25 Hz. The final design properties are summarized in Table 14.4.

Table 14.4: Rotor arm specifications

Parameter	Value	Unit
Material	*Beryllium*	-
Cross-section type	*Hollow Rectangular*	-
Outer height	60	mm
Inner height	58	mm
Outer width	40	mm
Inner width	38	mm
Mass	0.638	kg
Max. stress	35	MPa
Max. deflection	4	mm
Max. angular deflection	0.076	deg
Natural frequency	16.32	Hz
Material cost	2185.8	€

14.3.2. Landing Struts

For the final drone design, the distance between the ground and the bus has been assumed to be 50 cm.With a bus height of 20 cm, the assumed center of gravity location y_{cg} is equal to 0.7 m.From STR-SYS-13, the maximum slope for which the landing struts need to be designed is 15°. From Equation 14.4, and Equation 14.5,the required strut widths are 0.216 m and 0.401 m respectively. As the required width for landing is higher than for tipping, this distance distance becomes driving. To minimize the mass of the landing struts, they are attached at the lower side of the bus, the total length following from Equation 14.6, is then 0.756 m. Similar to the rotor arms, the hollow rectangle is the most optimal cross-section, following from the cross-sectional design space tool. It is assumed that in the case of tipping, the total weight of the drone is carried by two struts, thus each strut needs to withstand a force of 90.3432 N.To ensure this tipping scenario, six landing struts need to be attached to the bus structure. With these loads, the cross-sectional optimization tool determined that a wall thickness of 1mm, an outer width of 15 mm, and an outer height of 15 mm to be optimal. The final design properties are summarized in Table 14.5.

14.3.3. Bus

In Chapter 9, the required solar array area was determined to be 3.02 m^2, thus from Equation 14.3, it follows that the bus shall have a radius of 0.7 m. The bus was modelled as a hexagonal structure with thin plates on the sides held together by thin plates at the top and the bottom, as seen in Figure 16.5f. Due to the complicated boundary conditions, it is impossible to simplify this structure as a whole by applying simplified mechanics of materials formulas. However, whether the side plates can support the shear force created by the rotor arms can be established. The torsional load T_{rotor} can be neglected as it produces negligible stresses for the rotor arms, which would have an insignificant effect on a large plate. Based on the outer width of the rotor arm of 40 mm

Table 14.5: Landing struts specification

Parameter	Value	Unit
Material	*Beryllium*	-
Cross-section type	*Hollow Rectangular*	-
Outer height	15	mm
Inner height	13	mm
Outer width	15	mm
Inner width	13	mm
Length	0.7564	m
Mass	0.078 363	kg
Max. stress	250	MPa
Max. deflection	20.2	mm
Material cost	268.5	€

and a starting thickness of 1 mm, the shear stress through the plate at the connection point can be calculated as follows:

$$\sigma = \frac{F}{A} = \frac{V}{40 \cdot 1 \cdot 10^{-6}} = \frac{67.71}{40 \cdot 10^{-6}} = 1692750Pa$$

or 1.69 MPa. Therefore, a thickness of 1 mm is already conservative, however, it contributes to the calculation of the mass of the bus, with a high confidence that the final design of the bus will be lighter. The currently established properties and dimensions of the mass can be seen in Table 14.6.

Table 14.6: Bus structure specification

Param	Value	Unit
Material	*Cyanate Ester/CF*	-
Shape	*Hexagonal*	-
Radius	0.7	m
Plate height	20	cm
Plate length	80.8	cm
Plate thickness	1	mm
Total mass	3.64	kg
Material cost	797.16	€

14.3.4. Rotor Blade

Similarly to the research performed for the Martian Science Helicopter [21], the rotor blades consist of a thin composite layer and a foam core. Since the composite is the main load-carrying structure, this section focuses on sizing it. Using the results obtained through the aerodynamic analysis of the rotor blade in Chapter 8, it was possible to create an exact model of the blade using the 3DEXPERIENCE CAD environment. A render of the model can be seen in Figure 14.14a. During aerodynamic design, the blade's structural aspect was considered by opting for a thick root section that could handle the aerodynamic loads.

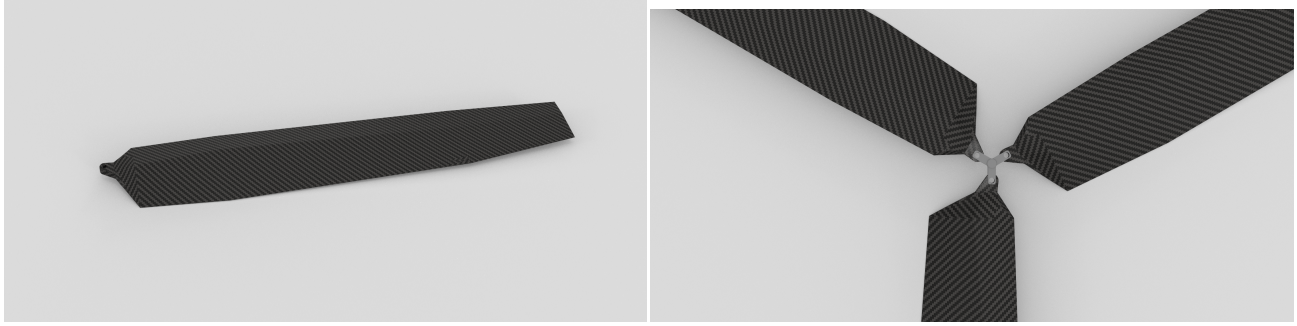

(a) A render of the rotor blade model produced through 3DEXPERIENCE

(b) Rotor blades attached to the hub

Figure 14.14: Rotor blades arranged in the hub

As explained in Chapter 8 the blade consists of 4 different airfoils arranged in stations along the length of the blade, starting at 8%. The surface is extrapolated between the stations. Between 0% and 8%, a simple hinged

structure has been implemented to allow the blade to fold during transport, as seen in Figure 14.14b. In reality, a more complicated mechanical system shall be implemented, allowing the blade to lock in place when deployed. The main objective of the design process for the blade structure is to determine the minimum thickness required for the blade to be able to withstand the tensile load created through the centripetal force. Through analysis of the CAD model, it was possible to acquire the centre of mass of the blade, where the centripetal force is assumed to be applied. The cross-section at that location, which for the final iteration of the blade lies at $537mm$ from the centre of the hub, can be seen in Figure 14.15.

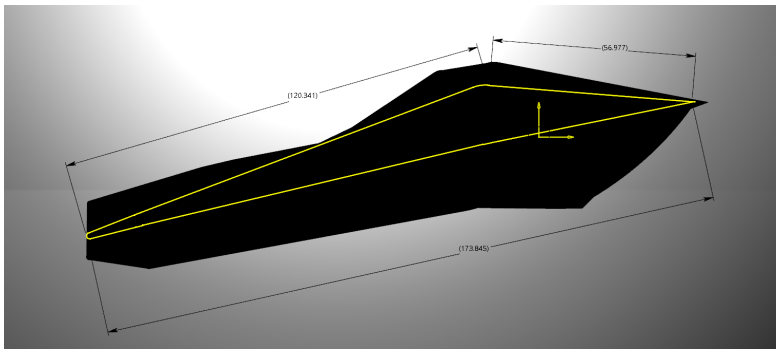

Figure 14.15: The cross-section of the rotor blade at the c.g. location

As explained in Section 14.2.8, the best material option for the blade is the Cyanate Ester/High Modulus Carbon Fiber composite. The calculations performed assume isotropic behaviour. The centripetal force applied to the cross-section can be calculated through Equation 14.19.

$$F_{\text{centripetal}} = m \cdot r \cdot \omega^2 = 0.076 \cdot 1.2 \cdot 151.1^2 = 2082.2 \text{ [N]} \tag{14.19}$$

It can be seen through Equation 14.19 that the centripetal force is related to the mass, which can be only obtained if an initial thickness is assumed. The stress through the cross-section can then be computed as follows through Equation 14.20.

$$\sigma = \frac{N}{A} = \frac{F_{\text{centripetal}}}{\text{perimeter} \cdot t} = \frac{2082.2}{250 \cdot 10^{-3} \cdot 0.1 \cdot 10^{-3}} = 59.49 \text{ [MPa]} \tag{14.20}$$

By manually iterating through values with increments of 0.05 mm, the new mass could be obtained through the CAD model, and the stress could be computed. Through this method it was determined that the value of 0.1 mm was already sufficient to support the load. It is also important to obtain an idea regarding the stress concentration at the pin connection. The approach for the design of the lug is once again experimental and was performed with the help of 3DEXPERIENCE. The diameter of the pinhole was set to 10 mm. By looking at the top curve Figure 14.8, it can be seen that the stress concentration coefficient obtains a minimum value of 5 for a W/D ratio of approximately 2.5. Based on that, the width of the lug was set to 26.8 mm, as this accommodated the connection with the root of the aerodynamic part of the blade. Using the formulas described in Section 14.2.5, the peak stress can be calculated. Again, the resulting stresses are well within the capabilities of the material. At this stage of the project, it is not needed to delve further into the structural analysis and optimization of a highly specific connection. Applying Equation (14.17) results in a natural frequency of 19.2 Hz, which is within the rotational frequency range of the motors. However, as will be explained through the FEM results in Section 14.4.2 is not currently clear whether the frequency of the motors is capable of triggering this vibrational mode. It should also be noted that the effect of a foam core is not considered at this stage. It is possible that slight structural modifications could raise sufficiently the natural frequency of the flapping mode. The resulting parameters of the blade are summarised in Table 14.7.

14.4. Verification and Validation

The following section focuses on the verification and validation performed on the design tools used to size the structural components. This plays a vital role in ensuring the correctness of the obtained results. First, in Section 14.4.1 the general approach to verifying the design tools is approached. Afterwards, in Section 14.4.2, the approach to verification using Finite Element Method analysis is discussed.

Table 14.7: Rotor blade specifications

Param	Value	Unit
Material	*Cyanate Ester/HM CF*	-
Cross-section type	*Variable*	-
Length	1.2	m
Thickness	0.1	mm
Pin diameter	10	mm
Lug width	26.8	mm
Mass	76	g
Max. stress	59.49	MPa
Max. lug stress	38.7	MPa
Natural frequency	19.2	Hz
Material cost	299.6	€

14.4.1. Verification

The design tools have been verified by performing back-of-the-envelope calculations using the Math CAD platform[1] . After the optimization script outputted a resulting configuration for a beam structure, all the intermediate and final values were manually calculated. This ensured that the optimization script calculated the properties and the performance characteristics of the beam correctly. Additionally, various code integration tests were performed, to ensure that the optimization algorithm was generating the required range of configurations and was properly grading them to come to the optimal solution.

14.4.2. Validation

To ensure the validity of the design of the various structural components, Finite Element Method (FEM) analysis was performed using the ANSYS Static Structural tool. For this purpose, the modelled components were first exported from 3DEXPERIENCE as *.step* 3D objects. They were then imported to ANSYS, meshed with emphasis on critical points and edges, and the appropriate materials, boundary conditions and loads were imposed. A deformation and stress analysis was performed for all parts to ensure that the maximum deformations and stresses were within a reasonable margin from the predicted values.

Rotor Arm FEM Results
Static Structural Analysis

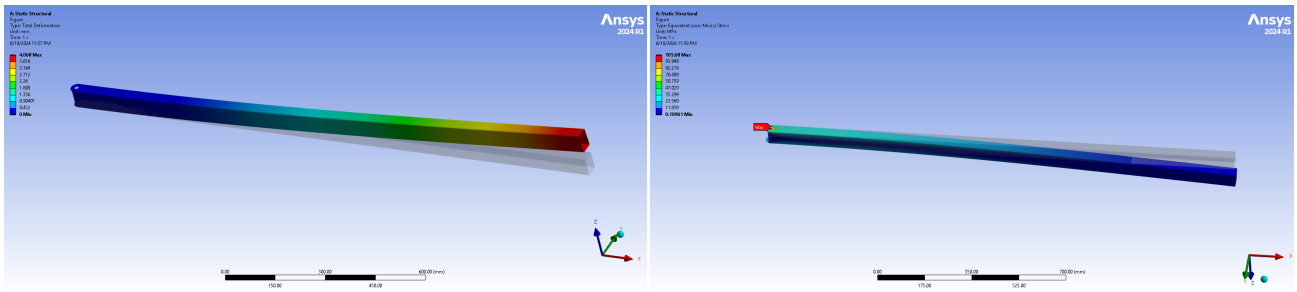

(a) Total deformation result of Rotor Arm FEM (Scale = 18)

(b) Equivalent stress result of Rotor Arm FEM

Figure 14.16: FEM simulation of the rotor arm

As can be seen through Figure 14.16a, the maximum deformation at the tip of the beam due to the combination of the bending and torsional deformations is 4.068 mm. This is on par with the 4 mm deflection computed by the sizing tool. With regards to the stresses, it can be seen in Figure 14.16b that a maximum stress of 105.68 MPa occurs at the pin connection on the constrained end of the beam. This was anticipated, due to the stress concentration that occurs on such a joint. In that case, the stress concentration factor K_t would be equal to $K_t = 105.68/35 = 3.02$, which is quite a low value, considering Figure 14.8.

Dynamic Analysis

After a static structural analysis is performed, the meshed geometry and the results can be used to perform

[1] URL: https://www.mathcad.com/ [cited on 18 Jun 2024]

a dynamic analysis of the structure. In Table 14.8, the natural frequencies for the top 6 modes as well as the participation factor in all directions can be seen.

Table 14.8: Modal frequencies and participation factor results for Rotor Arm

Mode	Frequency (Hz)	X Direction	Y Direction	Z Direction
1	10.76	1.82E-07	4.21E-02	-1.74E-05
2	16.387	-1.14E-04	1.73E-05	4.19E-02
3	153.27	-7.45E-07	1.27E-02	4.42E-06
4	231.09	1.78E-04	-4.19E-06	1.28E-02
5	489.66	-7.87E-06	6.83E-03	1.19E-05
6	706.33	4.07E-02	-3.55E-06	2.62E-03

The participation factor indicates how a force in the corresponding direction can trigger the specific vibrational mode. We can see that forces in the Z Direction can excite the 2nd and 4th modes. The 2nd mode has a natural frequency of 16.387 Hz, which is in line with the manual calculation results presented in Section 14.3. The maximum deformation that can occur if this mode is triggered can be seen in Figure 14.17 and amounts to 25 mm. However, as explained earlier, this mode is not expected to be triggered during regular operation.

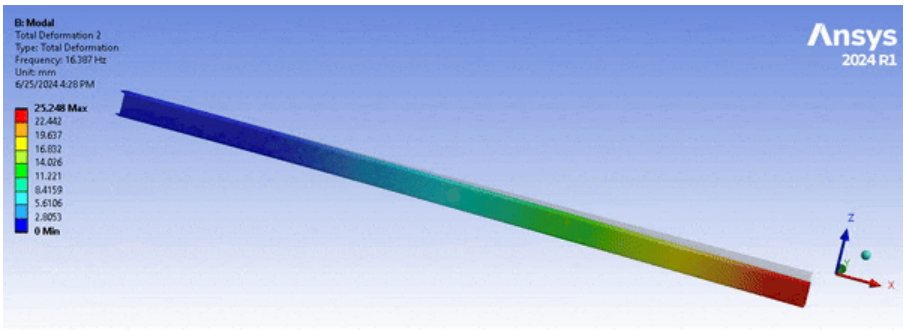

Figure 14.17: Animation of rotor arm vibrating under 2nd mode (click to watch)

Landing Strut FEM Results

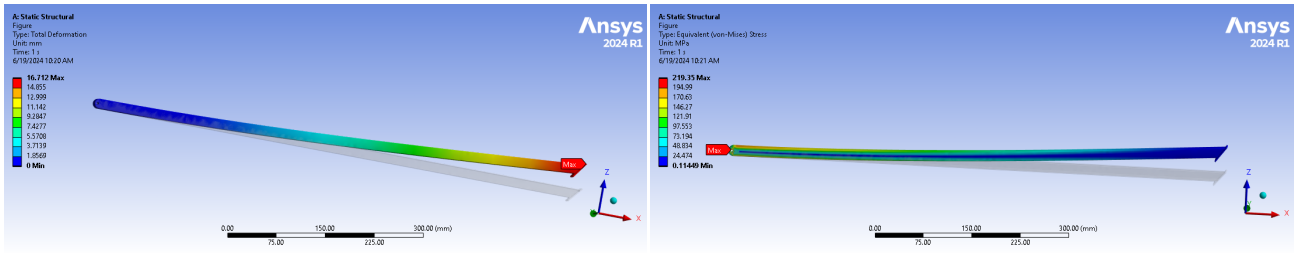

(a) Total deformation result of the rotor arm FEM (Scale = 2.8)

(b) Equivalent stress result of the landing strut FEM

Figure 14.18: FEM simulation of the landing strut

The deformation and stress results of the FEM analysis of the landing strut can be seen in Figure 14.18a and Figure 14.18b respectively. The maximum deformation value recorded by the simulation is 16.7 mm, which is slightly different than the calculated value of 20 mm. This discrepancy can be attributed to the slightly different geometry of the landing strut model compared to the simple beam assumption used in the model. Additionally, a cylindrical connection is used as a boundary condition in the FEM model, which has introduced discrepancies in the maximum stress. As can be seen through Figure 14.18b, the maximum stress reaches a value of 219.35 MPa at the face of the cylindrical joint. This is because the cylindrical face is loaded in torsion to withstand the rotation of the strut. In reality, a more complex mechanism would constrain the landing strut from rotating past the maximum angle, therefore eliminating the stress from the cylindrical face.

Rotor Blade FEM Results

Performing a FEM analysis on the rotor blade proved to be more complicated due to the complexity of the geometry. Meshing proved to be difficult for the thin structure of the blade, and creating a point load to

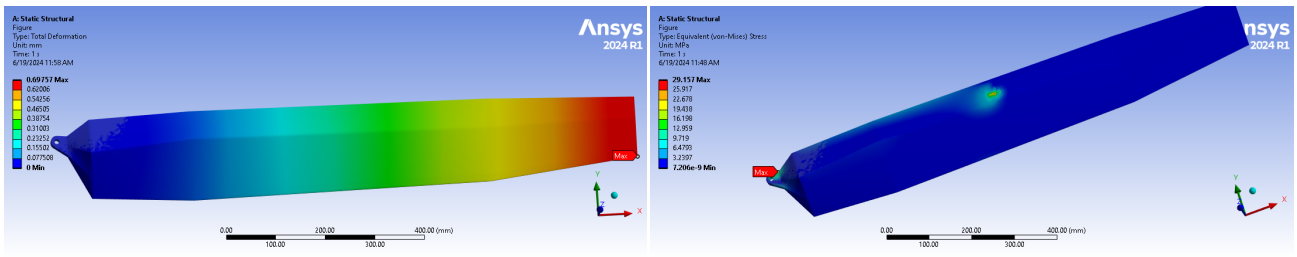

(a) Total deformation result of the rotor blade FEM (Scale = True)

(b) Equivalent stress result of the rotor blade FEM

Figure 14.19: FEM simulation of the rotor blade

represent both of the centripetal and thrust forces introduced singularities. However, it can be seen that the resulting deformation of 0.67 mm and the maximum stress of 29.157 MPa is well within the limits of the material. However, it should be noted that during operation the maximum deflection is expected to occur due to vibrations related to the aerodynamic performance of the blade, such as the vortex shedding frequency. A modal analysis could be performed for a simplified model of the blade. The frequencies and participation factors can be seen in Table 14.9

Table 14.9: Modal frequencies and participation factor results for the rotor arm

Mode	Frequency (Hz)	X Direction	Y Direction	Z Direction	X Rotation	Y Rotation	Z Rotation
1	19.6	-1.08E-04	-2.39E-04	6.59E-03	-0.23365	-5.1881	-0.19577
2	30.501	7.17E-05	2.73E-05	-1.90E-05	4.84E-04	3.05E-02	2.47E-02
3	34.6	2.51E-05	-3.15E-05	3.51E-05	-1.15E-03	-2.24E-02	-2.44E-02
4	36.446	2.53E-05	-4.40E-05	2.32E-03	-9.44E-02	-5.10E-02	-3.42E-02
5	38.2	-5.10E-05	-3.91E-05	8.38E-06	-1.89E-04	-1.54E-02	-3.31E-02
6	40.67	2.33E-05	7.46E-05	3.58E-04	-1.48E-02	8.71E-02	6.05E-02

The first mode is the one corresponding to flutter, as can be seen in Figure 14.20. The frequency lies within the possible rotational frequencies of the motor during operation. However, it is unclear whether the rotation around the vertical (z) axis can trigger this eigenmotion. As can be seen from the table, the largest participation factor corresponds to rotation around the Y-axis instead. Therefore, further investigation into the vibrational performance of the blade should be performed during subsequent phases of the project, along with a more thorough analysis of the aerodynamic dynamic loads that the structure might be subjected to. Additionally, the effect of a foam core should be analysed, as it is expected to increase the natural frequencies.

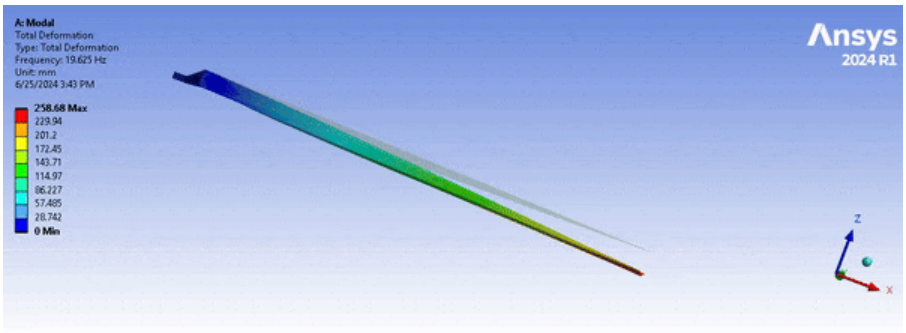

Figure 14.20: Animation of the flapping eigenmotion (click to watch)

Overall, it is important to note that even though Ansys Mechanical is validated software for static and other types of analysis, it is still possible to get flawed results due to incorrect simulation setup. Therefore, the most trustworthy validation approach for structural design remains the experimental approach, comprising producing a structure and testing it in a setup that can reproduce the loads during operation.

15 Rock Collection System

***Author**: Maurits*

In this chapter, the design process of the rock collection system for picking up Martian rocks is explored. The main focus of the chapter is on the design process. Beforehand in Section 15.1, the requirements specific to the robotic arm are reviewed and briefly discussed. Afterwards, Section 15.2 briefly explains how the team came to the robotic arm concept and why other concepts were discarded. Following, Section 15.3 extensively discusses the design process of the robotic arm, including such aspects as structural calculations, material selection and motor selection. Section 15.4 is focused on verifying and validating the models used during the design process. Lastly, Section 15.5 briefly discusses the final design parameters and performance.

15.1. Requirements

This section briefly introduces the requirements for designing the rock collection system. The requirements are summarised in Table 15.1.

Table 15.1: Most important requirements for the rock collection system design. Verification of these requirements falls under the responsibility of the structures and materials and payload lead engineers.

ID	Requirement	Verification Method
RCS-SYS-01	The rock collection system shall be able to pick up Martian rocks with a mass of up to 3 kg	Demonstration
RCS-SYS-02	The rock collection system shall be able to pick up Martian rocks with a size up to 10 cm × 10 cm × 10 cm	Demonstration
RCS-SYS-03	The rock collection system shall be able to pick up Martian rocks within a range of 30 cm from the centre of the Martian drone	Demonstration
RCS-SYS-04	The rock collection system shall be able to pick up Martian rocks without tensile yielding	Test
RCS-SYS-05	The rock collection system shall be able to pick up Martian rocks without shear yielding	Test
RCS-SYS-06	The rock collection system shall be able to pick up Martian rocks without torsional yielding	Test
RCS-SYS-07	The rock collection system shall have a total bending deflection of at most 5 mm when picking up Martian rocks	Test
RCS-SYS-08	The rock collection system shall have a total angular deflection of at most 1° when picking up Martian rocks	Test

15.2. Design Introduction

The design of the pick-up mechanism started with choosing an overall design concept and a grabbing mechanism. Two main concepts were considered: a linear motion rail system and a robotic arm. The linear motion rail system is synonymous with a claw machine, using rails to allow for horizontal translation and a separate mechanism for vertical translation. The robotic arm is often seen in automated factory lines, functioning similarly to a human arm. Using joints, the arm can rotate and translate in any direction, giving it free range.

The team decided to go forward with the robotic arm for several reasons. First, linear motion systems are constrained to the rails and require a large structure to increase their range slightly. On the other hand, a robotic arm has more freedom and is, in theory, capable of reaching outside its ground footprint. Secondly, rail systems are often relatively heavy due to the necessity of strong, stiff beams, and an additional mechanism for vertical movement. Lastly, storage was also a concern. A robotic arm is easier to fold, limiting its required volume. In a linear motion system, the grabber is suspended below the system, or a complex system is required for efficient storage.

The team explored numerous options for the grabbing mechanism and determined three feasible concepts; a claw-based system, a scoop-based system and a suction system. The suction system was discarded, due to Martian conditions, specifically the dust. The suction system would collect dust, adding useless weight, before picking up the desired rock. Furthermore, the seal between the system and the rock can not be guaranteed

limiting its performance. Storage considerations were again important, which caused the exclusion of the scoop system. The team removed a dedicated storage compartment for the rock to save space. Consequently, the grabber system had to store the rock, which a scoop system could not do securely.

Afterwards, the team researched the claw mechanisms, ranging from a simple two-fingered claw to a heavy-industry grabbing mechanism. After researching all available options, the team decided to use a peel-clamshell hybrid design. This design incorporates advantageous aspects of both. The orange peel aspect ensures that the forces can be dispersed over multiple fingers therefore lowering the required grabbing force, while the clamshell design ensures the grabber has some digging capabilities in case the rock is buried slightly into the ground.

15.3. Methodology

This section focuses on the robotic arm design process. First, a breakdown of the robotic arm structure is provided in Section 15.3.1. Following, Section 15.3.2 discusses the important loading cases for each section of the structure, and Section 15.3.3 elaborates on the design tools used for their design. Finally, Sections 15.3.4 and 15.3.5 detail the selection process of the materials and motors, respectively.

15.3.1. Structural Breakdown

The team decided to model the robotic arm after a human arm. This means the robotic arm has a claw (or hand), a forearm and an upper arm, each with its design. Very early on in the design of the robotic arm, it was discovered that the design would be limited by its total mass, and motor performance instead of the structural design. Therefore, the lengths of each section were chosen to optimize this.

The claw of the arm is the main grabbing mechanism. It was designed as a peel-clamshell hybrid grabber, as discussed earlier in Section 15.2. Additionally, the claw has a total height of 15 cm to allow the $10\,\text{cm}^3 \times 10\,\text{cm}^3 \times 10\,\text{cm}^3$ rock to fit well within the claw and leave enough room for the structure to keep the claw and motors together. Furthermore, a T-cross-section was chosen as it has sufficient area for effective contact with rock and adequate bending performance. Regarding motors, the claw itself will have one motor, which will be used for opening and closing the fingers.

The claw is connected to the forearm by the wrist. The wrist contains two motors, permitting the claw to rotate in up-down and side-to-side motions. This allows the claw to pick up rocks at slight inclines and optimize the angle at which it grabs the rock. The wrist motors will be placed at the end of the forearm. The forearm was designed to be 25 cm long, optimizing for the motor torque requirement and the arm's range and mass.

The forearm and upper arm are connected by the elbow, which holds one motor, allowing an up-down motion. This motion is required for flush storage against the drone body and better accuracy when moving the arm. This motor is, again, located at the end of the upper arm. The upper arm was designed to be 30 cm long for similar reasons as the forearm. Lastly, the shoulder connects the upper arm to the drone bus. Two motors allowing the arm to rotate around the centre axis and an up-down motion are stored inside the drone's body. The combination of motors described above should allow the arm to reach any rock regardless of obstructions.

All parameters discussed above are the driving design parameters for the arm's design. The lengths of each section, the number of motors and their location determine the loading on the structure, which is discussed further in Section 15.3.2.

15.3.2. Loading

To be able to design the claw and arm sections, it is important to understand and visualize the loading each section experiences. Furthermore, the most critical load cases should be analyzed before designing. This section is split into two main parts. First, the loading of the claw is discussed, and afterwards, the loading of the arms is explored.

It is also important to note that safety factors are included in the entire design. This safety factor combines the required safety factor set by NASA [57] and an additional safety factor due to the new technology, assumptions and uncertainties. For instance, one important assumption is that the arm will move slowly enough such that the force caused by the acceleration can be neglected. Therefore, a total safety factor of 1.5 is used throughout the design process, denoted by SF.

Claw

Discovering the most critical load case ensures the claw can pick up the 3 kg rock and hold on to it. From an initial analysis, the most limiting and common load case is when the claw closes around the rock. Analyzing the free-body diagram (FBD) displayed in Figure 15.1 below, the forces on one finger of the claw can be calculated through a simple force equilibrium, as shown in Equation 15.1

$$\downarrow + \sum F_y : -F_n \cdot \mu_s + \frac{W}{n_{fingers}} \leq 0 \tag{15.1}$$

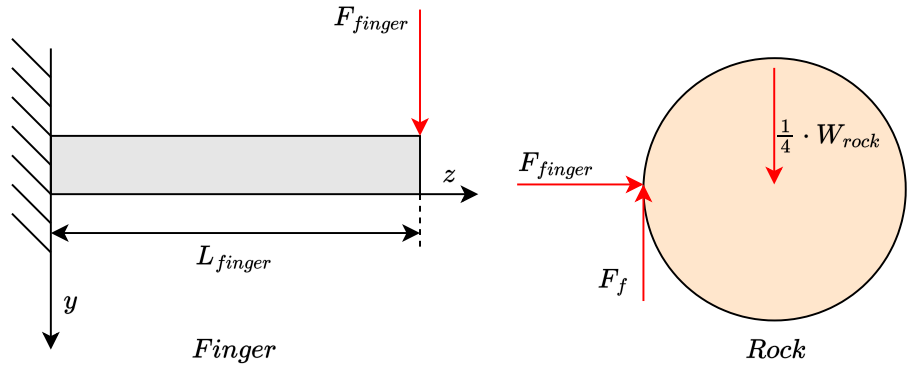

Figure 15.1: Free body diagram of the forces acting on one finger of the claw of the robotic arm

In this formula, μ_s is the static friction coefficient conservatively estimated to be 0.5 [61]. Furthermore, $n_{fingers}$ are the number of fingers applying the force, and F_{finger} is the force acting on the fingers, which is equal in magnitude but opposite in direction to the normal force. Therefore, the required finger force can be calculated with Equation 15.2

$$F_{finger} = \frac{SF \cdot g_{mars} \cdot m_{rock}}{\mu_s \cdot n_{fingers}} \tag{15.2}$$

This force causes a bending moment and a shear force on the finger. Assuming the top end of the finger is clamped due to the motor's resistance, the internal forces and bending moment can be calculated. This is visualized in Figure 15.2. In this diagram F I equal to F_{finger} as defined in Equation 15.2.

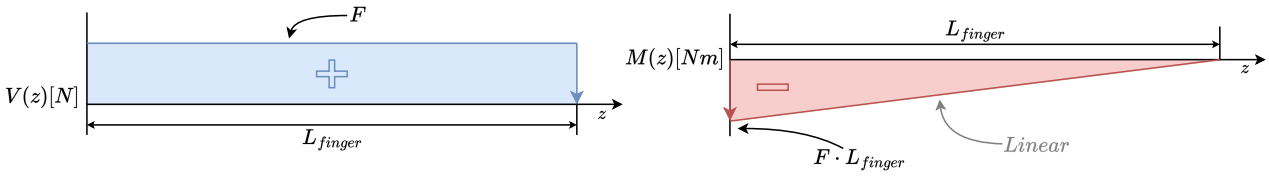

Figure 15.2: Internal shear forces and bending moment diagrams for one finger of the claw of the robotic arm.

From the diagrams, the maximum internal loading in one finger can be deduced, which is used for sizing the claw structure.

Another loading case to consider for the claw is the situation in which the claw is rotated in a horizontal position such that the entire weight of the rock rests on one finger. The internal shear force and bending moment diagrams can again be represented by Figure 15.2; however, F is equal to the weight of the rock, W_{rock}, for this case. Again, the diagrams display that the maximum internal shear force and moment occur at the root of the finger.

Lastly, a specific loading case for the T-beam cross-section needs to be discussed. A moment will be created if the claw touches the rock at the far end of the flange, as shown in Figure 15.3 below. This moment will cause stress in the connection between the web and the flange. While it's difficult to estimate the full extent of this stress, it can be estimated relatively easily; this is discussed more extensively in Section 15.3.3

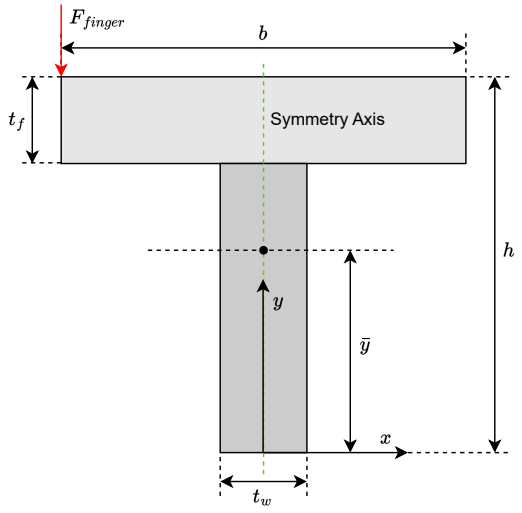

Figure 15.3: Schematic of a T-beam cross-section, depicting dimensions, and a limiting load case

Arm

Due to the similarity between the two sections of the robotic arm, their loading will be discussed collectively. There are two limiting cases to consider when looking at the robotic arm. The first is a horizontal case, where the weight force of all components, both structural and motors, and the rock weight act perpendicular to the arm, as shown in Figure 15.4. In this case, the arm experiences an internal shear force and bending moment. The loading diagrams for this case are presented in Figure 15.5

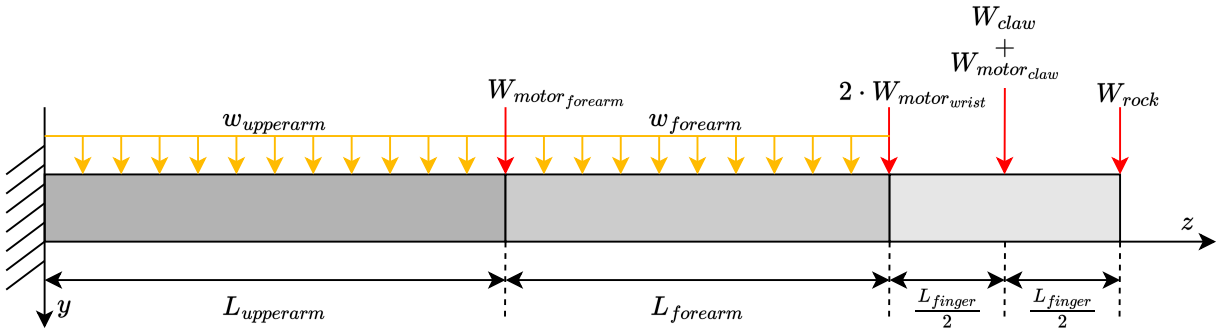

Figure 15.4: Free body diagram of the forces acting on the entire robotic arm

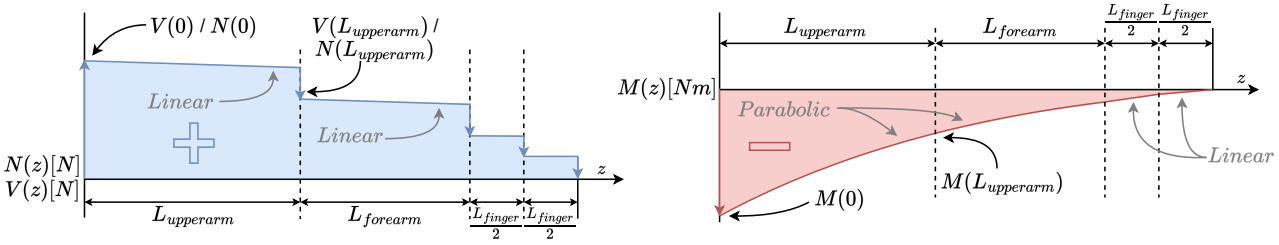

Figure 15.5: Internal shear forces and bending moment diagrams for the entire robotic arm

Both diagrams show the loading throughout the entire arm, including the claw. Furthermore, the vertical lines depict the separation of the different sections. The maximum shear force experienced by the forearm and upper arm can be extruded from the combination of the FBD and the loading diagram, and are written out in Equation 15.3 and Equation 15.4 respectively,

$$V_{forearm} = V(L_{upperarm}) = W_{rock} + W_{claw} + W_{motor_{claw}} + 2 \cdot + w_{forearm} \cdot L_{forearm} \tag{15.3}$$

$$V_{upperarm} = V(0) = V_{forearm} + W_{motor_{forearm}} + w_{upperarm} \cdot L_{upperarm} \tag{15.4}$$

The bending moment is calculated from these two equations by multiplying each force by the distance from the root of the forearm and upper arm. Furthermore, the structure must counteract its torque when a motor is active. Therefore, this additional moment was accounted for during the design and quantified by the motor's output torque. For a similar reason, each arm will also experience a torque, which was accounted for accordingly.

The other load case to consider for the arms is when the arm is completely vertical. In this case, all weights act parallel to the arm's length, causing it to experience tension only. The loading diagram for this case can again be visualised by the left side of Figure 15.5, replacing $V(z)$ by $N(z)$. Again, the vertical lines depict the separation of the different sections.

15.3.3. Design Tools

Having explored the limiting load cases, the arm design could start. As stated in Section 15.1, the arm should be able to pick up a 3kg rock (RCS-SYS-01), and a rock of at most 10cm^3 (RCS-SYS-02). Therefore, designing the claw first, and continuing through the arm upwards, ensures each section meets the requirements and is designed to hold the weight of the section before it.

The tool used for the design of the robotic arm split the design into three sections. Each design loop starts with creating an array of possible dimensional configurations. The specific dimensions depend on the cross-section used. From this, it calculates cross-sectional properties such as area and moment of inertia. The bending stress was estimated by combining these properties with the maximum bending moment from the loading diagrams. The tool then uses a Pareto front optimizer to find the design with the lowest bending stress at each mass value, as the bending stress was deemed the most critical. An example of a Pareto front is displayed in Figure 15.6. A final design is then chosen manually. Finally, the structure is checked for deflection and failure in other ways, and the final mass is calculated. Please note that the structural mass of each section is doubled to account for additional structures for connecting the different sections, holding the motors and electrical wiring.

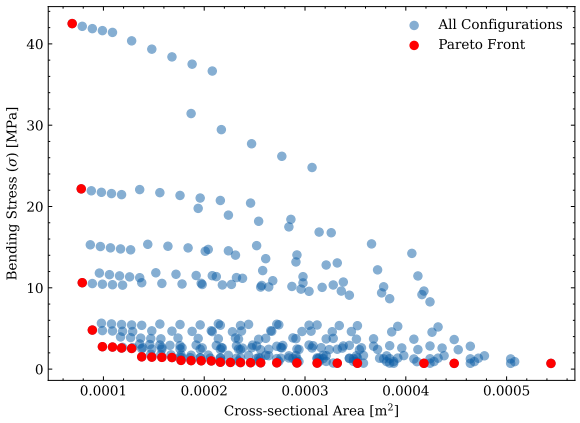

Figure 15.6: Pareto front example, plotting the most optimal solutions for bending stress and cross-sectional area. Note: The amount of configuration has been significantly reduced for increased readability.

Claw

For the claw design, the first iterations were run using a rectangular cross-section. This cross-section is optimised to a thin square beam of 1 cm^2. The claw design was therefore deemed limited by its functionality and manufacturability, rather than the yield stress due to bending. Consequently, the cross-section was changed to a T-shape cross-section to ensure the finger made sufficient contact with the rock and could mostly enclose it. For a T-shape cross-section, the area and the mass moment of inertia are calculated as shown in Equation 15.5, Equation 15.6 and Equation 15.7, using the dimensions shown previously in Figure 15.3.

$$A_f = b \cdot t_f + t_w \cdot (h - t_f) \tag{15.5}$$

$$\bar{y} = \frac{b \cdot t_f \cdot (h - \frac{t_f}{2}) + \frac{t_w}{2} \cdot (h - t_f)^2}{A} \tag{15.6}$$

$$I_{xx} = \frac{b \cdot t_f^3 + t_w \cdot (h - t_f)^3}{12} + b \cdot t_f \cdot (h - \frac{t_f}{2} - \bar{y})^2 + t_w \cdot (h - t_f) \cdot (\frac{(h - t_f)}{2} - \bar{y})^2 \tag{15.7}$$

The maximum bending stress in the finger can then be calculated with the formula depicted below in Equation 14.13, taking the maximum distance from the neutral axis to find the maximum bending stress. Depending on the cross-section parameters, this may be at the bottom of the web or the top of the flange.

The software then optimizes the cross-section using a Pareto front, which finds the most efficient solutions based

on the given parameters. The two parameters in question are the bending stress and cross-sectional area. The cross-sectional measures the mass, as the length and density are constant. This allows the team to select the most efficient cross-section for a specific bending stress.

After selecting the cross-section, several other important stress and structural considerations are calculated to ensure the fingers do not fail. The shear stress due to the finger force and tensile stress due to the rock resting on the fingers are calculated using respectively Equation 15.8 below, and Equation 14.9,

$$\tau = \frac{V}{A} \tag{15.8}$$

Furthermore, after selecting a material, the deflection due to bending is also checked to ensure that requirements RCS-SYS-07 and RCS-SYS-08 are met. For this, the most limiting case is used, which is the force being applied at the very end of the finger. Therefore, Equation 14.12 can be used to calculate the absolute deflection as measured from the root.

Additionally, the flange buckling due to compressive stress should also be considered. While not all fingers will experience compressive stress, the flange will experience this compressive stress. Thus, the overall performance of the finger will be negatively affected. To estimate the stress at which the flange buckles Equation 15.9, was used [56].

$$\sigma_{cr} = C\frac{\pi^2 \cdot E}{12(1-\nu^2)}\left(\frac{t}{b}\right)^2 \tag{15.9}$$

For the flange case, C was taken as 0.425 [56] as only the edge connected to the flange can be considered simply supported, while all others are free.

Arm

A circular cross-section was used for the arms as it has excellent torsional performance and sufficient bending performance. Again, first, the area and mass moment of inertia can be calculated with Equation 15.10 and Equation 15.11 below.

$$A_a = \frac{\pi(d_{out}^2 - d_{in}^2)}{4} \tag{15.10}$$

$$I_{xx} = \frac{\pi(d_{out}^4 - d_{in}^4)}{64} \tag{15.11}$$

From this, the maximum bending stress can again be calculated with Equation 14.13, using half the outer diameter for the y-coordinate.

The software again provides the optimized cross-section for bending stress at each area. Which can then be selected for further analysis. During this analysis, the shear stress for the horizontal load case and tensile stress for the vertical load case are calculated with Equation 15.8 and Equation 14.9, respectively.

When the motors are active, they exert a torsion load on the arm, which has to be countered. The torsional stress and deflection caused by this force can be calculated with Equation 14.11 and Equation 14.10, respectively. In these equations, J is the polar moment of inertia and is equal to half of I_{xx} for hollow-circular cross-sections.

Furthermore, to estimate the deflection due to bending, the principle of superposition has to be used due to the different loads applied to the arms. For this, forces will have to be moved to the end of each arm section, and a corresponding bending moment has to be added. Additionally, the weight of the beam is modelled as a distributed load. Therefore the bending deflection can calculated with Equation 15.12 [55]

$$\delta = \delta_M + \delta_V + \delta_w = \frac{M \cdot L^2}{2E \cdot I} + \frac{P \cdot L^3}{3E \cdot I} + \frac{w \cdot L^4}{8E \cdot I} \tag{15.12}$$

Lastly, buckling has to be taken into account. This was estimated using Equation 15.13, a formula specifically for the buckling of hollow circular beams [59].

$$\sigma_{cr} = E\left(9\left(\frac{t}{R}\right)^{1.6} + 0.16\left(\frac{t}{L}\right)^{1.3}\right) \tag{15.13}$$

15.3.4. Material Selection

Generally speaking, material selection is an iterative procedure. However, an initial material was selected to allow for some preliminary force, stress, and deflection calculation. More specifically, for all three parts of the robotic arm, Aluminum 6063-T6 was used. Afterwards, the computed stresses were used to help select a new, more optimal material.

The robotic arm's material selection followed a similar strategy as explained in Section 14.2.8. The Granta software [62] was used to select materials. The first plots were created for the most important material properties. Afterwards, limits were imposed on those properties based on the requirements or stresses experienced by the system. Finally, the most optimal material was selected by maximizing a material index specific to this case.

Claw

The first calculations of the claw's performance with Aluminum 6063-T6 showed extremely low stresses. Moreover, the deflection of one finger was also far below the requirements. Therefore, the limits set on the yield strength and Young's modulus left many suitable materials.

Despite the low stresses and deflection, the team set out to minimize the deflection and weight of the claw. Since the finger can be modelled as a flat plate, $\sqrt[3]{E}/\rho$ [60, p.418] had to be minimized to find the best material for the minimum weight design of stiff plates. There is an argument for modelling the fingers as the beam, which would require $\sqrt{E}/\rho$ to be minimized, but this does not change the material selection significantly.

After removing all unoptimised materials, four materials were left. These materials and their important characteristics are summarized in Table 15.2

Table 15.2: Final material selection for the different parts of the rock collection mechanism. Note: All composites are quasi-isotropic. [62]

Material	**Density [kgm^{-3}]**	**Young's modulus [GPa]**	**Yield Strength [MPa]**	**Embodied Energy [MJkg^{-1}]**	**Price [€ kg^{-1}]**
BMI/HS carbon fiber, woven prepreg	1510 - 1570	47.5 - 55.3	353 - 389	729 - 804	134 - 161
Epoxy/HS carbon fiber, UD prepreg	1550 - 1580	49.7 - 60.1	603 - 738	693 - 764	34.9 - 38.8
Cyanate ester/HM carbon fiber, UD prepreg	1620 - 1670	101 - 115	607 - 738	725 - 799	196 - 219
Beryllium, grade SR-200, sheet, 0.5 to 6.35 mm thick	1840 - 1860	290 - 315	340 - 450	6080 - 6700	571

A final selection was made from the materials presented in Table 15.2. Due to the high embodied energy of beryllium, it was discarded as a feasible option for the claw. Furthermore, for the claw the extremely high Young's modulus and yield strength were unnecessary. Cyanate ester/HM carbon fibre was discarded due to it having slightly higher density and embodied energy than the other two composites. The two remaining composites are virtually the same in all parameters, except for Yield strength. However, the final decision was based on the durability of the materials. BMI/HS carbon fibre is significantly more durable in case of UV radiation, an important parameter for Martian vehicles, and was therefore chosen as the final material for the claw of the robotic arm.

Arm

The material selection for the arm followed a similar procedure. The maximum tensile stresses calculated after the first iteration cycle were imposed as a limit. Afterwards, $\sqrt{E}/\rho$ [60, p.418] was minimized to find the optimal material for stiff beams and shafts. Coincidentally, the final materials available were the same as those for the finger. Therefore, the final selection presented in Table 15.2 also applies to the forearm and upper arm of the rock collection mechanism.

The final selection was again similar to the claw. Due to the higher bending moments experienced by the arm, deflection is more prominent, Consequently, Young's modulus was a more important property to consider than for the claw. Therefore, BMI/HS carbon fibre and Epoxy/HS carbon fibre were discarded. Finally, beryllium was discarded for a similar reason as the claw, leaving Cyanate ester/HM carbon fibre as the best material for the arm sections. Outside of the properties presented in Table 15.2, Cyanate ester/HM carbon fibre shows good durability in UV-radiation and excellent fatigue properties.

15.3.5. Motor Selection

Selecting motors significantly depends on the mass of structural components and the other motors. For each motor, the required torque was calculated based on the mass of all components ahead of it and the distance to the motor's position. This is summarized in Equation 15.14 below.

$$T_{motor} = \sum^{n} m_i \cdot g_{mars} \cdot SF \cdot d_i \tag{15.14}$$

With the required torque, the Maxon Group's catalogue[1] was used to find the correct motor gearbox combination. Maxon Group manufactures lightweight precision motors, also used in Perseverance's arm[2] . Due to the small form factor of the Maxon Group motors, they often require a gear system to reach the required torque, complicating the selection procedure. Despite this, they are still the most optimal motors for the robotic arm.

First, a gear system was selected based on the required output torque from Equation 15.14. The gear system's efficiency and reduction ratio were then used to calculate the motor's required output torque. Since the efficiency of a gear is the fraction of output over input power, the torque is also affected. Therefore, this was taken into account when selecting a motor, which was chosen according to the calculated torque requirement. Fortunately, the Maxon Group's website automatically excludes any incompatible motors. This process was repeated for each motor location. Finally, each motor-gear combination was accompanied by a standard servo controller of 7 g and a price of € 97.68. A summary of the selected motor-gear combinations and their performance is shown in Table 15.3 for the motors and Table 15.4 for the gears

Table 15.3: Motors selected for each motor location in the robotic arm and their performance. Note: All motors are brushless and contain Hall sensors.

Motor Location	Motor	Torque [mNm]	Input Power [W]	Efficiency	Mass [g]	Price
Claw	ECX SPEED 16 M Ø16 mm	4.58	27.6	80%	50	€234.84
Wrist	EC-max 22 Ø22 mm	10.2	15.0	64%	83	€208.41
Forearm	EC-max 30 Ø30 mm	34.9	34.56	75%	195	€253.89
Upper arm	EC 45 flat Ø42.9 mm	57.1	25.92	77%	75	€99.47

Table 15.4: Gears selected for each motor location in the robotic arm and their performance

Motor Location	Gearbox	Torque [Nm]	Reduction Ratio	Efficiency	Mass [g]	Price
Claw	GPX 19 HP Ø19 mm	2.0	1526:1	55%	63	€225.57
Wrist	GP 22 HP Ø22 mm	3.4	850:1	49%	91	€ 294.52
Forearm	GP 32 HP Ø32 mm	8.0	913:1	60%	249	€ 294.41
Upper arm	GP 42 C Ø42 mm	15.0	936:1	64%	560	€ 387.36

15.4. Verification and Validation

This section focuses on the verification and validation methods performed on the design tools for the robotic arm. Verification and validation both play an integral role in ensuring the correctness of the model and creating confidence in the achieved results.

15.4.1. Verification

Verification of the tool used for designing the robotic arm was achieved in a variety of ways. First, the formulas discussed above in Section 15.3 were compared to the equations in the code, to ensure they had been implemented correctly. This was then extended to manual unit tests. During these tests, simple values were used as inputs, and the output was compared to manually calculated outputs using other tools, such as Excel, Desmos or simply pen and paper. These tests were performed for each equation, to find and fix any errors.

After checking the validity of each function, the verification continued with larger subsystem tests, which checked a larger portion of the design tool. Some basic parameters would be provided to the code. The result partway through the process was compared to manually calculated values to ensure correctness.

Lastly, a couple of system tests were performed to ensure all equations were connected as expected, values were

[1] URL: https://www.maxongroup.nl/maxon/view/catalog/ [cited on 5 Jun 2024]]

[2] URL: https://www.maxongroup.com/en-gb/knowledge-and-support/blog/maxon-and-the-samples-of-martian-soil-81532 [cited on 5 June 2024]

stored effectively, and no data was lost. These tests were again performed with some basic parameters, and the output was compared to manually calculated values.

In the end, the entire design tool was verified through a multitude of tests. During the verification process, multiple errors were caught, and fixed accordingly. In the end, sufficient confidence was created in the design tool, for the team to continue to the iteration phase.

15.4.2. Validation

The team intended to perform a FEM analysis of the robotic arm to validate the structure and ensure it functions as intended without failure. Unfortunately, the team was not able to create an accurate model of the robotic arm, meaning the FEM analysis would be untrustworthy. Therefore, the validation of the robotic arm is left as future development, after a more accurate assembly of the robotic arm is created.

15.5. Results

This section focuses on the final design of the robotic arm. This final design was achieved after iterating materials, motors and geometrical parameters to find the optimal configuration. However, the selected motors have to be checked, before going into detail about the final design. After calculating the required torque at each motor location, the final motor selection was made as discussed in Section 15.3.5. In Table 15.5 the required torque at each motor location, and the available torque for each selected motor-gear combination is provided.

Table 15.5: Required torque and available torque at each motor location in the robotic arm.

Motor Location	Required Torque	Available Torque	Units
Claw	1.25	2.0	N m
Wrist	2.66	3.4	N m
Forearm	7.86	8.0	N m
Upper arm	14.95	15.0	N m

Claw

For the design of the claw, the team discovered that the forces acting on the claw were not limiting the design. Instead, the functionality and manufacturability of the claw were leading the design. Consequently, a slightly heavier design was chosen to ensure the claw could pick up rock up to a size of 10 cm^3.

Furthermore, after the verification process, it was discovered that the most limiting loading case was not the rock grabbing as stated earlier in Section 15.3.2. Instead, the rock resting on one finger caused the largest stresses in the fingers of the claw. As stated in Section 15.3.4 the material selected for the claw is BMI/HS carbon fiber, woven prepreg, quasi-isotropic layup.

A summary of the design geometrical parameters for the claw of the rock-grabbing system is provided below in Table 15.6. While the finger width, when curved around a circle, does not allow for full enclosure of a 10 cm^3 rock, the gaps ($\approx$ 2.5 cm) between the finger are too small for any rock of significant interest to fall out.

Table 15.6 also presents the stresses acting on the claw in the most limiting loading cases. It can be deduced from these values that the claw does not fail in any of the loading cases and is capable of picking up rocks up to 3 kg.

Table 15.6: Design parameters for final claw design of the rock collection system, the forces acting on the claw, and the stresses caused by these forces.

Geometrical parameters of the claw

Parameter	Value	Unit
Length	0.15	m
Finger Width	0.084	m
Finger Depth	0.038	m
Flange Thickness	0.001	m
Web Thickness	0.001	m
Number of Fingers	4	-
Finger Mass	0.0285	kg
Total Claw Mass	0.228	kg

Structural performance of the claw

Parameter	Value	Unit
Finger Force	8.37	N
Maximum Shear Force	16.74	N
Maximum Shear Stress	0.138	MPa
Maximum Bending Moment	2.51	N m
Maximum Bending Stress	7.07	MPa
Maximum Bending Deflection	0.029	mm
Critical Buckling Stress	10.5	MPa
Stress in Web-Flange Connection	28.12	MPa

Arm

For the arm design the limiting case was found to be the fully horizontal position, as discussed in Section 15.3.2. This was further confirmed during the design process, where the maximum stress was caused by the bending moments in this loading case. After optimizing the arms structures for this loading case a final design was achieved. The internal shear force and bending moment loading diagrams for this final design are presented in Figure 15.7

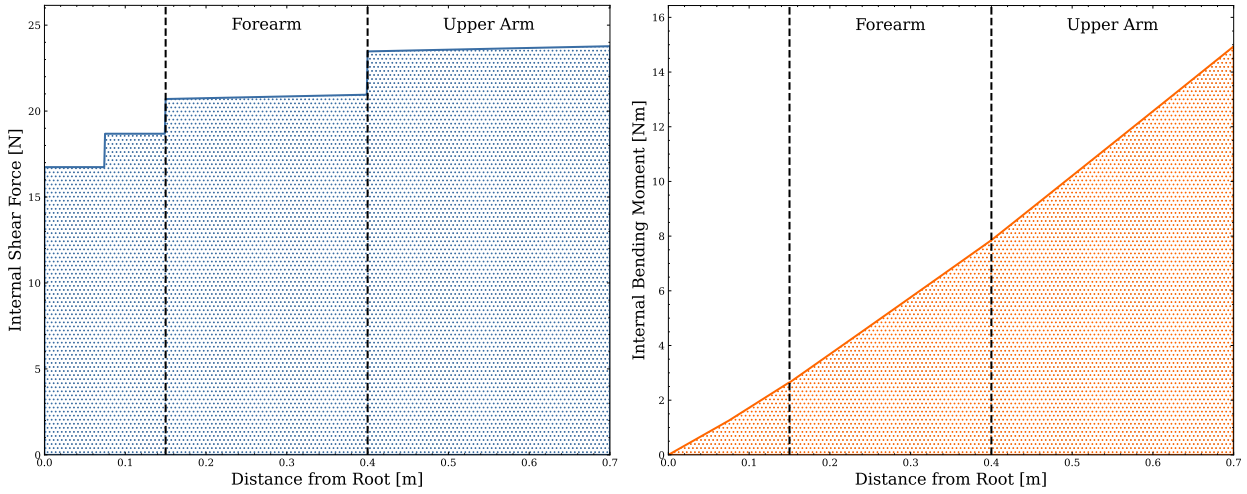

(a) Internal shear force diagram

(b) Internal bending moment diagram

Figure 15.7: Internal force and moment diagrams for the final arms design, the vertical lines depict the beginning and end of each arm section

From these diagrams, the maximum shear force and bending moments were used to size the arm structure. This resulted in the geometrical parameters as presented in Table 15.7. Furthermore, the material used for both arm sections is Cyanate ester/HM carbon fibre, unidirectional prepreg, quasi-isotropic lay-up as discussed in Section 15.3.4. The length of the entire arm, 55 centimetres, allows the rock collection system to have a range of approximately 37.7 centimetres as measured from the centre of the drone. This is a conservative estimate that does not take into account the length of the claw itself, which may add to the range of the drone.

Finally, Table 15.7 also presents the forces and stresses acting on each arm section in the most limiting loading case. From these values, it can be concluded that the arms do not fail during the rock collection procedure, for rock up to 3 kg.

Table 15.7: Design parameters for final arm section designs of the rock collection system, the forces acting on the arm section, and the stresses caused by these forces.

Parameter	Forearm	Upper arm	Unit
Length	0.25	0.30	m
Outer Diameter	0.035	0.035	m
Inner Diameter	0.034	0.034	m
Mass	0.045	0.054	kg
Maximum Shear Force	20.95	23.77	N
Maximum Shear Stress	0.387	0.439	MPa
Maximum Bending Moment	11.26	22.95	N m
Maximum Bending Stress	24.44	49.80	MPa
Maximum Bending Deflection	0.365	1.137	mm
Maximum Torsional Stress	3.689	8.680	MPa
Maximum Angular Deflection	0.089	0.252	deg

Cost

A short cost estimation can also be completed for the robotic arm. Since the motors are off-the-shelf products, and the price of the materials can be taken from the Granta software [62], a final estimate of the cost of the robotic arm can be made. The total motor cost comes out to 3574.31€, while the material cost is in total 57.60€. This gives the robotic arm a total cost of 3631.91€.

16 Final Design

***Authors**: Salar, Florian, Dionysis, Li, Sebastien, Raf, Diede*

In the previous chapters, a methodology was provided for developing the preliminary design of various subsystems. This chapter brings all systems together into an integrated final design.

First, in Section 16.1, the final system iterations of the drone's subsystems is detailed. Then, technical budgets are discussed in Section 16.2. Afterwards, technical block diagrams concerning the electrical power system, hardware and software, data handling and communication are provided in Section 16.3, Section 16.4 and Section 16.5 respectively. Section 16.6 then lays out the final system layout, followed by the iterations. Lastly, Section 16.7 discusses the system-level functional flow diagram and functional breakdown structure.

16.1. System Iteration

***Authors**: Salar*

Every subsystem described from Chapter 8 to Chapter 14 was developed with a corresponding design tool, such that a system-wide iteration could be carried out. This process is described by Figure 16.1.

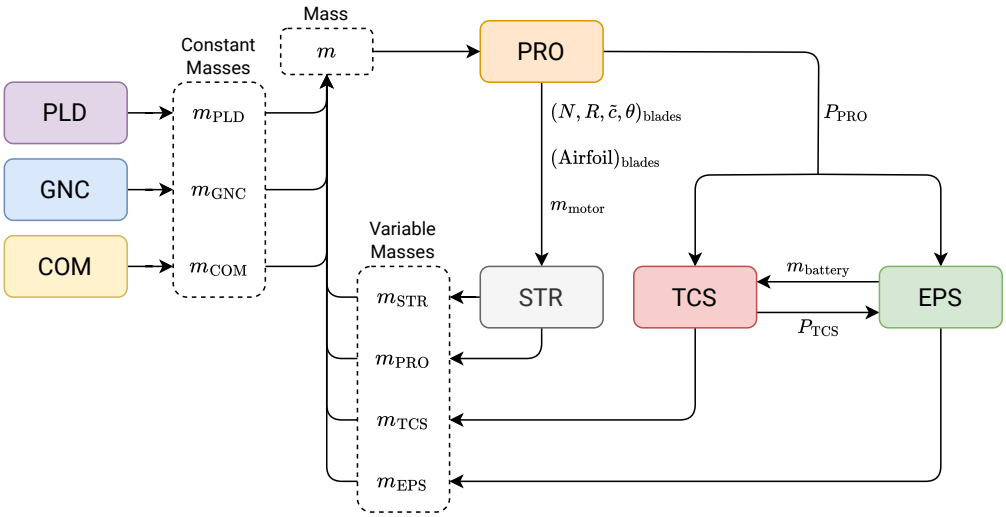

Figure 16.1: System-wide sizing iteration flowchart.

The system iteration begins with an initial "origin" guess for the total mass. A lower value than that of the mass budget was selected as this represents the natural process of convergence of a system mass, as well as the fact that various subsystems (such as power) have masses determined by discrete jumps in values (such as the number of battery strings). Table 16.1 displays the subsystem masses at iteration i. The tolerance for convergence was set to be 1 %, so the system converged at the fifth iteration, but an additional iteration was carried out to confirm convergence. This led to a total system mass of 48.68 kg.

Table 16.1: System-wide iteration table.

i	*0*	*1*	*2*	*3*	*4*	*5*	*6*	**Unit**
m_{PLD}		8.85	8.85	8.85	8.85	8.85	8.85	kg
m_{GNC}		1.30	1.30	1.30	1.30	1.30	1.30	kg
m_{COM}		0.25	0.25	0.25	0.25	0.25	0.25	kg
m_{PRO}		4.10	4.17	4.16	4.51	4.53	4.50	kg
m_{EPS}		16.14	18.23	19.91	20.04	20.04	20.18	kg
m_{TCS}		3.83	4.35	5.06	5.35	5.65	5.65	kg
m_{STR}		7.55	7.95	7.95	7.95	7.95	7.95	kg
m	40.00	42.03	45.10	47.47	48.25	48.56	48.68	kg
Δm		+5.1	+7.3	+5.3	+1.6	+0.6	+0.2	%

16.2. Budgets

Authors: *Salar*

After the final iteration, detailed budgets for each system were made. This begins with the mass and power budgets, deriving directly from the intermediate steps of the iteration. These are shown in Table 16.2.

Table 16.2: MEALS final budget breakdown

Mass budget

	Mass	**Unit**
Payload	8.85	kg
Scanning	3.30	kg
Collection	2.55	kg
Rock	3.00	kg
Avionics	1.55	kg
GNC	1.30	kg
Comms	0.25	kg
Propulsion	4.50	kg
Motors	2.50	kg
Rotors	2.00	kg
Power	20.18	kg
Array	6.04	kg
Battery	10.25	kg
Other	3.89	kg
Thermals	5.65	kg
Motor Fins	4.03	kg
Battery	0.32	kg
Other	1.30	kg
Structures	7.95	kg
Bus	3.65	kg
Arms	3.83	kg
Struts	0.47	kg
Subtotal	48.68	kg
Contingency	2.44	kg
Total	51.12	kg

Power budget

	Power	**Unit**
Payload	45	W
Scanning	10	W
Collection	35	W
Rock	-	W
Avionics	55	W
GNC	54	W
Comms	1	W
Propulsion	7387	W
Motors	7387	W
Rotors	-	W
Power	-	W
Array	-	W
Battery	-	W
Other	-	W
Thermals	25	W
Motor Fins	-	W
Battery	25	W
Other	-	W
Structures	-	W
Bus	-	W
Arms	-	W
Struts	-	W
Subtotal	7512	W
Contingency	376	W
Total	7888	W

In Table 16.2, a 5% contingency is applied on the subtotals of each budget to account for additional weight (e.g. fasteners) and power consumption (e.g. data processing) added in detailed design. This contingency is not large, as most subsystems already carry margins. It is interesting to note that the mass and power have decreased greatly from the baseline budgets. This makes sense, as the earlier budgets carried major contingencies accounting for uncertainties in design choices. The mass budget, when compared to the preliminary mass budget of the selected design, increased slightly; this is primarily due to an underestimation of the mass of the power subsystem, particularly the solar array requirements.

16.3. Electrical Block Diagram

***Authors**: Florian*

An electrical block diagram of the system is presented in Figure 16.2. This diagram illustrates all voltage lines present in the system. The power generation system is controlled by an MPPT, which optimises the solar arrays' performance based on the environmental conditions and converts the voltage received from the arrays to the bus voltage of 60 V. The power received is then distributed to the various power users within the system. Excess power is directed to the battery via a charge/discharge controller. When power demand exceeds supply, the discharge controller draws power from the battery and distributes it to the low and high-voltage systems.

Power is supplied to the low-voltage systems through a DC/DC step-down converter, which reduces the voltage to 24 V. The various subsystems are responsible for further voltage conversions to provide power to their respective components. High-voltage systems receive power at 60 V, requiring no voltage conversion. The propulsion system's power draw is then regulated by motor controllers, which provide the necessary power to each individual motor for control of the generated thrust.

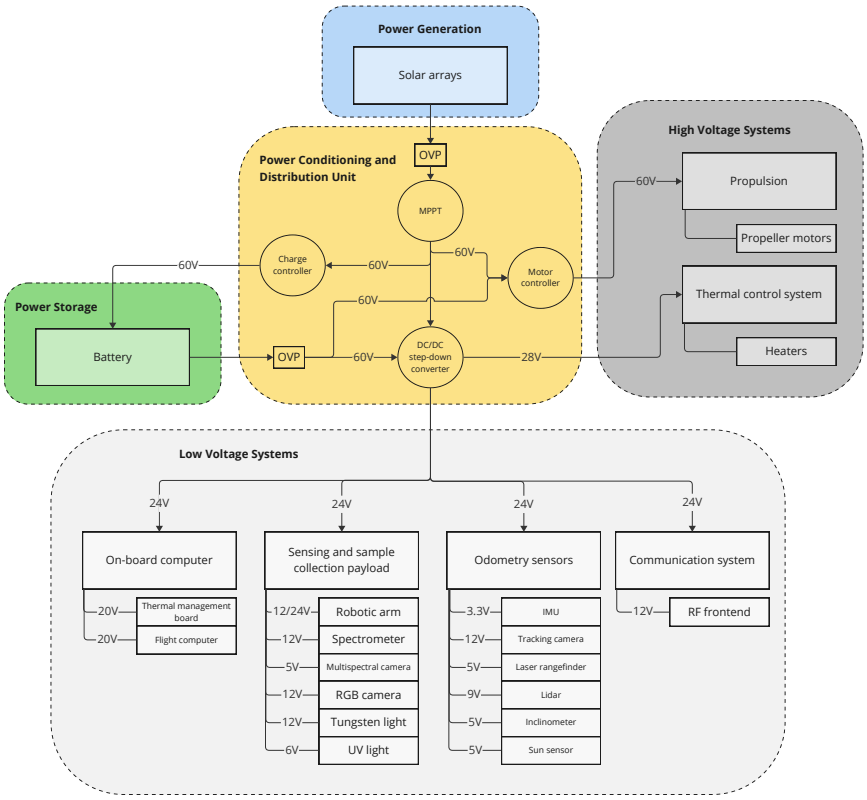

Figure 16.2: Electrical block diagram for MEALS.

16.4. Hardware Diagram

***Author**: Li*

The following section presents the final hardware diagram of the final design, in which the interfaces between the main subsystem components are laid out graphically. The diagram can be seen in Figure 16.3.

This diagram includes the main hardware components, such as sensors, lights, communication antennae, and actuators, to provide a thorough understanding of how different components are linked. The blue lines indicate data interfaces, the red lines denote power interfaces (for which a more detailed version with the respective voltages can be found in Section 16.3), and the black lines indicate mechanical interfaces between parts. The relevant type of connector/data protocol is also indicated where applicable for the electrical components. Note that most mechanical interfaces concerning the main structure are not indicated in this diagram, as they are further divulged in the system layout section, along with a more detailed CAD model of the final design.

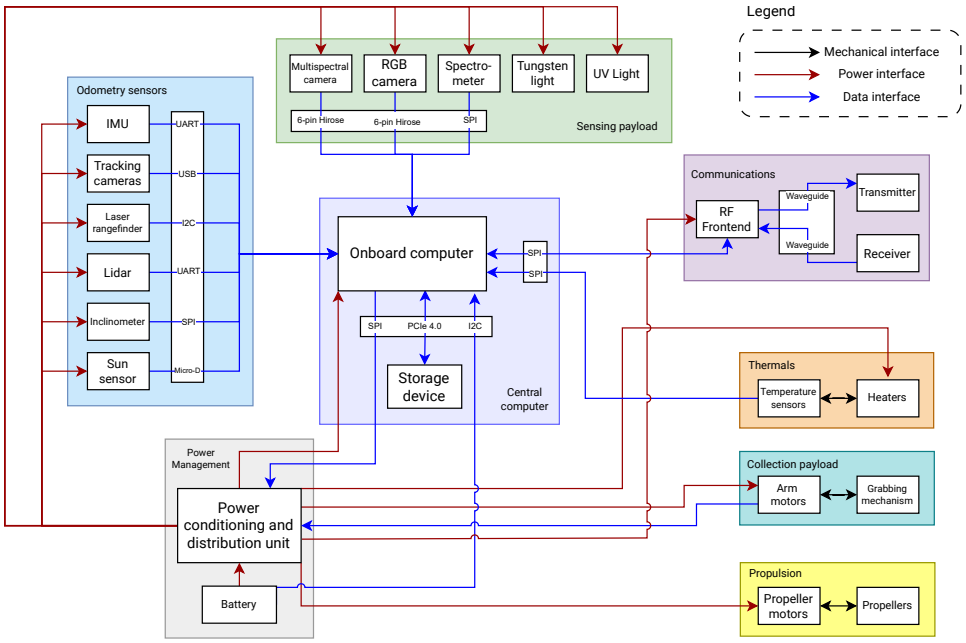

Figure 16.3: Hardware diagram for MEALS

16.5. Software, Data Handling and Communication Diagram

***Authors**: Li, Sebastien*

A software diagram is included along with the respective data flows between the subsystem components to further illuminate the final system operations. The diagram, which can be found below, also presents the communication protocol between MEALS, the ground station, and Earth.

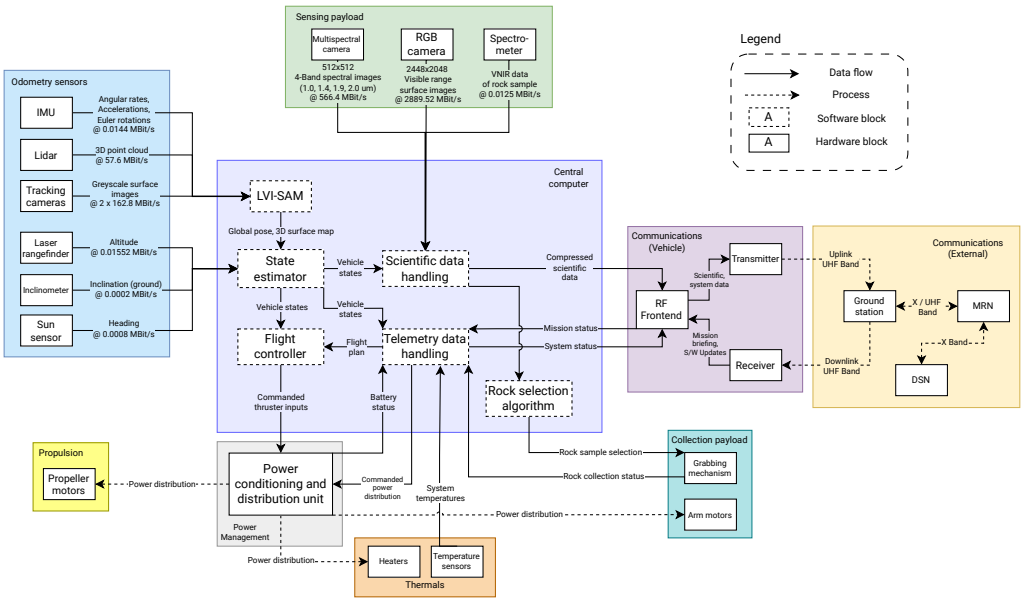

Figure 16.4: Software, data handling and communication diagram for MEALS.

Figure 16.4 contains the same hardware elements as previously detailed in Figure 16.3. Note that the central computer is now broken down into different software blocks, as these run simultaneously in the OBC. Solid lines indicate all the data flows and rates where information is available. The dotted lines represent other processes, such as communication links and power distribution.

External communication is only performed with the ground station, which sends the respective data to Earth. Similarly to Perseverance, the communication with Earth is performed via the Mars Relay Network (MRN) to

the Deep Space Network (DSN)[1] . The ground station shall use X-band and UHF-band to communicate with the MRN, which will relay the data via X-band to Earth. The DNS in Spain, California, USA, and Canberra will capture this data. This system allows the drone to communicate with Earth even if not in view.

16.6. System Layout

Authors: *Dionysis*

In this section, the system's layout is presented from both an external and internal perspective. In figure 16.5a, a render of the assembly in the deployed configuration can be seen.

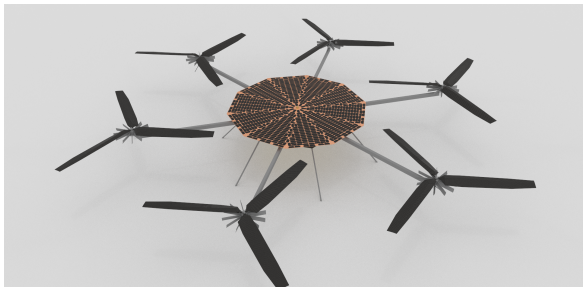

(a) Isometric view of the preliminary drone assembly.

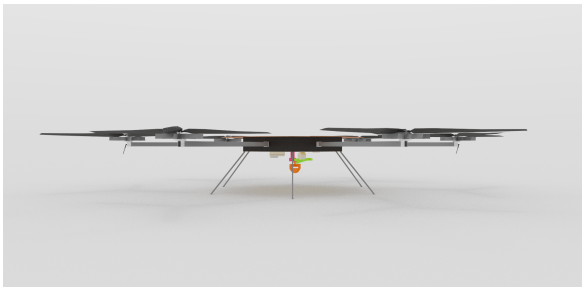

(b) Side view of the preliminary drone assembly.

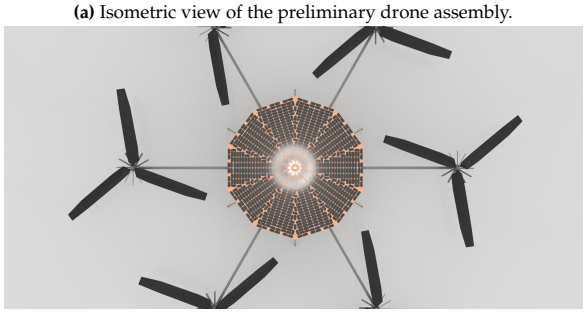

(c) Top view of the preliminary drone assembly.

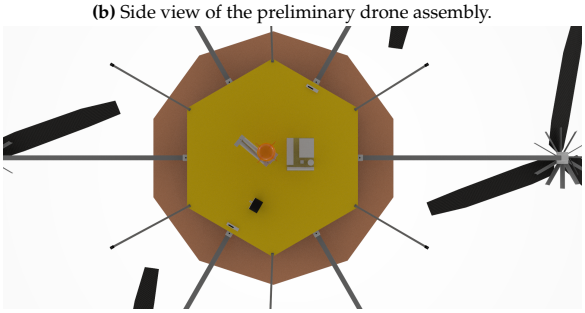

(d) Bottom view of the preliminary drone assembly.

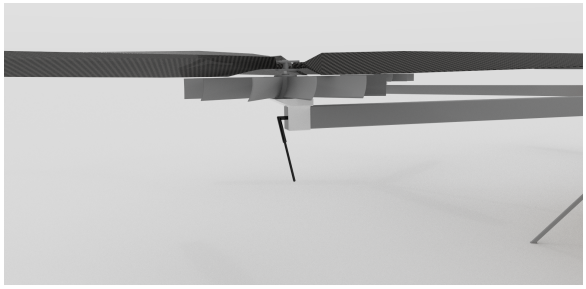

(e) Render of the rotor assembly and antenna.

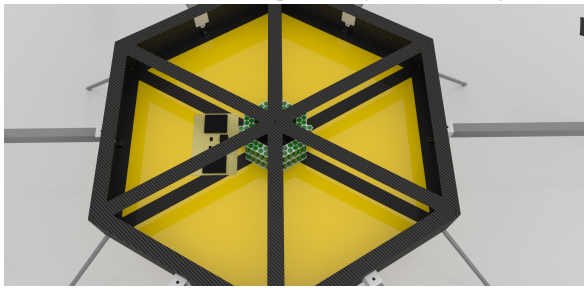

(f) Render of the rotor assembly and antenna.

Figure 16.5: Different views of the system layout

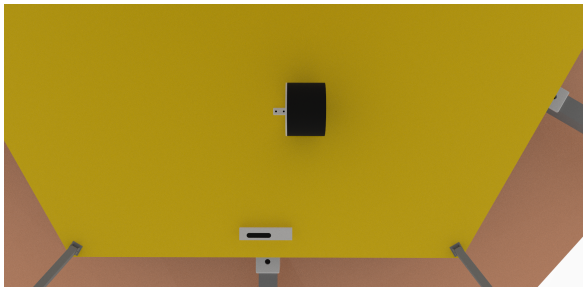

(a) LIDAR and tracking camera at the underside of the drone.

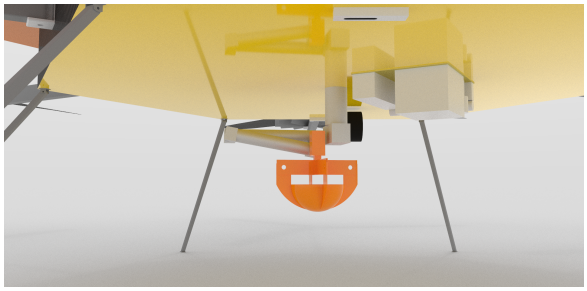

(b) Render of the rock collection mechanism.

Figure 16.6: Close-up renders of the components under the bus.

The main body of the drone features a hexagonal shape, with six rotor arms extending from it, connected via

[1]URL: https://www.nasa.gov/centers-and-facilities/jpl/the-mars-relay-network-connects-us-to-nasas-martian-explorers/ [cited on 17 June 2024]

lugs. Each arm terminates in a rotor assembly with a motor, cooling fins and blades mounted on a central hub, as seen in Figure 16.5e. Two opposite arms also feature an antenna, angled at 45° for optimal coverage. Positioned on top of the main body is a solar array, centrally equipped with a sun sensor, as illustrated in Figure 16.5c. The side view, depicted in Figure 16.5b, reveals six landing legs extending from the main body. The underside of the drone hosts the rock collection mechanism, the scientific payload, and the guidance, navigation, and control (GNC) cameras, as shown in Figure 16.5d and Figure 16.6a. A closer look at the rock collection mechanism is presented in Figure 16.6b. Finally, the internal view of the system can be seen in Figure 16.5f. This view is not particularly detailed as this is not possible at this project stage. However, the battery assembly can be seen at the centre, as well as an avionics module. With regards to dimensions, the deployed system has a diameter of 7.32 m, tip to tip, whereas in the folded configuration, it can fit in the Mars2020 aeroshell [20], as seen in Figure 7.3.

16.7. Functional Flow and Breakdown Structure

***Authors**: Li, Dionysis, Diede, Raf*

In this chapter, a system-level functional analysis is performed as a foundational step in the process of generating requirements for the drone design. This analysis yields two important diagrams, the Functional Flow Diagram (FFD) and Functional Breakdown Structure (FBS), providing different overviews of the system's capabilities. In Section 16.7 and Section 16.7 the processes followed to elaborate each diagram are presented respectively.

Functional Flow Diagram

The FFD aims to provide a high-level chronological overview of the system's actions. The functions included in this diagram are the "time-dependent" functions, meaning they cannot occur until other tasks have been completed. Three levels of detail have been explored for the FFD, with sub-tasks being derived one level deeper later in the FBS. The highest levels are defined as follows: first, the system has to undergo production activities, which include manufacturing, assembly, testing, etc. The launch and deployment phase follows afterwards, which lasts until the drone is deployed on the Martian surface. Subsequently, the mission operations phase is where the scientific mission will be carried out, and finally, the system's end-of-life is achieved. These can be seen in the top half of the FFD. For the mission operations phase, the third level of detail was explored for the most critical functions in the FFD, which can be observed in the bottom half of the figure. As can be seen from the figure, the drone first receives a mission briefing from the ground station, indicating the area to be scanned and characteristics of interest. Then, it goes through standard operations and performs the scientific mission. This can be broken down into two parts. First, the drone performs a reconnaissance of the area, identifying objects of interest. If a suitable sample is found, it will be picked up and flown back to the ground station for further analysis. If not, the scanned area has no samples of interest so that the drone will fly back to the ground station for a new mission briefing.

Functional Breakdown Structure

Following the FFD, an FBS is derived, further breaking down the functional analysis to a deeper level. The first and second levels of the functional breakdown structure are mostly similar to the first and second levels of the functional flow diagram. At the third level, time-independent functions are also included in the FBS. An additional time-independent function is also analysed in the second level of phase 2, namely the maintenance of vital functions, which runs continuously in parallel to all mission operations. Moreover, the responsible subsystems that carry out each function are identified.

0
Undergo Production

- **0.1** Undergo manufacturing
- **0.2** Undergo assembly
- **0.3** Undergo testing
- **0.4** Undergo transportation
- **0.5** Undergo integration

1
Launch & Deploy

- **1.1** Perform pre-launch operations
- **1.2** Launch
- **1.3** Enter Martian atmosphere
- **1.4** Perform landing operations
- **1.5** Deploy
- **1.6** Perform system tests

2
Perform Mission Operations

- **2.1** Receive mission briefing
- Mission end?
  - Yes → **3.1** Perform final system check
  - No → **2.2** Perform pre-flight checks
- **2.2** Perform pre-flight checks
- Tests passed?
  - No → **2.4** Conduct contingency operations
  - Yes → **2.3** Take-off
- **2.3** Take-off
- **2.5** Fly to designated area
- **2.6** Perform reconnaissance
- Suitable sample found?
  - No → **2.8** Land near ground station
  - Yes → **2.7** Perform sample collection
- **2.7** Perform sample collection
- **2.8** Land near ground station

3
Conduct End-of-life Operations

- **3.1** Perform final system check
- **3.2** Perform predetermined end of mission operation
- **3.3** Report end of mission

Legend

- **ID** Function — Function block
- Flow connection line (Level 1)
- Flow connection line (Levels 2/3)

3rd level FFD

2.4 Conduct contingency operations

- **2.4.1** Run diagnostics
- **2.4.2** Report malfunction to ground operations
- **2.4.3** Restart system

2.7 Perform sample collection

- **2.7.1** Select sample
- **2.7.2** Fly to sample
- **2.7.3** Collect sample with mechanism
- **2.7.4** Return sample to ground station

2.6 Perform reconnaissance

- **2.6.1** Verify drone position
- **2.6.2** Initialise scanning instruments
- **2.6.3** Perform topological and geological survey
- **2.6.4** Identify objects of interest in area

Perform Mission

0 Undergo Production

- 0.1 ALL — Undergo manufacturing
- 0.2 ALL — Undergo assembly
- 0.3 ALL — Undergo testing
  - 0.3.1 STR — Undergo structural tests
  - 0.3.2 EPS — Undergo power tests
  - 0.3.3 ALL — Undergo thermal tests
  - 0.3.4 ALL — Undergo radiation tests
  - 0.3.5 ALL — Undergo initial flight test
  - 0.3.6 ALL — Undergo final qualification
- 0.4 ALL — Undergo transportation
- 0.5 STR — Undergo integration
  - 0.5.1 STR — Assume launch configuration
  - 0.5.2 STR — Be attached to launch vehicle

1 Launch & Deploy

- 1.1 ALL — Perform pre-launch operations
  - 1.1.1 COM — Initiate communication with ground segment
  - 1.1.2 GNC — Perform system health check
- 1.2 ALL — Launch
  - 1.2.1 ALL — Lift off
  - 1.2.2 ALL — Get into transfer orbit
- 1.3 ALL — Enter Martian atmosphere
- 1.4 ALL — Perform Martian entry operations
  - 1.4.1 ALL — Perform orientation manoeuvres
  - 1.4.2 ALL — Decelerate
  - 1.4.3 ALL — Perform initial contact with Martian soil
- 1.5 ALL — Deploy
  - 1.5.1 STR — Separate from lander
  - 1.5.2 ALL — Perform deployment operations
  - 1.5.3 ALL — Turn on system
- 1.6 ALL — Perform system tests
  - 1.6.1 COM — Test communication links
  - 1.6.2 EPS — Test power systems
  - 1.6.3 PRO|GNC — Test flight systems
  - 1.6.4 PLD — Test payload

2 Perform Mission Operations

- 2.1 COM|GNC — Receive mission briefing
  - 2.1.1 COM — Receive mission objectives
    - 2.1.1.1 - **COM** - Receive area of interest
    - 2.1.1.2 - **COM** - Receive target interest requirements
  - 2.1.2 GNC — Check quality of received data
    - 2.1.2.1 - **GNC** - Check for corrupted data
    - 2.1.2.2 - **GNC** - Check for incomplete entries
- 2.2 ALL — Perform pre-flight checks
  - 2.2.1 ALL — Check subsystems
    - 2.2.1.1 - **GNC**- Check status of subsystems
    - 2.2.1.2 - **ALL** - Check responsiveness of subsystems
  - 2.2.2 GNC — Check environment
    - 2.2.2.1 - **GNC** - Check atmospheric conditions
    - 2.2.2.2 - **GNC** - Check take-off area for obstacles
  - 2.2.3 EPS — Check power levels
    - 2.2.3.1 - **EPS** - Check battery health
    - 2.2.3.2 - **EPS** - Check battery charge
  - 2.2.4 PLD — Check payload readiness
    - 2.2.4.1 - **PLD** - Check rock sampling tool
    - 2.2.4.2 - **PLD** - Check scientific instruments
  - 2.2.5 GNC — Check software status
    - 2.2.5.1 - **GNC** - Check control software status
    - 2.2.5.2 - **GNC** - Check communication software status
    - 2.2.5.3 - **GNC** - Check devices' firmware status
    - 2.2.5.4 - **GNC** - Check memory allocation
  - 2.2.6 GNC — Develop flight plan
- 2.3 PRO|GNC — Take-off
  - 2.3.1 GNC — Calibrate attitude sensors
    - 2.3.1.1 - **GNC** - Wait for stable values
    - 2.3.1.2 - **GNC** - Perform calibration
  - 2.3.2 PRO — Perform take-off procedures
    - 2.3.2.1 - **GNC** - Turn on propulsion system
    - 2.3.2.2 - **PRO** - Lift-off
- 2.4 ALL — Conduct contingency operations
  - 2.4.1 GNC — Run diagnostics
    - 2.4.1.1 - **GNC** - Run diagnostics on sensors
    - 2.4.1.2 - **GNC** - Run diagnostics on payload instruments
    - 2.4.1.3 - **GNC** - Run diagnostics for actuators
  - 2.4.2 COM — Report malfunction to ground station (if in range)
    - 2.4.2.1 - **GNC** - Compile malfunction logs
    - 2.4.2.2 - **COM** - Send malfunction logs
  - 2.4.3 ALL — Restart system
    - 2.4.3.1 - **ALL** - Shutdown subsystems
    - 2.4.3.2 - **GNC** - Reboot OBC
    - 2.4.3.3 - **ALL** - Turn on subsystems
- 2.5 PRO|GNC — Fly to designated area
  - 2.5.1 GNC — Fly in correct direction
    - 2.5.1.1 - **GNC** - Determine heading
    - 2.5.1.2 - **GNC** - Control direction of velocity
  - 2.5.2 GNC — Maintain stable flight
    - 2.3.2.1 - **GNC** - Counteract turbulence
    - 2.3.2.2 - **GNC** - Stabilise rotations and translations
  - 2.5.3 PRO — Provide thrust
    - 2.3.2.1 - **PRO** - Provide torque on rotors
    - 2.3.2.2 - **PRO** - Convert torque to thrust
- 2.6 PLD|EPS|GNC — Perform reconnaissance
  - 2.6.1 GNC — Verify drone position
    - 2.6.1.1 - **GNC** - Determine altitude
    - 2.6.1.2 - **GNC** - Determine Martian coordinates
  - 2.6.2 EPS|GNC — Initialise scanning instruments
    - 2.6.2.1 - **EPS** - Power up instruments
    - 2.6.2.2 - **GNC** - Check equipment health status
  - 2.6.3 PLD|GNC — Perform geological survey
    - 2.6.3.1 - **GNC** - Follow flight path
    - 2.6.3.2 - **PLD** - Scan area
    - 2.6.3.3 - **PLD** - Compile data into 3D map
  - 2.6.4 PLD — Identify objects of interest
    - 2.6.4.1 - **PLD** - Detect anomalies in topological properties
    - 2.6.4.2 - **PLD** - Detect anomalies in geological properties
- 2.7 PLD|GNC|PRO — Perform sample collection
  - 2.7.1 PLD — Select sample
    - 2.7.1.1 - **PLD** - Determine sample material characteristics
    - 2.7.1.2 - **PLD** - Determine sample size
  - 2.7.2 GNC|PLD — Land at sample location
    - 2.7.2.1 - **GNC** - Land accurately
    - 2.7.2.2 - **PLD** - Determine sample location
  - 2.7.3 PLD — Collect sample
    - 2.7.3.1 - **PLD** - Grab sample with rock collection arm
    - 2.7.3.2 - **PLD** - Retract arm back into stowed position with rock sample
- 2.8 ALL — Land near ground station
  - 2.8.1 GNC — Determine landing spot
    - 2.8.1.1 - **GNC** - Check proximity of ground station
    - 2.8.1.2 - **GNC** - Check for accessible points
    - 2.8.1.3 - **GNC** - Select optimal spot based on available info
  - 2.8.2 PRO|GNC — Carry out landing procedures
    - 2.8.2.1 - **PRO|GNC** - Fly towards landing site
    - 2.8.2.2 - **PRO|GNC** - Descend
    - 2.8.2.3 - **PRO|GNC** - Touchdown
  - 2.8.3 COM — Communicate data with ground station
    - 2.8.3.1 - **COM** - Establish communication link
    - 2.8.3.2 - **COM** - Transmit telemetry data
    - 2.8.3.3 - **COM** - Transmit scientific data
  - 2.8.4 ALL — Hibernate until further instructions
- 2.9 ALL — Perform vital functions
  - 2.9.1 EPS — Manage power
    - 2.9.1.1 - **EPS** - Generate power
    - 2.9.1.2 - **EPS** - Distribute power
    - 2.9.1.3 - **EPS** - Store power
  - 2.9.2 GNC — Perform data handling operations
    - 2.9.2.1 - **PLD|GNC** - Acquire payload data
    - 2.9.2.2 - **GNC** - Enable communication between subsystems
    - 2.9.2.3 - **PLD|GNC** - Acquire sensor data
    - 2.9.2.4 - **GNC** - Create data logs
  - 2.9.3 GNC — Perform attitude control
    - 2.9.3.1 - **GNC** - Determine attitude from sensor data
    - 2.9.3.2 - **GNC** - Determine the required attitude
    - 2.9.3.3 - **GNC** - Apply change in attitude through actuators
  - 2.9.4 GNC|PRO — Manage system thermals
    - 2.9.4.1 - **GNC** - Monitor component temperatures
    - 2.9.4.2 - **GNC|PRO** - Perform temperature adjustment
    - 2.9.4.3 - **PRO** - Throttle system to avoid damage
  - 2.9.5 GNC — Perform GNC operations
    - 2.9.5.1 - **GNC** - Establish current position
    - 2.9.5.2 - **GNC** - Determine navigation plan
    - 2.9.5.3 - **GNC** - Adjust flight path

3 Conduct End-of-life Operations

- 3.1 GNC — Perform final system checks
- 3.2 ALL — Perform EOM operations
  - 3.2.1 PRO|GNC — Land near groundstation
  - 3.2.2 PLD — Gather environmental data
  - 3.2.3 COM — Communicate gathered data to ground station
- 3.3 COM — Report end of mission

Legend

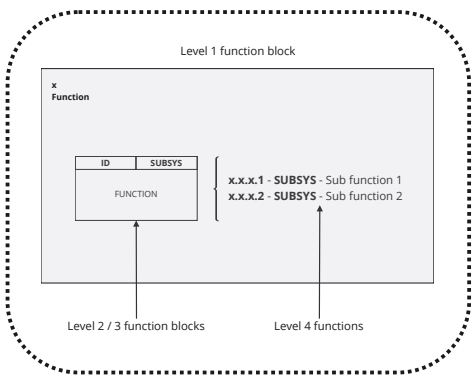

Abbreviations:

GNC: Guidance, Navigation and Control
COM: Communication
EPS: Electrical power system
OBC: Onboard computer
PLD: Payload
PRO: Propulsion
STR: Structures

17 Design Feasibility Analysis

***Authors**: Salar, Maurits, Florian, Dionysis, Li, Jesse*

This chapter evaluates the feasibility of the drone design. Various analyses are performed to assess the viability of the final design from multiple perspectives.

First, a flight performance analysis is provided in Section 17.1. Then, Section 17.2 details the robustness of the design through a sensitivity analysis. Section 17.3 involves the verification of requirements using a compliance matrix, whereas Section 17.4 provides the V&V procedures to be implemented for the final design. Lastly, Section 17.5 concerns the reliability, availability, maintainability and safety analysis of the final design.

17.1. Performance Analysis

***Authors**: Salar*

Now that a bottom-up design of the rotor exists, a detailed flight performance model has been made. All performance calculations use non-dimensionalised variables; the airspeed V is non-dimensionalised to the advance ratio $\mu = V/V_t$ where V_t is the blade tip speed, known from Section 8.2. For thrust and power, coefficient forms are used. The calculations in this section rely heavily on the blade model from Chapter 8. Using thrust and power coefficients, the performance curves can be calculated for a variety of conditions. It is important to consider that performance plots in this section are all per individual rotor; summing them gives the total rotor system power. This is intentionally conservative as the effects of interference due to the upwash flow field and elliptical distribution between adjacent disks are ignored [7].

17.1.1. Rotor Wake

Forward flight analysis starts with the calculation of the wake properties of the rotor. This begins by calculating the (small) angle of incidence $i = D/W$ where D is the parasite drag of the helicopter and W is the weight [7]. This equation is valid for non-climbing flight, which is the cruise case considered in flight performance. To estimate the parasite drag area, the empirical relation from Johnson is used [7]:

$$f = \frac{D}{q} = 2.5K\left(\frac{m}{1000}\right)^{2/3} \tag{17.1}$$

In Equation 17.1, K is a unit conversion factor from Imperial units, equal to 0.15737. This is the rotorcraft parasite drag per unit dynamic pressure q. From here, the drag itself can be computed as a function of the advance ratio:

$$D = fq = f\frac{1}{2}\rho V^2 = f\frac{1}{2}\rho V_t^2\mu^2 \tag{17.2}$$

This gives the angle of incidence required as a function of advance ratio:

$$i = \frac{D}{\mathrm{W}} = \frac{1}{2}\frac{f\rho V_t^2}{mg}\mu^2 \tag{17.3}$$

Wake properties follow using the angle of incidence i and mean inflow in hover:

$$\lambda_h = \frac{C_{P_i}}{C_T} \tag{17.4}$$

Here, the subscript h indicates hover, and the coefficients are known from Section 8.2. In forward flight, there are two components to inflow:

$$\lambda = \mu\tan i + \lambda_i \tag{17.5}$$

The first term, named normal inflow, is caused by the perpendicular (to the rotor) component of the fluid flow encountered by the rotor disk, due to its angle of incidence. The following Newton-Raphson iteration can be

used to compute λ, making use of the normal inflow $\mu_z = \mu \tan i$:

$$\hat{\lambda}_0 = \frac{\lambda_h}{\sqrt{(\lambda_h + \mu_z)^2 + \mu^2}} + \mu_z \tag{17.6}$$

$$\hat{\lambda}_{in} = \frac{\lambda_h^2}{\sqrt{\hat{\lambda}_n^2 + \mu^2}} \tag{17.7}$$

$$\hat{\lambda}_{n+1} = \hat{\lambda}_n - \frac{\hat{\lambda}_n - \mu_z - \hat{\lambda}_{in}}{1 + \hat{\lambda}_{in}\hat{\lambda}_n / \left(\hat{\lambda}_n^2 + \mu^2\right)} \tag{17.8}$$

After convergence, λ and λ_i are known as functions of the advance ratio.

17.1.2. Forward Flight

In forward flight, the induced power coefficient decreases with the advance ratio; it is given by Equation 17.9

$$C_{P_i}(\mu) = \lambda_i(\mu) \cdot C_T \tag{17.9}$$

In this equation, C_T is the induced power coefficient known from hover design. The profile power coefficient now has a component due to the tangential velocity, and the integral from Equation 8.11 now contains an additional term [7]:

$$C_{P_o}(\mu) = \int_{\tilde{r}_0}^{1} \frac{1}{2}\sigma(\tilde{r}) \cdot c_d \tilde{r} \cdot \left(\tilde{r}^2 + \frac{1}{2}\mu^2\right) \mathrm{d}\tilde{r} \tag{17.10}$$

Lastly, the parasite power coefficient is calculated using the parasite drag area f from Equation 17.1:

$$C_{P_p}(\mu) = \frac{1}{2}\frac{f}{A}\mu^3 \tag{17.11}$$

Summing the three coefficients from Equation 17.9, Equation 17.10 and Equation 17.11 gives the power coefficient C_P of the rotor as a function of the advance ratio. It is interesting to notice that this is equivalent to the torque coefficient C_Q [7]. This results in the plot shown in Figure 17.1.

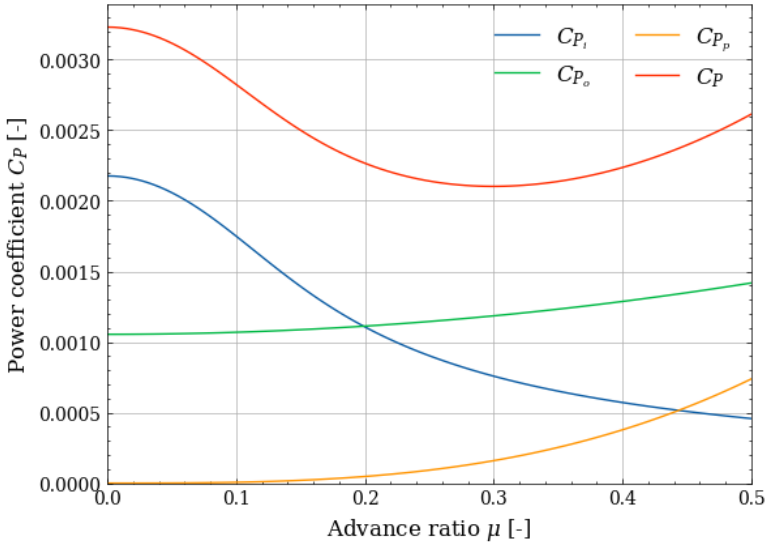

Figure 17.1: Power coefficients as a function of advance ratio

The power coefficient C_P in Figure 17.1 serves as a baseline function to calculate the power required under different conditions. The plot in the figure is independent of rotational speed, air density or other parameters; it is purely a property of the blade itself. As expected, induced power dominates at low advance ratios but quickly tapers off; profile power always has a presence, whereas parasite power only appears at high advance ratios due to the high airspeed. Equation 17.12 shows the maximum advance ratio at which drag divergence occurs. Per

NASA, a value of up to 0.95 for the advancing blade tip Mach number is acceptable without noticeable effects. The tip Mach number M_{tip}, equal to 0.7, comes from Section 8.2.

$$\mu_{\max} = \frac{M_{\text{at}}}{M_t} - 1 \tag{17.12}$$

Since the inputs to Equation 17.12 are design parameters, the maximum advance ratio is fixed at 0.357.

17.1.3. Flight Performance

In Chapter 8, the rotor blade was sized with a thrust-to-weight ratio of 1.3 in mind. When considering flight performance, the power required does not account for this ratio; excess power can be used for climbing or manoeuvring, hence the use of the margin in the first place. The use of nondimensional coefficients facilitates this process. Considering forward flight without climb, the equation for the thrust (equal to weight) is the following, where the tip speed has been separated into $V_t = \Omega R$, where Ω is the rotational speed of the rotor; this is the variable which affects the tip speed, depending on the thrust required. The maximal value of 1443 rpm is only necessary with a 1.3 margin in mind.

$$mg = C_T \rho A R^2 \Omega^2 \tag{17.13}$$

Solving for the rotational speed gives:

$$\Omega = \sqrt{\frac{mg}{C_T \rho A R^2}} \tag{17.14}$$

This value can now be used (alongside the constant rotor radius R to get the tip speed) to dimensionalise calculations. The airspeed V for a given set of conditions is given by:

$$V = \mu \Omega R \tag{17.15}$$

Similarly, the required power P is given by:

$$P = C_P \rho A R^3 \Omega^3 \tag{17.16}$$

The dimensionalising values in Equation 17.15 and Equation 17.16 are all constants for a given set of environmental conditions, allowing for performance plots to be made. Using Figure 17.1 as a reference, a performance plot is shown in for the standard hover conditions (no thrust margin) in the selected limiting environmental case (minimum density) from Section 8.2.3 in Chapter 8. Figure 17.2 shows a performance plot for the hexacopter in

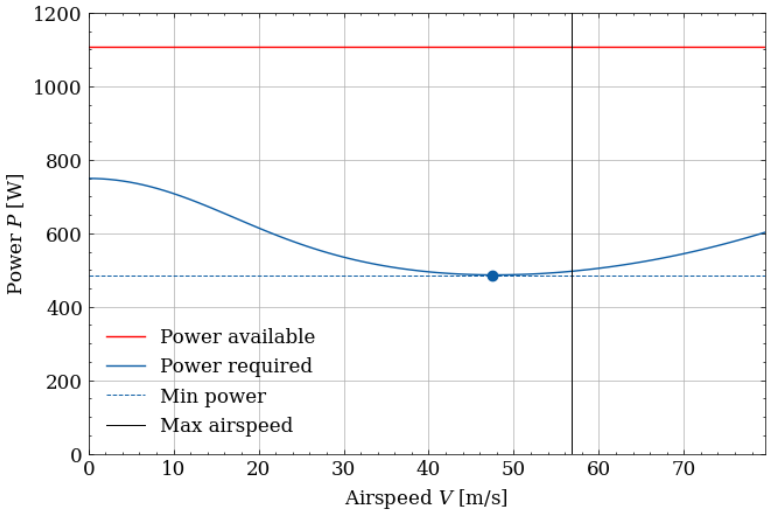

Figure 17.2: Required and available power as a function of airspeed in limiting conditions

minimum density (limiting) conditions, where the density ρ is equal to 0.0127 kg m^{-3}. In these conditions, it can still be observed that the thrust margin provides substantial excess power if it is required for climb, even in pure hover. Given that the rock collection system in Chapter 15 is designed with a 1.5 safety factor, this thrust margin allows for unaffected performance at an increased rock mass of up to 4.5 kg, well above the requirement.

The maximum power used is in hover, equal to 749 W. Meanwhile, the minimum power required of 486 W occurs at an airspeed of 47.4 m s^{-1}; this is the theoretical optimum for endurance. For a pure cruise endurance calculation, considering the maximum battery capacity of 2301 W h from Chapter 9, the motor efficiency of 90 % from Chapter 8 and all six rotors operational, the maximum endurance is 42 minutes. This is a theoretical flight performance maximum in pure cruise. The electrical power and thermal control systems have been designed with the endurance requirement already in mind, which serves as a verification for compliance with the requirement.

It is valuable to check compliance with the range requirement. While the theoretical optimum could be used, endurance airspeed is already large, due to the considered conditions. As a result, checking for range compliance at this airspeed is sufficient. Multiplying the airspeed by the endurance gives over 100 km of range, well beyond the requirement. This does not necessarily mean the drone will ever fly this distance, as it assumes a permanent, high-speed cruise. In general, it is important to remember that these flight performance calculations are made to verify the design's robustness under different conditions and that the subsystems have built-in performance margins. This range check isolates endurance and rock mass as independent, limiting user requirements.

Lastly, the performance variation is checked at different density conditions to confirm that this prior analysis is valid for the extreme case. Four equally spaced values of density are used, covering the relevant range according to the Mars Climate Database model at the selected location [4]

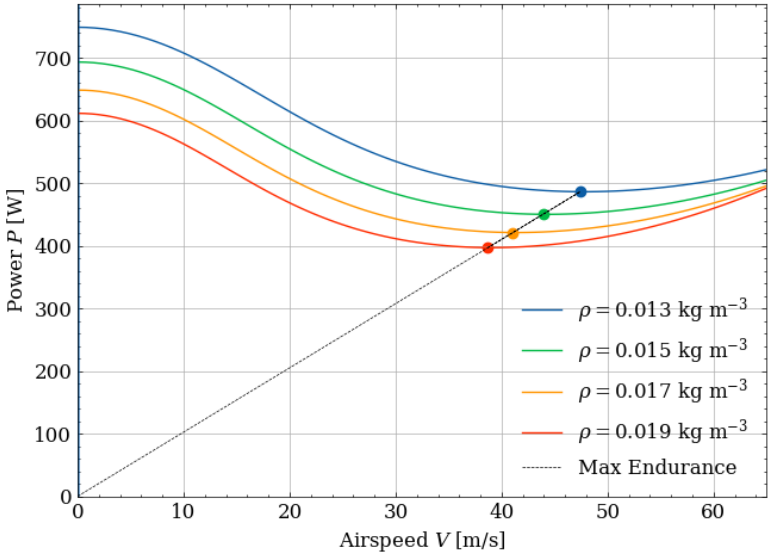

Figure 17.3: Variation of performance with air density

As expected, increased density results in less power and a lower range of airspeeds. Equation 17.14 can be substituted into Equation 17.15 and Equation 17.16 to get Equation 17.17:

$$V = \frac{1}{C_T^{1/2}} \sqrt{\frac{mg}{\rho A}} \cdot \mu \qquad P = \frac{1}{C_T^{3/2}} mg \sqrt{\frac{mg}{\rho A}} \cdot C_P(\mu) \tag{17.17}$$

Equation 17.17 displays the transformations used to generate performance plots from the characteristic C_P–μ plot of the rotor, Figure 17.1. In both cases, the only external variation for a given blade design and hexacopter mass is due to the air density ρ, and both airspeed and power scale with the inverse square root of air density. Essentially, considering the plot in Figure 17.2 to be a locus of initial (V, P) pairs, every pair of coordinates has both of these scaled by $\sqrt{\rho_0/\rho}$, where ρ_0 is the initial air density and ρ is the updated value (corresponding to the different air densities). This includes the minimum power point (optimal for endurance), hence the line from the origin connecting the points for each curve.

Since range is not a demanding requirement, very high speeds are not necessary, given that endurance is met. The endurance speed corresponding to the highest density is selected as a reference, thus 38.1 m s^{-1}; this also provides a margin between the cruise speed and the airspeed at which drag divergence becomes non-negligible. In the limiting density case, this corresponds to a cruise rotor power of exactly 500 W. This is still approximately 67 % of hover power, well below the maximum estimate of 75 %.

17.2. Sensitivity Analysis

***Authors**: Salar, Maurits*

Whereas the performance analysis observed the effect of varying external parameters on the *selected* design's performance, the sensitivity analysis carries out a new system-wide iteration after a changed parameter. The driving user requirements were particularly considered. These were the 30 min endurance and 3 kg rock mass requirements. The 20 km range requirement was not considered, as the endurance requirement already results in a design that exceeds this range requirement.

Table 17.1: User requirement sensitivity analysis

Initial values

i	0	Unit
m_{PLD}	8.85	kg
m_{GNC}	1.30	kg
m_{COM}	0.25	kg
m_{PRO}	4.50	kg
m_{EPS}	20.18	kg
m_{TCS}	5.65	kg
m_{STR}	7.95	kg
m	48.68	kg
Δm	–	%

Endurance 5% increase

i	1	2	Unit
m_{PLD}	8.85	8.85	kg
m_{GNC}	1.30	1.30	kg
m_{COM}	0.25	0.25	kg
m_{PRO}	4.50	4.53	kg
m_{EPS}	20.44	20.44	kg
m_{TCS}	5.65	5.75	kg
m_{STR}	7.95	7.95	kg
m	48.94	49.07	kg
Δm	+0.5	+0.3	%

Rock mass 5% increase

i	1	2	Unit
m_{PLD}	8.99	8.99	kg
m_{GNC}	1.30	1.30	kg
m_{COM}	0.25	0.25	kg
m_{PRO}	4.50	4.53	kg
m_{EPS}	20.18	20.18	kg
m_{TCS}	5.65	5.65	kg
m_{STR}	7.95	7.95	kg
m	48.82	48.85	kg
Δm	+0.3	+0.1	%

Table 17.1 shows three tables; a set of origin values (iteration 0), from Section 16.1; system-wide iterations with the endurance increase, until convergence; and the same for the rock mass increase. The symbol i denotes the iteration number. The same criteria for convergence were used as in the design iteration from Section 16.1; one iteration within a 1% mass increase and a subsequent iteration with a smaller relative increase to confirm convergence.

In the case of endurance, the first system-wide iteration initially only affects the electrical power and thermal control systems. This is because the two subsystems are sized according to the mission profile derived from the endurance requirement. After this increase, the mass increment is already within the convergence constraint; to confirm convergence, a full system iteration is carried out as described by Figure 16.1. The iteration resulted in a final mass of 49.07 kg. Table 17.2 displays the changes in design parameters due to this increase in endurance.

Table 17.2: Changes in design parameters due to endurance increase

Parameter	Initial Value	Final Value	Unit	Change
Endurance	30	31.5	min	+5.0 %
Maximum Rotor Power	1108	1117	W	+0.8 %
Rotor Solidity	0.163	0.164	–	+0.6 %
Solar Array Mass	6.036	6.304	kg	+4.4 %
Cooling Fin Mass	5.254	5.456	kg	+3.8 %

Since the design of the rock collection mechanism depends on the rock mass, a 5% increase in said rock mass will only directly affect the payload subsystem. The increased rock mass caused the motors in the elbow and shoulder of the robotic arm to fail. Switching the motors for new motors was not an option due to the limitation of the motor catalogue. Instead, the forearm was shortened by 1 cm, and the upper arm by 1.5 cm. A shorter arm leads to lower bending moments and, therefore, lower required motor torques. While a shorter arm is not preferred, it does not affect the mission significantly as it is still within the limit of the landing accuracy determined by the control system in Figure 11.10. After the first iteration and the second system-wide iteration, the mass converged to a final value of 48.85 kg. Table 17.3 below displays the changes in the important design parameters due to the rock mass increase.

Table 17.3: Changes in design parameters due to rock mass increase

Parameter	Initial Value	Final Value	Unit	Change
Rock Mass	3.0	3.15	kg	+5.0 %
Maximum Rotor Power	1108	1113	W	+0.5 %
Rotor Solidity	0.163	0.165	-	+1.2 %
Robotic Arm Length	0.55	0.525	m	-4.5 %

17.3. Compliance Matrix

***Authors**: Florian, Salar*

In Table 17.4, the compliance of the final design with user and subsystem requirements is presented. For any requirements that are not met, a rationale is provided, explaining the reasons and implications of non-compliance. It is important to note that at this stage of the design process, many requirements cannot be fully verified until testing is conducted. Requirements that the current design meets according to analysis but still need confirmation through detailed design phase testing are marked with an asterisk (*).

Table 17.4: Requirement compliance matrix

User requirements

Req. ID	Complied?
STK-USER-01	Yes*
STK-USER-02	Yes*
STK-USER-03	Yes*
STK-USER-04	Yes*
STK-USER-05	Yes*
STK-USER-06	Yes*
STK-USER-07	No
STK-USER-08	Yes
STK-USER-09	Yes
STK-USER-10	Yes*
STK-USER-11	Yes*
STK-USER-12	Yes*
STK-USER-13-I	Yes
STK-USER-14-I	No
STK-USER-15-I	Yes
STK-USER-16	Yes*

Propulsion

Req. ID	Complied?
PRO-SYS-01	Yes*
PRO-SYS-02	Yes*
PRO-SYS-03	Yes
PRO-SYS-04	Yes*
PRO-SYS-05	Yes
PRO-SYS-06	No
PRO-SYS-03-10	No
PRO-SYS-03-01-I	Yes
PRO-SYS-03-02-I	Yes
PRO-SYS-03-03-I	Yes
PRO-SYS-03-04-I	Yes
PRO-SYS-02-01	Yes*
PRO-SYS-02-02	Yes*
PRO-SYS-02-03	Yes*
PRO-SYS-02-04	Yes*
PRO-SYS-07	Yes*

Guidance, navigation and control

Req. ID	Complied?
GNC-SYS-01	Yes
GNC-SYS-01-01	Yes*
GNC-SYS-01-02	Yes*
GNC-SYS-01-03	Yes*
GNC-SYS-01-04-I	Yes*
GNC-SYS-01-05	Yes*
GNC-SYS-02	Yes*
GNC-SYS-02-01	Yes*
GNC-SYS-02-02	Yes*
GNC-SYS-02-02-01	Yes*
GNC-SYS-02-02-02	Yes*
GNC-SYS-03-I	Yes*
GNC-SYS-03-01-I	Yes*
GNC-SYS-03-02-I	Yes*
GNC-SYS-04-I	Yes*
GNC-SYS-05-I	Yes*
GNC-SYS-06-I	Yes*
GNC-SYS-07-I	Yes*
GNC-SYS-08-I	Yes*

Structures and materials

Req. ID	Complied?
STR-SYS-01	Yes
STR-SYS-02	Yes
STR-SYS-02-05	Yes
STR-SYS-03	Yes
STR-SYS-08	Yes
STR-SYS-05	Yes*
STR-SYS-15	Yes*
STR-SYS-07	Yes*
STR-SYS-12	Yes
STR-SYS-13	Yes*
STR-SYS-14	Yes
STR-SYS-09	Yes
STR-SYS-11	Yes

Payload and instrumentation

Req. ID	Complied?
PLD-SYS-04	Yes*
PLD-SYS-04-01	Yes*
PLD-SYS-04-03	Yes
PLD-SYS-06	Yes*
PLD-SYS-06-01	Yes

Communications

Req. ID	Complied?
COM-SYS-01	Yes
COM-SYS-03	Yes
COM-SYS-03-04	Yes

Electrical power

Req. ID	Complied?
EPS-SYS-02-01-I	Yes*
EPS-SYS-03-I	Yes*
EPS-SYS-06-I	No
EPS-SYS-07	Yes
EPS-SYS-10-02-I	Yes
EPS-SYS-11-I	Yes*
EPS-SYS-13-I	Yes*
EPS-SYS-14-I	Yes*
EPS-SYS-16	Yes
EPS-SYS-17	Yes*

Thermal control

Req. ID	Complied?
TCS-SYS-01-04-01-I	Yes*
TCS-SYS-01-06-01	Yes*
TCS-SYS-01-07-01	Yes
TCS-SYS-01-08-01	Yes*
TCS-SYS-01-08-02	Yes*
TCS-SYS-01-09-01	Yes
TCS-SYS-01-09-02	Yes
TCS-SYS-01-09-03	Yes*

Rock collection

Req. ID	Complied?
RCS-SYS-01	Yes
RCS-SYS-02	Yes
RCS-SYS-03	Yes
RCS-SYS-04	Yes
RCS-SYS-05	Yes
RCS-SYS-06	Yes
RCS-SYS-07	Yes
RCS-SYS-08	Yes

Some requirements in Table 17.4 have not been complied with. The details of such requirements are summarised and explained in Table 17.5:

Table 17.5: Requirements not complied by the current design

ID	Requirement	Reason for non-compliance
STK-USER-07	The Martian Drone shall be capable of real-time communication with a Mars ground station.	Infeasible in the Martian environment
STK-USER-14-I	The Martian Drone shall help answer the question: "Did life ever exist on Mars?"	Can only be verified after mission completion
PRO-SYS-06	The propulsion system shall be able to perform dust removal operations	Irrelevant, as the selected motor has a protection class of at least IP54 and a closed design
PRO-SYS-03-10	The propulsion system shall produce enough thrust with two rotors inoperative	Infeasible within constraints, drone designed for one-rotor inoperative
EPS-SYS-06-I	The power distribution system shall be designed to provide a peak power of 7387 W, the power usage when the drone's six rotors operate at a T/W of 1.3	To be confirmed by further analysis in detailed design

17.4. Verification and Validation Procedures

Authors: *Dionysis, Li*

Apart from the verification and validation of the design tools performed as part of subsystem designs, which were presented in their respective chapters, it is important to consider the V&V process of the final design as a whole. In Chapter 4 the system requirements were presented to the reader. In order to perform verification, one of the following methods were proposed:

- **Analysis**: Analysis requires theoretical and empirical methods in agreement with the Stakeholders.
- **Inspection**: Inspection requires visual determination of physical characteristics of the product.
- **Demonstration**: Demonstration requires the operation or relevant function to be performed during the mission or of a test article.
- **Test**: Testing the product requires functions and performance to be measured of a part of the system under representative simulated environments with verified equipment.
- **Review**: Review requires approved documentation that shows beyond doubt that the requirement is met.

As a follow-up to the verification plan initially derived during the formulation of the requirements, more detailed tests will be suggested to account for the verification and validation of the system components of the final design. Some of these tests are proposed as follows:

- **Powertrain performance test**: A stress test for the powertrain of the drone shall be conducted, during which the actual performance characteristics of the designed system will be established. The motors and propellers would be integrated on a test bench, ideally placed in conditions that reflect the Martian atmosphere. The powertrain's power consumption, output and efficiency can be assessed during such a test.
- **Thermal-Vacuum (TV) test**: A robustness test for the propulsion system shall be performed during which the resistance of the rotors to dust, temperature and other environmental conditions can be assessed.
- **Radiation test**: The individual components, with emphasis on the electronics, will be subjected to the expected level of radiation on the Martian surface.
- **Dust resistance test**: Critical components such as motors, solar arrays and electronics shall be protected from environmental dust, which is a key factor on Martian soil. The system will be subjected to dust particles to ensure that this is the case and no significant damage due to foreign particles are sustained.
- **Vibration, Shock and Acoustics (VSA) test**: During the preliminary design of the drone structure, mostly static structural loading scenarios were considered. However, assessing the structure's capability to withstand vibrations and shock loads that occur during operation is important.
- **Stress and Fatigue test**: The cyclic loading of load-carrying parts of the structure makes it susceptible to fatigue failure. Even though materials with high fatigue resistance have been chosen, it is important to verify that fatigue failure occurs at a sufficiently high cycle number.
- **Field flight test**: The flight controller will be implemented on an Earth-based hexacopter to validate the robustness of the proposed control system. Real-life data will be measured, which can be used to validate the hexacopter dynamic model used to develop the flight controller.
- **Software-in-the-Loop (SIL) test**: This test involves testing the flight control software in a simulated Martian environment. This test can help verify the flight software and help detect bugs before integrating with hardware. Such tests can be implemented in robotics simulation software such as Gazebo [1] .
- **Electronics integration test**: A system-level integration test will be carried out to ensure that the hardware components work together and perform the desired functions.
- **Battery Cycling test**: Li-Ion batteries degrade as they are used. To ensure the compatibility of the selected batteries with the mission, they shall be cycled, charged and discharged at rates comparable to those during operation. The battery degradation statistics derived from such a test can provide confidence for the power storage system.
- **Solar Array Performance test**: The capability of the solar array to charge the batteries should be assessed under representative conditions for the Martian environment. The correct Martian light spectrum,

[1] URL: https://gazebosim.org/home [cited on 18 Jun 2024]

intensity, and temperature variations on the solar cells and the batteries through the charging cycles shall be reproduced for this test.

- **Robotic Arm Functional test**: A robotic arm to collect rock samples will be developed for this mission. The capability of the arm to collect samples similar to those present in the intended operation environment shall be tested, and its resistance to the stresses experienced during such operation shall be verified.
- **Communications Link Test**: To ensure reliable communication between the drone and the ground station, it is important to assess the performance of the communication system under conditions that replicate the range and attenuation expected in the Martian environment.
- **Electromagnetic Compatibility (EMC) test**: Such a test would ensure the system's capability to operate in Mars's electromagnetic environment.

17.5. RAMS Analysis

***Authors**: Jesse*

This section outlines the RAMS characteristics of the mission, thereby providing a detailed analysis of the drone's performance on Earth and Mars. This includes an assessment of its reliability, availability, maintainability and safety considerations to ensure secure operations.

Reliability

Ensuring the reliability of the drone requires extensive long-term testing to quantify the reliability of the various subsystems accurately. As such, achieving high reliability involves integrating redundant systems, which are key for meeting the mission's requirements. However, adding such redundancy is not always effective and can increase risk. To mitigate these risks, it is essential to ensure that component failures are independent, thereby avoiding dependencies where failures might have a common source [63].

These redundant systems directly translate to various subsystems. Firstly, to ensure the GNC's subsystem reliability, two onboard computers and Fisheye cameras are included for redundancy, and two independent Inertial Measurement Units, capable of determining the drone's linear acceleration and angular rate, are present. Lastly, to prevent electrical failures, redundant wiring to the rotor arms is incorporated, ensuring that a single point of failure in the wiring does not disrupt the entire system.

Achieving high reliability in a complex system is challenging. New technologies are often prone to design errors and operational problems that can only be detected and corrected through extensive testing and operational experience. To mitigate these issues, the drone uses existing, flight-proven technologies for some critical components, such as the motors of the grabbing mechanism and the rotors. This reduces the risk of design flaws and operational issues, as these technologies have already undergone testing and have established reliability. Long-term testing is conducted to detect potential design errors and operational problems. This process involves simulated Martian conditions to test if the drone can withstand and operate effectively in the Martian environment.

Maximising reliability also involves using clean rooms throughout the assembly process, which minimises the risks of exposure to contaminates and affects the system in space. Clean rooms are further elaborated upon in Chapter 18.

Availability

The availability of the drone is related to its operational status at any given time. On Mars, maximising the availability of the drone primarily involves its ability to perform the mission, which depends on several environmental factors. One of the most important considerations is power generation, as its performance can be severely impacted by Martian dust storms, which can block sunlight and accumulate on the solar arrays. Moreover, there is a high probability that the solar flux will deviate from the simulated conditions. It was therefore decided to use solar arrays, spanning a total of $3.02\,m^2$ and have batteries capable of storing up to 2375 W h of energy to maintain operation during prolonged periods of low sunlight.

Atmospheric conditions on Mars also significantly affect the drone's availability. The thin Martian atmosphere poses unique challenges for flight. Therefore, the most extreme environmental conditions were assumed to maximise availability, with atmospheric temperatures ranging from 253.15 K to 304.48 K.

Lastly, the drone's mission profile also greatly affects its availability. The typical mission requires the drone to fly for up to 30 minutes while carrying Martian rocks weighing up to three kilograms. The drone must be capable of completing its mission within the constraints of its power supply and environmental challenges, potentially leading to fewer available operational windows.

Maintainability

Since the drone will operate on Mars, only autonomous maintainability is possible. Physical maintainability is difficult to achieve on Mars, since physical reparations of parts are not feasible. Therefore, Maintenance procedures can be divided into scheduled and non-scheduled maintenance.

Scheduled maintenance checks are sent from the ground station to the drone. These checks include a variety of tasks designed to monitor and preserve the health of the drone's systems. Scheduled maintenance involves routine checks and preventative measures, such as dust cleaning procedures, battery health checks, or a full communication system test. Furthermore, regular software updates will be sent to the drone to address potential bugs.

In addition to scheduled maintenance, non-scheduled maintenance procedures, which address unforeseen failures or issues, must also be considered. This includes an autonomous fault detection system and a response mechanism such that the drone responds accordingly to reduce the impact.

Safety

The last aspect of the RAMS analysis is the safety of the system. This can be divided into safety considerations both on Earth and on Mars. The main responsibilities on Earth follow NASA's Michoud Safety protocols [2] :

- **Mission & Flight Safety**: ensure the safe and proper execution of all development, manufacturing and integration efforts
- **Personal & Workforce Safety**: comply with all health, safety and federal guidelines
- **Facilities & Environmental Safety**: conduct routine quality-assurance checks on all hardware, tools and other resources to ensure adherence to workplace and environmental safety guidelines

The points above are especially important in the context of handling Beryllium; a toxic metal that is used in certain components of the drone. Different regulatory agencies exist, including the Occupational Safety and Health Administration and the United States Department of Energy, each having separate rules on Beryllium exposure. For instance, the former sets an permissible exposure limit of $2.0\,\mu g\,m^{-3}$, averaged over an 8 h work shift. A safe workplace shall also be created, through the use of three control methods, including engineering controls, administrative controls and personal protective equipment [3] . More requirements on Beryllium are stated in the Occupational Safety and Health Administration Beryllium Standard [4] , and should be followed carefully when handling the metal on Earth.

Safety on Mars can be maintained using fail-safe systems that have sufficient redundancy in the design and are closely related to the reliability characteristics. Most design components rely on the electrical power subsystem, requiring extensive testing. As such, these subsystems are critical in ensuring the system's safety. The drone will have a reduced power mode, allowing it to conserve energy during periods of low sunlight or other unfavourable conditions. This mode would reduce non-essential functions, focusing power on critical systems, such as the thermal control subsystem.

Upon completing testing, the drone can be integrated into the aeroshell and the launch vehicle. To obtain the safety approval needed for this integration, it must be demonstrated that the drone and the company's operations at Guiana Space Centre, where Ariane 6's launch site is located, adhere to the centre's Safety Regulations. This process involves multiple stages, where the company submits documents detailing and describing hazardous elements and their subsequent processing. The company should prepare these documents and send them to Arianespace, which assists in coordinating with Guiana Space Centre's Authorities [14].

[2]URL: https://www.nasa.gov/michoud-assembly-facility/michoud-safety/ [cited on 11 June 2024]
[3]URL: https://www.energy.gov/sites/prod/files/2014/09/f18/communicating_0.pdf [cited on 25 June 2024]
[4]URL: https://www.osha.gov/laws-regs/regulations/standardnumber/1910/1910.1024 [cited on 25 June 2024]

18 Future Development

***Authors**: Jesse, Maurits, Florian, Vini*

In this chapter, the future development of the drone is investigated. This will first be done through a production plan, in Section 18.1, which includes the manufacturing, assembly and integration considerations of the drone. Then, in Section 18.2, a project design and development logic diagram, and post-DSE Gannt chart is provided, explaining the activities to be performed after DSE. Finally, a cost breakdown is provided in Section 18.3, which identifies the elements that drive the future costs of the project.

18.1. Manufacturing, Assembly and Integration Plan

***Authors**: Jesse*

After approval of the final design of the drone, manufacturing of the different components can initiate. To make the manufacturing process of the drone as sustainable as possible, emphasize will be placed on minimising waste. Additive manufacturing provides a promising solution to this challenge. Unlike traditional methods, additive manufacturing minimises material usage by only adding material where needed. A notable milestone in the use of 3D printing for space exploration was achieved by NASA's Curiosity rover, which included a 3D-printed ceramic part within its Sample Analysis at Mars instrument . Building on this success, NASA's Perseverance rover also features 3D-printed metal parts, further demonstrating the reliability and advantages of this technology in Mars' harsh environment[1] . While 3D printing is a promising alternative, other manufacturing processes must also be evaluated based on the expected quality of the final product. Precision machining, for instance, is a popular technique for fabricating components. Using computer numerical controlled (CNC) machines, precision machining ensures that components are manufactured with high accuracy and tight tolerances. Depending on the chosen manufacturing process, potential manufacturing facilities can be decided upon. For instance, at the Johnson Space Center, relevant manufacturing processes are supported through three advanced facilities, as summarised below[2] .

- **JSC Central Manufacturing**: facilitates the production of flight hardware, ground support hardware, and prototype hardware, and provides expertise in precision machining, sheet metal fabrication, welding, coatings and heat treating
- **Additive Manufacturing Laboratory**: facilitates the production of plastic and metal components through 3D printing methods
- **White Sands Test Facility**: facilitates prototyping and production of parts for in-flight usage and ground equipment, and provides CNC machining and welding machines

Manufacturing of components will only be applicable to parts that are designed in-house, such as the robotic arm, rotor blades or landing struts. Off-the-shelf products are readily available and therefore require no specific manufacturing process.

The assembly of the drone then occurs at a designated area. Potential locations include Airbus Bremen, which played a crucial role in the assembly of three European Service Modules [3] . Similarly, final assembly of NASA's products occur at NASA's Jet Propulsion Laboratory. The assembly process is divided into sub-assembly and main assembly procedures. Sub-assembly involves tasks such as assembling the rotors, constructing the central frame, or assembling the robotic arm. These assemblies are a combination of parts that are designed in-house and off-the-shelf products. The propulsion sub-assembly, for example, is a combination of the NOVA 1 motor and the rotor blades. Sub-assembly of the bus includes the installation of sensors, camera's, spectrometer and other electronic devices. The main assembly includes the attachment of these sub-assemblies and ensure connectivity between the subsystems.

[1] URL: https://www.nasa.gov/centers-and-facilities/jpl/nasas-perseverance-rover-bringing-3d-printed-metal-parts-to-mars/ [cited on 17 June 2024]

[2] URL: https://www.nasa.gov/reference/jsc-assembly-integration/ [cited on 17 June 2024]

[3] URL: https://www.airbus.com/en/newsroom/press-releases/2023-02-airbus-european-service-modules-three-in-a-row [cited on 17 June 2024]

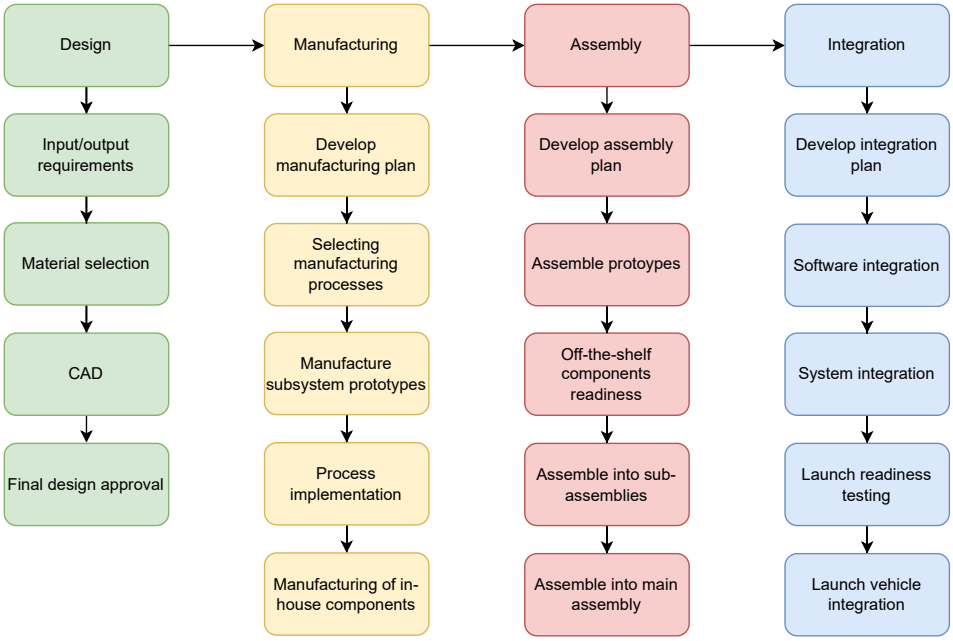

Figure 18.1: Manufacturing, assembly and integration plan flow diagram

To make sure that collected rock samples are protected from Earthly contaminates, Planetary Protection and Contamination Control requirements have to be followed throughout the assembly process. Assembly and testing therefore take place in cleanrooms to eliminate microscopic contaminants that could damage sensitive equipment. Personnel working in these areas must wear protective clothing. Special attention will be given to contamination sensitive hardware, also referred to as Sample Intimate Hardware (SIH). SIH, such as the robotic arm, directly contacts the sample material and requires the most strict and sterile assembly techniques, in a cleanroom with at least an ISO 5 rating [64].

After the assembly phase, final integration techniques of the full system take place. This step involves relevant software integration and connectivity between the subsytems. Testing of the complete system can then be conducted for validating the system's readiness for launch. Key tests include vibrational tests, thermal vacuum tests, spin balance testing, and electromagnetic interference testing[4] . Such tests can be performed at facilities like ESA's ESTEC Test Centre, which offers an extensive range of testing procedures. Upon successful completion of testing, the drone can be installed into the aeroshell and the launch vehicle. Integration with the launch vehicle, the Ariane 6, occurs at the Guiana Space Centre located in French Guiana. The centre's Payload Preparation Complex (EPCU) facilitates the activities leading up to integration with the launch vehicle [14]. To ensure smooth integration with the launch vehicle, the design must meet mass constraints, volume constraints of the launch vehicle fairing, and the load constraints imposed by the launch environment.

A flow diagram is shown in Figure 18.1, providing an overview of the manufacturing, assembly and integration phases of the production plan.

18.2. Project Design and Development Logic

***Authors**: Maurits, Florian*

While the final preliminary design presented in Chapter 16 incorporates a lot of detail, the project itself is far from over. Therefore, a project design and development logic diagram and post-DSE Gannt chart were created. The project design and development logic is a flow chart depicting the order of activities that have to be performed after the DSE. These activities have been split into eight phases, taking inspiration from the development process used by ESA[5] and NASA[6] .

[4]URL: https://skyrora.com/launch-vehicle-payload-integration/ [cited on 17 June 2024]
[5]URL: https://www.esa.int/Science_Exploration/Space_Science/Building_and_testing_spacecraft [cited on 11 Jun 2024]
[6]URL: https://www.nasa.gov/reference/3-0-nasa-program-project-life-cycle/ [cited on 11 Jun 2024]

First, the Martian drone has to be detailed. Each subsystem must designed in detail, followed by subsystem development testing and software development. Afterwards, several plans have to be created, including manufacturing, integration and operations plans. This phase ends with a critical design review and production readiness review.

After these two reviews, prototypes will be manufactured for each subsystem. This phase, called the prototype manufacturing list, starts with prototype manufacturing, followed by some initial subsystem-level tests to ensure each prototype is manufactured up to standard. The phase only ends after sufficient performance has been achieved.

Following this three prototypes are assembled, specifically the structural and thermal prototype, the engineering prototype, and the qualification prototype. Each prototype undergoes rigorous testing in the prototype testing phase, which ends after sufficient performance is achieved.

The fourth phase is the flight model manufacturing phase. In this phase, the actual flight model is manufactured and assembled. Following this, the flight model is tested rigorously. If the performance of the flight model is sufficient the system goes on to the final phases.

To prepare for the launch a flight readiness review is made, operators are trained, and the launch, operations and ground support are prepared. Afterwards, the Martian Drone is launched. During the journey to Mars, the drone will be maintained and monitored, before arriving on Mars after approximately 7 months[7] . From this point on the drone will collect scientific data, which can be processed and analysed. The drone will also be monitored and maintained throughout its operations. If the drone has deteriorated to an unacceptable extent, the End-of-Life phase is initiated, during which the project is finalized, and the system is shut off.

A Gannt chart is also created for the remaining tasks after the DSE has ended and can be found after the project design and development logic diagram. ESA's project timeline was the base for the time estimates of each phase. Furthermore, the Gantt chart incorporates some margins for each phase in case of unexpected events. Lastly, there is a slight gap between the flight model testing phase and the launch phase due to the launch windows for Mars. Currently, the Martian Drone is scheduled to launch in May of 2035.

[7]URL: https://science.nasa.gov/planetary-science/programs/mars-exploration/mission-timeline/ [cited on 11 Jun 2024]

Preliminary Design (DSE)

Detail Martian Drone Design

Detail Propulsion System Design
Detail Drone Structure Design
Detail EPS Design
Detail Scientific Payload Design
Detail GNC System Design
Detail Thermal Control Design
Detail Design of Communications
Detail Ground Station Design

Detail Rotor Design
Detail Motor Design
Detail Drone Bus Design
Detail Propeller Arm Design
Detail Landing Strut Design
Detail Solar Array Design
Detail Power Storage Design
Detail Wiring Design
Detail Scanning Instruments Design
Detail Robotic Arm Design

Perform Subsystem Development Testing
Finalize Software Development
Create Manufacturing Plan
Develop System Testing Plan
Develop Operations Plan
Develop Integration Plan
Develop Verification and Validation Plan
Refine Risks and Contingency Strategies
Prepare Critical Design Review
Prepare Production Readiness Review

Manufacture Subsystem Prototypes
Manufacture Structure Prototype
Manufacture Propulsion System Prototype
Manufacture Robotic Arm Prototype
Manufacture All Other Subsystems
Perform Structure Stress Test
Perform Rotor Blade Stress Test
Perform Robotic Arm Stress Test
Perform Landing Strut Impact Load Test
Perform Structure Fatigue Test
Perform Rotor Blade Fatigue Test
Perform Robotic Arm Fatigue Test

Perform Subsystem Level VSA Test
Perform Subsystem Level VT Test

Insufficient

Evaluate Performance

Sufficient

Assemble Structural and Thermal Prototype
Assemble Engineering Prototype
Assemble Qualification Prototype
Perform System VSA Test
Perform System TV Test
Perform Environmental Test
Perform System Stress Test
Perform System Fatigue Test
Perform System Performance Test

Evaluate Performance

Sufficient

Insufficient

Manufacture Propulsion System
Manufacture Drone Structure
Manufacture Robotic Arm
Manufacture EPS
Manufacture GNC System
Manufacture Thermal Control System
Manufacture Communication System
Manufacture Scanning Instruments

Assemble Martian Drone Flight Model

Perform Full Scale VSA Test
Perform Software Test
Perform Electronics Test
Perform Full Scale TV Test
Perform Flight Modes/Procedures Test
Perform Communication Test
Perform Navigation and Pointing Test

Evaluate Performance

Insufficient

Sufficient

Prepare Flight Readiness Review

Write Operator Manual/Handbook
Train System Operators
Prepare Launch, Operations and Ground Support

Confirm Support System are Ready for Flight

Proceed to Launch Operations

Transport Drone to Launch Site
Integrate Drone into Launch Vehicle
Launch Martian Drone
Drone Deployment & Operational Testing

Collect Scientific Data
Maintain and Upgrade System
Train Replacement Operators
Process and Analyze Mission Data
Address Problems/Failures

Identify and Update Risks

Apply for Mission Extensions

Evaluate Mission Status

Prepare for Deactivation/ Decommisioning

Shutdown System and Operations

Complete Post-Mission Evaluation Reports

Develop Final Mission Report

End Project

Legend

- Detailed Design Phase
- Prototype Manufacturing
- Prototype Testing
- Flight Model Manufacturing
- Flight Model Testing
- Launch
- Operations
- End-of-Life

ID	Task Name	Duration
1	**1. Create Detailed Drone Design**	**48 months**
2	**1.1. Detail Martian Drone Design**	**30 months**
3	**1.1.1. Detail Propulsion System Design**	**30 months**
4	1.1.1.1. Detail Rotor Design	15 months
5	1.1.1.2. Detail Motor Design	15 months
6	**1.1.2. Detail Drone Structure Design**	**30 months**
7	1.1.2.1. Detail Drone Bus Design	10 months
8	1.1.2.2. Detail Propeller Arm Design	10 months
9	1.1.2.3. Detail Landing Strut Design	10 months
10	**1.1.3. Detail EPS Design**	**30 months**
11	1.1.3.1. Detail Solar Array Design	10 months
12	1.1.3.2. Detail Power Storage Design	10 months
13	1.1.3.3. Detail Wiring Design	10 months
14	**1.1.4. Detail Scientific Payload Design**	**30 months**
15	1.1.4.1. Detail Scanning Instruments Design	15 months
16	1.1.4.2. Detail Robotic Arm Design	15 months
17	1.1.5. Detail GNC System Design	15 months
18	1.1.6. Detail Thermal Control Design	15 months
19	1.1.7. Detail Design of Communications	15 months
20	1.1.8. Detail Ground Station Design	15 months
21	1.2. Perform Subsystem Development Testing	2 months
22	1.3. Finalize Software Development	6 months
23	1.4. Create Manufacturing Plan	3 months
24	1.5. Develop Integration Plan	3 months
25	1.6. Develop System Testing Plan	3 months
26	1.7. Develop Verification and Validation Plan	3 months
27	1.8. Develop Operations Plan	6 months
28	1.9. Refine Risks and Contigency Strategies	2 months
29	1.10. Prepare Critical Design Review	2 months
30	1.11. Prepare Production Readiness Review	2 months
31	**2. Manufacture Prototype**	**18 months**
32	**2.1. Manufacture Subsystem Prototypes**	**6 months**
33	2.1.1. Manufacture Structure Prototype	6 months
34	2.1.2. Manufacture Propulsion System Prototype	6 months
35	2.1.3. Manufacture Robotic Arm Prototype	6 months
36	2.1.4. Manufacture All Other Subsystems Prototypes	6 months
37	**2.2. Perform Structural Tests**	**6 months**
38	2.2.1. Perform Structure Stress Test	3 months
39	2.2.2. Perform Landing Strut Impact Load Test	3 months
40	2.2.3. Perform Structure Fatigue Test	3 months
41	2.2.4. Perform Rotor Blade Stress Test	3 months
42	2.2.5. Perform Rotor Blade Fatigue Test	3 months
43	2.2.6. Perform Robotic Arm Stress Test	3 months
44	2.2.7. Perform Robotic Arm Fatigue Test	3 months
45	2.3 Perform Subsystem Level VSA Test	3 months
46	2.4 Perform Subsystem Level TV Test	3 months
47	**3. Test Prototype**	**18 months**
48	**3.1. Assemble Prototypes**	**6 months**
49	3.1.1. Assemble Structural and Thermal Prototype	6 months
50	3.1.2. Assemble Engineering Prototype	6 months
51	3.1.3. Assemble Qualification Prototype	6 months
52	**3.2 Perform System Tests**	**12 months**
53	3.2.1. Perform System VSA Test	6 months
54	3.2.2. Perform System Stress Test	3 months
55	3.2.3. Perform System Fatigue Test	3 months
56	3.2.4. Perform System TV Test	6 months
57	3.2.5. Perform Environmental Test	6 months
58	3.2.6. Perform System Performance Test	6 months
59	**4. Manufacture Flight Model**	**18 months**
60	**4.1. Manufacture Flight Model Subsystems**	**8 months**
61	4.1.1. Manufacture Propulsion System	8 months
62	4.1.2. Manufacture Drone Structure	8 months
63	4.1.3. Manufacture Robotic Arm	8 months
64	4.1.4. Manufacture EPS	8 months
65	4.1.5. Manufacture GNC System	8 months
66	4.1.6. Manufacture Thermal Control System	8 months
67	4.1.7. Manufacture Communication System	8 months
68	4.1.8. Manufacture Scanning System	8 months
69	4.2. Assemble Martian Drone Flight Model	10 months
70	**5. Test Flight Model**	**18 months**
71	5.1. Perform Full Scale VSA Test	5 months
72	5.2. Perform Full Scale TV Test	5 months
73	5.3. Perform Software Test	5 months
74	5.4. Perform Flight Modes/Procedures Test	5 months
75	5.5. Perform Electronics Test	5 months
76	5.6. Perform Communication Test	5 months
77	5.7. Perform Navigation and Pointing Test	8 months
78	**6. Launch Martian Drone**	**6 months**
79	6.1. Prepare Flight Readiness Review	2 months
80	**6.2. Prepare Launch and Operations**	**3 months**
81	6.2.1. Write Operator Manual/Handbook	3 months
82	6.2.2. Train System Operators	3 months
83	6.2.3. Prepare Launch, Operations and Ground Support	3 months
84	6.2.4. Confirm Support System are Ready for Flight	1 month
85	**6.3. Perform Launch Operations**	**1 month**
86	6.3.1. Transport Drone to Launch Site	0.5 months
87	6.3.2. Integrate Drone into Launch Vehicle	0.5 months
88	***Launch Martian Drone***	0 months
89	**7. Perform Operations**	**36 months**
90	7.1. Drone Deployment & Operational Testing	3 months
91	7.2. Collect Scientific Data	12 months
92	7.3. Process and Analyze Mission Data	12 months
93	7.4. Maintain and Upgrade System	31 months
94	7.5. Address Problems/Failures	31 months
95	7.6. Train Replacement Operators	36 months
96	7.7. Identify and Update Risks	3 months
97	7.8. Apply for Mission Extensions	1 month
98	**8. Perform End-of-Life Iterations**	**5 months**
99	8.1. Prepare for Deactivation/Decommisioning	1 month
100	8.2. Shutdown System and Operations	1 month
101	8.3. Complete Post-Mission Evaluation Reports	1 month
102	8.4. Develop Final Mission Report	1 month
103	8.5. End Project	1 month

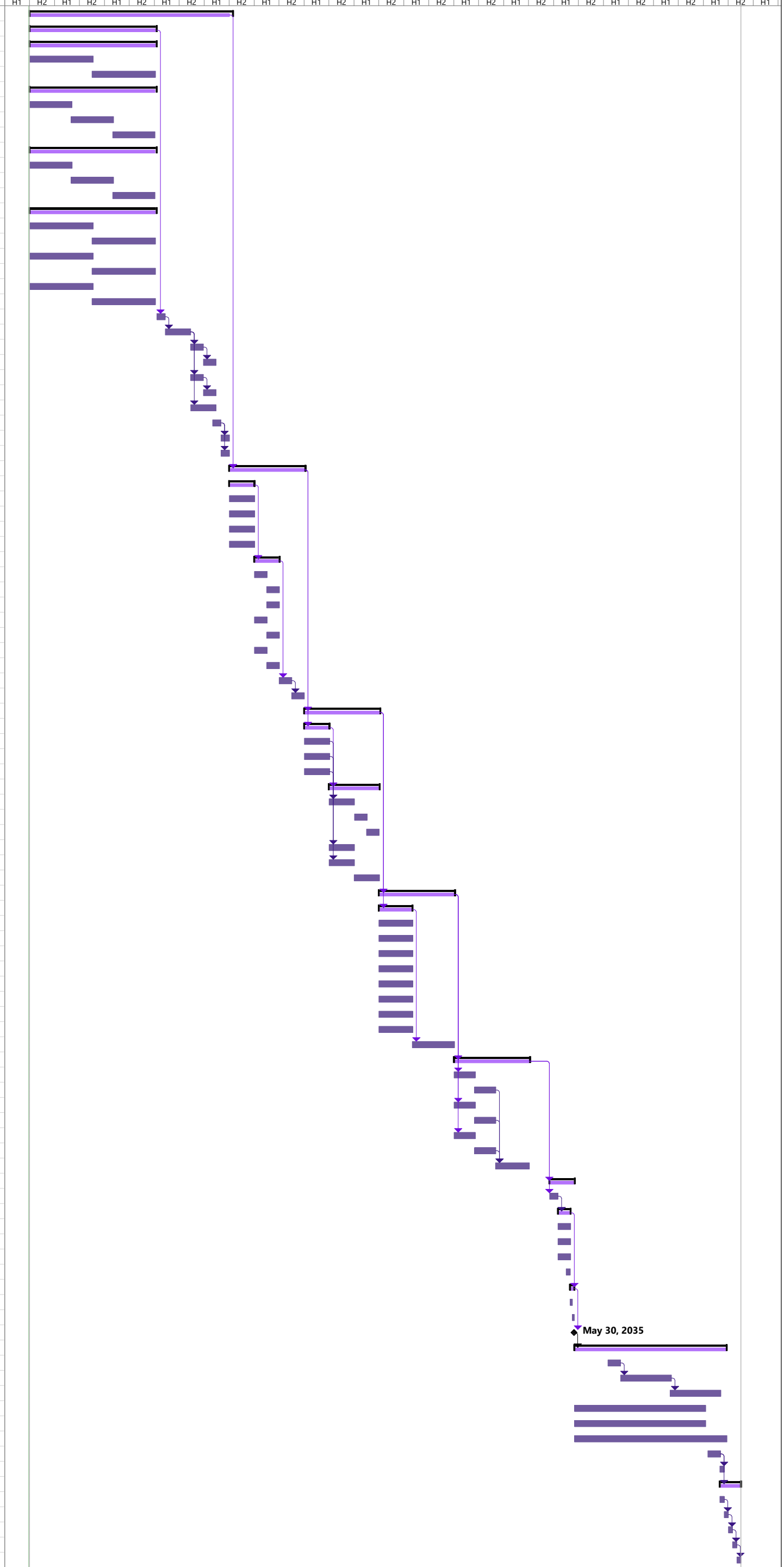

Project: PDDL
Date: Jun 25 '24

Task	Project Summary	Manual Task	Start-only	Deadline			
Split	Inactive Task	Duration-only	Finish-only	Progress			
Milestone	Inactive Milestone	Manual Summary Rollup	External Tasks	Manual Progress			
Summary	Inactive Summary	Manual Summary	External Milestone				

18.3. Cost Breakdown Structure

***Authors**: Vincent, Maurits*

The following section presents the cost breakdown structure of the post-DSE activities. From the activities defined in Section 18.2, the elements driving the future costs were identified, and the future mission phase-specific costs were estimated.

Certain assumptions had to be made so that the analysis could be performed. First, it was assumed that the project would be developed in-house except for part manufacturing, as no agency has yet acquired the project. The second one consisted of assuming an initial fund allocation of 30 000 000€ to the development of workshops and offices, and another 300 000€ per phase for the required upkeep of these infrastructures. The workspace cost is based on the cost required to build a 3600 m^2 clean room capable of hosting three drone prototypes[8] , as well as the purchase of an industrial property[9] and required renovations and furnishing.

The number of employees required to develop the drone varies with the phases. The most intensive phase is the detailed design phase, which was estimated to require a team of 60 engineers and a management team of 15 employees. While the management team stays constant throughout, the engineering team decreases to 40 engineers for the phases after the detailed design. Since the drone is autonomous, less maintenance is necessary, therefore the engineering team is reduced further to 30. Lastly, the team is reduced to 15 for the end-of-life phase, as most engineers will likely be reassigned to more important future projects. The employees' salaries have been assumed to be equal for management and engineering. The monthly wage estimate is based on ESA's net wage for low-experienced engineers[10] and converted to gross wage[11] . This results in an estimated cost 11 000€ per month per employee. The licences required for the engineers to perform their work efficiently have been assumed to be 50€ per month per engineer.

In the case of testing, the hourly rate has been assumed to be 150€ per hour, based on a cost estimation from the Delft University of Technology's Aircraft Hall[12] . While the different prototypes and final flight models will be assembled in-house, the part acquisition costs have been taken from the previous sections' defined cost estimates. Due to a lack of information, the part manufacturing costs have not been considered in this analysis.

It is assumed that the drone will be launched with an Ariane 6, with a launch cost of 77 000 000€.Based on these assumptions and the durations defined in Section 18.2, the total mission cost can be estimated to be 219 825 374€ FY2024. Due to the significant number of assumptions presented to achieve this result, the total cost must be considered with high uncertainty.

[8]URL: https://www.mecart-cleanrooms.com/learning-center/cost-cleanroom-per-square-foot/ [cited on 19 June 2024]
[9]URL: https://www.fundainbusiness.nl/en/bedrijfshal/oldenzaal/object-43419321-newtonstraat-14/ [cited on 19 June 2024]
[10]URL: https://esamultimedia.esa.int/docs/careers/Table_Staff_Salaries.pdf [cited on 18 June 2024]
[11]URL: https://thetax.nl/ [cited on 19 June 2024]
[12]Communication with Dave Ruijtenbeek, dd. 28 Jun 2024

0
Martian Drone
€ 219 825 374

1
Detailed Design Phase
€ 69 856 500

1.1
Personnel
75 | € 39 600 000

1.1.1
Management
15 | € 7 920 000

1.1.2
Engineering
60 | € 31 680 000

1.2
Hardware and Licences
€ 256 500

Laptop:€ 1500
Licence:€ 50/month

1.3
Workspace
€ 30 000 000

Property: € 2 250 000
Renovation:€ 2 000 000
Clean room:€ 23 250 056
Amenities:€ 2 500 000

2
Prototype Manufacturing
€ 13 720 143

2.1
Personnel
55 | € 10 890 000

2.1.1
Management
15 | € 2 970 000

2.1.2
Engineering
40 | € 7 920 000

2.2
Hardware and Licences
€ 36 000

2.3
Workspace Upkeep
€ 300 000

2.4
3x Prototypes
€ 2 350 143

2.4.1
Manufactured Parts
€ 84 891

Mat Rotor Arm:€ 6 559.20
Mat Struts:€ 805.40
Mat Bus:€ 56 002.60
Mat Rotor Blades:€ 21 012.50
Mat Rock Fondler:€ 171
Safety: 1.5x

2.4.2
COTS
€ 2 265 252

EPS:€ 2 061 000
PLD:€ 128 649
GNC:€ 75 603

2.5
Structural Testing
€ 144 000

3
Prototype Testing
€ 11 511 000

3.1
Personnel
55 | € 10 890 000

3.1.1
Management
15 | € 2 970 000

3.1.2
Engineering
40 | € 7 920 000

3.2
Hardware and Licences
€ 36 000

3.3
Workspace Upkeep
€ 300 000

3.4
Prototype Testing
€ 288 000

4
Flight Model Manufacturing
€ 12 009 381

4.1
Personnel
55 | € 10 890 000

4.1.1
Management
15 | € 2 970 000

4.1.2
Engineering
40 | € 7 920 000

4.2
Hardware and Licences
€ 36 000

4.3
Workspace Upkeep
€ 300 000

4.4
Flight Model
€ 783 381

4.4.1
Manufactured Parts
€ 28 297

Mat Rotor Arm:€ 2 185.80
Mat Struts:€ 268.50
Mat Bus:€ 18 667.50
Mat Rotor Blades:€ 7004.20
Mat Rock Fondler:€ 171

4.4.2
COTS
€ 755 084

EPS:€ 687 000
PLD:€ 42 883
GNC:€ 25 201

5
Flight Model Testing
€ 11 658 600

5.1
Personnel
55 | € 10 890 000

5.1.1
Management
15 | € 2 970 000

5.1.2
Engineering
40 | € 7 920 000

5.2
Hardware and Licences
€ 36 000,00

5.3
Workspace Upkeep
€ 300 000,00

5.4
Prototype Testing
€ 432 000

6
Launch
€ 80 942 000

6.1
Personnel
55 | € 3 630 000

6.1.1
Management
15 | € 990 000

6.1.2
Engineering
40 | € 2 640 000

6.2
Hardware and Licences
€ 12 000

6.3
Workspace Upkeep
€ 300 000

6.4
Launch
€ 77 000 000

7
Operations
€ 18 174 000

7.1
Personnel
45 | € 17 820 000

7.1.1
Management
15 | € 5 940 000

7.1.2
Engineering
30 | € 11 880 000

7.2
Hardware and Licences
€ 54 000

7.3
Workspace Upkeep
€ 300 000

8
End-of-life
€ 1 953 750

8.1
Personnel
30 | € 1 650 000

8.1.1
Management
15 | € 825 000

8.1.2
Engineering
15 | € 825 000

8.2
Hardware and Licences
€ 3 750

8.3
Workspace Upkeep
€ 300 000

Legend

ID
Phase
Number of Employees | Cost per Phase

19 Conclusion

***Authors**: Jesse, Salar*

With recent advancements in Martian exploration, highlighted by the successful flight of Ingenuity on April 19 2021, the feasibility of propelled flight on Mars was demonstrated. As such, this report set out to provide a preliminary design of the Martian Explorer for Astrobiological and Lithological Studies (MEALS), a hexacopter capable of continuous flight for 30 minutes on Mars, a flight range of 20 kilometres and identification, collection and transportation of three kilograms of Martian rocks. The aim of this report was to provide an overview of the design process and how a preliminary design was established. This was done through the development of various technical subsystems, while also taking sustainability and the current market landscape into account. Additionally, the report looked into the feasibility of the final design and discussed future developments of the project.

A market analysis was first conducted, in which an initial cost target for the project was developed, such that a competitive budget could be determined. The analysis revealed a competitive yearly target cost of $30M. With a total mission length of 12 years, a total cost of $360M was assumed.

A sustainability strategy highlighted the way the mission contributed to sustainability efforts. End-of-life, environmental, social and economic sustainability contributions were investigated. Operations at the system's end-of-life conditions included different scenarios. In terms of environmental sustainability, the Martian Drone project aimed to align with the United Nations Sustainable Development Goals by considering sustainable production methods and the product's overall contribution to sustainability. Other United Nations Sustainable Development Goals were taken into account to ensure social and economic sustainability.

The operations and logistics of the mission were also discussed. All aspects of the mission timeline from launch operations to entry, descent and landing and surface operations on Mars were covered. The Mars 2020 aeroshell was chosen as the entry capsule. The flight profile for a typical mission was also presented, revealing a total flight time of 1560 s.

The preliminary design involved the development of various subsystems. First, the propulsion system was discussed. A methodology based on the blade element momentum theory was used throughout the process. Three different airfoils were selected, showing improved performance for low Reynolds numbers compared to nominal airfoils. Lastly, an optimisation algorithm based on an evolutionary algorithm was implemented to maximise in-flight performance and minimise the rotor's power consumption. Three blades per rotor, having a radius of 1.2 m, were considered, together capable of achieving a thrust-to-weight ratio of 1.3. A figure of merit of 0.65 was found, 7 % higher than Ingenuity's rotor. The NOVA 1 motor was selected, which proved to provide sufficient performance characteristics.

The development of the electrical power system involved the analysis of power generation throughout the Martian year. Power generation was achieved with 3 m^2 photovoltaic solar panels, whereas a 2375 W h Lithium-ion battery was selected for power storage. The influence of environmental challenges, including dust, radiation and electromagnetic spectrum shift, was also investigated, showing significant design implications for the subsystem. With an efficiency of 32 % at nominal conditions, the Quadruple Junction GaAs Solar Cell from Azur Spaces were currently found to be the best-performing solar cells and were therefore selected. The analysis led to an array of the architecture of 900 cells in a 20S45P configuration.

The thermal control subsystem focused on maintaining the systems' temperature within the operational temperature range. For this, solar radiation, albedo, black-body planetary radiation, and convection were considered during the analysis. To maintain the operating temperatures of the motors and batteries, cooling fins were added to the former, whereas heating foils were investigated for the latter. The final subsystem design was based on an optimisation process, with no system exceeding its operational temperature range.

The system design also entailed the design of the guidance, navigation and control subsystem. Together with numerous sensors, the Lidar-Visual-Inertial odometry algorithm LVI-SAM will determine the drone's state and position. The main advantages of this framework were its high robustness, high accuracy and

effectiveness in feature-less environments. Sensors consist of a fisheye camera, Lidar, Inertial Measurement Unit, Inclinometer and a Sun Sensor. A preliminary flight computer and controller were also developed. Additionally, a nonlinear dynamic model of the hexacopter was simulated and a cascaded PID-like controller was implemented. Controllability was verified by analysis of a short flight, proving stability, controllability and achievability of the flight profile. Simulations also showed that the drone landed with a landing distance accuracy smaller than 0.38 m in more than 95% of the cases.

The payload of the drone consists of various instruments. For the spectrometer, the MicrOmega device was chosen, due to its low weight and low power consumption. The artificial light source needed to illuminate the sample is a tungsten-halogen light, while an RGB camera and Multispectral camera would be used to generate a 3D mapping of the selected area. A rock identification algorithm was also created for rock identification. A birds-eye and a close-up scanning mode were also decided on, scanning at the height of 75 m and 10 m, respectively.

To maintain communication with the ground station, a communications subsystem was developed. By calculating the data budget and the link budget, it was found that a monopole antenna would suffice for drone communication.

Next, a method was presented to size the rotor arms, bus and landing struts, and loading scenarios were distinguished. An optimization tool has also been developed to specify the exact geometry and material of the beam. Materials were selected using Ansys Granta EduPack software. For both the landing struts and rotor arms, beryllium, along with a hollow rectangular shape, were found to be the optimal material and cross-section. The bus was shaped as a hexagonal, made from Cyanate Ester/Carbon Fibre. The rotor blades were chosen to be made from Cyanate Ester/HM Carbon Fibre.

To pick up the Martian rocks, a design for a robotic arm was provided. This will be achieved by a claw, specifically designed as a peel-clamshell hybrid grabber. The claw will allow the drone to pick up and store $10\,cm^3 \times 10\,cm^3 \times 10\,cm^3$ of rocks. It was decided that for all parts of the robotic arms, BMI/HS carbon fibre will be used, due to its high durability against UV radiation. Different motor-gearbox combinations were also chosen for the robotic arm, derived from Maxon Group's catalogue. A total cost of 3631.91€ was estimated for the arm.

Finally, various recommendations can be made moving forward with the design. For the propulsion system, scheduling constraints meant it was not possible to select airfoils with the same level of detail as the rest of the blade; numerical data from literature had to be used. In a detailed design phase, parametrisation of different airfoil options via their chordwise thickness and camber distributions, potentially divided into stations within the chord to facilitate iteration. Besides an optimisation algorithm, a further level of detail could be added by carrying out computational fluid dynamics simulations of different airfoils; this could be extended to the rotor blade as well as the full helicopter to avoid the need for empirical relations to estimate drag.

Structural considerations in the rotor design were also based on literature; this calls for the use of aerostructural simulations to extract flapping and lagging dynamics of the blade, as well as exact displacements. Combining these with finite-element vibrational analysis would be valuable in both reaching a more optimised design, as well as adding precision to the performance analysis. Within the structure, a more detailed finite-element analysis of the full hexacopter should be carried out to appropriately validate the design. Alongside this, the detailed design of the joints for the folding mechanism is essential, as missing the dimensional constraints would warrant the need for a new aeroshell.

The electrical power and thermal control subsystems were closely tied in the system-wide iteration, and throughout the process, it was concluded that a more concurrent development process would likely improve the final design. Ideally, an integrated design tool for these two subsystems would be preferred. Once that is achieved, integration with the propulsion subsystem would allow for direct inclusion of thermal limitations in performance analysis. Within the thermal control system itself, it is recommended to integrate the avionics and power distribution boards into the insulation, as well as implement a more active heating system so that heat-sensitive components can start functioning at their optimal temperatures.

Within the payload subsystem, it is recommended to select more customised sensors and cameras, or develop these in-house. While costs would go up, scientific equipment is instrumental to the success of the mission. The last priority would be to do so for the rotor motors, as the selected motor already has relatively high customisation potential at a fixed cost. Overall, the work documented in this report should serve as a necessary foundation to successfully finalise the MEALS project, and deliver the next breakthrough in planetary science.

References

[1] Chaired by M. Mischna Mars Concurrent Exploration Science Analysis Group and B. Horgan. *MEPAG MCE-SAG Final Report (2023)*. Tech. rep. Mars Exploration Program Analysis Group, July 2023, pp. 1–94.

[2] Manfred "Dutch" von Ehrenfried. *Perseverance and the Mars 2020 Mission: Follow the Science to Jezero Crater*. Springer, 2022.

[3] M. Golombek et al. "Selection of the Mars Science Laboratory Landing Site". In: *Space Science Reviews* 170.1–4 (July 2012), pp. 641–737.

[4] Ehouarn Millour et al. "The Mars Climate Database (Version 6.1)". In: (Sept. 2022).

[5] Melissa S. Rice et al. "A detailed geologic characterization of Eberswalde crater, Mars". In: *MARS* 8 (May 2013), pp. 15–57.

[6] J.F.W. Koning, E.A. Romander, and W. Johnson. *Comparison of Mars Aircraft Propulsion Systems*. Tech. rep. NASA/CR—2003-212350. NASA - Glenn Research Center, May 2003.

[7] Wayne Johnson. *Rotorcraft Aeromechanics*. Cambridge Aerospace Series. Cambridge University Press, Apr. 2013.

[8] Tixiao Shan et al. *LVI-SAM: Tightly-coupled Lidar-Visual-Inertial Odometry via Smoothing and Mapping*. 2021.

[9] N. K. McKeown and M. S. Rice. "Detailed Mineralogy of Eberswalde Crater". In: *42nd Annual Lunar and Planetary Science Conference*. Lunar and Planetary Science Conference. Mar. 2011, p. 2450.

[10] Federico Furlán et al. "CNN Based Detectors on Planetary Environments: A Performance Evaluation". In: *Frontiers in Neurorobotics* 14 (Oct. 2020).

[11] Hou Zhenlong et al. "Intelligent Lithology Identification Methods for Rock Images Based on Object Detection". In: *Natural Resources Research* 32.6 (Oct. 2023), pp. 2965–2980.

[12] Vaitua Leroi, Jean-Pierre Bibring, and Michel Berthe. "Micromega/IR: Design and status of a near-infrared spectral microscope for in situ analysis of Mars samples". In: *Planetary and Space Science* 57.8–9 (July 2009), pp. 1068–1075.

[13] Nacer Chahat et al. "The Mars Helicopter Telecommunication Link: Antennas, Propagation, and Link Analysis". In: *IEEE Antennas and Propagation Magazine* 62.6 (Dec. 2020), pp. 12–22.

[14] Arianespace. *Ariane 6 User's Manual*. 2021.

[15] David W. Way et al. "Mars Science Laboratory: Entry, Descent, and Landing System Performance". In: *2007 IEEE Aerospace Conference*. IEEE, 2007.

[16] RJ Hamann and MJL van Tooren. *Systems Engineering & Technical Management Techniques - part 1*. en. CD-rom, reader. Delft University of Technology, Faculty Aerospace Engineering, 2003.

[17] *The Sustainable Development Goals Report 2023 : Special Edition*. New York: United Nations, Oct. 2023.

[18] Emmanuel Aramendia et al. "Global energy consumption of the mineral mining industry: Exploring the historical perspective and future pathways to 2060". In: *Global Environmental Change* 83 (Dec. 2023), p. 102745.

[19] Vincenzo Lunetto et al. "Sustainability in the manufacturing of composite materials: A literature review and directions for future research". In: *Journal of Manufacturing Processes* 85 (Jan. 2023), pp. 858–874.

[20] Karl T. Edquist et al. "Analysis of Mars 2020 Entry Vehicle Aerothermal Flight Data". In: *Journal of Spacecraft and Rockets* 60.4 (July 2023), pp. 1201–1219.

[21] Shannah Withrow et al. "Mars Science Helicopter Conceptual Design". In: *ASCEND 2020*. American Institute of Aeronautics and Astronautics, Nov. 2020.

[22] Witold J. Koning, Ethan A. Romander, and Wayne Johnson. "Optimization of Low Reynolds Number Airfoils for Martian Rotor Applications Using an Evolutionary Algorithm". In: *AIAA Scitech 2020 Forum*. American Institute of Aeronautics and Astronautics, Jan. 2020.

[23] Phillip M. Munday et al. "Nonlinear Lift on a Triangular Airfoil in Low-Reynolds-Number Compressible Flow". In: *Journal of Aircraft* 52.3 (May 2015), pp. 924–931.

[24] F.J. Argus, Ament G.A., and Koning W.J.F. *NDARC NASA Design and Analysis of Rotorcraft*. Tech. rep. NASA/TP-2015-218751. 2020.

[25] I.S. Bensignor. *Development of a Propulsion Rotor Performance Model for Ultra-Low Reynolds Number Flow (Re < 105)*. Tech. rep. The Ohio State University, 2021.

[26] Bruni L. "Aerodynamic performance of different airfoils for a future Mars Helicopter". Master's thesis. Politecnico Di Torino, 2020.

[27] Han Yang and Ramesh K. Agarwal. "CFD Simulations of a Triangular Airfoil for Martian Atmosphere in Low-Reynolds Number Compressible Flow". In: *AIAA Aviation 2019 Forum*. American Institute of Aeronautics and Astronautics, June 2019.

[28] Mohamad Faiz Ahmad et al. "Differential evolution: A recent review based on state-of-the-art works". In: *Alexandria Engineering Journal* 61.5 (May 2022), pp. 3831–3872.

[29] D.G. Mayer, B.P. Kinghorn, and A.A. Archer. "Differential evolution – an easy and efficient evolutionary algorithm for model optimisation". In: *Agricultural Systems* 83.3 (Mar. 2005), pp. 315–328.

[30] Wayne Johnson. *NDARC NASA Design and Analysis of Rotorcraft*. Technical Publication NASA/TP-2015-218751. NASA Ames Research Center, 2017.

[31] Wiley J. Larson and J.R. Wertz. *Space Mission Analysis and Design*. en. 3rd ed. Space Technology Library. Dordrecht, Netherlands: Springer, Sept. 1999.

[32] Claire Newman et al. "Toward More Realistic Simulation and Prediction of Dust Storms on Mars". In: *Vol. 53, Issue 4 (Planetary/Astrobiology Decadal Survey Whitepapers)* 53.4 (Mar. 2021).

[33] Geoffrey A. Landis and Thomas W. Kerslake. *Mars Solar Power*. Tech. rep. NASA: Glenn Research Center, Nov. 2004.

[34] Geoffrey A. Landis. "Dust obscuration of Mars solar arrays". In: *Acta Astronautica* 38.11 (June 1996), pp. 885–891.

[35] M. T. Lemmon et al. "Lifting and Transport of Martian Dust by the Ingenuity Helicopter Rotor Downwash as Observed by High-Speed Imaging From the Perseverance Rover". In: *Journal of Geophysical Research: Planets* 127.12 (Dec. 2022).

[36] Lyndsey McMillon-Brown et al. "A study of photovoltaic degradation modes due to dust interaction on Mars". In: *Solar Energy Materials and Solar Cells* 221 (Mar. 2021), p. 110880.

[37] Geoffrey Landis and Dan Hyatt. "The Solar Spectrum on the Martian Surface and its Effect on Photovoltaic Performance". In: *2006 IEEE 4th World Conference on Photovoltaic Energy Conference*. IEEE, 2006.

[38] Donald M. Hassler et al. "Mars' Surface Radiation Environment Measured with the Mars Science Laboratory's Curiosity Rover". In: *Science* 343.6169 (Jan. 2014).

[39] K.S. Jefferies. *Analysis of Costs of Gallium Arsenide and Silicon Solar Arrays for Space Power Applications*. Tech. rep. 19810011645. Mar. 1981.

[40] Yuliya Preger et al. "Degradation of Commercial Lithium-Ion Cells as a Function of Chemistry and Cycling Conditions". In: *Journal of The Electrochemical Society* 167.12 (Jan. 2020), p. 120532.

[41] Fabio Acquaviva. "Mars Drone Design & Thermal Analysis". Master's thesis. Politecnico Di Torino, 2019.

[42] Stefano Cappucci and Michael T Pauken. "Thermal performance of Ingenuity, the Mars Helicopter". In: *International Conference on Environmental Systems*. 51st International Conference on Environmental Systems, July 2022.

[43] Gaetano Quattrocchi et al. “The thermal control system of NASA’s Curiosity rover: a case study”. In: *IOP Conference Series: Materials Science and Engineering* 1226.1 (Feb. 2022), p. 012113.

[44] Stephane Gendron et al. “Phoenix Mars Lander Mission: Thermal and CFD Modeling of the Meteorological Instrument based on Flight Data”. In: *40th International Conference on Environmental Systems*. American Institute of Aeronautics and Astronautics, July 2010.

[45] F.P. Incropera et al. *Fundamentals of Heat and Mass Transfer*. 6th ed. Nashville, TN: John Wiley & Sons, Sept. 2006.

[46] Byoung Hoon An, Hyun Jung Kim, and Dong-Kwon Kim. “Nusselt number correlation for natural convection from vertical cylinders with vertically oriented plate fins”. In: *Experimental Thermal and Fluid Science* 41 (Sept. 2012), pp. 59–66.

[47] Sherif A. S. Mohamed et al. “A Survey on Odometry for Autonomous Navigation Systems”. In: *IEEE Access* 7 (2019), pp. 97466–97486.

[48] Julius A. Marshall, Wei Sun, and Andrea L’Afflitto. “A survey of guidance, navigation, and control systems for autonomous multi-rotor small unmanned aerial systems”. In: *Annual Reviews in Control* 52 (2021), pp. 390–427.

[49] David S. Bayard et al. “Vision-Based Navigation for the NASA Mars Helicopter”. In: *AIAA Scitech 2019 Forum*. American Institute of Aeronautics and Astronautics, Jan. 2019.

[50] S. Molli et al. “Design and performance of a Martian autonomous navigation system based on a smallsat constellation”. In: *Acta Astronautica* 203 (Feb. 2023), pp. 112–124.

[51] Kattupalli Venkateswara Rao and Abraham T. Mathew. “Dynamic modeling and control of a hexacopter using PID and back stepping controllers”. In: *2018 International Conference on Power, Signals, Control and Computation (EPSCICON)*. IEEE, Jan. 2018.

[52] Henry Stark and John W Woods. *Probability and random processes with applications to signal processing*. 3rd ed. Pearson, 2002.

[53] Zhiping He et al. “Spectrometers based on acousto-optic tunable filters for in-situ lunar surface measurement”. In: *Journal of Applied Remote Sensing* 13.02 (June 2019).

[54] Sean Borman and Robert L. Stevenson. *Spatial Resolution Enhancement of Low-Resolution Image Sequences A Comprehensive Review with Directions for Future Research*. Tech. rep. Lab. Image and Signal Analysis, University of Notre Dame, July 1998.

[55] Russell C Hibbeler. *Mechanics of materials in SI units*. en. Sept. 2017.

[56] T H G Megson. *Aircraft Structures for Engineering Students*. en. Elsevier, 2017.

[57] NASA Standard. *Structural Design and Test Factors of Safety for Spaceflight Hardware*. Version B w/CHANGE 3. ACTIVE. NASA HQ, Office of the Chief Engineer, Aug. 6, 2014.

[58] Niels Leergaard Pedersen. “Stress concentration and optimal design of pinned connections”. In: *The Journal of Strain Analysis for Engineering Design* 54.2 (Feb. 2019), pp. 95–104.

[59] B.T.C. Zandbergen. *Spacecraft (bus/platform) design and sizing*. Delft University of Technology, 2021.

[60] Michael F Ashby. *Materials Selection in Mechanical Design*. en. 2nd ed. Oxford, England: Butterworth-Heinemann, June 1999.

[61] R. Sullivan et al. “Cohesions, friction angles, and other physical properties of Martian regolith from Mars Exploration Rover wheel trenches and wheel scuffs”. In: *Journal of Geophysical Research* 116.E2 (Feb. 2011).

[62] ANSYS Inc. *Ansys GRANTA EduPack software*. Version 2023 R2. Cambridge, UK, 2024.

[63] H.W. Jones. *Common Cause Failures and Ultra Reliability*. Technical Publication. NASA Ames Research Center, 2012.

[64] Silverman M. and Lin J. *Mars 2020 Rover Adaptive Caching Assembly: Caching Martian Samples for Potential Earth Return*. Tech. rep. 20220000873. NASA, May 2020.